MAGNETIC RESONANCE IMAGING AND SPECTROSCOPY IN THE FEMALE PELVIS

BY

LANETTE FRIESEN

A Thesis Submitted to the
Faculty of Graduate Studies
in Partial Fulfillment of the Requirements
for the Degree of

DOCTOR OF PHILOSOPHY

Interdisciplinary Program
Departments of Physics and Chemistry
University of Manitoba
Winnipeg, Manitoba, Canada

And

Institute for Biodiagnostics
National Research Council
Winnipeg, Manitoba, Canada

THE UNIVERSITY OF MANITOBA

FACULTY OF GRADUATE STUDIES

*****

COPYRIGHT PERMISSION PAGE

MAGNETIC RESONANCE IMAGING AND SPECTROSCOPY IN THE FEMALE PELVIS

BY

LANETTE FRIESEN

A Thesis/Practicum submitted to the Faculty of Graduate Studies of The University of Manitoba in partial fulfillment of the requirements of the degree of DOCTOR OF PHILOSOPHY

ABSTRACT

The work presented in this thesis involves magnetic resonance imaging (MRI) and spectroscopy (MRS) in the female pelvis. The ability of MRS to grade pre-cancerous lesions of the uterine cervix was examined, and a technique for acquisition of *in vivo* MR spectra of the human ovary was developed.

Cancer of the uterine cervix is thought to be preceded by dysplastic lesions called cervical intraepithelial neoplasia (CIN). Current methods of grading the degree of CIN are subject to high inter- and intra-observer variability. In this study, one dimensional ^{1}H MR spectra were obtained from biopsies of the uterine cervix. Multivariate methods of analysis were employed to classify the spectra according to the clinical diagnoses of non-dysplastic, CIN grade 1 (CIN 1), CIN 2, and CIN 3.

The differences in the MR spectra were small, making classification difficult. A set of spectra were consistently misclassified by each of the multivariate methods. It was concluded that either the clinical diagnoses were inaccurate, or the MRS technique detected biochemical changes that were not morphologically manifest. The accuracy of classification of spectra into two adjacent classes was comparable to that of non-adjacent classes. This result did not support, but can not refute, the theory that cervical lesions follow a continuous progression from CIN 1 to CIN 3.

Detection and accurate diagnosis of abnormalities of the ovaries is difficult because the ovaries are situated deep within the pelvis, making them inaccessible to examination. In this study, three aspects of *in vivo* MR spectroscopy of the ovaries were examined. First, the most suitable coils for transmitting and receiving signal from the ovaries at 1.5 Tesla were chosen. Second, methods of locating the ovaries in the MR images were examined. Third, a method of obtaining spectra from the ovaries was designed that compensated for motion within the pelvis.

It was found that the whole body coil could be used to obtain uniform excitation within the pelvis. A circularly polarized surface coil was used to receive the signal rather than the whole body coil because it gave better signal to noise ratios. Premenopausal ovaries were most easily identified in T_2-weighted images, and postmenopausal ovaries were identified in T_1-weighted images. Fast scout images were obtained periodically during spectroscopic acquisition in order to track the motion of the ovary as it was displaced by the expanding urinary bladder. Pelvic motion caused frequency shifts and phase changes in the individual acquisitions of the FID. Correction prior to averaging yielded a significant improvement in the signal to noise ratio.

It was concluded that magnetic resonance imaging and spectroscopy can be used to examine structures in the female pelvis. ^{1}H MRS, in conjunction with multivariate methods, provided information regarding the progression of dysplastic lesions of the uterine cervix. Techniques developed in this thesis may be used to obtain *in vivo* MR spectra from the human ovary.

ACKNOWLEDGEMENTS

First and foremost, I would like to express my gratitude to my supervisor, Dr. Ian C. P. Smith, for his support and continuous encouragement throughout my research.

I would also like to thank the members of my advisory committee – Dr. Jeff Bews for numerous helpful suggestions, Dr. Norm Davison for encouraging me, prodding me, and always making time for conversations in his office, Dr. Ted Schaefer for his understanding and wisdom, and Dr. Joe O'Neil for readily becoming a member of my committee in my last year.

Several colleagues at the Institute for Biodiagnostics, National Research Council, have made this work possible. I thank Dr. Tedros Bezabeh for being my chemistry consultant, but more importantly, for being a good friend and always bringing me a reason to smile, Dr. Jonathan Sharp for his expertise in *in vivo* MRS, Anne Daley for her support, Dr. Eduardo Krupnik for his friendship, and also for teaching me anatomy and physiology, Dr Jian-Ming Zhu for patiently answering all my MR questions, and Dr. Laura McIntosh for proof-reading portions of my thesis. I would especially like to thank Scott King. Without his friendship, encouragement, and discussions regarding our theses, this thesis would not have been possible.

I would like to thank my medical collaborators – Drs. Fernando Guijon, Mark Heywood, Gary Krepart, Robert Lotocki, and Maria Paraskevas. Special thanks is given to the staff at the St. Bonface MRI Centre for their willingness to teach me the practical aspects of MR imaging, and Patrick Purtill who spent countless hours sharing his knowledge of the hardware of MRI systems.

Most of all, I would like to thank David Waldner, and my family. David's support, care, and constant faith in me helped me to see this work through. My family's love, support, and belief that I could accomplish my goals kept me going through many hard times. Most importantly, I thank my parents for supporting my choices, for teaching me to see the joy in all my activities, and especially, for always being proud of me.

TABLE OF CONTENTS

LIST OF FIGURES

LIST OF TABLES

LIST OF ABBREVIATIONS AND SYMBOLS

ANN	Artificial Neural Network
$\mathbf{B}_o$	static magnetic field
$\mathbf{B}_1$	radio frequency magnetic field
CHESS	CHEmical Shift Selective
CIN	Cervical Intraepithelial Neoplasia
CIS	Carcinoma *In Situ*
CP	Circularly Polarized
CT	Computed Tomography
E	Energy
EFS	Enhanced Forward Selection
FFT	Fast Fourier Transform
FID	Free Induction Decay
FISP	Fast Imaging with Steady-state Precession
FSH	Follicular Stimulating Hormone
FWHM	Full Width, Half Maximum

G	gradient magnetic field
H	Hamiltonian
$\hbar$	$h/2\pi$
h	Planck's constant
HPV	Human PapillomaVirus
Hz	Hertz
I	nuclear spin angular momentum
IDL	Interactive Data Language
J	scalar coupling constant, or spin-spin coupling constant
LDA	Linear Discriminant Analysis
LH	Luteinizing Hormone
M	Molar
M	net, macroscopic magnetization
m	eigenvalues of the spin angular momentum, **I**
MHz	MegaHertz

mM	milliMolar
MR	Magnetic Resonance
MRI	Magnetic Resonance Imaging
MRS	Magnetic Resonance Spectroscopy
mT/m	milliTesla per meter
PABA	Para-AminoBenzoic Acid
PBS/D_2O	Phosphate Buffered Saline in deuterated water (D_2O)
PPM	Parts Per Million
RF	Radio Frequency
SAR	Specific Absorption Rate
SE	Spin Echo
SIL	Squamous Intraepithelial Lesion
SNR	Signal to Noise Ratio
STEAM	STimulated Echo Acquisition Mode
T	Tesla
T_1	spin-lattice relaxation time

T_2	spin-spin relaxation time
TE	Echo Time
TM	Mixing Time
TR	Repetition Time
TSE	Turbo Spin Echo
TVS	TransVaginal ultraSonography
δ	chemical shift
γ	gyromagnetic ratio
μ	dipolar magnetic moment of a nucleus
ρ	spin density distribution
σ	shielding constant
ω_o	Larmor frequency

INTRODUCTION

The first reports of the nuclear magnetic resonance phenomenon were published in 1946 by research groups led by Felix Bloch and Edward Purcell (Bloch *et al.* 1946, Purcell *et al.* 1946). While nuclear magnetic resonance (NMR) was first used in the areas of physics and chemistry, unpublished reports suggest that some of the early pioneers had visions that NMR could someday be applied to biological systems (Mansfield and Morris 1982). In 1973, the first two-dimensional proton magnetic resonance images were produced (Lauterbur 1973). Since this time, the technology of nuclear magnetic resonance has advanced rapidly. Today, magnetic resonance imaging (MRI) is used routinely in the clinical setting to obtain *in vivo* images of the human body for the purpose of diagnosis of many different diseases. Clinical acceptance of magnetic resonance spectroscopy (MRS) as a diagnostic tool is only now beginning.

Magnetic resonance spectroscopy allows qualitative and quantitative analysis of the chemical composition of tissue. Because disease processes are associated with biochemical changes, MRS can differentiate healthy tissue from diseased tissue based on biochemical differences in the tissue (Mountford *et al.* 1993). It is believed that the biochemical processes involved in disease progression precede clinical manifestation. If this is correct, MRS may provide an early method of detection and diagnosis of disease.

Diagnosis of gynecological abnormalities is difficult because many of these diseases manifest deep within the pelvis. In many cases, diagnosis can not be made

without the assistance of surgery. Conversely, some gynecologic diseases, such as those in the vagina and cervix, are accessible to visual examination, but current diagnostic methods are inaccurate. In this thesis, two gynecological structures – the uterine cervix and the ovary – are examined.

Due to accessibility of the uterine cervix to visual examination and improved screening programs that detect pre-cancerous lesions, the incidence of cervical cancer in Canada has dropped dramatically in recent years. Unfortunately, the present screening methods suffer from high inter- and intra-observer variability in grading of the pre-cancerous lesions. This leads to over-treatment in some cases and under-treatment in others.

Abnormalities of the ovaries, such as infertility and ovarian cancer, are normally difficult to detect and diagnose due to the location of the ovaries deep within the pelvis and the lack of symptoms associated with ovarian disease. Malignant ovarian cancer is commonly detected in advanced stages of progression resulting in high mortality rates. Improvements in ultrasound, computed tomography (CT), and MRI have had little impact on the diagnosis and treatment of ovarian abnormalities.

This thesis involves magnetic resonance imaging and spectroscopy of structures in the female pelvis. The purpose of this thesis is two-fold. First, the suitability of MRS for grading the pre-cancerous lesions of the uterine cervix will be determined. Second, the techniques required to obtain *in vivo* MR spectra of the human ovary will be developed.

PART 1

BASIC PRINCIPLES OF MAGNETIC RESONANCE

1.1 Fundamentals of Magnetic Resonance

1.1.1 Nuclei in a Static Magnetic Field

Magnetic resonance (MR) occurs in systems which contain magnetic moments and angular momentum. Many atomic nuclei contain both of these properties. Consider a nucleus with an intrinsic spin angular momentum **I**. If this spin angular momentum is non-zero, the nucleus has a dipolar magnetic moment $\boldsymbol{\mu}$ given by:

$$\boldsymbol{\mu} = \gamma\hbar\mathbf{I} \qquad [1.1]$$

where γ is a proportionality constant that is characteristic of the nucleus, called the gyromagnetic ratio, and $\hbar$ is equal to $h/2\pi$ where h is Planck's constant. When a nucleus with non-zero spin angular momentum is placed in a static magnetic field $\mathbf{B}_o$, an interaction takes place between the nuclear magnetic moment and $\mathbf{B}_o$ leading to new energy levels for the nucleus. This interaction is described by the Hamiltonian, H, according to:

$$H = -\boldsymbol{\mu} \cdot \mathbf{B}_o = -\gamma\hbar\mathbf{I} \cdot \mathbf{B}_o \qquad [1.2]$$

If the external magnetic field is along the z axis,

$$H_z = -\gamma\hbar B_o I_z \qquad [1.3]$$

where H_z is known as the Zeeman Hamiltonian. The eigenvalues of this Hamiltonian are multiples of m, which are the eigenvalues of I_z. Thus, the allowed energies, or Zeeman energies, of the nucleus are given by:

$$E = -\gamma\hbar B_o m \qquad [1.4]$$

where m describes the energy levels of the nucleus and m is equal to I, I-1, ..., -I. A nucleus with a non-zero spin angular momentum, in a static magnetic field, has $2I + 1$ equally spaced energy levels that are dependent on the strength of the magnetic field and the characteristics of the nucleus. Transitions may only occur between adjacent levels, whose separation, ΔE, is:

$$\Delta E = -\gamma\hbar B_o \qquad [1.5]$$

This set of energy levels may be detected when an interaction causes a transition to occur between levels. Since conservation of energy must be obeyed, the interaction required to produce a transition requires a frequency, ν_o, satisfying:

$$\nu_o = \frac{\Delta E}{h} = \frac{-\gamma B_o}{2\pi} \qquad [1.6]$$

From this, the angular frequency of the interaction is:

$$\omega_o = -\gamma B_o \qquad [1.7]$$

From classical mechanics, it is known that a torque acts on a magnetic moment in a magnetic field. This is given by:

$$\frac{d\mu}{dt} = \mu \times \gamma \mathbf{B}_o = \mu\gamma B_o \sin\theta \qquad [1.8]$$

A magnetic moment at an arbitrary angle θ with respect to the magnetic field will experience a torque that causes the moment to precess about the direction of the field.

The rate of this precession is equal to γB_o, the Larmor frequency. Note that the Larmor frequency is equivalent to the angular frequency required to produce a transition between energy levels given in equation [1.7].

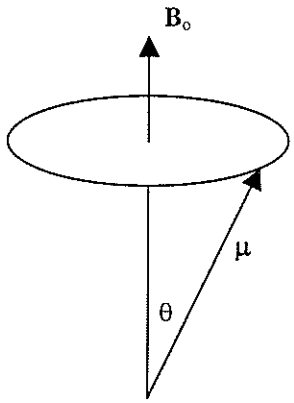

Figure 1.1: Precession of a nuclear magnetic moment μ at an angle θ about an external magnetic field B_o for a spin with I = 1/2.

To this point, only a single nucleus has been examined. Consider now an ensemble containing a large number, N, of similar nuclei with a spin of 1/2 at thermal equilibrium with the surroundings at temperature, T. When the ensemble of spins is placed in a static magnetic field, B_o, the ratio of the population of spins in the lower energy level, N_+, to the population of spins in the upper energy level, N_-, is given by Boltzmann's law.

$$\frac{N_+}{N_-} = \exp\left(\frac{2\mu B_o}{kT}\right) \approx 1 + \frac{2\mu B_o}{kT} \qquad [1.9]$$

where k is the Boltzman constant. The series expansion of the exponential is accurate because at normal experimental temperatures, the exponent is small. At room temperature, spins exposed to a 1 Tesla (T) magnetic field will populate both the upper and lower energy levels with a higher population in the lower level (N_+). The excess

population in N_+, however, is on the order of 10^{-6}. While small, this excess results in a net, macroscopic magnetization, **M**, for the ensemble of spins. **M** is always parallel to B_o, as given by:

$$M = \frac{N_o \gamma^2 \hbar^2 B_o}{3kT} I(I+1) = \chi B_o \qquad [1.10]$$

where N_o is the total number of spins, and χ is the bulk magnetic susceptibility. Note that the magnetic susceptibility is dependent on the temperature of the spins. Hence, the magnetic susceptibility of an ensemble of spins in the liquid state is different than χ for the same spins in the gaseous state. The net magnetization is proportional to the strength of the magnetic field, and thus, as B_o increases, the magnitude of M also increases.

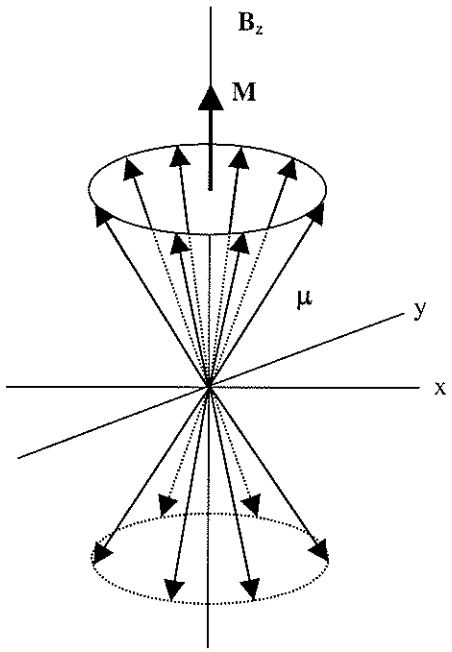

Figure 1.2: Precession of an ensemble of spins with magnetic moments, **μ**, around a static magnetic field along the z axis, $\mathbf{B}_z$, resulting in a net magnetization, **M**.

1.1.2 Perturbation of the Spins by an Alternating Magnetic Field

As previously discussed, transitions of the nuclear spins occur between adjacent energy levels when energy at the Larmor frequency is applied to the system. This energy may be in the form of an alternating magnetic field, $\mathbf{B}_1$, applied in the plane perpendicular to $\mathbf{B}_o$. This alternating field is often referred to as a radio frequency, or rf, field because the Larmor frequencies of nuclear spins typically fall in the radio frequency region of the spectrum. The rf field may be modeled as two circularly polarized components, each of amplitude B_1, one of which rotates clockwise, B_L, and the other which rotates counterclockwise, B_R, as illustrated in Figure 1.3.

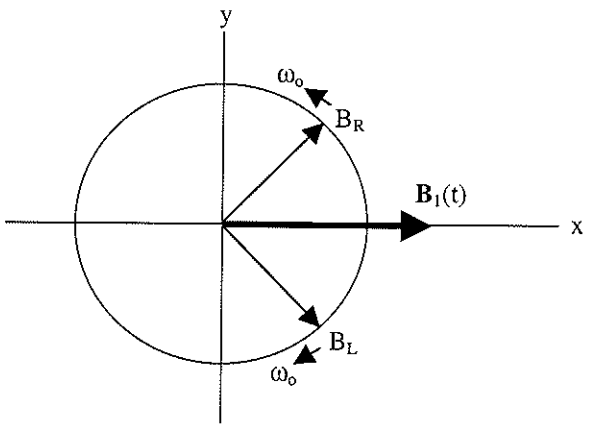

Figure 1.3: Alternating rf magnetic field, $\mathbf{B}_1$, modeled as two circularly polarized components rotating at the Larmor frequency, ω_o.

The equations describing the two components of the rf field are given by:

$$B_R = \frac{B_1}{\sqrt{2}}(\mathbf{i}\cos\omega t + \mathbf{j}\sin\omega t) \qquad [1.11]$$

$$B_L = \frac{B_1}{\sqrt{2}}(\mathbf{i}\cos\omega t - \mathbf{j}\sin\omega t) \qquad [1.12]$$

It can be shown that the component of the field which rotates in the direction opposite to the precession of the total magnetic moment of the ensemble of nuclear spins may be neglected. Thus, the component that precesses in the same sense as the spins, and is responsible for transitions of the spins between energy levels, may be written as:

$$B_1(t) = B_1(\mathbf{i}\cos\omega_o t - \mathbf{j}\sin\omega_o t) \qquad [1.13]$$

The total magnetic field to which the nuclei are exposed now consists of the sum of the static and alternating fields.

$$\mathbf{B}(t) = \mathbf{i}B_1\cos\omega_o t - \mathbf{j}B_1\sin\omega_o t + \mathbf{k}B_z \qquad [1.14]$$

Equation [1.8] describes the time dependent changes in the magnetic moment of a single spin caused by a static magnetic field. Since the total macroscopic magnetization, **M**, is the vector sum of the individual magnetic moments in an ensemble, equation [1.8] becomes:

$$\frac{d\mathbf{M}}{dt} = \mathbf{M}\times\gamma\mathbf{B} = M\gamma B\sin\theta \qquad [1.15]$$

From equation [1.14], the total magnetic field, **B**, is time-dependent and therefore the angle, θ, between **M** and **B** is also time-dependent. The analysis of θ is simplified by conversion from the laboratory reference frame to a rotating reference frame that rotates about the z-axis at the frequency, ω, of the alternating magnetic field. In this reference frame, the effective magnetic field becomes:

$$\mathbf{B}_{eff} = \mathbf{i}B_1 + \mathbf{k}\left(B_o - \frac{\omega}{\gamma}\right) \qquad [1.16]$$

where B_1 is arbitrarily set along the x-axis. When the frequency of the alternating field is equal to the precession rate of the nuclei, or the Larmor frequency, ω is equal to $\omega_o = \gamma B_o$ and the rotating field becomes:

$$\mathbf{B}_{eff} = \mathbf{i}B_1 \qquad [1.17]$$

This condition is known as resonance. From equations [1.15] and [1.17], it can be seen that at resonance, **M** will experience a torque due to $\mathbf{B}_1$ and thus, will precess about the x-axis of the rotating frame. The angle, θ, through which **M** rotates in a period of time t_p is given by:

$$\theta = \gamma B_1 t_p \qquad [1.18]$$

Note that the rotation is dependent on B_1. When the influence of B_1 is removed, the spins relax to their equilibrium state.

1.1.3 Relaxation

Relaxation of the nuclear spins after perturbation occurs in two forms. The first occurs when the spins interact with each other to cause dephasing of the net magnetization in the xy-plane. This interaction is called spin-spin, or transverse relaxation, and is denoted by T_2. The second form of relaxation involves the interaction of the spins with their surroundings, causing the net magnetization to return to the z-axis. The characteristic time for this interaction is called the spin-lattice, or the longitudinal relaxation, and is denoted by T_1. The rate of relaxation of **M** as a result of these relaxation processes is given by the following three equations.

$$\frac{dM_x}{dt} = -\frac{M_x}{T_2} \qquad [1.19]$$

$$\frac{dM_y}{dt} = -\frac{M_y}{T_2} \qquad [1.20]$$

$$\frac{dM_z}{dt} = -\frac{M_z - M_o}{T_1} \qquad [1.21]$$

where M_o is the initial net magnetization before perturbation. The relaxation processes are such that $T_2 \leq T_1$.

Solution of equation [1.15] using equations [1.14], [1.19] to [1.21] yields a set of three differential equations, known as the Bloch equations, that describe the net magnetization in the laboratory reference frame.

$$\frac{dM_x}{dt} = \gamma\left(M_y B_o + M_z B_1 \sin\omega_o t\right) - \frac{M_x}{T_2}$$

$$\frac{dM_y}{dt} = \gamma\left(-M_x B_o + M_z B_1 \cos\omega_o t\right) - \frac{M_y}{T_2} \qquad [1.22]$$

$$\frac{dM_z}{dt} = \gamma\left(-M_y B_1 \cos\omega_o t - M_x B_1 \sin\omega_o t\right) - \frac{M_z - M_o}{T_1}$$

The Bloch equations may be solved for each situation given the appropriate boundary conditions. Many MR experiments can be described using these equations.

1.1.4 Basic MR Experiments

1.1.4.1 Single RF Pulse Sequence

It is now possible to describe an elementary MR experiment. For simplicity, this experiment will be described in a reference frame that rotates at the Larmor frequency. Consider a net macroscopic magnetization, **M**, of an ensemble of spins placed in a static

magnetic field, $\mathbf{B}_o$, whose direction is along the z axis. Application of $\mathbf{B}_1$ along the x-axis with precession rate equal to the Larmor frequency will cause **M** to rotate around the the x-axis. $\mathbf{B}_1$ can be applied for a short time, t_p, so that **M** rotates by 90^0, placing it along the y-axis, as in Figure 1.4A and B. After $\mathbf{B}_1$ is removed, relaxation of the magnetization begins immediately. Although the transverse and longitudinal relaxations occur simultaneously, they are illustrated separately in Figures 1.4B and C for clarity.

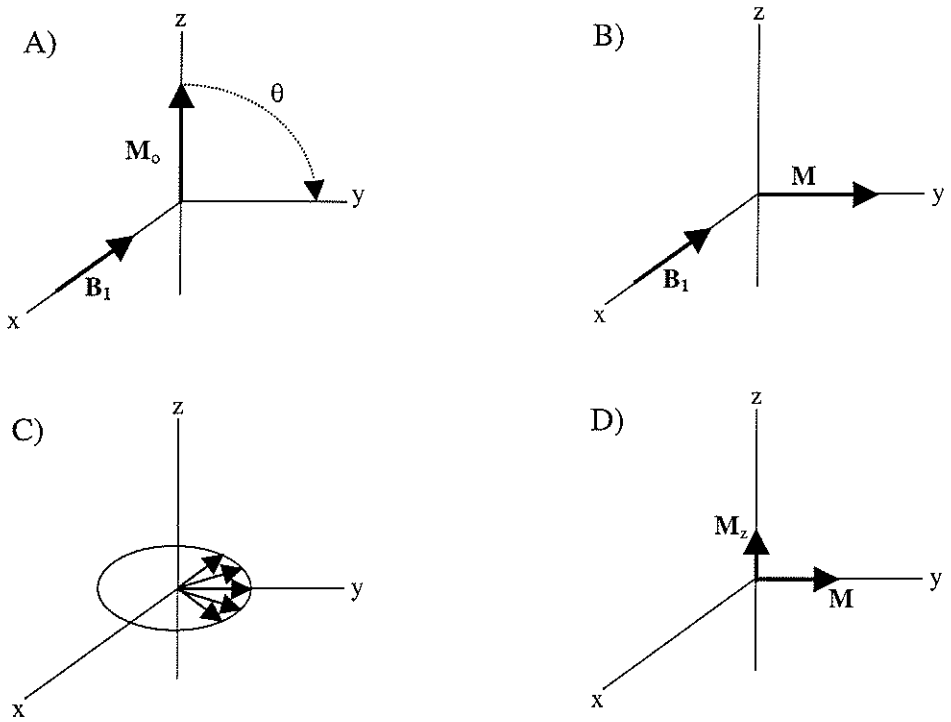

Figure 1.4: A) Initial magnetization $\mathbf{M}_o$ in a static magnetic field along the z-axis. Application of B_1 causes rotation of $\mathbf{M}_o$. B) After t_p, **M** has rotated to the y-axis. When $\mathbf{B}_1$ is removed, relaxation occurs. C) Transverse relaxation causing dephasing of the spins. D) Partial longitudinal relaxation causing **M** to return to its initial value along z.

1.1.4.2 Spin Echo Pulse Sequence

Typically, MR experiments involve the application of more than one pulse of the rf field. The first multiple rf pulse experiment was published by Hahn in 1950. This experiment, called a spin echo, forms the basis of many present day MR experiments. Consider an ensemble of spins that has been rotated to the y-axis by the application of $\mathbf{B}_1$ along the x-axis. Initially, the spins are coherent with the net magnetization along the y-axis as in Figure 1.4B, but inhomogeneities in the static magnetic field quickly causes the spins to dephase. Some spins will rotate clockwise, while others rotate counterclockwise, as illustrated in Figure 1.5A. After a time TE, application of a second rf pulse along the x-axis for twice the length of the first pulse causes the dephasing spins to rotate around the x-axis by 180^0 (Figure 1.5B). This changes the relative directions of precession of the spins (Figure 1.5C). After a time equal to TE the spins will refocus along the negative y-axis to form a 'spin echo', $\mathbf{M}_{echo}$ (Figure 1.5D). TE is known as the echo time. It should be noted that the magnitude of $\mathbf{M}_{echo}$ is slightly less than that of $\mathbf{M}_o$ due to T_1 relaxation.

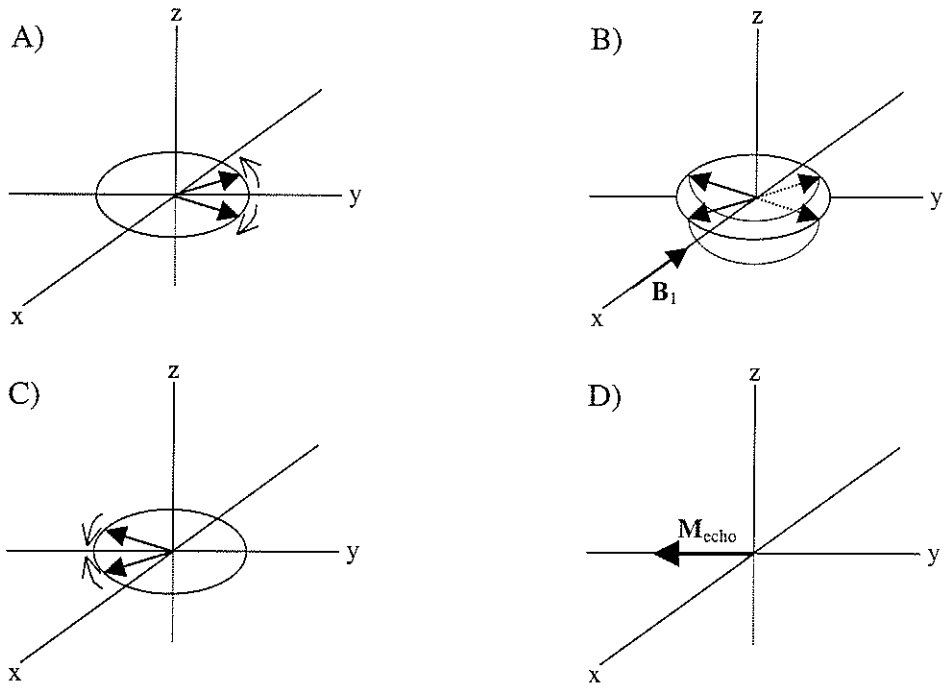

Figure 1.5: A) Dephasing of $\mathbf{M}_o$ due to T_2 relaxation. B) 180^0 rotation of the spins by application of a second $\mathbf{B}_1$ pulse. C) After the 180^0 pulse, the relative directions of precession of the spins is reversed. D) The spins refocus along the negative y-axis to form a spin echo.

1.1.4.3 Stimulated Echo Pulse Sequence

A different type of echo, called a stimulated echo, may be formed by a pulse sequence containing three 90^0 rf pulses. The evolution of **M** in this sequence is illustrated in Figure 1.6. The first $\mathbf{B}_1$ pulse is applied along the x-axis and rotates the ensemble of spins by 90^0 to place the net magnetization along the y-axis (Figure 1.6A). During a time TE, T_2 relaxation will cause the spins to dephase in the transverse plane (Figure 1.6B). A second 90^0 rf pulse, again applied along the x-axis, will rotate the spins into the xz-plane (Figure 1.6C). During a time TM, inhomogeneities in the static

magnetic field cause each magnetization vector to spread into a cone as the spins dephase with respect to the xy-plane. Thus, only the z-components contribute to the net magnetization (Figure 1.6D). Application of a third 90^0 rf pulse returns the spins to the ±y-axis (Figure 1.6E). After a time TE, the spins will again rephase along the y-axis to form the stimulated echo (Figure 1.6F). It is important to note that the maximum signal obtained from the stimulated echo is approximately half that of the maximum signal obtained from the spin echo.

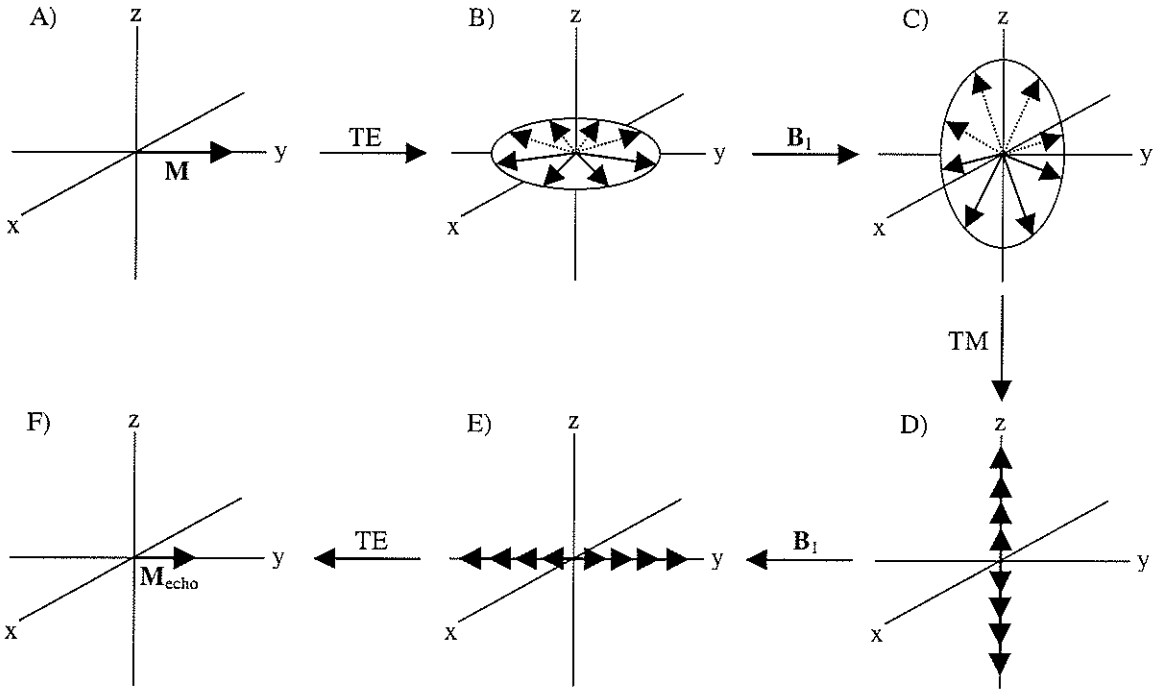

Figure 1.6: Stimulated echo pulse sequence. Refer to text for details.

1.1.4.4 Signal Acquisition

The energy of the spins and the rate at which they relax after perturbation, or excitation, by $\mathbf{B}_1$ can be measured using a coil with the plane of the coil perpendicular to $\mathbf{B}_o$. Faraday's law states that a changing magnetic flux in a coil induces a current. When

excited by the rf pulse, the precessing spins create an alternating magnetic field that may be measured by the current it induces in the coil. At the time immediately after excitation, the direction of the magnetic flux produced by the spins is perpendicular to the plane of the coil, but as the spins relax, this component decays. The plot of the signal intensity, S(t), of the current induced in the coil is a measure of the free induction decay (FID) of the spins. Typically, the signal received from the spins is not viewed in the time domain, but in the frequency domain, which is obtained by Fourier transformation of S(t).

$$S(\omega) = \int S(t)\exp(i\omega t)dt \qquad [1.23]$$

The Fourier transform of S(t) yields a real component, Re(ω), and an imaginary component, Im(ω), such that:

$$\mathrm{Re}(\omega) \quad \alpha \quad \frac{T_2}{1+4\pi^2(\omega_o-\omega)^2T_2^2} \qquad [1.24]$$

$$\mathrm{Im}(\omega) \quad \alpha \quad \frac{(\omega_o-\omega)T_2^2}{1+4\pi^2(\omega_o-\omega)^2T_2^2} \qquad [1.25]$$

The imaginary component is called the dispersion spectrum. The real component is called the absorption spectrum, and it describes a Lorentzian line shape. The full-width of the line at half its maximum intensity (FWHM) is theoretically equal to $1/\pi T_2$, but experimentally, the line shapes are often not Lorentzian and the line widths are wider than predicted theoretically. Static magnetic field inhomogeneities, $\Delta\mathbf{B}_o$, cause slight variations in the local magnetic field experienced by the individual spins. These inhomogeneities enhance transverse relaxation and increase the widths of the spectral lines. The time constant governing this decay is denoted by T_2^*, which is always less than T_2.

1.1.5 Chemical Shift

The energies of nuclei in a magnetic field are dependent on the strength of the magnetic field, and on the magnetic characteristic of the nuclei expressed by γ (equation [1.4]). Measurement of like nuclei in a molecule, however, does not yield a single energy. For example, measurement of the protons in ethyl alcohol (CH_3-CH_2-OH) gives rise to three different energies, or peaks, in the MR spectrum. The differences between the energies are called chemical shifts and are due to changes in the local magnetic fields of the nuclei caused by motion of the electrons in the electron clouds surrounding the nucleus. The external magnetic field induces motion of the electrons, creating an orbital current with an associated local magnetic field. This local magnetic field opposes the external field at the nucleus, reducing the total magnetic field experienced by the nucleus, and its resonant energy. The magnitude of this shielding of the nucleus depends on the chemical environment of the electrons and nucleus. The change in the effective magnetic field at the nucleus may be described by:

$$B = B_o(1-\sigma) \qquad [1.26]$$

where σ is the shielding constant and is typically much less than unity. The variations in the local magnetic fields of the nuclei cause slightly different precession rates for the nuclei. These precession rates are expressed in terms of the chemical shift, δ, as defined by:

$$\delta_i = \left(\frac{\nu_r - \nu_i}{\nu_o} \right) x10^6 \qquad [1.27]$$

where ν_r is the frequency of a reference nucleus, ν_i is the frequency of the nucleus in question, and ν_o is the frequency of the applied $\mathbf{B}_1$ field. Normally, the protons in

tetramethylsilane (TMS) are used as the reference and their chemical shift is arbitrarily set to zero. Note that the chemical shift is a dimensionless ratio, and thus values measured at different static magnetic field strengths may be compared. The range of chemical shifts possible for a given nucleus varies greatly depending on the position of the nucleus in the periodic table. The normal range of chemical shifts for protons is approximately 10ppm.

1.1.6 Scalar Coupling

The local magnetic field experienced by a nucleus is further modified by the interactions between two nuclei. This interaction is called scalar, or spin-spin, coupling. It involves the transfer of information from one nucleus to an adjacent nucleus via a chemical bond. Distortion of the electron cloud at a nucleus k is detected through a chemical bond by nucleus i. This causes a small change in the local magnetic field experienced by nucleus i which is described by the spin-spin Hamiltonian.

$$H_{scalar} = 2\pi J_{ik} \mathbf{I}_i \cdot \mathbf{I}_k \qquad [1.28]$$

where J_{ik} is the coupling constant between nuclei i and k. Recall that the z projection of $\mathbf{I}$ has 2I+1 eigenvalues. Each energy state of $\mathbf{I}_k$ will cause a slightly different change in the local magnetic field experienced by $\mathbf{I}_i$. The result is to split the energy level of $\mathbf{I}_i$ into $2I_k+1$ new energy levels.

The effects of this energy level splitting on the MR spectrum is to split the observed resonance of a single nucleus into multiple resonances, or a multiplet. For example, consider once again the ethyl alcohol molecule. The chemical shift difference

between the three methyl protons is zero giving rise to a single resonance, but the protons of the methylene group are coupled to the methyl protons. Since the proton has a spin of ±1/2, the methylene protons may both have spins of +1/2 (respresented by ↑↑), or may both have spins of –1/2 (represented by ↓↓), or the first may be +1/2 and the second –1/2 or *vice versa* (↑↓ and ↓↑). Note that spin $\mathbf{I}_i$ will see ↑↓ and ↓↑ as equivalent. This gives rise to splitting of the energy level of the protons of the methyl group into three different energy levels, resulting in three resonances, or peaks in the spectrum. The intensity of the peaks is proportional to the number of contributing energy levels as illustrated in Figure 1.7 for the methyl and methylene resonances of ethyl alcohol.

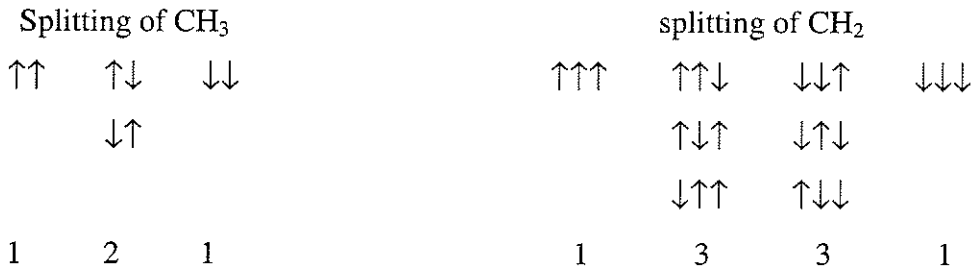

Figure 1.7: Scalar coupling in the ethyl alcohol molecule. Splitting of the methyl protons by the methylene protons is illustrated by the possible spin states of the methylene protons. The relative intensities of the spectral peaks are shown beneath. A similar representation is given for the splitting of the methylene protons by the methyl protons.

1.2 Principles of Magnetic Resonance Imaging (MRI)

1.2.1 Slice Selection

It has been shown that MR spectra of relatively small, homogeneous samples can be obtained by placing the sample in a static magnetic field and exciting the nuclei with an alternating field. The same principles may be applied to obtain MR images of a localized portion of a sample.

Recall from equation [1.7] that the rate of precession of the nucleus is proportional to the strength of the static magnetic field. If a linear magnetic field gradient, $\mathbf{G_r}$, is superimposed on $\mathbf{B_o}$ along the direction $\mathbf{r}$, the rate of precession becomes dependent on position according to:

$$\omega = \gamma(B_o + rG_r) \qquad [1.29]$$

where r is the position of the spin with respect to the gradient field. The Hamiltonian describing the interaction of the static and gradient magnetic fields with the nuclear magnetic moment (equation [1.2]) becomes:

$$H = -\gamma\hbar(\mathbf{I}\cdot\mathbf{B_o} + \mathbf{I}\cdot\mathbf{G}\cdot\mathbf{r}) \qquad [1.30]$$

where $\mathbf{G}$ is a tensor. Since the magnitude of the $\mathbf{B_o}$ along the z-axis is typically much greater than the magnitude of the applied gradient fields, the x and y components of $\mathbf{G}$ have negligible effect on $\mathbf{I}$. Thus, only gradients of $\mathbf{B_o}$ along the z-axis need consideration and may be denoted as:

$$G_x = \frac{\partial B_z}{\partial x} \qquad G_y = \frac{\partial B_z}{\partial y} \qquad G_z = \frac{\partial B_z}{\partial z} \qquad [1.31]$$

The magnitude of the gradient magnetic fields used in MRI is normally on the order of between 1 and 10 milliTesla per meter (mT/m).

It is obvious that nuclei in a plane perpendicular to the z-axis all have the same Larmor frequency. Then, application of $\mathbf{B}_1$ at a frequency ω in the presence of a gradient magnetic field would excite a plane of nuclei with $\omega_o=\omega$. In practice, nuclei are excited in a thin slice rather than a plane. This is referred to as slice selection. The nuclei in the slice have frequencies equal to $\omega \pm \Delta\omega$. The position of the excited slice is controlled by manipulation of the frequency of $\mathbf{B}_1$. The thickness of the slice is determined by the bandwidth of the rf pulse and by the amplitude of $\mathbf{G}$. From equation [1.29], the thickness of a selected slice, Δz, is given by:

$$\Delta z = \frac{\Delta\omega}{\gamma G_z} \qquad [1.32]$$

Thus, slice thickness decreases as the magnitude of the gradient increases. In equation [1.32], the selected slice was arbitrarily chosen perpendicular to the z-axis. The selected slice may be oriented in any direction by proper application of the field gradients during excitation by $\mathbf{B}_1$.

1.2.2 Frequency Encoding

While selective excitation of the nuclei within a slice allows localization of a slice of the sample, localization of the nuclei within the slice is also desired. This may be accomplished by frequency encoding the spins. Consider a sample in which a slice of nuclei has been excited by the slice selection method. Frequency encoding involves

application of a gradient magnetic field during acquisition of the MR signal from the slice of excited nuclei. Because the nuclei in the slice precess at different frequencies depending on their location with respect to this second, frequency encoding gradient, the frequency of the acquired signal is dependent on the location of the nuclei with respect to the direction of the frequency encoding gradient (equation [1.29]). The signal arising from the slice is:

$$S(t) = C\int \rho(\mathbf{r}) \exp\{i\gamma \mathbf{G} \cdot \mathbf{r}t\} d\mathbf{r} \qquad [1.33]$$

where C is a proportionality constant, $\rho(\mathbf{r})$ is the normalized spin density distribution with respect to $\mathbf{r}$ of the nuclei in the slice, and $\mathbf{G}$ is a time independent magnetic gradient applied during acquisition. Typically, the detected signal is mixed with a reference signal set to ω_o. The resulting signal is the difference frequency and oscillates at $\gamma\mathbf{G}\cdot\mathbf{r}$. Thus, the $\gamma\mathbf{B}_o$ component in equation [1.33] has been neglected.

Fourier transformation of equation [1.33] yields:

$$\rho(\mathbf{r}) = \frac{1}{C}\int S(t) \exp\{-i\gamma \mathbf{G} \cdot \mathbf{r}t\} dt \qquad [1.34]$$

This equation is integral to MRI. It shows that the MR signals acquired in the presence of a magnetic field gradient can be reconstructed in the spatial domain via Fourier transformation. The reconstruction contains an image of the nuclear spin density along the direction of the gradient. Thus, the nuclei may be localized in one of the two dimensions of a selected slice.

1.2.3 Phase Encoding

Localization of the nuclei in the second dimension of the slice, the third and final dimension of the sample, is achieved by phase encoding. Consider, once again, a slice of nuclei that have been excited by the slice selection method. After excitation, application of a gradient magnetic field for a time t will cause the nuclei to precess through an angle $\phi(r)$ that is dependent on the position of the nuclei with respect to the direction of the gradient.

$$\phi(\mathbf{r}) = \gamma \mathbf{G} \cdot \mathbf{r}t \qquad [1.35]$$

Note that application of a third gradient field at a later time and along a different direction than the phase encoding gradient does not eliminate the spatially dependent phase information imparted to the spins.

1.2.4 Basic MR Imaging Experiment

A basic two dimensional MR imaging sequence combines the concepts of slice selection, phase encoding, and frequency encoding. Consider a gradient field applied along the z-axis in conjunction with a 90^0 rf pulse with frequency equal to ω. This causes the nuclei in the slice with precession rates equal to $\omega \pm \Delta\omega$ to be excited, or rotate into the transverse plane. Localization has been achieved along one of the dimensions. After excitation, a phase encoding gradient is applied along the y-axis for a time t_{ef}, which is called the evolution period. During this time, the spins evolve at different rates depending on their location with respect to the direction of the phase encoding gradient. Finally, after the evolution period, a frequency encoding gradient is applied along the x-axis during acquisition. During the acquisition period, the spins precess at different rates

depending on their location with respect to the direction of the frequency encoding gradient. Thus, localization is achieved along the second dimension. This sequence of pulses is repeated multiple times with the amplitude of the phase encoding gradient incremented by a small amount in each successive experiment. The rate of change of the phase in the acquisitions gives localization along the third, and final, dimension. This simple two dimensional MR imaging pulse sequence is displayed in Figure 1.8.

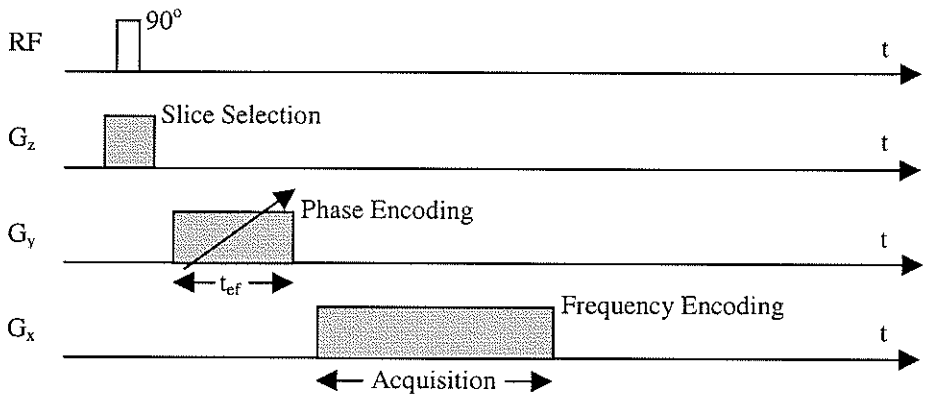

Figure 1.8: Basic two dimensional MR imaging sequence. The phase encoding gradient is incremented for each successive acquisition of the FID.

The final signal acquired from this simple pulse sequence may be described by a form of equation [1.33].

$$S(t) = C\int \rho(x,y)\exp[i\gamma(G_y y + G_x x)t]dxdy \qquad [1.36]$$

Note that the effects of relaxation have been ignored. Equations [1.33] and [1.36] are commonly expressed in terms of a spatial frequency domain called k-space. This spatial frequency, **k**, is defined as:

$$\mathbf{k} = \gamma \mathbf{G} t \qquad [1.37]$$

Substitution of [1.37] into [1.36] yields:

$$S(k_x, k_y) = C\int \rho(x, y)\exp[i\gamma(k_y y + k_x x)t]dxdy \qquad [1.38]$$

A two dimensional inverse Fourier transformation yields a two dimensional representation, or image, of the spin density distribution within the slice.

k-space is often used to describe the effects of gradients on magnetic fields. The scan of k-space in the simple experiment described here is illustrated in Figure 1.9. The direction in which k-space is scanned is determined by the amplitudes of the phase and frequency encoding gradients and the times of acquisition. Multiple methods of k-space sampling have been developed, and these methods define unique MR imaging methods.

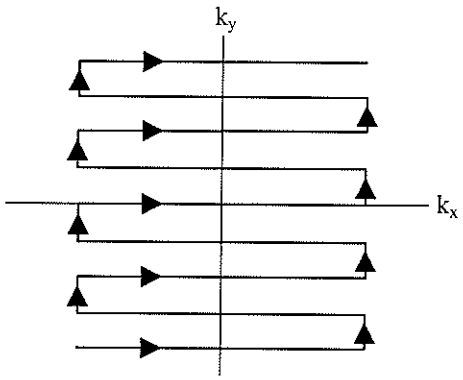

Figure 1.9: Scan of k-space accomplished by the basic MR imaging sequence shown in Figure 1.8. The arrows indicate the direction in which k-space is scanned.

1.3 Localized Magnetic Resonance Spectroscopy (MRS)

The principles used in MRI may be used to obtain MR spectra of a localized portion of a sample. While many localized MRS sequences have been developed and are described in the literature, only two of these will be described here. These two sequences – PRESS and STEAM – are used most commonly in the clinical setting. They are based on the principle of slice selection.

1.3.1 Point-Resolved Spectroscopy (PRESS)

The PRESS sequence (Bottomley 1984) involves the application of three slice selective gradients in conjunction with three rf pulses to form a double spin echo. A double spin echo sequence involves a 90° excitation pulse, followed by a 180° refocusing pulse to refocus the spins (illustrated in Figure 1.5), followed by a second 180° refocusing pulse. The PRESS pulse sequence is illustrated in Figure 1.10. The first 90° pulse and slice selective gradient will excite the nuclei in a slice. During a time $TE_1/4$, equal to one quarter of the total echo time, TE, the spins will dephase in the transverse plane. After this time, a 180° rf pulse is applied in conjunction with a slice selective gradient in a direction orthogonal to the first gradient. At a time $TE_1/4$, the spins will refocus, but further dephasing is allowed during a time $TE_2/4$. After this second time period, a second 180° rf pulse is applied with a slice selective gradient that is orthogonal to both of the previous slice selective gradients. Finally, after a time $TE_2/4$, the spins will refocus and the signal from the spin echo is acquired. The three orthogonal slice selective gradients define a cubic volume at their intersection. Only the spins in this cubic volume will be refocused, and therefore observed, at the time of acquisition.

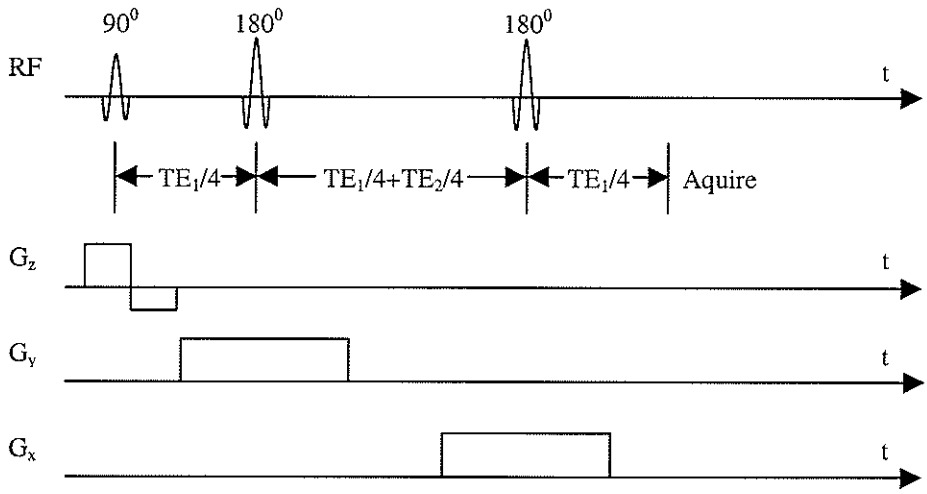

Figure 1.10: PRESS pulse sequence. This pulse sequence uses three slice selective gradients in conjunction with three rf pulses to produce a double spin echo.

1.3.2 Stimulated Echo Acquisition Mode (STEAM)

The STEAM sequence (Frahm *et al.* 1987) involves the application of three slice selective gradients in conjunction with three 90^0 rf pulses to form a stimulated echo. The STEAM sequence is illustrated in Figure 1.11. The first 90^o pulse and slice selective gradient will rotate the nuclei in a slice onto the y-axis. During a time TE/2, equal to half the total echo time, TE, the spins will dephase in the xy-plane. At the end of this time, a second 90^o pulse and slice selective gradient orthogonal to the first slice selective gradient will rotate the dephased spins into the xz-plane. During the mixing time, TM, the xy-components of the spins will dephase as was described for the simple stimulated echo sequence in section 1.1.4.3. Note that gradients are applied in all three directions during the mixing time. These gradients, called spoiler gradients, cause dephasing of the xy-components of the magnetization, as well as signal from outside the volume of interest. At the end of the mixing time, the spins are rotated back into the xy-plane by another 90^0 pulse in conjunction with a slice selective gradient that is orthogonal to the

previous two slice selective gradients. After a time TE/2, a stimulated echo is formed and the MR signal is acquired. As with PRESS, the three slice selective gradients form a cubic volume at their intersection, and only the spins in this volume are refocused at the time of acquisition. Note that additional gradients are applied between the first two 90^0 pulses and after the final 90^0 pulse. These gradients refocus any dephasing of the spins caused by imperfections in the gradients during slice selection.

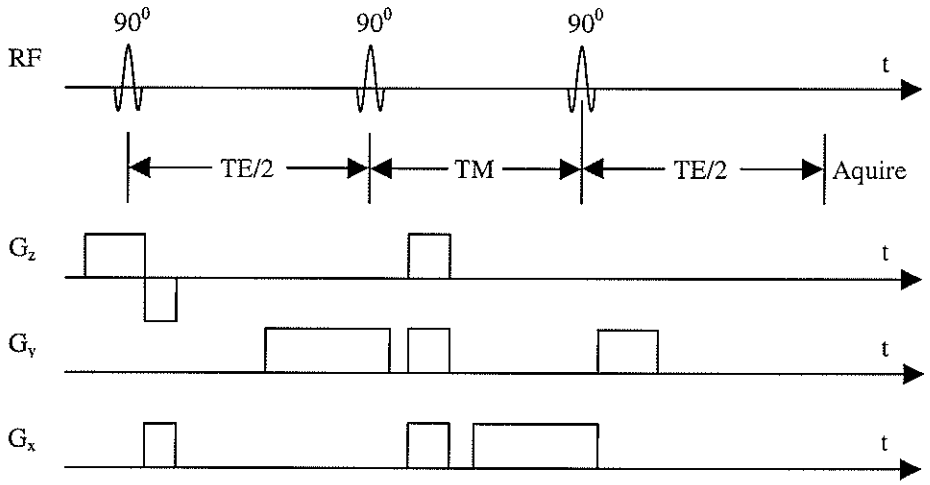

Figure 1.11: STEAM pulse sequence. This pulse sequence uses three slice selective gradients in conjunction with three 90^0 rf pulses to produce a stimulated echo.

Recall from sections 1.1.4.2 and 1.1.4.3 that the signal acquired from the simple stimulated echo sequence with no slice selective gradients was half the intensity of that acquired from the spin echo sequence. Hence, the signal obtained using the STEAM sequence will be half that obtained using the PRESS sequence. STEAM is also more sensitive to motion than PRESS, but it has the advantage of shorter echo times. This may reduce the effects of motion and more importantly, offers the additional benefit of allowing observation of metabolites with very short T_2 relaxation times (Moonen *et al.* 1989).

1.4 References

Bloch F, Hansen WW, Packard M. Nuclear Induction. *Phys. Rev.* **69**: 127, 1946.

Bottomley PA. Selective volume method for performing localized NMR spectroscopy. U.S. Patent 4 480 228, 1984.

Callaghan PT. Principles of nuclear magnetic resonance microscopy. Oxford University Press, Oxford, UK, 1991, 75-77. 93-96, 122-124.

Farrar TC and Becker ED. Pulse and Fourier transform NMR; Introduction to theory and methods. Academic Press Inc., Orlando, Florida, 1971, 1-30.

Frahm J, Merboldt K-D, Hänicke W. Localized proton spectroscopy using stimulated echoes. *J. Magn. Reson.* **72**: 502-508, 1987.

Goldman M. The fundamentals of NMR. In *Proceedings of the International School of Physics; Physics of NMR Spectroscopy in Biology and Medicine.* B Maraviglia, ed. North Holland Physics Publishing, Amsterdam, The Netherlands, 1988, 24-28.

Hahn EL. Spin echoes. *Phys. Rev.* **80**: 580-594, 1950.

Harris RK. Nuclear magnetic resonance spectroscopy; A physiochemical view. Pitman Books Ltd, London, UK, 1983, 1-19, 47-51, 70, 183-190, 212-213.

Homans SW. A dictionary of concepts in NMR. Oxford University Press, New York, 1992, 182-183.

Lauterbur PC. Image formation by induced local interactions: Examples employing nuclear magnetic resonance. *Nature* **242**: 190-191, 1973.

Ljunggren S. A simple graphical representation of Fourier-based imaging methods. *J. Magn. Reson.* **54**: 338-343, 1983.

Mansfield P. Imaging by nuclear magnetic resonance. *J. Phys. E.: Sci. Instrum.* **21**: 18-30 1988.

Mansfield P and Grannell PK. "Diffraction" and microscopy in solids and liquids by NMR. *Phys. Rev. B: Solid State* **12**: 3618-3634, 1975.

Mansfield P and Morris PG. NMR imaging in biomedicine; Supplement 2, Advances in magnetic resonance. Academic Press, New York, 1982, 1-154.

Moonen CTW, von Kienlin M, van Zijl PCM, Cohen J, Gillen J, Daly P, Wolf G. Comparison of single-shot localization methods (STEAM and PRESS) for *in vivo* proton NMR spectroscopy. *NMR Biomed.* **2**: 201-208, 1989.

Mountford CE, Lean CL, Mackinnon WB, Russell P. The use of proton MR in cancer pathology. *Annu. Rep. NMR Spectrosc.* **27**: 173-215, 1993.

Oldendorf W and Oldendorf W Jr. MRI primer. Raven Press Ltd., New York, 1991.

Purcell EM, Torry HC, Pound RV. Resonance absorption by nuclear magnetic moments in a solid. *Phys. Rev.* **69**: 37, 1946.

Rothwell WP. Nuclear magnetic resonance imaging. *Appl. Opt.* **24**: 3958-3968, 1985.

Shaw D. Fourier transform N.M.R. spectroscopy. Elsevier Science Publishers, Amsterdam, The Netherlands, 2nd ed. 1984, 1-35, 261-265

Slichter CP. Principles of magnetic resonance. Springer-Verlag, Berlin, Germany, 2nd ed. 1978, 1-43, 57-58.

Smith SA, Palke WE, Gerig JT. The Hamiltonians of NMR, Part I. *Concepts Magn. Reson.* **4**: 107-144, 1992.

Wehrli FW. Principles of magnetic resonance. In *Magnetic Resonance Imaging.* DD Stark and WG Bradley, eds. Mosby Year Book, St. Louis, 2nd ed. Vol. 1, 1992, 3-20.

Wood ML. Fourier imaging. In *Magnetic Resonance Imaging.* DD Stark and WG Bradley, eds. Mosby Year Book, St. Louis, 2nd ed. Vol. 1, 1992, 21-66.

PART 2

^{1}H MRS OF THE UTERINE CERVIX

2.1 Introduction

Squamous cancer of the uterine cervix is normally a slowly progressing disease which may take as long as 10 years to progress to carcinoma in situ (Appleby 1995, Mezrich 1994). For this reason, the existence of a biological marker for the disease would allow screening and very early treatment, thus reducing the mortality rate. While no biological marker has been found, it is believed that abnormalities on the cervix, known as dysplastic lesions, are precursors to cervical cancer. With the recent emphasis on screening and the early treatment of dysplastic lesions, the incidence of cervical cancer has dropped dramatically. In 1998, it is estimated that cervical cancer will have the eleventh highest incidence of all types of cancer in Canadian women and the fourteenth highest mortality rate (National Cancer Institute of Canada 1998). The incidence and mortality rates are much higher in developing countries, making cervical cancer the second most common cancer in women and overall, the fifth most common cancer worldwide (Armstrong *et al.* 1992). The incidence and mortality rate have dropped dramatically since 1969 when cervical cancer had the third highest incidence and sixth highest mortality rate of all cancers in women (National Cancer Institute of Canada 1998). Further reduction in the incidence of cervical cancer is hindered in part by women's lack of understanding of the need for regular screening, but is also greatly

complicated by difficulties in diagnosing dysplastic lesions correctly. In order to discuss the difficulties involved with diagnosis, it is helpful to understand the structure of the uterine cervix.

2.1.1 Anatomy of the Uterine Cervix

The uterine cervix (term taken from the Latin, meaning neck) forms a connection between the uterus and the vagina (Figure 2.1). It is continuous with the body of the uterus and is cylindrical in shape, measuring 2-4cm in length in adult women who are not pregnant. The junction between the uterus and cervix is called the internal os. The lower portion of the cervix extends into the vagina such that the vagina circumferentially attaches to the cervix, dividing it into an upper portion, the endocervix, and a lower portion, called the exocervix. Typically, the cervix is directed downward and posteriorly into the vagina. The vaginal end of the exocervix has a convex elliptical surface. The opening to the exocervix, the external os, is circular in nulliparous women and slit-like in parous women. (Kurman 1987, Lewis and Chamberlain 1989, Mezrich 1994, Sloane 1985)

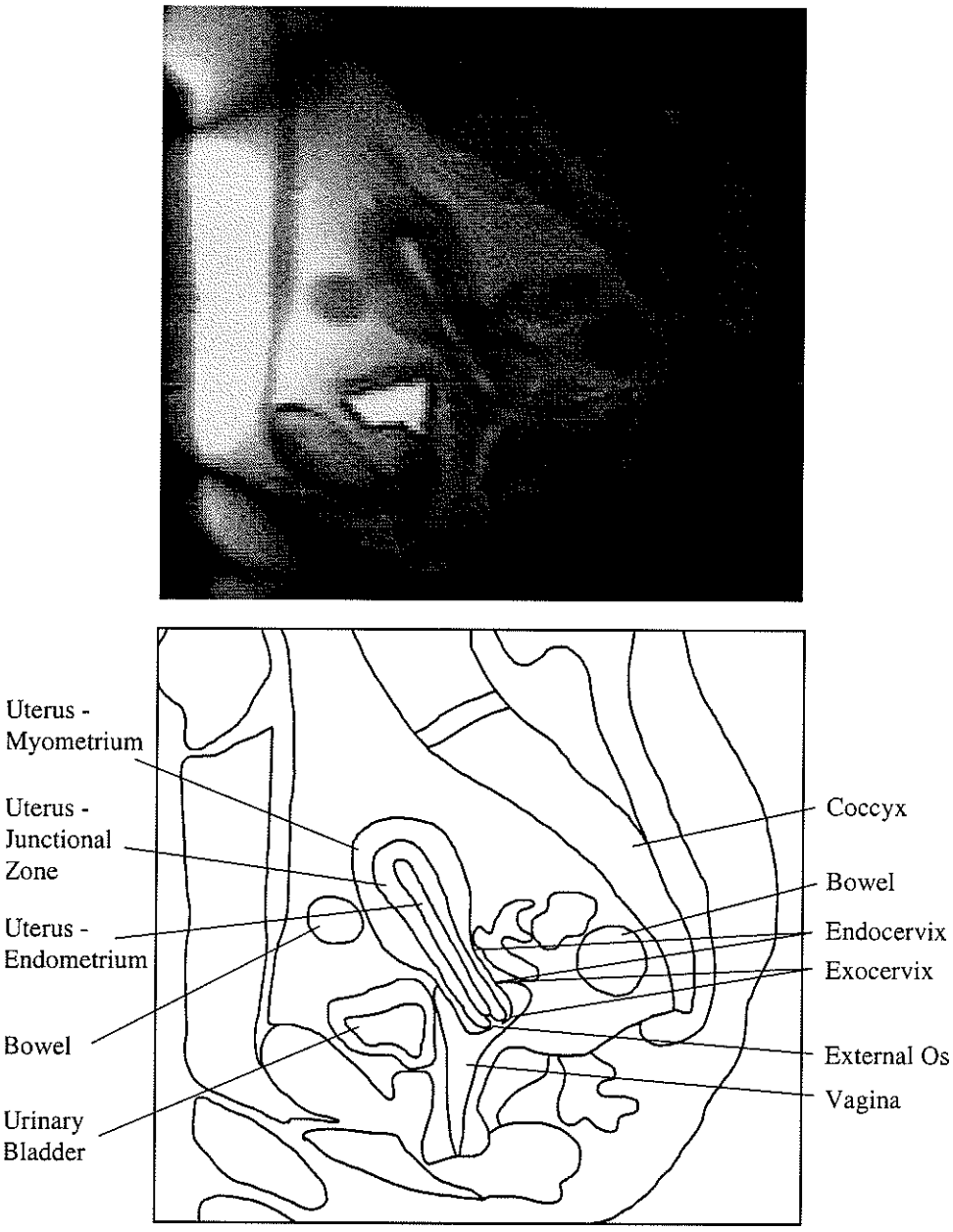

Figure 2.1: Sagittal T_2-weighted image of the female pelvis and corresponding contour image.

The walls of the cervix are composed of fibromuscular tissue and are lined on the interior by a single layer of columnar epithelium resting on a basement membrane. Many glands are contained in the walls of the endocervical canal. Under hormonal control,

these glands produce and secrete mucus that varies in amount and quality during the menstrual cycle. The external suface of the exocervix is covered with stratified squamous epithelium similar to that which lines the vagina. The endocervical canal and the vaginal surface of the exocervix meet at the external os. The exact location of the juncture is variable and may either be slightly within the endocervical canal or on the external surface of the vaginal portion of the exocervix. This junction is known as the squamocolumnar junction, or the transformation zone. It is an area of rapid cell division. (Kurman 1987, Lewis and Chamberlain 1989, Mezrich 1994, Sloane 1985)

2.1.2 Cervical Dysplasia

Cervical abnormalities in the endocervix are difficult to examine due to difficulty in accessing them. Conversely, the great elasticity of the vagina allows easy visualization of the exocervix and external os. Ninety to ninety-five percent of cervical carcinomas originate in the transformation zone (Lewis and Chamberlain 1989, Mezrich 1994) and approximately 75% of all cancers occur in the epithelial tissue (Burghardt *et al.* 1993), thus allowing easy examination of high risk areas. It is in the epithelium of the transformation zone that dysplastic lesions occur. Dysplasia is a change in the size, shape, and/or organization of the cells (Miller and Brackman Keane 1987). Cells which are said to be dysplastic are approximately two-thirds the size of normal cells, while the area of the nucleus of a dysplastic cell is approximately four times the area of a normal nucleus. As cells become dysplastic, their shape changes from predominantly polygonal to round-oval forms (Coppleson 1992).

2.1.3 Human Papillomavirus

While no biological marker has yet been found, many risk factors are associated with cervical dysplasia, such as onset of coitus at an early age, multiple sexual partners, a sexual partner who has had multiple sexual partners, a history of venereal disease, cigarette smoking, lower socioeconomic status, and a history of dysplasia of the genital tract (Wilkinson 1990). Most disturbing is the well known link between cervical dysplasia and the sexually transmitted Human Papillomavirus, HPV (Reviewed in Bosch *et al.* 1997, Reid *et al.* 1982, Richart *et al.* 1998). Due to dramatically changed sexual habits during the past two decades, there has been a rapid increase in HPV infection rates (reviewed in Daley 1998, Higgins and Smith 1997, Syrjänen 1989). Estimations of the number of women infected with HPV range from 5% to 80% (reviewed in Breitenecker and Gitsch 1992, Cannistra and Niloff 1996, Daley 1998, Higgins and Smith 1997, Steben 1994, Syrjänen 1989). The broad range of incidence figures reported may depend on the modality of detection and the extreme fluctuating course that HPV runs from manifest to subclinical or latent infection (Bosch *et al.* 1997, Breitenecker and Gitsch 1992, Syrjänen 1989). HPV is a DNA virus that causes koilocytosis, which is exhibited as hollowed or concave cellular structure, and/or condyloma, which is manifest in the form of wart-like lesions (Alani and Münger 1998, Higgins and Smith 1997, Kurman 1987 p. 188). Over 90 types of HPV have been identified of which about 20 infect the cervix (Schiffman 1993, Alani and Münger 1998).

While the role of HPV in cervical disease is not yet fully understood (Reid *et al.* 1987), mounting evidence supports the association between this sexually transmitted

disease and cervical cancer. The link is supported by the dramatic increase in HPV infection, especially in young women (age 15 to 24), and the corresponding increase in the rate of cervical dysplasia in the same age group (Daley 1998, Syrjänen 1989). Stronger support is lent by the fact that HPV is found in as many as 90-95% of cervical cancer lesions (Daley 1998, Higgins and Smith 1997, Reid *et al.* 1982, Sherman 1994, Shah 1992, zur Hausen 1991). The consistency of these findings in different countries with different study designs and different laboratory methods makes it unlikely that the results are due to bias, and thus it has been established that a subset of HPV's are the precursors to cervical dysplasia and cancer (Bosch *et al.* 1997, Richart *et al.* 1998). The most common HPV types found in the cervix can be divided into low, intermediate, and high oncogenic risk as follows (Richart *et al.* 1998, Shah 1992, Stratton and Ciacco 1994, Syrjänen 1989):

Table 2.1: HPV Type Associated with Degree of Oncogenic Risk

Oncogenic Risk	HPV Type
Low Risk	6, 11, 42, 43, 44
Intermediate Risk	31, 33, 35, 51, 52
High Risk	16, 18, 45, 56

Not all women with HPV types in the high risk group will develop cervical cancer. Although the presence of HPV is not necessary for the development of cervical cancer, analysis of high grade dysplastic cervical lesions and malignant cervical tumours normally reveals HPV infection with types in the high risk group (Burghardt *et al.* 1994,

Cannistra and Niloff 1996, Ferenczy and Winkler 1987). It is important to note that while HPV is linked to cervical disease, it is estimated that only approximately 5-15% of HPV infections will progress to cervical cancer (Daley 1998, Higgins and Smith 1997, Richart *et al.* 1998, Syrjänen 1989). The presence of HPV alone is insufficient to cause cervical cancer.

2.1.4 Clinical Classification of Dysplasia

In the early 1960's, a classification system was developed which defined dysplasia as cervical intraepithelial neoplasia (CIN) and divided the severity of dysplasia into three grades, mild, moderate, and severe (Figure 2.2). CIN 1 is mild dysplasia, CIN 2 corresponds to moderate dysplasia, and CIN 3, severe dysplasia. Normal squamous epithelial tissue in the cervix is composed of layers of cells. The basal layer, or base, is the active layer where cells are produced. These cells slowly rise to the surface or top layer of the epithelium and are sloughed off. The basal cells are typically pyramidal or polygonal in shape with rounded nuclei. As the cells rise to the top of the epithelial layer, they assume a more flattened, or elliptical, shape. In the case of CIN 1, only a few of the cells at the basal layer are abnormal. They are irregularly ordered, but resemble normal cells. In the case of CIN 3, almost the entire epithelial layer contains irregularly ordered, abnormal cells. As previously discussed, the size of the dysplastic cells are approximately two-thirds the size of normal cells, and the area of the nucleus of a dysplastic cell is approximately four times the area of a normal nucleus. The shape of the dysplastic cells has changed from predominantly polygonal to round-oval forms (Coppleson 1992). When the epithelial layer is entirely composed of abnormal cells of

irregular order and these cells have not invaded the basement membrane and underlying stroma, the lesion is described as carcinoma *in situ* (Miller and Brackman Keane 1987). Displayed in Figure 2.2A is a schematic representation of the progression of cervical dysplasia from normal cells to carcinoma *in situ* (CIS). Displayed in Figures 2.2B to 2.2E are cross sections of stained cervical tissue as viewed under a microscope. Note the change in size and shape of the cells with increasing grade of dysplasia.

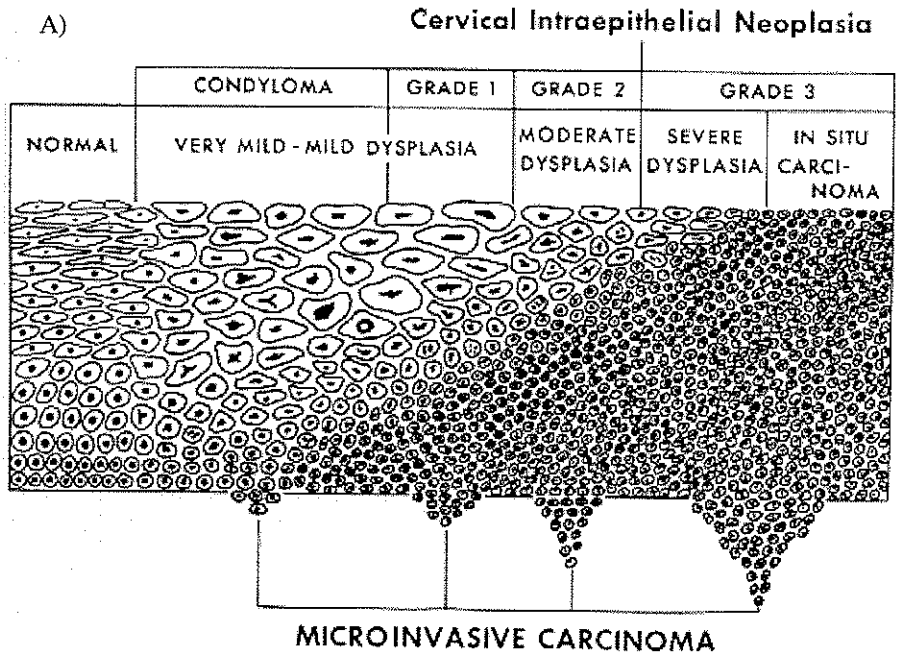

Figure 2.2: (Continued on next page) A) Schematic representation of normal cervical tissue and dysplastic cervical tissue progressing from mild dysplasia (CIN 1) to CIS. B-E) Magnification of cross sections of stained cervical tissue showing normal tissue (B), CIN 1 (C), CIN 2 (D), and CIN 3 (E). (Cross sectional images supplied by Dr. Maria Paraskevas, Department of Pathology, Health Sciences Centre.)

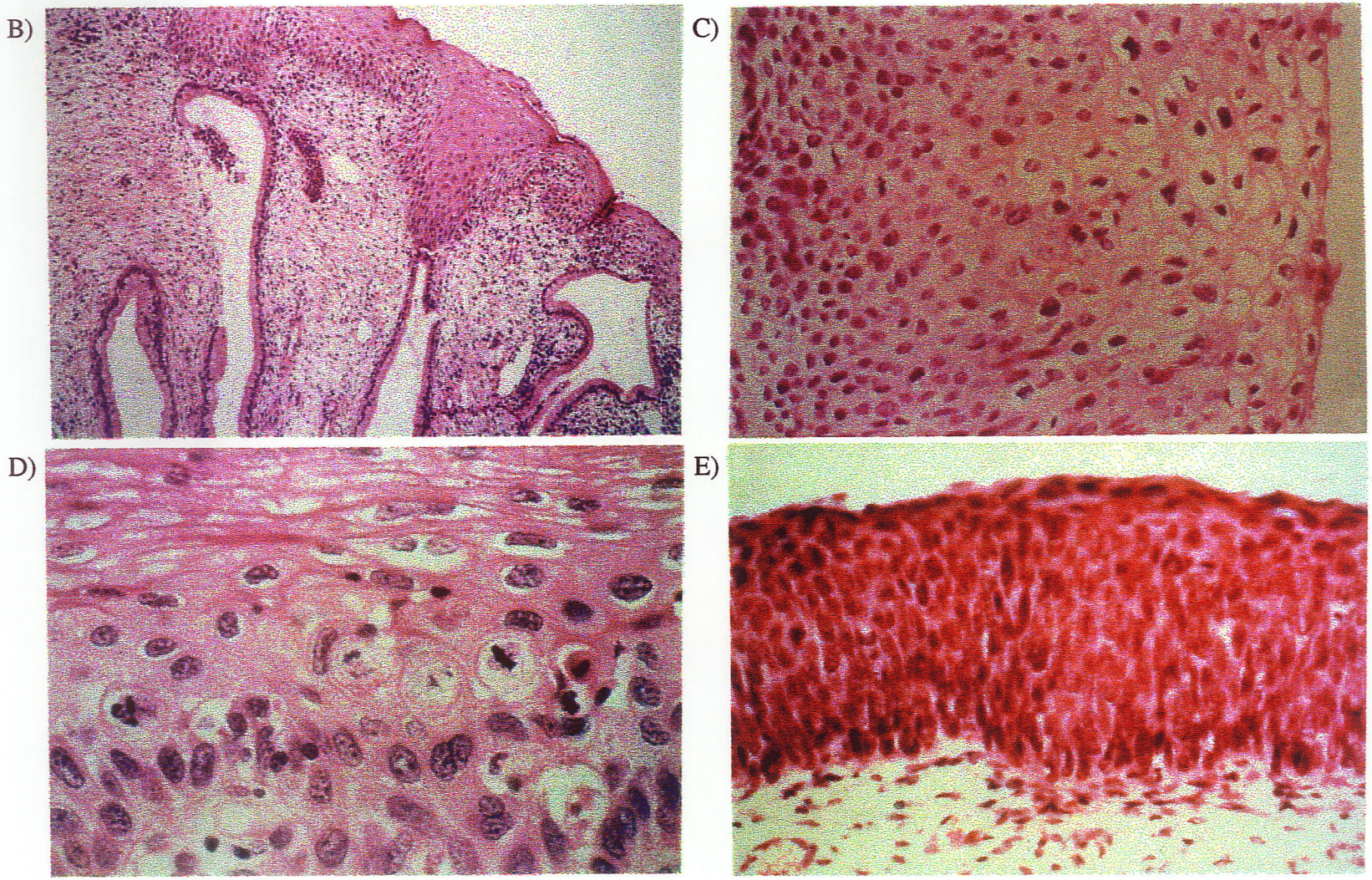

Figure 2.2: (Continued from previous page) B-E) Magnification of cross sections of stained cervical tissue showing normal tissue (B), CIN 1 (C), CIN 2 (D), and CIN 3 (E). (Images supplied by Dr. Maria Paraskevas, Health Sciences Centre.)

It is obvious that the CIN system of classification is subjective. Whether a pathologist will classify a lesion as CIN 1 or 2, for example, will depend on the experience of the pathologist as well as the pathologist's opinion regarding how many abnormal cells must be present before the classification must be upgraded to CIN 2. Ismail *et al.* (1989, 1990) circulated 100 cervical biopsy specimens to eight experienced pathologists. After each pathologist had examined and diagnosed them, the specimens were randomly re-ordered and each pathologist again examined and diagnosed all 100 specimens. This study found that at least two pathologists agreed on their diagnoses for only 51.7% of the specimens. Upon second examination of the same specimens, 65.57% of the pathologists' diagnoses agreed with their first diagnoses. Agreement was found to be poor for classification of CIN 1 and 2, mediocre for CIN 3, and excellent for invasive cancer. It was largely due to this poor reproducibility that a second method of classifying the severity of dysplasia was developed. This second method is known as the Bethesda classification system. It was first introduced in 1988 (National Cancer Intitute Workshop 1989) for the classification of abnormal Pap smears, but is now used frequently to refer to classification of colposcopically attained biopsies (Private communications with Dr. F. Guijon). This system divides dysplastic lesions into two rather than three classes. The first class, low grade squamous intraepithelial lesions (SIL), is identical to the previous system's classification of CIN 1 but also includes abnormalities which are HPV infected and not dysplastic. The second class, high grade SIL, includes the previous classifications of CIN 2 and 3 and carcinoma in situ (CIS) (Wilkinson 1990).

There is much controversy over the Bethesda system (reviewed in Appleby 1995, Valente 1994). Proponents of this two-tier system argue that since patients presenting with CIN 2, CIN 3, or CIS should receive the same treatment, distinction between these two classes is not necessary. Opponents of the Bethesda system point out that the combination of CIN 2, CIN 3, and CIS into one classification causes a significant loss of information. This may lead to over-treatment of moderately dysplastic lesions that if left on their own would regress. Opponents also contend that the definition of low grade SIL assumes that HPV infection will lead to cervical dysplasia, but since there is not yet agreement as to the role of HPV in the dysplastic chain, these two diagnostic classes should not be grouped together. There is concern that this classification will lead to clinicians ordering HPV DNA typing to see if the lesion is likely to progress. Since HPV and CIN 1 lesions can contain both low and high risk HPV types, and that lesions with high risk types can also regress, this may lead to over-diagnosis and inappropriate treatment. The division between the two classes assumes that there is a distinct separation between CIN 1 and CIN 2. This implies that CIN 1 lesions will regress, while CIN 2 lesions will always progress to CIN 3 and on to carcinoma, yet there is a lack of understanding regarding the progression/regression of lesions.

Two schools of thought exist regarding the progression/regression of cervical lesions. The first teaches that there is a continuous progression of lesions from CIN 1 to CIN 3 to carcinoma. While some lesions will regress, those that progress to carcinoma will pass through each grade - CIN 1 to CIN 2 to CIN 3 to CIS to cancer (Lewis and Chamberlain 1989). The second school of thought offers findings which contradict this

belief. For example, in some cases, invasive cancer has originated from lesions graded as CIN 2 or even CIN 1. Those who present these findings believe that not all cervical lesions follow the progression from CIN 1 to CIN 3, but that some lesions, if left untreated, will regress to normal (Burghardt *et al.* 1993).

2.1.5 Screening and Diagnosis of Dysplasia

Recently, the medical community has emphasized the need for screening for cancer of the uterine cervix (Valente 1994). The present method for screening women is the Papanicolaou, or Pap, smear in which cells are scraped from the exocervix. The cells are then analyzed by cytology, which involves observation of the shapes of the cells as well as their relative sizes and the sizes of the nuclei of the cells. The accuracy of diagnosis of cervical abnormalities from Pap smears is questionable. Reports on the accuracy of cytology vary greatly, ranging from 5% to 50% (reviewed in Appleby 1995, Burghardt *et al.* 1994, Valente 1994). In one study (Sherman *et al.* 1994), 200 Pap smears were reviewed by five cytopathologists. In only 29% of the smears did the cytopathologists' diagnoses agree. The low accuracy of the Pap smear may be attributed to inadequacy of sampling, inappropriate fixation and slide preparation, as well as the subjectivity of the cytopathologist. Further, any insult to the cervix, including intravaginal medications, douching, lubricants, tampons, and sexual intercourse, may produce false positives (Appleby 1995).

If abnormal cells are found in the Pap smear, the patient is referred for colposcopic examination. Colposcopy involves visual examination of the cervix using a

magnifying lens. The magnification of the cervix is less than a typical microscope. During this examination, weak acetic acid is sprayed on the cervix causing abnormalities to temporarily appear opaque and white, called acetowhite. Although the reaction which produces acetowhite epithelium is unknown, it is believed to be caused by a coagulation of keratin and/or proteins on the surface of the tissue (communications with Dr. F. Guijon). The acetowhite appearance may also be due in part to the increased nuclear and cellular density which prevents observation of the subepithelial vessels (Coppleson, 1992). A small biopsy of the abnormality, called a punch biopsy, is obtained. The biopsy is then examined histopathologically to confirm or exclude the presence of CIN and/or invasive cancer. Unfortunately, histopathology is also not infallible. As described earlier, subjectivity is introduced by the pathologist's determination of the separation between the various degrees of dysplasia. Also, histopathology suffers from sampling errors since only part of the biopsy obtained during colposcopic examination is used for diagnosis.

Despite the inaccuracy of cytology and histopathology, these methods have had a significant impact on the incidence of cervical cancer. A study by a Canadian Task Force illustrated the efficacy of screening for cervical cancer (Report of the Canadian Task Force 1976). From 1958 to 1972, the incidence of cervical cancer in British Columbia decreased dramatically as the number of women undergoing Pap smear screening increased. From 1983 to 1995, the incidence in Canada of invasive cervical cancer has decreased at an annual rate of 3-4% (Le *et al.* 1995). Conversely, the link between the sexually transmitted disease, HPV, and cervical dysplasia is of concern, particularly since

the incidence of HPV-infections of the female genital tract has risen drastically (Daley 1998, Syrjänen 1989). This may lead to an increased incidence of dysplastic lesions. A more accurate screening method for cervical dysplasia that does not suffer from the subjectivity and sampling errors of cytology and histopathology may lead to further reductions in the incidence of cervical cancer.

2.2 Hypothesis

It is hypothesized that magnetic resonance spectroscopy (MRS) in conjunction with multivariate analysis has the ability to differentiate between non-dysplastic cervical tissue, CIN 1, CIN 2, and CIN 3 based on biochemical information obtained from cervical punch biopsies.

2.3 Rationale

MRS allows determination of the biochemical composition of tissue with minimal insult to the tissue. This allows examination of the tissue by histopathology after MRS analysis. MRS also has the advantage that the entire biopsy is used for analysis, unlike histopathology where only serial sections of the biopsy are analyzed. Sampling errors are limited to those associated with the colposcopist's choice of the region for biopsy.

MRS has been used to compare the biochemical composition of biopsies taken from healthy cervices with those taken from preinvasive and invasive cervical

malignancies (Kuesel *et al.* 1992, Delikatny *et al.* 1993, Kuesel 1991, Mountford *et al.* 1990). It was found that the MRS biochemical fingerprint of normal cervical tissue is very different from that of cancerous cervical tissue. The MR spectra from biopsies of invasive cervical cancer were dominated by contributions from lipids while the spectra from preinvasive cervical lesions contained much less intense lipid peaks. Distinction of invasive from preinvasive lesions can also be accurately determined by histopathology. Delikatny *et al.* (1993) found that the spectral peaks at 0.9 ppm, 1.3 ppm, 3.8 ppm, and 4.2 ppm were of different intensities in dysplastic lesions as compared to invasive lesions. They used the ratios of the peak intensities at 1.3 ppm to 0.9 ppm and 3.8 ppm to 1.3 ppm to classify their spectra. These ratios were distinctly different for invasive cancer biopsies as compared to those of preinvasive lesions, with a Student's t-test of $p<0.0001$. Of greater clinical impact would be the ability to diagnose accurately the degree of cervical dysplasia, as well as the potential for cervical lesions to progress to carcinoma. The method of Delikatny *et al.* was not able to classify the MR spectra of dysplastic lesions according to the degree of dysplasia. This study examines the ability of MRS in conjunction with multivariate analysis to diagnose the degree of cervical dysplasia based on the biochemical content of cervical punch biopsies.

2.4 Materials and Methods

2.4.1 Magnetic Resonance Spectroscopy

Uterine cervical punch biopsies were obtained from 200 women. Since the cervix undergoes dramatic changes during pregnancy (Campion and Sedlacek, 1993), no biopsies were obtained from pregnant women. Biopsies were placed in phosphate-buffered saline in deuterated water (PBS/D_2O) and frozen in liquid nitrogen immediately after removal. Each biopsy was kept frozen no longer than 14 hours. Specimens were thawed and suspended in a glass capillary containing PBS/D_2O (Kuesel *et al.* 1992). A teflon plug was inserted into the end of the capillary to ensure that the tissue remained suspended (Figure 2.3). The capillary was then inserted into a 5mm tube containing PBS/D_2O and para-amino benzoic acid (PABA concentration 5mM for large biopsies and 0.5mM for small biopsies). The PABA solution was used as a chemical shift reference. Two doublets occur in the spectrum from the ring protons of the PABA molecule. The chemical shift of the highest field, doublet peak was set to 6.81ppm.

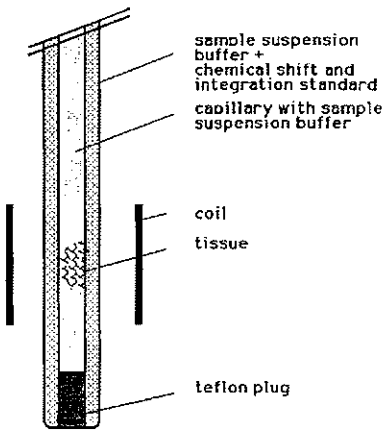

Figure 2.3: Schematic representation of the cervix biopsy suspended in the capillary.

One-dimensional ^{1}H MR spectra were obtained using water pre-saturation and a non-selective, 90^0 excitation pulse (pulse length was approximately 7μs), followed by acquisition (360 MHz, NS=256 or 640, SW=5KHz, RD=2.41s, TD=4K, temperature=37°C). After spectral acquisition, the specimens were fixed in formalin, weighed, and submitted for histopathology. The biopsies were processed, embedded in paraffin, and 5μm sections were cut and stained by hematoxylin and eosin. The slides were all reviewed by a single pathologist (Dr. Maria Paraskevas). The time between thawing and formalin fixation did not exceed 75 minutes. The first ten cases were biopsied next to the biopsy taken for histopathological examination and were examined in order to determine if the viability of the tissue for histopathological examination was compromised by the MRS study. The tissue was sufficiently preserved during the MRS study to be useful for histopathological analysis. For the remaining cases, only one biopsy was taken and this biopsy was used for both the MRS study and histopathology.

2.4.2 Data Preprocessing

Biopsies that contained significant quantities of blood yielded MR spectra with broad lines and were dominated by the blood. These spectra (N = 2) were eliminated from the study. Since the majority of dysplastic lesions occur in the epithelial tissue (Burghardt *et al.* 1993), and since different layers of tissue may have different biochemical contents (Brière *et al.* 1995, Moreno *et al.* 1993), spectra from biopsies that did not contain epithelial cells (N = 2), as determined by histopathology, were also removed from the study. The analysis was performed using remaining 196 spectra.

In order to remove the subjectivity inherent in phasing of the real and imaginary components of the spectra, the absolute magnitudes of the spectra were used in the multivariate analysis. The magnitude spectra were normalized such that the area in the region of low chemical shift relative to the suppressed water peak (0 ppm to approximately 4.5 ppm) was equal to one. Only the spectral region from 0.14 ppm to 4.30 ppm, consisting of 640 data points, was included in the analysis. Each spectrum was divided into equal regions and the intensities in each region were averaged. In order to determine the optimal number of regions, the analysis was performed using 64 and 128 equal regions. This served to simplify the analysis by minimizing the number of points used, as well as acting as a crude method of smoothing the data. The first derivatives of the spectra were also determined and used as alternate inputs for the analysis. Calculation of the first derivative removed any DC offset which may have existed in the spectra, thus eliminating this variable from the analysis. Histopathological and colposcopic reports were obtained for the biopsies. The spectra were grouped according to their clinical diagnoses of non-dysplastic, CIN 1, CIN 2, or CIN 3 ($N_{\text{Non-dysplastic}} = 68$, $N_{\text{CIN I}} = 46$, $N_{\text{CIN II}} = 32$, $N_{\text{CIN III}} = 50$). Spectra with clinical diagnoses of reactive or inflammatory changes and HPV were included in the non-dysplastic group. Only 19 of the 68 spectra in the non-dysplastic group had clinical diagnoses of normal. The final diagnosis of each case was based on the histopathological assessment and colposcopic impression.

2.4.3 Multivariate Analysis Methods

The preprocessed spectra were divided into a training set (N=112) and a test set (N = 84). The training set consisted of an equal number of spectra from each diagnostic

category. The spectral regions which best separate the spectra into their diagnostic classes were determined using an Enhanced Forward Selection (EFS)-based feature selector (Nikulin *et al.* 1998) described in Appendix 1. Once a set of regions which reliably classified the spectra was identified, the set was used as input for the various multivariate methods including linear discriminant analysis (LDA), using the Leave-One-Out cross-validation method to increase reliability, an artificial neural net-based classification method (ANN) which uses back propagation, and Stacked Generalization using the median method and Wolpert's method to combine the results of the LDA and ANN (Somorjai *et al.* 1995). The multivariate methods used are described in Appendix 1. From these analyses, the diagnostic classifications of the spectra in the test set were obtained. As a second method of analysis, every combination of ratios of the selected diagnostic regions was calculated, and the EFS-based feature selector was applied to determine which set of ratios of regions was diagnostic. The set of diagnostic ratios was submitted to the multivariate classifiers and the diagnostic classifications of the spectra in the test set were determined. This method of analysis was performed using the averaged spectra with 128 equal regions, the averaged spectra with 64 regions, and the first derivatives of the spectra averaged to yield 128 equal regions.

Each multivariate classifier assigned classification probabilities to the spectra. These probabilities are a measure of the certainty with which each spectrum was assigned to a class. Thus, the diagnoses determined by these methods were expressed in two ways - as a percentage of the total spectra classified correctly as compared to the clinical diagnoses, as well as the percentage of only those spectra classified with high probability

(≥75%) and classified correctly. The latter is referred to as the crisp classification accuracy. The classification accuracy of the test set was optimized by adjustments to the multivariate analysis technique, such as varying the number of diagnostic regions used as input for the LDA, or increasing or decreasing the learning rate of the neural net. The clinical diagnoses were the gold standard to which the multivariate analysis results were compared.

The spectral peaks found by Delikatny *et al.* (1993) to be different for invasive and preinvasive lesions were at 0.9 ppm, 1.3 ppm, 3.8 ppm, and 4.2 ppm. The peak ratios used for classification of the spectra were 1.3 ppm to 0.9 ppm and 3.8 ppm to 1.3 ppm. These regions and ratios were each selected from the spectra obtained in this study and were used as the input for the LDA.

This multivariate analysis was performed using four diagnostic classes – non-dysplastic, CIN 1, CIN 2, and CIN 3 – as well as two classes. The two class problems were:

Non-dysplastic, CIN 1	Versus	CIN 2, CIN 3
Non-dysplastic	Versus	CIN 1, CIN 2, CIN 3
Non-dysplastic, CIN 1, CIN 2	Versus	CIN 3
Non-dysplastic	Versus	CIN 1
Non-dysplastic	Versus	CIN 2
Non-dysplastic	Versus	CIN 3
CIN 1	Versus	CIN 2
CIN 1	Versus	CIN 3
CIN 2	Versus	CIN 3

In the first case, the training set consisted of 112 spectra, in the second two cases, the training sets contained 60 spectra, and in the last six cases, the training sets consisted of 50 spectra. Using the results from the first three cases – non-dysplastic and CIN 1 versus CIN 2 and CIN 3; non-dysplastic versus CIN 1, CIN 2, and CIN 3; and non-dysplastic, CIN 1, and CIN 2 versus CIN 3 - classification of the spectra into the four diagnostic classes was attempted. For each class, LDA provides a probability that each spectrum is classified in the given class. The probabilities obtained from the LDA of each of the three cases were averaged to obtain the probability of classification into four classes. For example, given the following probabilities for a single spectrum:

Table 2.2: Example of Classification Probabilities for a Single Spectrum

	Probability of Classification in Class 1	Probability of Classification in Class 2
Non-dysplastic, CIN 1 versus CIN 2, CIN 3	79.5%	20.5%
Non-dysplastic versus CIN 1, CIN 2, CIN 3	94.3%	5.7%
Non-dysplastic, CIN 1, CIN 2 versus CIN 3	86.2%	13.8%

the probability of classification into each class for the four class problem is determined as:

$$P_{class1} = \frac{79.5/2 + 94.3 + 86.2/3}{3} = 54.3\% \qquad P_{class2} = \frac{79.5/2 + 5.7/3 + 86.2/3}{3} = 23.5\%$$

$$P_{class3} = \frac{20.5/2 + 5.7/3 + 86.2/3}{3} = 13.6\% \qquad P_{class4} = \frac{20.5/2 + 5.7/3 + 13.8}{3} = 8.6\%$$

The spectrum is thus assigned to class 1 since this class has the highest probability.

2.5 Results

The sizes of the biopsies varied greatly. The wet weights of the 196 biopsies used for the multivariate analysis ranged from 0.94 mg to 33.52 mg. The mean weight was 8.39 mg with a standard deviation of ±6.03 mg. Because more signal is obtained from larger biopsies, the range of overall intensities of the spectra and signal to noise ratios was large. Normalization of the spectra prior to multivariate analysis removed the variability of the range of overall spectral intensities.

The spectra were grouped according to their four diagnostic classifications - normal, CIN 1, CIN 2, and CIN 3. The ranges and centroids of the spectra in each class are shown in Figure 2.4. No unique peaks are present which allow separation of the spectra into diagnostic classes. There is a wide range of peak intensities in each of the classes and a comparison shows significant overlap of the ranges between the four classes. An overlay of the centroids (Figure 2.5) reveals small differences between the four classes in terms of the peak intensities and peak widths. The spectra were also divided into two classes, with normal and CIN 1 diagnoses in one group, and CIN 2 and CIN 3 in another. The spectral ranges of the classes using two diagnostic classifications (Figure 2.6) also demonstrate a wide range in peak intensities and widths. The overlay of the centroids (Figure 2.7) shows slightly larger differences between classes than were observed in the centroids using four classes. The differences between the centroids, however, are still less than the ranges of the spectra in each class.

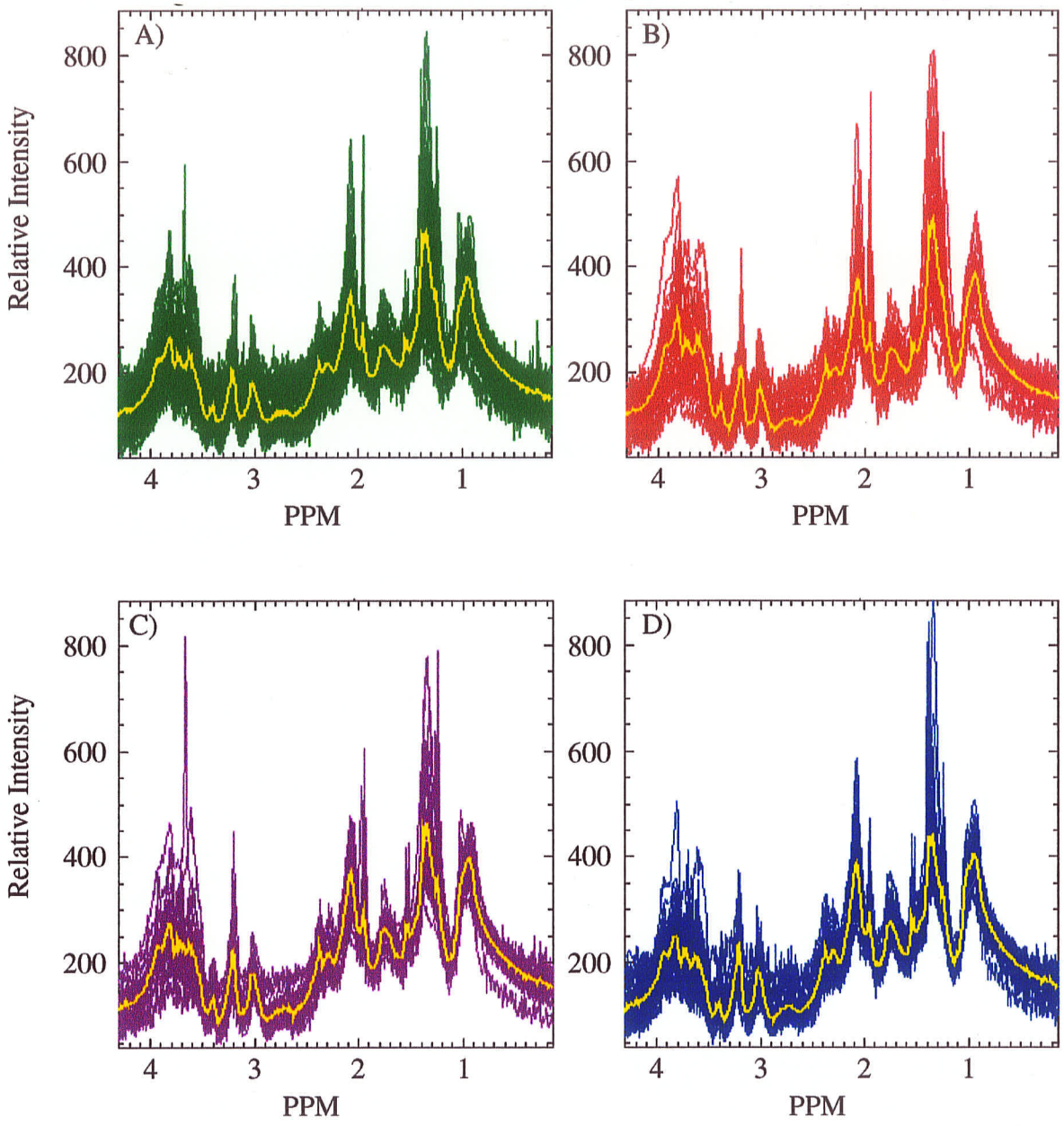

Figure 2.4: Spectra grouped according to the four histopathological diagnoses - A) non-dysplastic, B) CIN 1, C) CIN 2, and D) CIN 3. Centroids are illustrated in yellow.

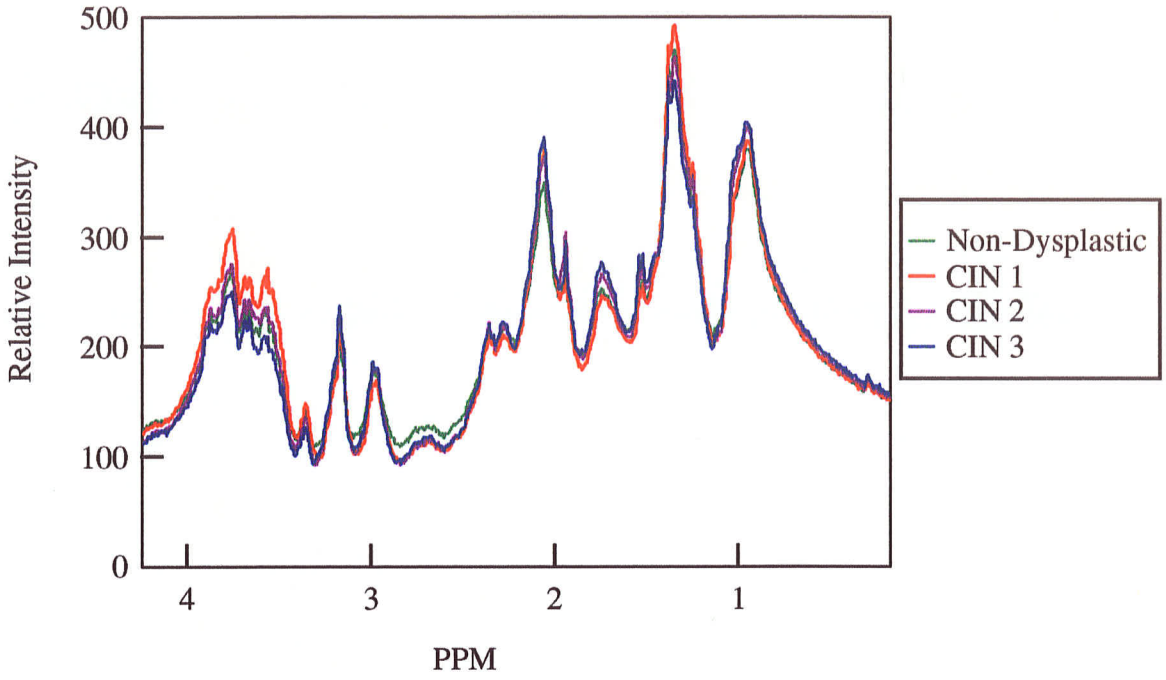

Figure 2.5: Centroids of the MR spectra classified in four diagnostic groups - non-dysplastic, CIN 1, CIN 2, and CIN 3.

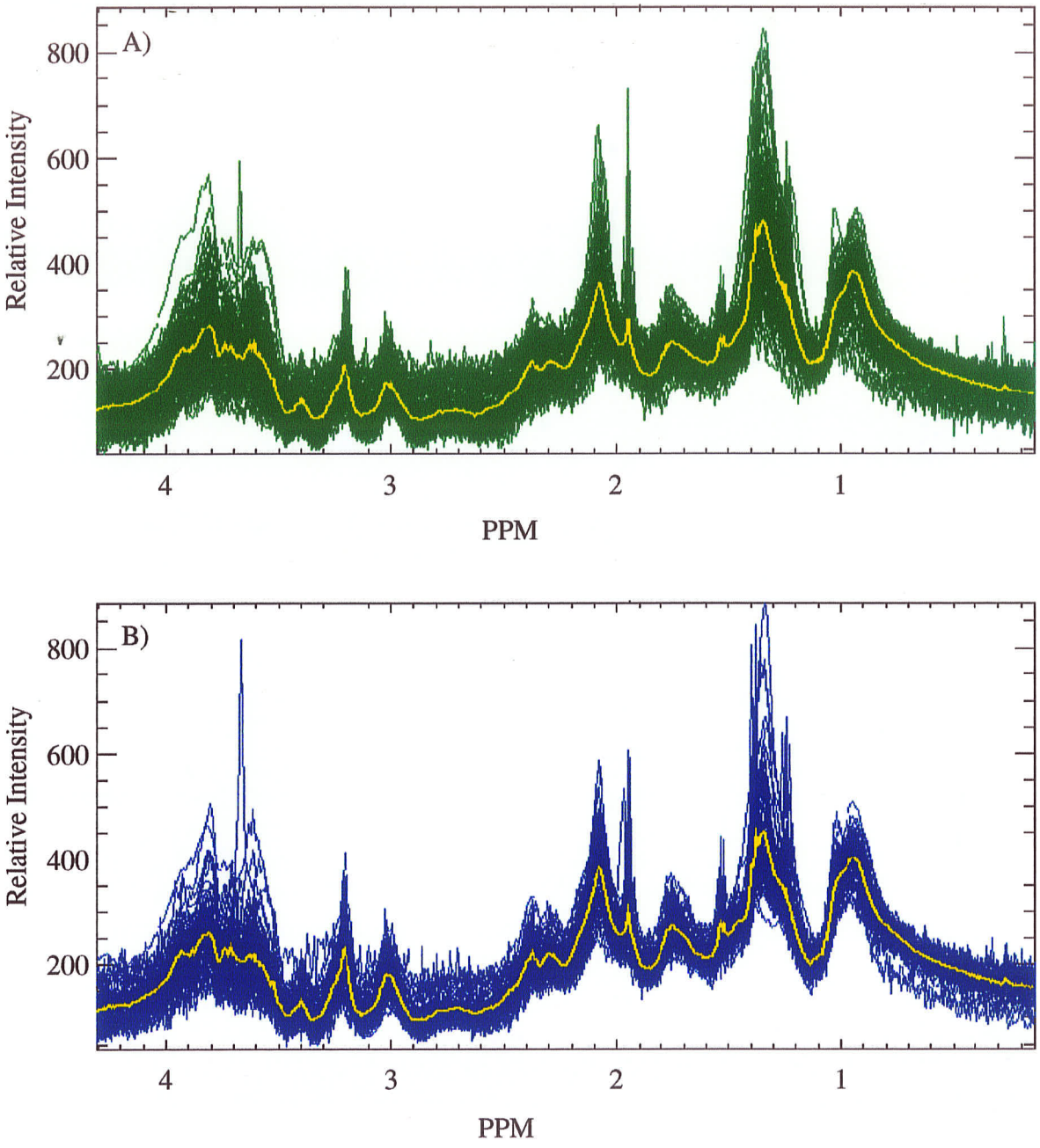

Figure 2.6: Spectra grouped according to two histopathological diagnoses - A) non-dysplastic and CIN 1 versus B) CIN 2 and CIN 3. Centroids are illustrated in yellow.

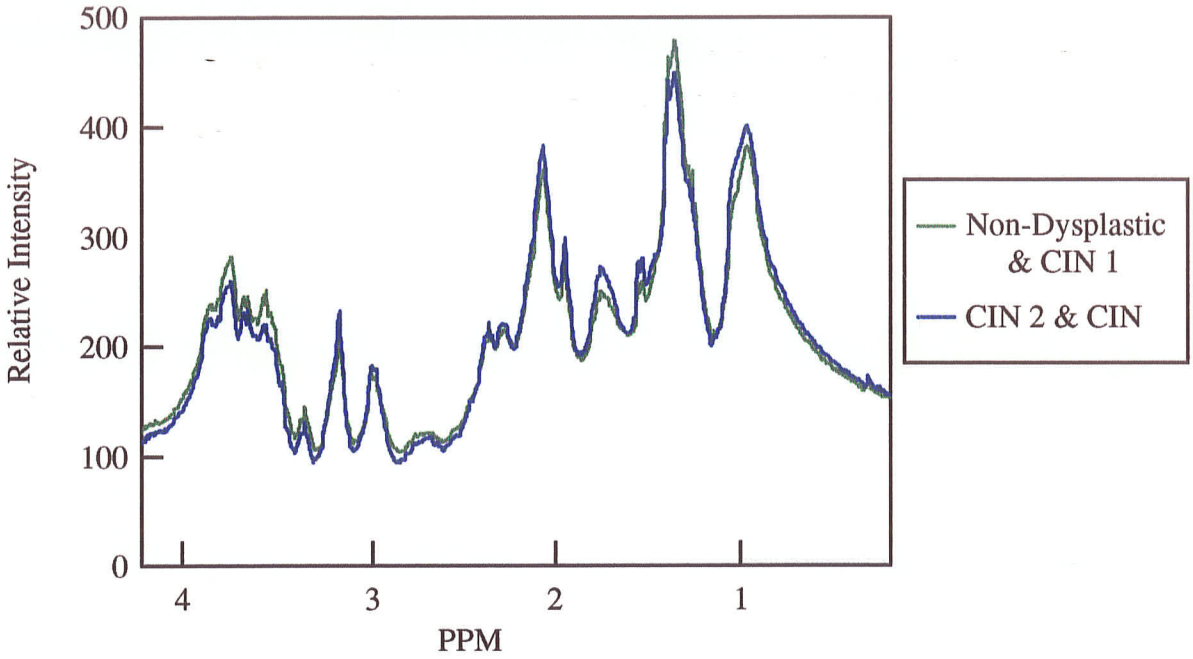

Figure 2.7: Centroids of the MR spectra classified in two diagnostic groups – non-dysplastic and CIN 1 vs CIN 2 and CIN 3.

The classification accuracy of the training and test sets were determined by the Linear Discriminant Analysis (LDA) for the four and two class problems that correspond to the two clinical diagnostic methods (Table 2.3). The four class problem corresponds to the CIN classification scheme, and the two class problem with non-dysplastic and CIN 1 versus CIN 2 and CIN 3 corresponds to the Bethesda classification system.

Table 2.3: Spectral Classification Accuracies as Compared to the Clinical Diagnoses Using the CIN and Bethesda Classification Systems

Class Definitions	Training Set	Training Set, Crisp Classification *	Test Set	Test Set, Crisp Classification *
CIN System – Non-dysplastic vs CIN 1 vs CIN 2 vs CIN 3	47.3%	60.0% (22.3%)	52.4%	51.8% (98.8%)
Bethesda System – Non-dysplastic and CIN 1 vs CIN 2 and CIN 3	93.8%	94.4% (96.4%)	70.2%	71.6% (96.4%)

*Value in brackets refers to percentage of the total number of spectra classified correctly or incorrectly with high probability (≥75%).

The values presented in Table 2.3 are those in which the method of analysis was optimized to yield the best test set classification accuracy. Several methods were tested for the two class problem in order to obtain an optimal result (Table 2.4). The accuracy of classification is presented as the percent of spectra whose diagnostic classifications, as determined by multivariate analysis, were in agreement with the clinical diagnoses. Also presented (Table 2.4) are the crisp classification accuracies, or the percentage of spectra classified correctly with high probability (≥75%). The percentage of the total number of spectra classified correctly or incorrectly with probability of 75% or greater is given in brackets. The classification accuracies are quite similar, ranging from 86.6% to 93.8% for the training set and 64.3% to 70.2% for the test set. LDA was performed using the intensities of the regions in the spectra, as well as ratios of these intensities. The use of ratios of the regions improved the test set classification accuracies by as much as 4.7%. The crisp classification accuracies for the training set increased by 0.6% to 9.7%, as

compared to the classification accuracies in which the spectra with low probabilities were included. In the test set, the crisp classification accuracies decreased when the first derivative of the spectra was used and increased by as much as 4.7% for the other multivariate strategies.

Table 2.4: Bethesda System (Non-dysplastic and CIN 1 versus CIN 2 and CIN 3) Classification Accuracies for each Multivariate Method

Multivariate Analysis Method	Training Set	Training Set, Crisp Classification *	Test Set	Test Set, Crisp Classification *
1) LDA using 6 of 128 Spectral Regions	87.5%	94.4% (79.5%)	65.5%	65.5% (100.0%)
2) LDA using 1 Region and 6 Ratios of Regions Generated from 6 of 128 Spectral Regions	91.1%	96.5% (76.8%)	70.2%	71.1% (98.8%)
3) LDA using 7 of 64 Spectral Regions	86.6%	92.0% (77.7%)	69.0%	69.0% (100.0%)
4) LDA using 2 Regions and 7 Ratios Generated from 7 of 64 Spectral Regions	90.2%	92.2% (80.4%)	70.2%	70.2% (100.0%)
5) ANN using 1 Region and 5 Ratios of Regions Generated from 6 of 128 Spectral Regions	89.3%	95.7% (83.0%)	67.9%	72.6% (86.9%)
6) Stacked Generalization - Median Method - using 1 Region and 5 Ratios of Regions Generated from 6 of 128 Spectral Regions	92.0%	94.4% (95.5%)	70.2%	71.2% (95.2%)
7) Stacked Generalization - Wolpert's Method - using 1 Region and 5 Ratios of Regions Generated from 6 of 128 Spectral Regions	93.8%	94.4% (96.4%)	70.2%	71.6% (96.4%)
8) First Derivative of Spectra, LDA, using 2 Regions and 5 Ratios of Regions Generated from 9 of 128 Spectral Regions	87.5%	97.2% (63.4%)	64.3%	63.9% (98.8%)

*Value in brackets refers to percentage of the total number of spectra classified correctly or incorrectly with high probability (≥75%).

The EFS-based feature selector found 5 regions from the 128 spectral regions to be diagnostic in the four class case. In the two class case, 6 regions were chosen from the 128 spectral regions for the LDA method (Table 2.4, method 1). Figures 2.8 and 2.9 show the centroids of the four and two class problems with the diagnostic regions highlighted. The centers of the five regions chosen in the four class case (Figure 2.8) are 1.11 ppm, 1.43 ppm, 1.46 ppm, 2.47 ppm, and 3.77 ppm. The centers of the six regions chosen in the two class case (Figure 2.9) are 1.11 ppm, 1.37 ppm, 1.46 ppm, 2.21 ppm, 2.44 ppm, and 3.51 ppm.

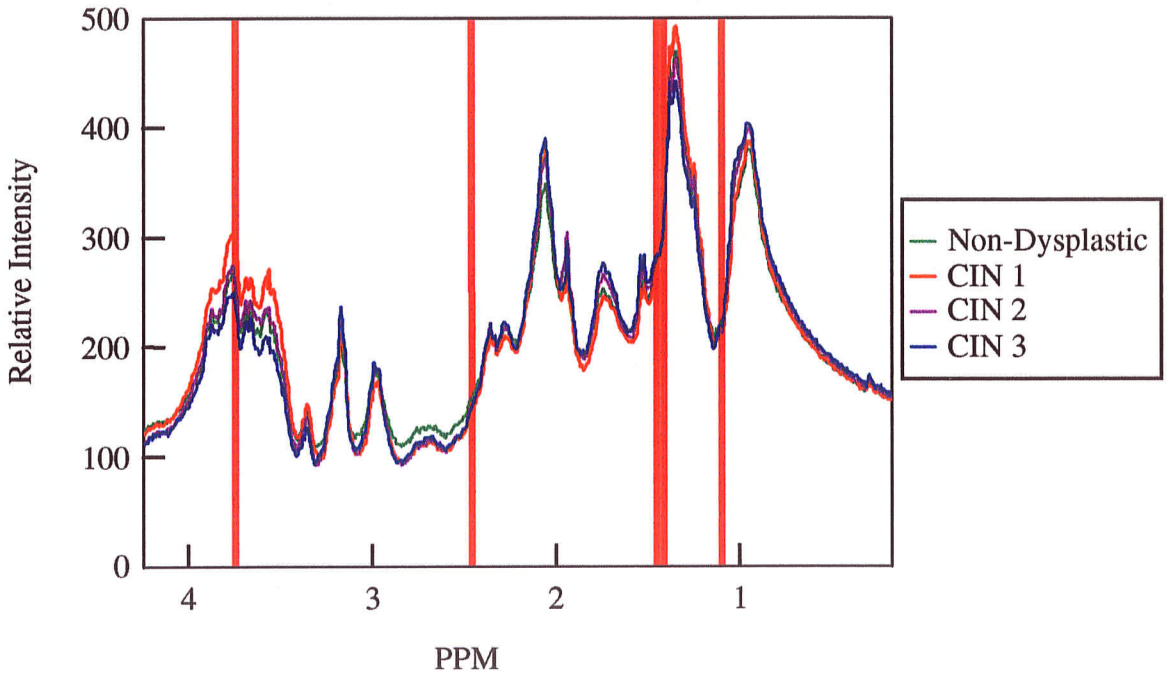

Figure 2.8: Centroids of the MR spectra classified in four diagnostic groups with the diagnostic regions highlighted.

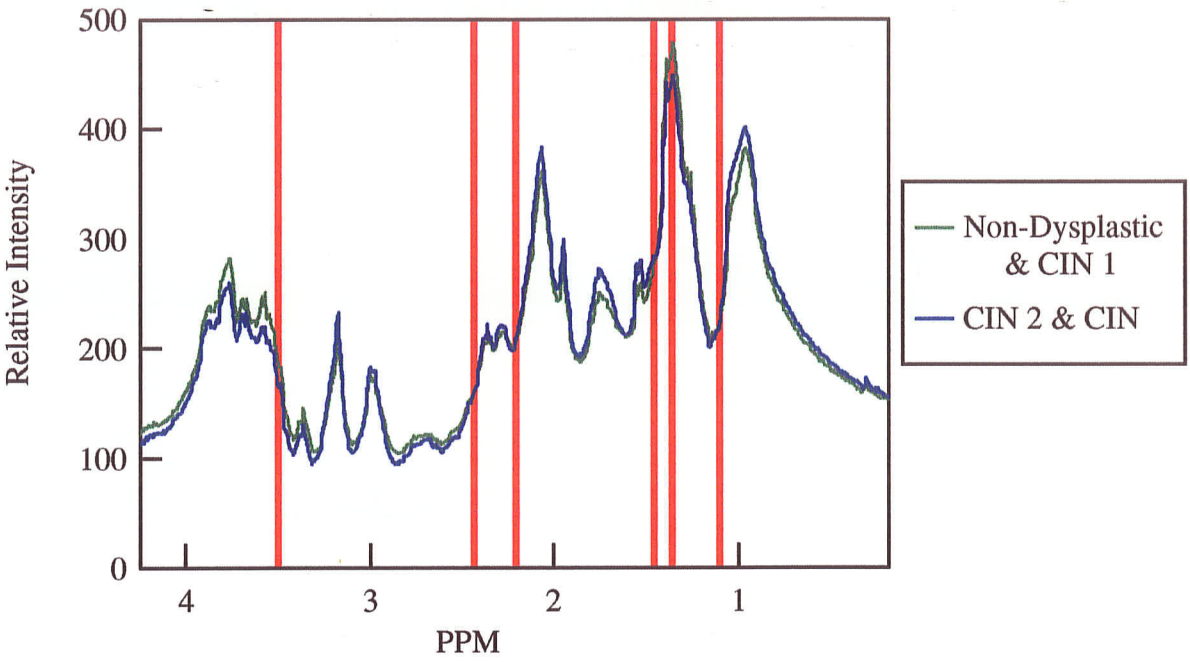

Figure 2.9: Centroids of the MR spectra classified in two diagnostic groups with the diagnostic regions highlighted.

The optimal classification accuracy of the four class problem was obtained using one region and four ratios of regions, while in the two class problem one region and five ratios of regions were used (Regions and ratios of regions are listed in Table 2.7). Note that in the two class case, the ratio of 1.46 ppm to 1.11 ppm was chosen by the EFS-based feature selector as a diagnostic ratio as well as the ratio of 1.11 ppm to 1.46 ppm. In essence, the same two peaks have been chosen as diagnostic regions twice as a means of weighting their effect on the classification. This serves to emphasize that this ratio and its inverse are important diagnostic attributes.

The regions and ratios of regions chosen by the EFS-based feature selector were not the same as those chosen by Delikatny *et al.* (1993) for their classification of the MR

spectra into invasive and preinvasive lesions. The regions and ratios used by Delikatny were selected from the spectra and were used as the input for LDA. The classification accuracies of the training and test sets for both selection of regions and ratios in the four class problem (CIN classification system) and the two class problem (Bethesda classification system) are given in Table 2.5.

Table 2.5: Spectral Classification Accuracies in Four and Two Classes Using the Regions and Ratios of Regions Determined by Delikatny *et al.* (1993) as the Input for LDA

Class Definitions	Training Set	Training Set, Crisp Classification *	Test Set	Test Set, Crisp Classification *
CIN System – Regions	30.4%	50.0% (8.9%)	34.5%	34.1% (97.6%)
CIN System – Ratios	33.0%	50.0% (5.4%)	28.6%	29.3% (97.6%)
Bethesda System – Regions	70.5%	76.7% (38.4%)	50.0%	50.0% (97.6%)
Bethesda System – Ratios	67.9%	88.2% (30.4%)	57.1%	57.8% (98.8%)

*Value in brackets refers to percentage of the total number of spectra classified correctly or incorrectly with high probability (≥75%).

In order to gain an understanding of the differences between the four diagnostic classes of non-dysplastic, CIN 1, CIN 2, and CIN 3, the classification accuracy was determined for every combination of two classes (Table 2.6). The spectra were also

classified in two classes first as non-dysplastic versus dysplastic and then as non-dysplastic, CIN 1, and CIN 2 versus CIN 3 (Table 2.6).

Table 2.6: Two Class Classification Accuracies Using LDA

Class Definitions	Training Set	Training Set, Crisp Classification *	Test Set	Test Set, Crisp Classification *
Non-dysplastic versus CIN 1, CIN 2, CIN 3	86.7%	89.4% (78.3%)	69.9%	69.9% (100.0%)
Non-dysplastic, CIN 1, CIN 2 versus CIN 3	80.0%	89.3% (46.7%)	78.7%	78.7% (100.0%)
Non-dysplastic versus CIN 3	86.0%	94.4% (72.0%)	73.5%	73.1% (98.5%)
Non-dysplastic versus CIN 2	98.0%	97.9% (94.0%)	74.0%	72.9% (96.0%)
CIN 1 versus CIN 3	100.0%	100.0% (98.0%)	82.6%	81.8% (95.7%)
Non-dysplastic versus CIN 1	88.0%	88.6% (70.0%)	65.6%	65.6% (100.0%)
CIN 1 versus CIN 2	90.0%	89.2% (74.0%)	75.9%	75.0% (96.6%)
CIN 2 versus CIN 3	82.0%	91.7% (72.0%)	74.2%	74.2% (100.0%)

*Value in brackets refers to percentage of the total number of spectra classified correctly or incorrectly with high probability (≥75%).

Using the results from the classifications of a) non-dysplastic and CIN 1 versus CIN 2 and CIN 3 (Table 2.3), b) non-dysplastic versus dysplastic (Table 2.6), and c) non-dysplastic, CIN 1, and CIN 2 versus CIN 3 (Table 2.5), the spectra were separated into

four diagnostic classes by averaging the probabilities of the classes for each spectrum. The overall classification accuracy obtained was 61.2%.

The regions and/or ratios of regions chosen by the EFS-based feature selector for each of the ten class definitions are given in Table 2.7. Four of the analyses were optimized using only regions. The addition of ratios of regions did not improve the classification accuracies. Five of the analyses were optimized using regions and ratios, and one analysis was optimized using only ratios of regions. No patterns were observed in the regions and ratios of regions chosen for the different class definitions.

The highest classification accuracy of the test set was obtained for the class definition of CIN 1 versus CIN 3 (Table 2.6) using two regions and seven ratios of regions in the spectra. These regions and ratios of regions were used to classify the spectra in every combination of two classes. The results are given in Table 2.8.

Table 2.7: Centers of Regions and/or Ratios Chosen by the Multivariate Methods for Each of the Class Definitions

Class Definition	Regions (ppm)	Ratios (ppm/ppm)
Non-dysplastic versus CIN 1 versus CIN 2 versus CIN 3	3.77	3.77/2.47, 2.47/1.11, 1.46/1.11, 1.43/1.11
Non-dysplastic & CIN 1 versus CIN 2 & CIN 3	1.11	1.11/3.51, 2.21/2.44, 2.21/1.46, 1.46/1.11, 1.11/1.46
Non-dysplastic versus CIN 1, CIN 2, & CIN 3	2.47, 2.21, 1.46, 1.40, 1.11, 1.07, 1.04	
Non-dysplastic, CIN 1, & CIN 2 versus CIN 3	2.50, 1.46, 1.43	
Non-dysplastic versus CIN 3	3.41, 3.31, 2.79	
Non-dysplastic versus CIN 2	3.12, 2.53, 2.47, 2.21, 1.98, 1.50, 1.11	
CIN 1 versus CIN 3	1.46, 1.37	3.38/2.28, 3.38/1.76, 1.76/3.38, 3.38/1.37, 2.44/1.95, 1.95/2.44, 2.44/1.37
Non-dysplastic versus CIN 1	3.77	3.25/3.87, 1.43/1.11, 0.20/1.11
CIN 1 versus CIN 2	0.75	3.10/2.89, 2.89/3.10, 1.37/3.10, 1.37/2.89, 1.04/2.89, 0.75/2.89, 0.75/1.37
CIN 2 versus CIN 3		3.67/3.25, 3.34/3.25, 2.08/3.34, 1.30/1.11

Table 2.8: Classification Accuracies Using the Regions and Ratios Chosen for CIN 1 Versus CIN 3

Class Definitions	Training Set	Training Set, Crisp Classification *	Test Set	Test Set, Crisp Classification *
Non-dysplastic vs CIN 1 vs CIN 2 vs CIN 3	35.7%	35.7% (25.0%)	40.5%	40.5% (100.0%)
Non-dysplastic & CIN 1 vs CIN 2 & CIN 3	82.1%	87.8% (73.2%)	61.9%	63.4% (97.6%)
Non-dysplastic vs CIN 1, CIN 2, & CIN 3	63.3%	72.4% (48.3%)	57.4%	57.0% (99.3%)
Non-dysplastic, CIN 1, & CIN 2, vs CIN 3	85.0%	92.1% (63.3%)	74.3%	74.4% (97.8%)
Non-dysplastic vs CIN 3	88.0%	92.7% (82.0%)	58.8%	59.1% (97.1%)
Non-dysplastic vs CIN 2	68.0%	70.8% (48.0%)	50.0%	51.1% (94.0%)
CIN 1 vs CIN 3	100.0%	100.0% (98.0%)	82.6%	81.8% (95.7%)
Non-dysplastic vs CIN 1	56.0%	60.9% (46.0%)	57.8%	61.0% (92.2%)
CIN 1 vs CIN 2	74.0%	73.3% (60.0%)	65.5%	65.5% (100.0%)
CIN 2 vs CIN 3	50.0%	33.3% (30.0%)	51.6%	53.3% (96.8%)

*Value in brackets refers to percentage of the total number of spectra classified correctly or incorrectly with high probability (≥75%).

2.6 Discussion

Visual examination of the spectra obtained from the cervical punch biopsies reveals no distinct peak or set of peaks which could be used for diagnosing the degree of dysplasia. There is a very large range of spectral peak intensities and peak widths in each of the four diagnostic groups (Figure 2.4). Since the degree of CIN is a measure of the thickness of cellular layers of the squamous epithelium showing abnormal morphology, one would expect the diagnosis of degree to be somewhat subjective, depending on the pathologist's appreciation of the delineation of the grades. This is not surprising in view of the large range of intensities observed in the spectra. Based on the wide range of spectra in each group and the small differences between the centroids of the classes (Figure 2.5), visual inspection of the spectra in terms of peak intensities and widths may not serve to separate the spectra accurately into classes which correspond to the clinical diagnoses. Computer-assisted multivariate methods of analysis are required.

Initially, the spectra were grouped into the four conventional diagnostic classes of non-dysplastic, CIN 1, CIN 2, and CIN 3. Classification by the multivariate methods yielded an accuracy of 46.4% for the training set (Table 2.3). The classification accuracy of the training set, however, is not a true test of the ability of the method to classify the spectra accurately, since any group of spectra can be separated into specific classes if enough parameters are considered (Somorjai *et al.* 1995). The true measure of the ability to classify the spectra accurately is found in the classification accuracy of the test set. Using the four diagnostic classes, the classification accuracy for the test set (Table 2.3) as determined using Linear Discriminant Analysis (LDA) and 5 ratios generated from 5 of

128 regions was 52.4%, whereas random classification would yield an accuracy of 25%. Elimination of the spectra classified correctly or incorrectly with probability less than 75% increased the accuracy of the training set significantly (60.0%), but only 22.3% of the spectra were classified with certainty (probability ≥75%). The crisp classification accuracy of the test set did not improve because almost all of the spectra (98.8%) were classified with high probability. The crisp classification accuracy and the low number of spectra classified with high probability in the training set suggest that the LDA was not well trained. Since the ranges of the spectra in each class suggest a continuous distribution from CIN 1 to CIN 3, it would not be surprising for spectra to be classified incorrectly into an adjacent class rather than the desired and clinically determined class. Examination of the distributions of the classifications revealed that this is not the case. In fact, in the extreme cases, spectra clinically diagnosed as non-dysplastic were classified as CIN 3 and vice versa.

The lack of high overall classification accuracy using four diagnostic classes could be attributed to the fact that the differences in the spectra of each diagnostic class are small. The multivariate classifiers, therefore, cannot readily be trained to identify four distinct classes. Theoretically, separation of the spectra into the two most extreme diagnostic cases, non-dysplastic and CIN 3, should be the easiest classification since one would expect that the biochemical differences between these classes would be maximal. Similarly, the spectra in classes CIN 1 and CIN 3 should exhibit fewer biochemical dissimilarities than the spectra in classes non-dysplastic and CIN 3, whereas the spectra in classes CIN 1 and CIN 2 would exhibit the least dissimilarities. It follows, therefore, that

if the spectra with diagnostic classes of non-dysplastic and CIN 1 were combined, and those in classes CIN 2 and 3 were combined, the differences in the spectra of class CIN 1 as compared to those of class CIN 2 would be enhanced, or weighted, by the dissimilarities between the spectra in classes non-dysplastic and CIN 3. The classifier could then be trained to separate the spectra into two classes. The two class analysis does not differentiate spectra with diagnoses of CIN 1 from those with diagnoses of non-dysplastic. This does not pose a problem in terms of determining the clinical treatment of the patient since the classification scheme separates the spectra according to the treatment regimens recommended by the majority of physicians. Patients with diagnoses of CIN 2 and CIN 3, or class two in this study's two class analysis, should be treated, whereas patients with diagnoses of non-dysplastic and CIN 1, class one in this study, should not be treated.

The spectral ranges for the two class problem, non-dysplastic and CIN 1 versus CIN 2 and CIN 3, were plotted (Figure 2.6). As in the four class problem, the spectral ranges are large and appear to overlap between the two classes. No difference between the two classes in terms of peak intensities and peak widths can be determined by visual examination. The centroids of the two classes (Figure 2.7) exhibit larger differences than were observed in the centroids of the four class problem. For instance, the differences in the centroids at 0.9, 1.6, 1.8, and 2.0 ppm, appear to be enhanced in the two class problem. Consideration of the spectral ranges, however, reveals that these differences are still within the ranges of the spectra, and separation of the spectra into diagnostic classes can not be accomplished without the aid of computer-assisted multivariate methods.

An initial attempt to classify the spectra into two groups yielded results which were much more promising than those found for the four class problem. Hence, the four class problem was abandoned and an effort was made to maximize the classification accuracy of the test set for the two class problem. Eight of the multivariate analysis methods used are listed in Table 2.4 along with the training and test set classification accuracies.

Calculation of the first derivative of the spectra removed any DC offsets which may have existed in the spectra, thus removing any classification error arising therefrom. The classification accuracy of the test set obtained using the first derivatives of the spectra as input for the multivariate analysis was 64.3%. This is slightly lower than the other classification accuracies listed in Table 2.4. Furthermore, the percentage of spectra classified with high probability was quite low in the training set, 64.3%, and removal of the spectra from the test set which were classified with low probability caused the classification accuracy to drop to 63.9%. The decrease in the classification accuracy was due to elimination of spectra that were correctly classified with low probability. It would appear that DC offset was not a factor in the analysis.

The classification accuracies obtained when LDA was performed using regions from the spectra which were smoothed over 5 points to obtain 128 subregions (Table 2.4, Method 1) were 87.5% for the training set and 65.5% for the test set. The same analysis using the spectra smoothed over 10 points to obtain 64 subregions (Table 2.4, Method 3)

resulted in classification accuracies of 86.6% and 69.0% for the training and test sets respectively. The classification accuracy for the test set using the spectra smoothed over 10 points was higher by 3.5%, suggesting that the reduction of noise caused by averaging over 10 points as compared to 5 points was significant. When ratios were used for the analysis along with the regions, however, the accuracy for the test sets with the spectra smoothed over five and ten points were identical. Smoothing over 10 points rather than 5 did not significantly improve the classification accuracy.

If the biochemical changes which lead to dysplasia involved independent changes in the concentrations of one or more molecular species, accurate diagnoses could be made using only certain regions in the spectra, and one would not expect the classification accuracy to improve with the use of ratios of the regions. The addition of ratios to the analysis using the spectra averaged to obtain 64 spectral regions (Table 2.4, Methods 3 and 4) resulted in an increase in the training set classification accuracy of 3.6% and a slight increase of 1.2% in the test set. When the spectra were averaged to obtain 128 spectral regions (Table 2.4, Methods 1 and 2), the training and test set classification accuracies increased by 3.6% and 4.7%, respectively, with the use of ratios. Although these increases are not large, they do imply that the biochemical changes leading to dysplasia are not due to independent changes in one or more molecular species. Rather, the biochemical changes are complex, interdependent variations in the concentrations of multiple molecular species which are observable in the MR spectra as relative changes in peak intensities and widths.

The optimal training set classification accuracy, 93.8%, for the two class problem was obtained using the combination of LDA and ANN through Wolpert's stacked generalization method (Table 2.4, Method 7). Examination of Table 2.4 reveals, however, that four of the eight different multivariate strategies yielded a test set classification accuracy of 70.2% (Table 2.4, Methods 2, 4, 6, and 7). Since the range in training set classification accuracies for these four methods is only 3.6%, and since the true test of the multivariate method is the classification accuracy of the test set, these four methods yielded equivalent results. Examination of the crisp classifications revealed similar findings. The increase in the classification accuracies when spectra with low classification probabilities (<75%) were removed was not significant for these four methods. The largest increase was 1.6%. The percentage of spectra classified correctly or incorrectly with high probability differs slightly for each method, ranging from 95.2% to 100.0%. It could be argued that the analysis using LDA with the 2 regions and 7 ratios of regions generated from 7 of 64 spectral regions (Table 2.4, Method 4) yielded the best results since 100.0% of the spectra in the test set were classified with high probability (≥75%). The multivariate methods, however, are most robust when the fewest number of spectral regions and ratios of regions are used. The stacked generalization method used the fewest regions and ratios of regions and gave the best results in terms of the training set classification accuracy and the crisp classification in the test set (Tables 2.4, Method 7). It is also desirable, however, to use the simplest analysis possible in order to ensure that the analysis is robust and can be accomplished in a minimal amount of time. The method in which one region and six ratios of regions generated from six of 128 spectral regions was input for the LDA (Table 2.4, Method 2) yielded almost identical results to

the stacked generalization using Wolpert's method and does not require the use of both LDA and ANN. Further, this method averages over five points rather than ten, and thus, loses less information in the averaging process than is lost when averaging over larger numbers of points. Thus, LDA averaging over five points is the analytical method of choice (Table 2.4, Method 2).

A classification accuracy in the test set of 70.2% meant that thirty-five of the spectra in the test set were misclassified. Examination of the classification results for each spectrum in each of the applied methods revealed that fourteen of the spectra were misclassified by all or almost all of the multivariate classifiers. Removal of these fourteen spectra from the test set resulted in an increase in the two class classification accuracy of the test set from 70.2% to 84.3%. This increase in the classification accuracy was significant, and thus warranted a close examination of the spectra which were consistently misclassified. No unique attribute could be identified in these spectra which would suggest that they are outliers. The histopathological specimens and clinical findings for these fourteen patients as well as fifteen other patients with frequently misclassified spectra were re-examined. The majority of the original clinical diagnoses were confirmed. In three cases, however, additional information was available. In one of these cases, the patient had originally been diagnosed with CIN 1, and was not treated. Six months after this diagnosis, the patient returned for a second biopsy and was diagnosed with CIN 2. The MRS analysis was performed on the first biopsy which was clinically diagnosed as a CIN 1 lesion, however, the MRS analysis consistently classified this biopsy to the class containing lesions with diagnoses CIN 2 and CIN 3. This suggests

that either the original clinical diagnosis, possibly due to sampling error, or that the MRS analysis detected progression of the biochemistry of the cervical lesion from CIN 1 to CIN 2 before progression in morphology occurred. In two of the twelve consistently misclassified cases, the patients were diagnosed as non-dysplastic, but on follow-up visits, were diagnosed with CIN 1. While the spectra obtained from these two cases should still be classified in the non-dysplastic and CIN 1 class, even with the additional information from the follow-up visits, it may be that the MRS is detecting the progressive potential of the lesions. It is possible that the lesions which were classified incorrectly by the MRS technique had begun to progress or regress. This progression/regression may be initiated by MRS observable biochemical changes that precede the morphological changes. A follow-up study could determine whether morphological changes would occur to confirm the MRS diagnoses. This is not possible for the present cohort since the majority of patients diagnosed with CIN, including CIN 1, were treated. A long term study is required in which patients who refuse treatment for dysplastic lesions would be followed.

A previous study by Delikatny *et al.* (1993) found that differentiation of invasive cervical cancer specimens from preinvasive lesions could be accomplished based on the ratios of the peak intensities at 1.3 ppm compared to 0.9 ppm, and 3.8 ppm compared to 1.3 ppm. Spectra of invasive and preinvasive lesions also showed significant differences in the maximum intensity of peaks at 0.9 ppm, 1.3 ppm, 3.8 ppm, and 4.2 ppm. It was not possible, however, to differentiate between the three grades of CIN using these peak intensities and ratios of peak intensities. In the present study, regions near to but not

identical to these were found to be diagnostic by the EFS-based feature selector (Figures 2.8 and 2.9 and Table 2.7). In order to determine if LDA could classify the spectra according to the peak intensities chosen by Delikatny *et al.* (1993), regions centered at the peaks chosen by Delikatny *et al.* (1993) were selected from the spectra that were averaged over 5 points. Rather than comparing the peak intensities at these points, the regions were used as the input for the LDA. This analysis was repeated using the two ratios of regions chosen by Delikatny *et al.* (1993). The classification accuracies of the training and test sets for the four class problem (CIN classification system) and the two class problem (Bethesda classification system) are given in Table 2.5. In the four class case, the classification accuracies of the training and test sets for both the selection of regions and ratios of regions are only slightly higher than random classification, 25%. The number of spectra in the test set classified correctly or incorrectly with high probability is less than 10%. This implies that the LDA was not trained well. In the two class case, the classification accuracies of the training set were somewhat better (70.5% and 67.9%) with more spectra classified with high probability (more than 30%), but the classification accuracies of the test set were poor. In the case where the regions were the input for the LDA, the classification accuracy of the test set was random (50%). This is in agreement with the findings of Delikatny *et al.* (1993). The peaks at 0.9 ppm, 1.3 ppm, 3.8 ppm, and 4.2 ppm are not diagnostic of the degree of dysplasia present in cervical tissue biopsies.

Classification of the spectra was performed with the spectra grouped according to non-dysplastic versus dysplastic, and non-dysplastic, CIN 1, and CIN 2 versus CIN 3.

The classification accuracies of the test set were 69.9% and 78.7%, respectively. Using these results, and the results from the classification of non-dysplastic and CIN 1 versus CIN 2 and CIN 3, it is possible to separate the spectra into the four diagnostic classes of the CIN classification system. Using these three classifications, the overall classification accuracy obtained for all the spectra (training and test sets combined) was 61.2%. This is significantly higher than the classification accuracy of 52.4% obtained for the test set when LDA was used to classify the spectra into four classes. An accuracy of 61.2%, however, is not clinically useful.

The results given to this point suggest that the differences in the spectra grouped according to the clinical diagnoses are small. Since the morphological changes associated with dysplasia follow a continuous linear progression from non-dysplastic to CIN 3, the MRS observable biochemical changes may also show a continuous progression from non-dysplastic to CIN 3. If this is the case, it would be reasonable to predict that the multivariate analysis would yield higher classification accuracies for two classes that are not adjacent. For example, spectra with clinical diagnoses of non-dysplastic should be more easily separated by the multivariate method from spectra with clinical diagnoses of CIN 2 and CIN 3 than from CIN 1. Multivariate analysis was performed for every combination of two classes. The classification accuracies obtained are given in Table 2.6. Four of the six class definitions yielded similar results with test set classification accuracies between 73% and 76%. Classification of non-dysplastic versus CIN 1 was significantly worse than the other classifications with a test set classification accuracy of 65.6%, and CIN 1 versus CIN 3 was significantly better with a test set classification

accuracy of 82.6%. One would expect that non-dysplastic versus CIN 3 would classify with equal or better accuracy than CIN 1 versus CIN 3. This was not the case. Further, the classification accuracies of adjacent classes were not consistently worse than classes that were not adjacent. These results do not support, but can not refute, the hypothesis that the biochemical changes follow a continuous progression from non-dysplastic to CIN 3. Examination of the regions selected as diagnostic for each of the class definitions is necessary in order to gain an understanding of the biochemical differences between spectra from each of the four diagnostic classes.

Chemical species which may contribute to major peaks in the MR spectra of cervical biopsies are as follows:

Table 2.9: Chemical Species Contributing to Peaks in ^{1}H MR Spectra of the Cervical Tissue Biopsies (Sze and Jardetzky 1990a, b)

Peak Position	Contributing Chemical Species
0.9 ppm	$-CH_3$
1.3 ppm	$-CH_2-$
1.6 ppm	$-CH_2-CH_2-COO$
2.0 ppm	$-CH_2-C=C-$
2.2 ppm	$-CH_2-COO$
2.7 ppm	$-C=C-CH_2-C=C-$
3.0 ppm	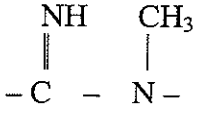
3.2 ppm	$-N-CH_3$
3.45 ppm	$-CH_2-SO_3$
3.5 - 4.2 ppm	Protons of cyclic compounds

The regions and/or ratios of regions selected by the EFS-based feature selector are listed in Table 2.7 for each of the class definitions. In many cases, diagnostic regions were chosen on the sides of spectral peaks. Spectra obtained from tissue biopsies are complicated by resonances from many different biochemicals. A single peak may be broad, with contributions from multiple molecular species. The variations in the line widths found to be diagnostic by the EFS-based feature selector may be attributed to broadening and narrowing of the peaks as the concentrations of the contributing chemical species change. While some spectral regions were chosen for more than one class definition, no region was consistently chosen for all of the class definitions. Four class

definitions used only regions with no ratios, suggesting that the biochemical changes in these cases are not interdependent. Conversely, one definition used only ratios, which would suggest that in this case, the biochemical changes are completely interdependent. No trend was observed in the regions and/or ratios chosen. This also does not support, but can not refute, the hypothesis that the MR observable biochemical changes which occur in cervical lesions follow a continuous linear progression from non-dysplastic to CIN 3.

Classification of non-dysplastic versus CIN 1 yielded a classification accuracy (65.6%) that was significantly lower than the accuracies of the other two class definitions (Table 2.6). The LDA had difficulty distinguishing between non-dysplastic and CIN 1. This may be attributed to the abnormalities present in the non-dysplastic tissue. The non-dysplastic group consisted of biopsies with clinical diagnoses that were not dysplastic, but not necessarily normal. Included in this group were biopsies diagnosed with reactive changes, HPV infection but no dysplasia, cervicitis or inflammation, and metaplasia. Less than 30% of these biopsies were truly normal. Thus, biochemical changes have occurred in these biopsies that may or may not be related to dysplastic changes. The non-dysplastic group is not a good control group. The control group should contain only biopsies with clinical diagnoses of normal. Since healthy cervices are not normally biopsied, it is not possible to obtain an appropriate control group.

Classification of CIN 1 versus CIN 3 yielded a classification accuracy for the test set (82.6%) that was significantly higher than the accuracies of the other two class

definitions (Table 2.6). If the biochemical changes that occur with progression of disease are similar but of different scales at each stage of the progression, the regions and ratios of regions chosen for the classification of CIN 1 versus CIN 3 could be used to classify the spectra in the other class definitions with accuracy as well. The classification accuracies obtained for each of the class definitions when the regions and ratios of regions chosen for CIN 1 versus CIN 3 were applied are listed in Table 2.8. The accuracies range from 40.5% to 74.3% for the test sets. They are all significantly lower than the values obtained when the EFS-based feature selector was used to determine unique diagnostic regions and/or ratios of regions for each class definition (compare to Tables 2.3 and 2.6). The crisp classifications of the test sets do not significantly improve the results. Only the class definition of non-dysplastic, CIN 1, and CIN 2 versus CIN 3 yielded a reasonably accurate classification for the test set (74.3%). This is somewhat surprising in light of the fact that the regions and ratios chosen for the CIN 1 versus CIN 3 class definition were very different than those originally chosen for the non-dysplastic, CIN 1 and CIN 2 versus CIN 3 case (Table 2.7). In fact, in this case, only three regions were used with no ratios of regions. Since the classification of non-dysplastic versus CIN 1 was poor (Table 2.6), one would expect the classification accuracies of non-dysplastic versus CIN 3, and CIN 1 versus CIN 3 to be similar when the same regions and ratios of regions were applied to both class definitions. This was not the case (Table 2.7). Further, only regions were chosen by the EFS-based feature selector for classification of non-dysplastic versus CIN 3, and these regions were very different than the regions and ratios of regions chosen for the classification of CIN 1

versus CIN 3. These results suggest that there are differences in the biochemistry of tissue biopsies with diagnoses of non-dysplastic and CIN 1.

The classification of the spectra according to the clinical diagnoses of non-dysplastic, CIN 1, CIN 2, and CIN 3 is complicated by several factors. First, the classifications obtained using the MR spectra and the multivariate methods were compared to the clinical diagnoses. The clinical diagnoses are based on the combination of the cytological report, the colposcopic impression, and the histopathological report. As previously discussed, the accuracy of cytology is low. The colposcopic impression is based on what the examining gynecologist observes, making it subjective and insufficient for accurate diagnosis. Histopathology is also somewhat subjective with low diagnostic accuracy. While Burghardt *et al.* (1994) state that the combination of cytology and histopathology allow detection of CIN with an accuracy that approaches 99%, the accuracy of grading the degree of dysplasia may be much lower. The classifications in this study have been compared to the clinical diagnoses which are not 100% accurate. If the true diagnoses could be used for comparison, the classification accuracies obtained by the MRS and multivariate methods may increase.

Cervical lesions are often so small that a single punch biopsy will remove the entire lesion and may include some of the tissue surrounding the lesion. This may complicate the MR spectra. It is possible for two lesions with different grades of dysplasia to exist immediately adjacent to one another (Burghardt *et al.* 1994). The MR spectrum from a biopsy composed of two lesions with differing grades of dysplasia will

exhibit a combination of the two types of biochemical changes. If the biochemical changes progress from CIN 1 to CIN 3 and the biopsy contains equal portions from a CIN 1 lesion and a CIN 3 lesion, for example, the MRS and multivariate method may classify the spectrum incorrectly as CIN 2. If the biochemical changes do not progress, but rather are different at each stage of progression of the lesion, changes may occur in the MR spectra which correlate to more than one diagnostic classification. This, too would make classification by the multivariate method difficult.

It is known that MR spectra differ for different organs of the body and for different disease processes (Mountford *et al.* 1996). Further, MRS studies of human and rat colon tissue have shown that the appearance of the MR spectrum differs for each of the different layers of tissue in the colon (Brière *et al.* 1995, Moreno *et al.* 1993). Using infrared spectroscopy, Krupnik *et al.* (1998) confirmed that the biochemical composition of the different layers of tissue in the rat colon give rise to different absorption peaks in the infrared spectra. It is reasonable to believe that the different types of tissue present in the uterine cervix will also give rise to different MR spectra. Ninety to ninety-five percent of cervical lesions originate in the transformation zone, and this is where the columnar epithelium of the endocervix meets the squamous epithelium of the exocervix. Hence, biopsies of cervical lesions will contain varying quantities of columnar and squamous epithelial cells. It is possible that the MR spectra differ as the relative quantities of columnar and squamous epithelial cells present in the tissue biopsy vary. This would complicate the spectra making diagnosis of the degree of dysplasia difficult. In this MRS study, only biopsies from the transformation zone were examined, and these

contained either only squamous epithelial cells or both squamous and columnar epithelial cells.

Several biochemical changes not related to the dysplastic process may also be visible in the MR spectra. First, the cervix undergoes changes through the menstrual cycle and after menopause. It is known that glycogen concentrations in the cervix increase during the period of ovulation, and decrease after ovulation and after menopause (Kurman 1987, Gilks *et al.* 1989). Because glycogen is a large, relatively immobile molecule, it is unlikely that it would be observed in MR spectra. It is probable, however, that other biochemical changes, some of which may be triggered by changing glycogen concentrations, also occur in the cervix through the menstrual cycle and during menopause. These changes may cause variations in the MR spectra. Second, it is known that some dysplastic lesions progress to invasive cancer while others regress to normal. There may be MR observable biochemical changes associated with the potential for progression which partially mask the MR features which are due to the dysplastic changes. As previously discussed, a follow-up study of untreated patients is necessary. Finally, the presence of sexually transmitted diseases, such as herpes, human immunodeficiency virus (HIV), clamidia, and human papillomavirus (HPV), may play a role in the changing biochemistry of the cervix, and thus cause variations in the MR spectra. Particularly important are the changes caused by HPV, because HPV has been linked to dysplasia and invasive cancer of the cervix. A study is required that attempts to correlate the MR spectra to the HPV type present in the tissue. Since there are approximately twenty HPV types that can occur in the cervix and multiple types can be

present simultaneously, it would be a formidable task to attempt to correlate the MR spectra to each of the HPV types. The types, however, can be grouped into low, intermediate, and high risk of progression to carcinoma. The MR spectra could be correlated to these three categories, thus providing a measure of the progressive potential of cervical lesions.

2.7 Conclusions

The differences in the MR spectra of non-dysplastic cervical tissue and cervical lesions do not allow classification by visual inspection nor by simple peak ratios. Classification of the spectra into four diagnostic groups – non-dysplastic, CIN 1, CIN 2, and CIN 3 - is difficult. Using multivariate methods, classification of the spectra into two classes – non-dysplastic and CIN 1 versus CIN 2 and CIN 3 – resulted in optimal classification accuracies of 91.1% for the training set and 70.2% for the test set. Fourteen spectra in the test set were consistently misclassified by the multivariate methods. It is hypothesized that in these cases, the MRS technique has detected changes in the biochemistry of the lesions which preceded the morphological changes.

Histopathology suggests that the morphological changes caused by dysplasia of the cervix follow a continuous progression from CIN 1 to CIN 3. In this study, the accuracy of classification of spectra into two adjacent diagnostic classes, such as CIN 1 versus CIN 2, was comparable to those of non-adjacent classes, such as non-dysplastic versus CIN 3. The regions and/or ratios of regions chosen for each combination of two

classes were different. This does not support, but can not refute, the hypothesis that the MR observable biochemical changes associated with dysplasia follow a continuous linear progression. The changes may be different at each stage of progression.

2.8 Future Perspectives

A greater knowledge of the biochemical changes involved with dysplasia may provide information regarding the progressive or regressive potential of cervical lesions. The multivariate methods are sensitive to small variations in the MR spectra, including variations in the noise. In this analysis, only crude methods were used to minimize the noise. Reduction of the noise in the spectra through more sophisticated techniques such as wavelet transforms may improve the classification accuracies.

Histopathology, which detects morphological changes in tissue, is not able to determine the progressive potential of pre-cancerous lesions of the cervix. Biochemical changes, however, may be associated with progressive potential. An MRS study is required where untreated lesions are followed through their dysplastic progression/regression in order to determine if MR observable biochemical changes can be seen that correlate to progressive potential.

Many factors may affect the biochemical content of the cervix. Biochemical changes, which may be observable in the MR spectra, occur through the menstrual cycle and after menopause. The mechanism of progression or regression of cervical lesions is

poorly understood and may be a source of variation in the MR spectra. The changes associated with the sexually transmitted disease HPV are of particular importance in light of the link between HPV and cervical dysplasia. If the MR spectra could be correlated to the presence of low, intermediate, and high grade HPV types, a measure of the progressive/regressive potential of cervical lesions would be available, and this would have a profound impact on clinical treatment. A study of the biochemical changes that occur in the cervix as a result of non-dysplastic events is necessary.

2.9 References

Alani RM, Münger K. Human papillomaviruses and associated malignancies. *J. Clin. Oncol.* **16**: 330-337, 1998.

Appleby J. Management of the abnormal Papanicolaou smear. *Med. Clin. North Am.* **79**: 345-360, 1995.

Armstrong BK, Muñoz N, Bosch FX. Epidemiology of cancer of the cervix. In *Gynecologic Oncology*. M Coppleson, ed. Churchill Livingstone, New York, 2nd ed. Vol. 1, 1992, 11.

Bosch FX, Muñoz N, de Sanjosé S. Human papillomavirus and other risk factors for cervical cancer. *Biomed. and Pharmacother.* **51**: 268-275, 1997.

Breitenecker G and Gitsch G. What's new in diagnosis and treatment of HPV-associated cervical lesions. *Path. Res. Pract.* **188**: 242-247, 1992.

Briére KM, Kuesel AC, Bird RP, Smith ICP. ^{1}H MR visible lipids in colon tissue from normal and carcinogen-treated rats. *NMR Biomed.* **8**: 33-40, 1995.

Burghardt E, Winter R, Tamussino K, Hellmuth P, Lahousen M, Haas J, Girardi F, Ebner F, Hackl A, Pfister H. Diagnosis and surgical treatment of cervical cancer. *Crit. Rev. Oncol. Hematol.* **17**: 181-231, 1994.

Campion MJ and Sedlacek TV. Colposcopy in pregnancy. *Obstet. Gynecol. Clin. North Am.* **20**: 153-163, 1993.

Cannistra SA and Niloff JM. Cancer of the uterine cervix. *N. Engl. J. Med.* **334**: 1030-1038, 1996.

Daley EM. Clinical update on the role of HPV and cervical cancer. *Cancer Nurs.* **21**: 31-35, 1998.

Delikatny EJ, Russell P, Hunter JC, Hancock R, Atkinson KH, van Haaften-Day C, Mountford CE. Proton MR and human cervical neoplasia: Ex vivo spectroscopy allows distinction of invasive carcinoma of the cervix from carcinoma in situ and other preinvasive lesions. *Radiology* **188**: 791-796, 1993.

Ferenczy A and Winkler B. Cervical intraepithelial neoplasia and condyloma. In *Blaustein's Pathology of the Female Genital Tract.* RJ Kurman, ed. Springer-Verlag, New York, 3rd ed. 1987, 181, 193.

Gilks CB, Reid PE, Clement PB, Owen DA. Histochemical changes in cervical mucus-secreting epithelium during the normal menstrual cycle. *Fertil. Steril.* **51**: 286-291, 1989.

Higgins PG, Smith PE. Assessing cervical cancer risk. *Lifelines* **1**: 43-47, 1997.

Ismail SM, Colclough AB, Dinnen JS, Eakins D, Evans DMD, Gradwell E, O'Sullivan JP, Summerell JM, Newcombe RG. Reporting cervical intra-epithelial neoplasia (CIN): Intra- and interpathologist variation and factors associated with disagreement. *Histopathology* **16**: 371-376, 1990.

Ismail SM, Colclough AB, Dinnen JS, Eakins D, Evans DMD, Gradwell E, O'Sullivan JP, Summerell JM, Newcombe RG. Observer variation in histopathological diagnosis and grading of cervical intraepithelial neoplasia. *Br. Med. J.* **298**: 707-710, 1989.

Krupnik E, Smith ICP, Bird RP, Jackson M. Infrared spectroscopic characterisation of putative premalignant lesions in the rat colon. *Appl. Spectrosc.* (in press), 1998.

Kuesel AC, Kroft T, Saunders JK, Prefontaine M, Mikhael N, Smith ICP. A simple procedure for obtaining high-quality NMR spectra of semiquantitative value from small tissue specimens: cervical biopsies. *Magn. Reson. Med.* **27**: 349-355, 1992.

Kuesel AC, Kroft T, Saunders JK, Prefontaine M, Mikhael N, Smith ICP. Cervical dysplasia: Characterization and staging by ^{1}H MRS. *Proc. Soc. Magn. Reson. Med.* 584, 1991.

Le ND, Marrett LD, Robson DL, Semenciw RM, Turner D, Walter SD. Canadian Cancer Incidence Atlas. Canada Communication Group – Publishing, Ottawa, Canada, Vol. 1, 1995.

Lewis TLT and Chamberlain GVP, eds. Gynaecology by Ten Teachers. Edward Arnold, London, England, 15th ed. 1989, 121-129.

Mezrich R. Magnetic resonance imaging applications in uterine cervical cancer. *Magn. Reson. Imaging Clin. N. Am.* **2**: 211-244, 1994.

Miller BF and Brackman Keane C. Encyclopedia and dictionary of medicine, nursing, and allied health. W.B. Saunders Company, Philadelphia, 4th ed. 1987.

Moreno A, Mercé R, Montane JM, Alonso J, Arús C. ^{1}H NMR spectroscopy of colon tumors and normal mucosal biopsies; Elevated taurine levels and reduced polyethyleneglycol absorption in tumors may have diagnostic significance. *NMR Biomed.* **6**: 111-118, 1993.

Mountford CE, Delikatny EJ, Dyne M, Holmes KT, Mackinnon WB, Ford R, Hunter JC, Truskett ID, Russell P. Uterine cervical punch biopsy specimens can be analyzed by ^{1}H MRS. *Magn. Reson. Med.* **13**: 324-331, 1990.

Mountford CE, Mackinnon WB, Russell P, Rutter A, Delikatny EJ. Human cancers detected by proton MRS and chemical shift imaging *ex vivo*. *Anticancer Res.* **16**: 1521-1532, 1996.

National Cancer Institute of Canada: Canadian Cancer Statistics 1998, Toronto, Canada, 1998.

National Cancer Institute Workshop. The 1988 Bethesda system for reporting cervical/vaginal cytological diagnosis. *JAMA* **262**: 931-934, 1989.

Nikulin AE, Dolenko B, Bezabeh T, Somorjai RL. Near-optimal region selection for feature space reduction: Novel preprocessing methods for classifying MR spectra. *NMR Biomed.* (in press), 1998.

Reid R, Greenberg M, Jensen AB, Husain M, Willett J, Daoud Y, Temple G, Stanhope CR, Sherman AI, Phibbs GD, Lorincz AT. Sexually transmitted papillomaviral infections. I. The anatomic distribution and pathologic grade of neoplastic lesions associated with different viral types. *Am. J. Obstet. Gynec.* **156**: 212-222, 1987.

Reid R, Stanhope CR, Herschman BR, Booth E, Phibbs GD, Smith JP. Genital warts and cervical cancer. I. Evidence of an association between subclinical papillomavirus infection and cervical malignancy. *Cancer* **50**: 377-387, 1982.

Report of the Canadian task force: Cervical cancer screening programs. I. Epidemiology and natural history of carcinoma of the cervix. *Can. Med. Assoc. J.* **114**: 1003-1012, 1976.

Richart RM, Masood S, Syrjänen KJ, Vassilakos P, Kaufman RH, Meisels A, Olszewski WT, Sakamoto A, Stoler MH, Vooijs GP, Wilbur DC. Human papillomavirus; IAC Task Force summary. *Acta. Cytol.* **42**: 50-58, 1998.

Schiffman MH. Latest HPV findings: Some clinical implications. *Contemp. Ob. Gy.* **38**: 27-40, 1993.

Shah KV. Human papillomaviruses and other biological markers in cervical cancer. In *The Epidemiology of Human Papillomavirus and Cervical Cancer.* N Muñoz, FX Bosch, KV Shah, A Meheus, eds. International Agency for Research on Cancer, Lyon, France, 1992, 209-218.

Sherman ME, Schiffman MH, Lorincz AT, Manos MM, Scott DR, Kurman RJ, Kiviat NB, Stoler M, Glass AG, Rush BB. Toward objective quality assurance in cervical cytopathology. *Am. J. Clin. Path.* **102**: 182-187, 1994.

Sloane E. Biology of Women. John Wiley and Sons, New York, 2nd ed. 1985, 42-44, 272-280.

Somorjai RL, Dolenko B, Nikulin AK, Pizzi N, Scarth G, Zhilkin P, Halliday W, Fewer D, Hill N, Ross I, West M, Smith ICP, Donnelly SM, Kuesel AC, Brière KM. Classification of ^{1}H MR spectra of human brain neoplasms: The influence of preprocessing and computerized consensus diagnosis on classification accuracy. *J. Magn. Reson. Imaging* **6**: 437-444, 1996.

Somorjai R, Nikulin AE, Pizzi N, Jackson D, Scarth G, Dolenko B, Gordon H, Russell P, Lean CL, Delbridge L, Mountford CE, Smith ICP. Computerized consensus diagnosis: A classification strategy for the robust analysis of MR spectra. I. Application to ^{1}H spectra of thyroid neoplasms. *Magn. Reson. Med.* **33**: 257-263, 1995.

Steben M (Principal Author), Boroditsky R, Parish B, Woodrow P, Miller D, Guimond J-V, Cabana D, Lalonde A, Lea R. Sexually transmitted diseases; Canadian guidelines: Then, now and the future. *SOGC Committee Opinion* No. 8, October 1994.

Stratton P and Ciacco KH. Cervical neoplasia in the patient with HIV infection. *Curr. Opin. Obstet. Gynecol.* **6**: 86-91, 1994.

Syrjänen KJ. Epidemiology of human papillomavirus (HPV) infections and their associations with genital squamous cell cancer. *APMIS* **97**: 957-970, 1989.

Sze DY and Jardetzky O. Determination of metabolite and nucleotide concentrations in proliferating lymphocytes by ^{1}H-NMR of acid extracts. *Biochim. Biophys. Acta.* **1054**: 181-197, 1990a.

Sze DY and Jardetzky O. Characterization of lipid composition in stimulated human lymphocytes by ^{1}H-NMR. *Biochim. Biophys. Acta.* **1054**: 198-206, 1990b.

Valente PT. Update on the Bethesda System for reporting cervical/vaginal diagnoses. In *Gynecologic Oncology: Controversies and New Developments.* ML Rothenberg, ed. Kluwer Academic Publishers, Boston, 1994, 15-28.

Wilkinson EJ. Pap smears and screening for cervical neoplasia. *Clin. Obstet. Gynecol.* **33**: 817-825, 1990.

Zur Hausen H. Human papillomaviruses in the pathogenesis of anogenital cancer. *Virology* **184**: 9-13, 1991.

PART 3

^{1}H MRS OF THE HUMAN OVARY

3.1 Introduction

The human ovary is a complex organ that undergoes radical changes throughout a woman's life. Each month throughout the child bearing years, the ovaries swell to as much as twice their normal size before ovulation and then shrink after ovulation. After menopause, the ovaries cease to ovulate and as a result, undergo further changes as they become even smaller. Each of these changes is associated with hormonal changes that can have a significant impact on the woman's day to day activities. With these large changes occuring throughout a woman's life-time, it is not surprising that a variety of ovarian abnormalities exist.

It is estimated that 10 to 18% of couples have infertility problems (Reviewed in Evers and Heineman 1990, Lewis and Chamberlain 1989, Sloane 1985) that are typically a result of several possible dysfunctions in both partners. Diagnosis of problems related to the woman is difficult since there are a variety of conditions that may cause infertility. When the cause is related to the ovaries, diagnosis is further complicated since many ovarian abnormalities are asymptomatic other than the inability of the couple to conceive.

More devastating than infertility is ovarian cancer. Cancer of the ovaries normally occurs in women as they approach menopause or after menopause, although some relatively rare types of ovarian cancer occur in younger women and girls (Hart 1992). Canadian women with no familial history of ovarian cancer face a 1 in 66.7 chance of developing ovarian cancer over their lifetimes. This incidence is not high, particularly compared to breast cancer where the lifetime incidence is 1 in 9.3 (National Cancer Institute of Canada 1998), but the mortality rates for these two types of cancer are disparate. Whereas 27% of women who develop breast cancer will die of their disease, approximately 60% of women who develop ovarian cancer will die of their disease (Canada Communication Group 1995, National Cancer Institute of Canada 1998). This poor prognosis is due to the aggressiveness of ovarian cancer and its asymptomatic nature. Tumour growth occurs quickly without causing significant pain, and as a result, approximately 75% of malignant ovarian cancers are in advanced stages with extensive metastases by the time of diagnosis (NIH Consensus Statement 1994).

Screening, detection and diagnosis of ovarian abnormalities is difficult due to the location of the ovaries deep within the pelvis. Inaccessibility also prevents direct observation of the ovaries. Despite this, the physiology of the ovary is well documented.

3.1.1 Anatomy and Physiology of the Ovary

Pre-menopausal, healthy ovaries are almond-shaped. The size of the ovary depends greatly on the age of the woman and the phase of the menstrual cycle; however, an ovary is typically ovoid in shape and measures approximately 3.0 to 5.0 cm in length,

by 1.5 to 3.0 cm by 0.6 to 1.5 cm in width (Clement 1987a, Jaffe *et al.* 1994). The surface of the ovary is covered by a single layer of epithelial tissue. A substantial basement membrane, the tunica albuginea, separates the surface cells from the underlying stroma within which are found follicles of varying stages of development. The follicles contain the oocytes, or eggs. Each oocyte is surrounded by granulosa cells which are in turn surrounded by a membrane referred to as the basal lamina. This membrane separates the follicle, containing the oocyte and associated granulosa cells, from the stroma (Adashi *et al.* 1996, and Hillier 1991). The appearance of the ovary, and particularly the follicles, changes dramatically during the menstrual cycle.

The length of the human menstrual cycle varies greatly between women. Although it is seldom constant from one cycle to the next for a given woman, the average length of a menstrual cycle is said to be 28 days. The activities of the ovary are summarized in Table 3.1, and the changes in concentrations of hormonal levels associated with the menstrual cycle are illustrated in Figure 3.1.

Table 3.1: Summary of the Activity of the Ovary Through the Menstrual Cycle.

Day of Menstrual Cycle	Activity of the Ovary
1	Beginning of Menses
5	End of Menses
12	End of Follicular Phase
13	Beginning of Ovulatory Phase Reduced blood flow to walls of follicle Cellular and biochemical changes in walls of follicle
14	Rupture of follicle (ovulation). Expulsion of follicular fluid and oocyte into fallopian tube
15 - 16	Beginning of formation of corpus luteum Granulosa cells in ruptured follicle proliferate and increase in diameter Accumulation of lutein in granulosa cells
16 - 18	Capillaries extend into walls of ruptured follicle
19 - 20	Completion of formation of corpus luteum
23 - 26	Corpus luteum begins to recede Decrease in amount of blood in capillaries followed by obliteration of vascular networks
23 - 28	Beginning of Follicular Phase Cells of follicles proliferate forming fluid filled cavity containing the oocyte

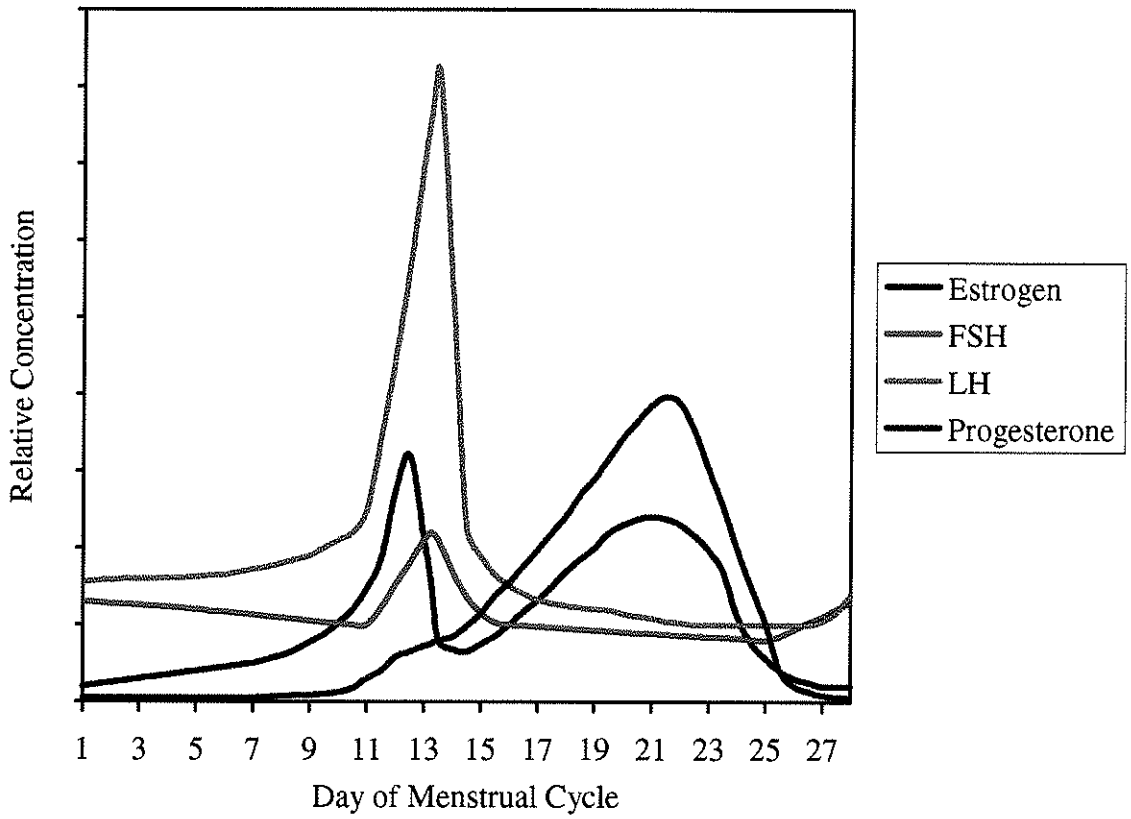

Figure 3.1: Relative concentrations of the hormones – estrogen, follicular stimulating hormone (FSH), luteinizing hormone (LH), and progesterone – through the normal menstrual cycle (Adapted from Speroff and Vande Wiele 1971).

By convention, the first day of the cycle is the first day of bleeding, or menses. Approximately 15 to 20 days prior to ovulation, or days 23 to 28 of the cycle, some of the follicles within the stroma of the ovaries begin to grow. This follicular growth is stimulated by an increase in the production of follicular stimulating hormone (FSH) by the pituitary gland. This is the beginning of the follicular phase of the menstrual cycle. The cells of the ovarian follicles proliferate forming a fluid filled cavity containing the oocyte, or egg. The follicles quickly exceed 1mm in diameter. More than 99.9% of all

follicles become atretic, or degenerate, at different stages of growth (Jaffe *et al.* 1994). Only one of these follicles, called the dominant follicle, will continue to grow, reach maturation, and ovulate. The dynamics of follicular growth are poorly understood. As a result, no mechanism exists which will allow prediction of which, or how many follicles will develop during a cycle or which follicle will reach maturation and ovulate. It is known, however, that the dominant follicle exhibits the greatest ability of all the follicles to synthesize estrogen; it has a more extensive and permeable capillary network; and it will inhibit development of the other follicles. Normally, follicles will form on both ovaries, but only one ovary will produce a dominant follicle. Typically, the dominant follicle will appear on alternate ovaries from one cycle to the next, and thus the ovaries take turns ovulating.

At approximately day 1 of the cycle, the level of FSH slowly begins to drop, and at the same time, the follicles begin to produce estrogen. The increase in the level of estrogen begins slowly and then rapidly increases. At the same time, there is a gradual increase in the level of luteinizing hormone (LH) (Mishell *et al.* 1971, Speroff and Vande Wiele 1971). The dominant follicle continues to grow throughout the follicular phase, ultimately achieving a size of approximately 20 - 26mm in diameter (Jaffe *et al.* 1994). The other follicles on both ovaries will slowly become atretic at various stages through the follicular phase. (Jaffe *et al.* 1994, Speroff and Vande Wiele 1971)

The follicular phase ends with a sudden rise in the level of estrogen signifying the beginning of the ovulatory phase. This next phase begins approximately 36 hours before

ovulation with a surge-like rise in the secretion of LH that is thought to be triggered by the previous rise in estrogen. Concomitant with the surge in LH is a much less intense rise in FSH and a drop in estrogen levels (Mishell *et al.* 1971, Speroff and Vande Wiele 1971). Ovulation occurs at approximately day 14 to 16 of the cycle. The mechanisms by which the hormonal changes that occur during the ovulatory phase influence ovulation are unclear, but their effects are to constrict the capillaries of the follicle resulting in reduced blood flow to the walls of the follicle, as well as to change the cytologic and biochemical characteristics of the follicular walls. Rupture of the follicle at the time of ovulation does not occur as a result of increased pressure on the walls of the follicle by the increased amount of follicular fluid since the pressure caused by the fluid remains constant throughout the follicular phase. Rupture is caused by weakening of the follicular wall. While weakening occurs over the entire follicular wall, rupture occurs only at the apex of the follicle at the surface of the ovary. Rupture of the follicle causes expulsion of the follicular fluid and the oocyte into the proximal fallopian tube. Around the time of ovulation, the basal body temperature normally increases by approximately $0.5^{O}C$ and remains elevated until the time of the next menstruation (Lewis and Chamberlain 1989, Sloane 1985). The level of progesterone begins to increase at the time of ovulation, and LH, FSH, and estrogen levels all decrease shortly after ovulation. The decrease in estrogen, however, is brief with levels rising again one or two days after ovulation during the next phase of the cycle, the luteal phase (Jaffe *et al.* 1994, Mishell *et al.* 1971, Speroff and Vande Wiele 1971).

The luteal phase of the menstrual cycle is characterized by a simultaneous rise and then decline in the levels of progesterone and estrogen with higher levels of progesterone than estrogen (Mishell *et al.* 1971, Speroff and Vande Wiele 1971). After ovulation, the wall of the follicle is not destroyed, but rather is reorganized transforming the follicle into the corpus luteum. Within a few hours of ovulation, the granulosa cells in the ruptured follicle proliferate and undergo an almost threefold increase in their original diameters. The yellow pigment, lutein, accumulates in the cells giving this phase of the cycle the name luteal, or luteinization phase. Over the 48 to 72 hours following ovulation, capillaries extend into the thickened walls of the ruptured follicle, and approximately half the time, penetrate the follicular wall filling the emptied cavity of the follicle with blood. By approximately 5 or 6 days after ovulation, the cells of the corpus luteum have achieved their maximum size and have transformed to luteal cells that are rich in lipids. The corpus luteum is extremely well vascularized and has one of the highest blood flows per unit mass of any gland in the body (Hillier 1991). It normally attains a diameter of approximately 10-20mm (Jaffe *et al.* 1994) and is responsible for the production and secretion of progesterone and estrogen. By about the eighth day after ovulation, or day 22 of the menstrual cycle, progesterone secretion is at a maximum. About 9 to 12 days after ovulation, levels of progesterone slowly decrease (Mishell *et al.* 1971, Speroff and Vande Wiele 1971). Two to five days before menses, or the menstrual period, the corpus luteum begins to regress provided that pregnancy has not occurred. At this time, there is initially a decrease in the amount of blood in the capillaries, followed by a decrease in the size of the corpus luteum and obliteration of the vascular networks until the corpus luteum recedes from the ovarian surface. (Jaffe *et al.* 1994, Speroff and Vande Wiele 1971)

The ability of a woman to conceive, called her *reproductive potential*, decreases with age. In a review of the literature regarding reproductive potential, Scott and Hofmann (1995) found evidence that this decline may be largely due to changes in the ovaries. Throughout life, there is a continuous decrease in the number of oocytes in the ovaries. At some point, there begins a significant depletion in the number and quality of the oocytes which is referred to as *diminished ovarian reserve*. The age of onset of perimenopause, which is the decline in reproductive potential and diminshed ovarian reserve, is highly variable. While the cause of decline in reproductive potential is unknown, a large increase in production of FSH and a much smaller increase in the production of LH has been observed at the same general time as ovarian reserve begins to diminish (reviewed in Jansen 1992, Miller and Keane 1987, O'Keane 1996, Scott and Hofmann 1995, Sloane 1985). In some women, normal menstrual cycles continue until the last menstrual period. More commonly, however, the length of the cycle begins to shorten and menses becomes irregular as successful follicular growth and ovulation does not occur in each cycle. Often, one ovary will discontinue cyclic activity before the other ovary which may result in successful ovulation only every second cycle (Jansen 1992, Miller and Keane 1987, Sloane 1985). Due to the irregularity of menstruation during the perimenopause, it is difficult to determine exactly when the menopause has occurred. Normally, it occurs around 50 years of age and is considered to be permanent when menstruation, or bleeding, has not occurred for a period of one year (Miller and Keane 1987, Sloane 1985). After menopause, the ovaries shrink in size, but activity in the ovaries does not necessarily cease. The elevated levels of FSH and LH which occurred during the perimenopause remain constant. In some cases, the ovaries still undergo

follicular development, although, the follicles seldom reach maturation and menstruation is rare. Postmenopausal ovaries produce and secrete negligible amounts of progesterone and estrogen, and thus, estrogen is derived from other sources (Jansen 1992, Hillier 1991, Sloane 1985).

3.1.2 Anatomy of the Female Pelvis

In order to determine accurately the location of the ovaries in the pelvic region, and to gain an understanding of the challenges associated with *in vivo* analysis of the ovaries, a basic knowledge of the anatomy not only of the ovaries, but also of the entire female pelvis is required. In theory, the ovaries are located on either side of the uterus. The uterus is superior to, and rests on top of the urinary bladder. It is suspended and held in place by 8 ligaments. Two of these ligaments, the broad ligaments, connect the sides of the uterus to the lateral walls of the pelvis (Figure 3.2).

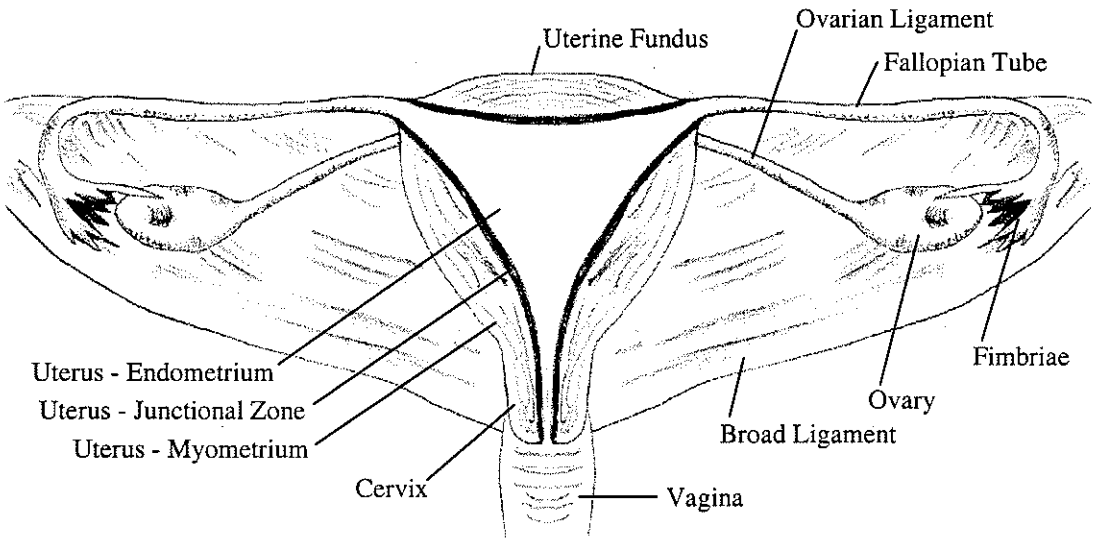

Figure 3.2: Schematic representation of the female reproductive organs, posterior view.

The ovaries and fallopian tubes are on the posterior side of the broad ligament. The fallopian tubes extend from the fundus of the uterus, or end of the uterus most distant from the vagina, to the sides of the pelvis. They are contained within the superior folds of the broad ligaments. The fallopian tubes are approximately 10-15cm in length, but are only a few millimeters in diameter. The end of the fallopian tube opposite the uterus is open to the abdomen and consists of many fingers, or fimbriae, through which the oocytes pass to enter the fallopian tube and ultimately the uterus. One of these fimbriae is attached to the ovary such that the ovary remains close to the end of the fallopian tube. The ovaries are inferior to the fallopian tubes. Anteriorly, they are attached to the posterior folds of the broad ligament. Further support is provided by the ovarian ligament which extends from the medial side of the ovary to the wall of the uterus slightly inferior to the insertion of the fallopian tube. The infundibulopelvic, or suspensory, ligament extends from the pelvic brim to the superior aspect of the lateral side of the ovary. The vessels which supply the ovary with blood course along the suspensory ligament. Estrogen dilates the vasculature of the uterus and ovaries while progesterone has the opposite effect. Hence, blood flow to the ovaries increases and decreases through the menstrual cycle. (Clement 1987a, Gray 1977, Jaffe *et al.*, 1994)

3.1.3 Abnormalities of the Ovaries

Due to the functional complexity of the ovaries, it is not surprising that a wide variety of ovarian abnormalities exist. These abnormalities can be divided into non-neoplastic abnormalities, or those abnormalities that do not involve uncontrolled and

progressive cell multiplication (Miller and Keane 1987), and benign and malignant abnormalities as follows (Lewis and Chamberlain 1989, Mack *et al.* 1992):

A) Non-neoplastic ovarian abnormalities
    1) Enlarged follicular cysts
    2) Enlarged corpus luteum cysts
    3) Polycystic ovarian disease
B) Benign and malignant abnormalities
    1) Tumours originating in the surface epithelium
    2) Germ cell tumours
    3) Sex cord stromal tumours
C) Metastatic tumours

3.1.3.1 Non-Neoplastic Ovarian Abnormalities

Follicular and corpus luteum cysts are part of the normal ovulatory function of the ovaries, as previously discussed. These cysts are normally small and are not considered abnormal. Occasionally, however, a follicular cyst may grow larger than normal. While these cysts commonly regress naturally, a cyst that exceeds five centimeters in diameter is considered abnormal. At the time of ovulation and the subsequent formation of the corpus luteum, there is always a small amount of bleeding where the follicular cyst has ruptured. If this bleeding is excessive, the corpus luteum will become distended with blood, possibly leading to delay of menstruation and/or pain (Lewis and Chamberlain 1989, Sloane 1985).

Polycystic ovarian disease is characterized by enlargement of the ovaries to two to five times their normal size as well as the presence of an abnormally large number of

small follicular cysts that vary in size but seldom exceed five millimeters in diameter. The follicular cysts seldom or never mature to the point of ovulation resulting in infrequent or absent menstruation and infertility (Lewis and Chamberlain 1989, Clement 1987b).

3.1.3.2 Benign and Malignant Abnormalities

Sex cord stromal tumours are variable in their origin and structure. They originate from the cell types that form the testes and the ovaries during fetal development, called the sex cord. Since they form in the stroma of the ovaries, they may contain one or more of the various types of cells found in the stroma. Sex cord stromal tumours account for approximately eight percent of all ovarian tumours. Of these, approximately half are benign, and those that are malignant are normally of a low grade of malignancy (Lewis and Chamberlain 1989, NIH Consensus Statement 1994, Young and Scully 1987).

Germ cell tumours are more common than sex cord stromal tumours, comprising approximately twenty percent of all ovarian tumours. Typically, they occur in girls and young women. The majority (95 to 99%) of these tumours are benign and consist of dermoid cysts (Lewis and Chamberlain 1989, NIH Consensus Statement 1994, Talerman 1987). Dermoid cysts are normally rich in lipids and very heterogeneous. They commonly contain skin, sebaceous and sweat glands, hair, cartilage, muscle, and calcium deposits in the form of bone or teeth (Lewis and Chamberlain 1989, Sloane 1985).

The most common ovarian tumours arise in the epithelium that covers the surface of the ovaries. These tumours account for 50% of all benign ovarian tumours and 85 to 90% of malignant tumours (Hart 1992). Epithelial tumours may be solid or cystic, or may contain both solid and cystic portions. The solid portions may be of varying cell types, or may be of a single cell type. Fluid in the cystic portions is normally rich in glycoproteins that differ in the amount of amino sugars (Lewis and Chamberlain 1989, Sloane 1985).

3.1.3.3 Metastatic Tumours

In some cases, the ovaries are the site of secondary tumours, or metastases, from other malignant cancers. One common example is tumours that result from endometriosis. Endometriosis is a disease in which cells from the endometrium, or inner lining, of the uterus are found in the form of growths, or lesions, outside of the uterus. These lesions are commonly found on the ovaries (Lewis and Chamberlain 1989).

3.1.4 Screening for Ovarian Abnormalities

The prognosis for patients diagnosed with ovarian disease in its early stages is much better than for those with advanced stages of disease. The five year survival rate for patients diagnosed with early stages of malignant ovarian cancer is greater than 90%, but for patients with advanced stages including metastases, it is only 15 to 20% (Reviewed in Look 1993). Accurate screening methods would greatly reduce the mortality rate due to ovarian cancer. Currently there are three screening tests available:

bimanual rectovaginal pelvic examination, CA-125 analysis, and transvaginal ultrasonography (TVS).

While bimanual rectovaginal pelvic examination may be performed at routine physical examinations, some ovarian abnormalities are too small to detect on manual examination, and some lie in a position such that they can not be felt. Further, this examination only detects the presence of an abnormal growth. It does not allow differentiation between benign and malignant tumours (Lewis and Chamberlain 1989, Look 1993, NIH Consensus Statement 1994). CA-125 is an antigen that was initially found to have elevated concentrations in more than 80% of malignant, epithelial, ovarian tumours. Unfortunately, only half of the patients with cancer in its early stages have elevated levels of CA-125, and a significant number of healthy women also have elevated levels of CA-125 (Forstner *et al.* 1995, Look 1993, Kuesel 1992, NIH Consensus Statement 1994). Hence, levels of this antigen can not be used as an accurate screening method. Finally, TVS allows accurate detection of ovarian growths. Attempts have been made to determine the malignant potential of detected abnormalities based on the size and cystic properties of the growth. These studies have met with limited success (Reviewed in Lewis and Chamberlain 1989, Look 1993, NIH Consensus Statement 1994). Due to the low incidence of malignant, ovarian cancer and the inaccuracy of screening methods, it has been estimated that screening of even 50% of postmenopausal women would generate charges of $2.7 million for every ovarian cancer that is found (Willson 1991).

An accurate screening method would be particularly beneficial for women with a familial history of ovarian cancer. Women with no familial history of ovarian cancer have approximately a 1.5% chance of developing ovarian cancer. Women with one first-degree relative with ovarian cancer have a 5% lifetime risk of developing ovarian cancer. With two or more first-degree relatives, the risk rises to 7%. These women are further at risk since 3% of those women with two or more family members affected by ovarian cancer have hereditary ovarian cancer syndrome. In these cases, the lifetime risk is approximately 40% to 50%. Because there is no way of detecting which of these women have hereditary ovarian cancer syndrome, all women with two first-degree relatives with ovarian cancer are considered at high risk and are treated assuming a 50% risk (Lynch *et al.* 1985, NIH Consensus Statement 1995). Since no screening method has been found to be reliable, annual pelvic examination is the only screening method recommended for low risk women. While studies have not shown that screening of high risk women will reduce the mortality rate from ovarian cancer, annual pelvic examination, CA-125 determinations, and TVS are recommended for women with a familial history of ovarian cancer who wish to maintain fertility. After childbearing is completed, or at least by the age of 35, it is recommended for high risk women that both ovaries be removed as a preventative measure (NIH Consensus Statement 1994).

3.1.5 Diagnosis and Treatment of Ovarian Abnormalities

Due to the lack of screening methods and the asymptomatic nature of the disease, ovarian abnormalities are normally found either by chance during routine pelvic examination or as a result of symptoms such as abdominal pain or rapidly increasing

abdominal girth. Selection of the most appropriate treatment for newly detected ovarian abnormalities is one of the most common dilemmas in gynecology (Lewis and Chamberlain 1989, Moore 1993, Outwater and Dunton 1995, Sloane 1985).

Non-neoplastic growths, such as unusually large follicular or corpus luteal cysts, normally go undetected unless they grow large enough to be felt during pelvic examination or cause pain. If detected, these cysts normally do not require treatment because they will recede spontaneously. The recommended treatment for unusually large cysts is careful observation using TVS. In some cases, however, non-neoplastic growths will persist, causing pain and irregular menstruation. In these cases, surgical removal of the growth may be necessary (Lewis and Chamberlain 1989, Sloane 1985). Other non-neoplastic abnormalities, such as polycystic ovarian syndrome, are normally corrected with hormonal therapy, but in some cases may require surgical management involving drilling of multiple holes through the epithelium of the ovary (Al-Took and Tulandi 1997, Sloane 1985).

Since it is often impossible to determine prior to surgery whether an ovarian tumour is benign or malignant, surgical removal of the growth is normally the first stage of treatment (Lewis and Chamberlain 1989, Moore 1993, Outwater and Dunton 1995, Sloane 1985). During surgery, it is of great importance that the entire pelvis is examined to determine if metastasis of malignant tumours has occurred. If the growth is benign, no further treatment is necessary. Approximately 10 to 20% of ovarian tumours are classified as tumours of low malignant potential, or the less commonly used terminology

of borderline (Reviewed in Hart 1992, Sutton 1993). These tumours are neither benign nor malignant. They are composed of cells which are clearly malignant but show no tendency to invade the stroma of the ovaries. Tumours of low malignant potential have a better prognosis and a five year survival rate of 92 to 100%, which is significantly higher than that for the truly malignant tumours (Reviewed in Hart 1992, Outwater and Dunton 1995). Due to the mixed nature of these tumours, determination of appropriate treatment is difficult. It is recommended that women presenting with ovarian tumours of low malignant potential, who have completed child-bearing, undergo a total hysterectomy including removal of both ovaries. There is no evidence which suggests that further treatment, such as chemotherapy or radiation, is of benefit unless there is recurrence and/or clinical progression (Morrow 1992, Mack *et al.* 1992, NIH Consensus Statement 1994, Sutton 1993).

If upon surgical examination the tumour is believed to be malignant, as much as possible of the metastatic growths should be removed since minimal residual tumour is associated with improved survival. Post-surgical treatment is based on whether metastasis to adjacent tissue has occurred. If no metastases are found, further treatment is normally not necessary. If metastases are present, surgery is normally followed by chemotherapy (Hoskins 1993, Moore 1993, NIH Consensus Statement 1994, Sloane 1985). Unfortunately, approximately half of the patients develop a resistance to the chemotherapy, and some patients do not respond at all. Chemotherapy rarely eliminates ovarian cancer even in patients who respond to the treatment. The poor response rate to chemotherapy along with the large number of women who present with advanced stages

of ovarian cancer (approximately 75%) lead to the high mortality rate from this disease (Lewis and Chamberlain 1989, McGuire 1993, Perez *et al.* 1993).

3.1.6 Current Imaging Modalities

3.1.6.1 Ultrasonography

Typically, ultrasound is the diagnostic imaging technique of choice because of its relatively low cost as compared to computed tomography (CT) and magnetic resonance imaging (MRI). Ultrasound allows accurate visualization of unusually large follicular cysts and polycystic ovarian syndrome. These conditions may be monitored using ultrasound without the need for surgical intervention (Jaffe *et al.* 1994). Enlarged corpus luteum cysts, however, are often indistinguishable from an ectopic pregnancy in ultrasound images (Jaffe *et al.* 1994). Ovarian cysts that result from endometriosis are also difficult to distinguish from other cysts (Jaffe *et al.* 1994, Lipson and Hricak 1996). Reports on the accuracy of differentiation of the different types of solid tumours using ultrasound vary (Jaffe *et al.* 1994, Lipson and Hricak 1996, Scoutt and McCarthy 1992, Willson 1991). The sensitivity for malignancy of ovarian tumours has been reported to be as low as 58% (Reviewed in Outwater and Dunton 1995, Scoutt and McCarthy 1992, Willson 1991). Further, ovarian tumours are often missed or not clearly defined by ultrasound because they may be beyond the range of the probe (Romero *et al.* 1995, Willson 1991), or air interfaces or extensive subcutaneous fat tissue may cause distortion of the signal (Prayer *et al.* 1993). As a result, most surgeons do not recommend the use of ultrasonography for diagnosis of ovarian tumours since the scan rarely provides additional useful information (Willson 1991). While ultrasound has not been shown to be

useful in the diagnosis of solid ovarian tumours, it is accurate, and used routinely, for monitoring ovulation as well as to diagnose and monitor the effects of treatments for infertility (Pierson *et al.* 1994b).

3.1.6.2 Computed Tomography (CT)

CT is often used when ultrasonographic findings are inconclusive (Friedman *et al.* 1994, Occhipinti *et al.* 1993). CT, like ultrasound, can accurately determine the presence of abnormally large follicular or corpus luteum cysts, but unlike ultrasound, normal ovaries are not normally visualized by CT. Further, CT is unable to resolve the numerous small follicular cysts associated with polycystic ovarian syndrome (Occhipinti *et al.* 1993) because of poor soft tissue contrast (Outwater and Dunton 1995). Dermoid cysts and their internal structures, including calcium deposits and hair, are particularly well visualized with CT and may be correctly diagnosed in about two thirds of patients with dermoid cysts (Friedman *et al.* 1994, Occhipinti *et al.* 1993). The internal architecture of other ovarian masses may not be well resolved (Occhipinti *et al.* 1993). CT is unable to differentiate cysts associated with endometriosis from other ovarian cysts (Friedman *et al.* 1994, Occhipinti *et al.* 1993). Differentiation of benign from malignant tumours using CT is difficult and has not been shown to be more accurate than ultrasound (Friedman *et al.* 1994, Lewis and Chamberlain 1989, Lipson and Hricak 1996, Occhipinti *et al.* 1993, Outwater and Dunton 1995, Scoutt 1992, Symonds *et al.* 1992).

3.1.6.3 Magnetic Resonance Imaging (MRI)

MRI provides accurate identification of normal ovaries in 87% to 96% of premenopausal women (Occhipinti 1994). Because of their smaller size and lack of follicular cysts, ovaries in postmenopausal women are much more difficult to locate with MRI (Occhipinti 1994, Occhipinti *et al.* 1993). Unlike ultrasound, MRI is not limited to visualization of structures close to the surface of the pelvis and/or the vagina. This is particularly helpful in women whose ovaries are displaced into the abdomen due to stretching of ligaments, growths within the uterus which displace the ovaries, or surgical displacement of the ovaries (Occhipinti 1994). Major structures of the female pelvis and their intensity in T_1- and T_2-weighted MR images are given in Table 3.2.

Table 3.2: T_1- and T_2-Weighted Signal Intensities of Anatomical Structures in the Female Pelvis (Hricak and Carrington 1991, Outwater and Dunton 1995, Outwater *et al.* 1996, Jaffe *et al.* 1994, Semelka *et al.* 1997)

Anatomic Structure	Intensity in T_1 Weighted Image	Intensity in T_2 Weighted Image
Bowel	Low to Intermediate	Low to Intermediate
Broad Ligament	Low	Low to Intermediate
Muscle	Low to Intermediate	Low
Corpus Luteal Cysts – no hemorrhaging – hemorrhaging	Low to Intermediate Intermediate to High	High Intermediate to High
Ovaries - Developing Follicles	Low to Intermediate	High
Ovaries - Stroma	Low to Intermediate	Intermediate
Urinary Bladder Wall	Low	Low
Urine	Low	High
Uterus - Internal Layer (Endometrium)	Low to Intermediate	High
Uterus - Central Layer (Junctional Zone)	Low to Intermediate	Low
Uterus - Outer Layer (Myometrium)	Low to Intermediate	Intermediate

Follicular and corpus luteum cysts are well depicted with MRI and use of contrast-enhanced T_1-weighted images improves characterization of these cysts. If hemorrhaging has occurred within the cyst, as is common in corpus luteum cysts, differentiation between symptomatic corpus luteum cysts and endometriosis is difficult (Occhipinti 1994, Occhipinti *et al.* 1993). Polycystic ovarian syndrome is well depicted by MR imaging, but differentiation of this disease from stromal hyperthecosis of the

ovary, characterized by an increase in the size of the ovaries due to growth of normal cells and excessive accumulations of lutein in the cells of the stromal layer (Miller and Keane 1987), is often not possible using MRI (Occhipinti 1994, Occhipinti *et al.* 1993). Reports on the accuracy with which MRI can differentiate between benign and malignant ovarian tumours vary. Some state that differentiation using MRI is no more accurate than CT or ultrasound and that the specificity of all three imaging modalities is not sufficient to distinguish benign from malignant tumours (Reviewed in Miralles 1996, Occhipinti *et al.* 1993, Outwater and Dunton 1995, Scoutt and McCarthy 1992). Others claim that MRI is at least equivalent and may be superior to CT. These studies report differentiation of benign from malignant tumours with accuracies from 86% to 97% (Reviewed in Lipson and Hricak 1996, Medl *et al.* 1995, Occhipinti *et al.* 1993, Romero *et al.* 1995, Symonds *et al.* 1992).

3.1.6.4 Summary of Imaging Methods

Ultrasound and MRI allow observation of healthy ovaries and accurate diagnosis of polycystic ovarian syndrome. Unusually large ovarian cysts are well depicted with ultrasound, CT, and MRI, but hemorrhagic, corpus luteum cysts are not well differentiated from ovarian implants associated with endometriosis. Reports on the accuracy with which benign ovarian tumours are distinguished from those that are malignant range from 52% to 97% for each of the three imaging modalities. Tumours of low malignant potential (borderline) can not be diagnosed with any of the imaging modalities. They are diagnosed exclusively by histopathological examination of surgically removed biopsies (Hart 1992).

While current imaging modalities provide a method of observing the normal cyclic changes in the ovaries as well as the manifestation of disease processes, the causes of these changes and the associated biochemical alterations remain poorly understood. Furthermore, no method exists for the early detection and screening of ovarian abnormalities such as ovarian cancer. An *in vivo* method that would allow examination of the biochemical changes in the ovaries could lead to a better understanding of the causes of ovulation, infertility, and ovarian tumours as well as a method of following the effects of drugs on the ovaries. This could have a profound impact on the treatment of ovarian abnormalities.

3.2 Hypothesis

It is hypothesized that *in vivo* ^{1}H magnetic resonance spectra can be obtained from healthy ovaries and abnormalities of the ovaries.

3.3 Objectives

The objectives of this work include determination of:

1) the best rf coil(s) for MRS of the ovaries from amongst the available coils;
2) a fast and accurate imaging protocol for location of the ovaries; and
3) a method for obtaining accurate in vivo spectra of the ovaries that corrects for the effects of motion within the pelvis.

3.4 Rationale

The ovaries undergo extreme changes through the menstrual cycle and during menopause as a result of hormonal stimulation. When the follicular and corpus luteum cysts that occur normally during the menstrual cycle become abnormally large, abnormal changes in hormonal levels may be observed (Jaffe *et al.* 1994, Pierson and Chizen 1994a). The concentration of these hormones is typically at the nanomolar level (Speroff and Vande Wiele 1971). While their concentration is too low to be detected using magnetic resonance spectroscopy (MRS), it is probable that other biochemical changes occur which can be measured with MRS.

Mackinnon *et al.* (1995) found that ^{1}H magnetic resonance spectra of surgically obtained ovarian biopsies could be used to differentiate normal/benign from malignant tumours with a sensitivity of 87% and a specificity of 91%. Tumours of low malignant potential could also be distinguished from malignant tumours. A similar study performed by Wallace *et al.* (1997) yielded a sensitivity of 100% and a specificity of 95%. This study also examined the ability of ^{1}H magnetic resonance spectroscopy to differentiate untreated ovarian cancer from recurrent ovarian cancer. The sensitivity and specificity of this analysis were found to be 92% and 100%, respectively. Provided that sufficient signal to noise is obtained, these results should be reproducible using *in vivo* ^{1}H MRS.

3.5 Materials and Methods

3.5.1 Coils

Three coils manufactured by Siemens were tested to determine their suitability for imaging and spectroscopy of the ovaries on a Siemens SP 1.5T magnet. The three coils used were:

1) Whole body coil - quadrature coil, transmit/receive
   - length = 90cm
   - inner diameter = 57cm

2) Helmholtz-type volume coil – quadrature coil, receive only
   - Inner coil = 15.5cm x 15.5cm
   - Outer coil = 18.0cm x 18.0cm
   - Maximum separation between coils ≈ 30cm

3) Circularly polarized (cp) surface coil - quadrature coil, receive only
   - Double ring coils = 10.3cm x 20.0cm
   - Single ring coil = 12cm x 23cm

The signal to noise ratios were determined for each coil using a spherical phantom (diameter = 18 cm) containing 0.1M acetate and 0.1M lactate. The loading of the whole body coil and the cp spine coil was increased by including a body loader phantom containing water. The coils of the Helmholtz-type volume coil were separated by the maximum distance possible to approximate the conditions of a patient positioned in the coil. The loading of the Helmholtz-type volume coil was not increased using the body loader phantom because the phantom was too large and did not fit between the coils. For each coil, a water suppressed spectrum was obtained from a 15x15x15mm^3 voxel at the center of the magnet using the STEAM sequence (Figure 3.3). The signal to noise ratio was determined from the acetate singlet at 1.92 ppm. The maximum intensities of the

magnitude FID's with no water suppression were determined at time zero using the same voxel. These intensities were also determined every 15 mm along each of the three axes in order to determine the signal falloff characteristics of the coils.

3.5.2 Patient Population

All women who participated in this study were recruited under the guidelines established by the National Research Council's Human Subjects Research Ethics Committee (HSREC). Ethical approval for this study was also obtained from the HSREC (protocol numbers 1994-4, 1995-24, and 1995-25). Magnetic resonance imaging and spectroscopy were performed on 22 premenopausal women (ages 21 – 47 years, mean age = 29.2 years), 2 perimenopausal women (ages 45 and 50), and 16 postmenopausal women (ages 52 – 77 years, mean age = 61.4 years; 1 to 32 years since last menses, mean = 10.0 years) with no a prior knowledge of ovarian abnormalities. Menopause was said to have occurred if at least one year had passed since the last menses. An additional 8 premenopausal women (ages 22 – 42 years, mean = 28.9 years) with no prior knowledge of ovarian abnormalities participated in the study six times during one menstrual cycle. They were asked to measure and record their temperature each morning using a basal body thermometer. MRS was performed on these women on the following six days:

1) The second day of menses
2) Approximately midway between the onset of menses and the day of ovulation
3) The day before ovulation
4) The day of ovulation
5) The day after ovulation
6) One week after the day of ovulation

Since the exact time of ovulation was initially unknown, the day of the second visit was estimated. The exact time of ovulation was determined using the ovulation predictor kit Conceive LH (registered trademark of Quidel). This predictor measures the concentration of luteinizing hormone in a urine sample. The predictor tests positive on the day before ovulation when the concentration of luteinizing hormone surges (Figure 3.1). All women who participated in the study were encouraged to limit their liquid intake on the day(s) of the study.

Two women were referred to the study by gynecological oncologists. One (27 years of age) presented clinically with a 5cm growth on the left ovary that was a suspected dermoid cyst. The other (46 years of age) had a 10cm growth that was diagnosed as adenocarcinoma. This woman was undergoing chemotherapy treatments at the time the MRS was performed.

Because this study was performed on a clinical MRI system, research time was limited. The system was available for research weekdays from 10:00pm to 7:00am, Tuesdays from 4:00pm to 6:00pm, and Saturday after 4:00pm to Monday at 7:00am. All of the premenopausal women who participated six times during one menstrual cycle were scheduled for the study between 10:00pm and midnight.

2.5.3 Imaging

The cp surface coil was chosen for imaging and spectroscopy of the ovaries. Imaging of the entire pelvis was required in order to locate the ovaries. In both pre- and postmenopausal women, an initial set of three 10mm slices was imaged using a FISP sequence (TE = 10ms, TR = 60ms, matrix = 128x256 with over sampling, total acquisition time = 10s). These images allowed localization of the uterus. The coil was adjusted to lie directly beneath the uterus. In premenopausal women, the T_2-weighted Turbo Spin Echo (TSE) sequence (Siemens supplied, TE = 91ms, TR = 5000ms, matrix = 128x256 with over sampling, 16 echo train, 4 acquisitions, total acquisition time = 2min, 57s) was used to obtain nine 4mm coronal slices with slice gaps of 4mm. The sequence was repeated with the nine slices shifted by 4mm. In this manner, contiguous, coronal slices were obtained. Using the same Turbo Spin Echo sequence, nine 4mm transverse slices were obtained. In postmenopausal women, the T_1-weighted Spin Echo sequence (TE = 17ms, TR = 480ms, matrix = 256x512 with over sampling, 2 acquisitions, total acquisition time = 4min, 9s) was used to acquire nine 4mm transverse slices with 4mm slice gaps. The sequence was repeated to obtain nine transverse slices shifted by 4mm and then nine coronal slices.

3.5.4 Spectroscopy

Once the ovaries were identified, a voxel was positioned on the ovary such that the voxel size was maximized but was entirely inside the ovary. Standard first order shimming was performed. Water suppression was obtained using the CHESS sequence (Haase *et al.* 1985), and was optimized by adjustment of the voltages of three Guassian

pulses. Images of the pelvis were once again obtained using a shortened form of the Turbo Spin Echo sequence (TE = 91ms, TR = 1550ms, matrix = 128x256 with over sampling, 2 acquisitions, total acquisition time = 35s) in premenopausal women, and a shortened form of the Spin Echo sequence (TE = 17ms, TR = 300ms, matrix = 192x512 with over sampling, 1 acquisition, total acquisition time = 61s) in postmenopausal women. The voxel was repositioned to account for movement of the ovary. Using the STEAM sequence (TE = 20ms, TR = 2000ms) shown in Figure 3.3, 32 water suppressed FID's were acquired in 67s. This protocol of scout imaging, voxel re-positioning and spectral acquisition was repeated to obtain a minimum of 128 and a maximum of 160 water suppressed FID's, and 32 FID's with no water suppression.

The acquired FID's were not averaged, but rather were stored in 32x1024 matrices. Since the Siemens spectroscopy software automatically averages the FID's as they are acquired, the STEAM sequence was run from the imaging software in order to store each acquisition without averaging. The radio frequency (rf) pulses were calculated externally using a modified version of the Siemens program SRFCALEX (modified by Dr. Jonathan C. Sharp, Research Officer, Institute for Biodiagnostics, National Research Council).

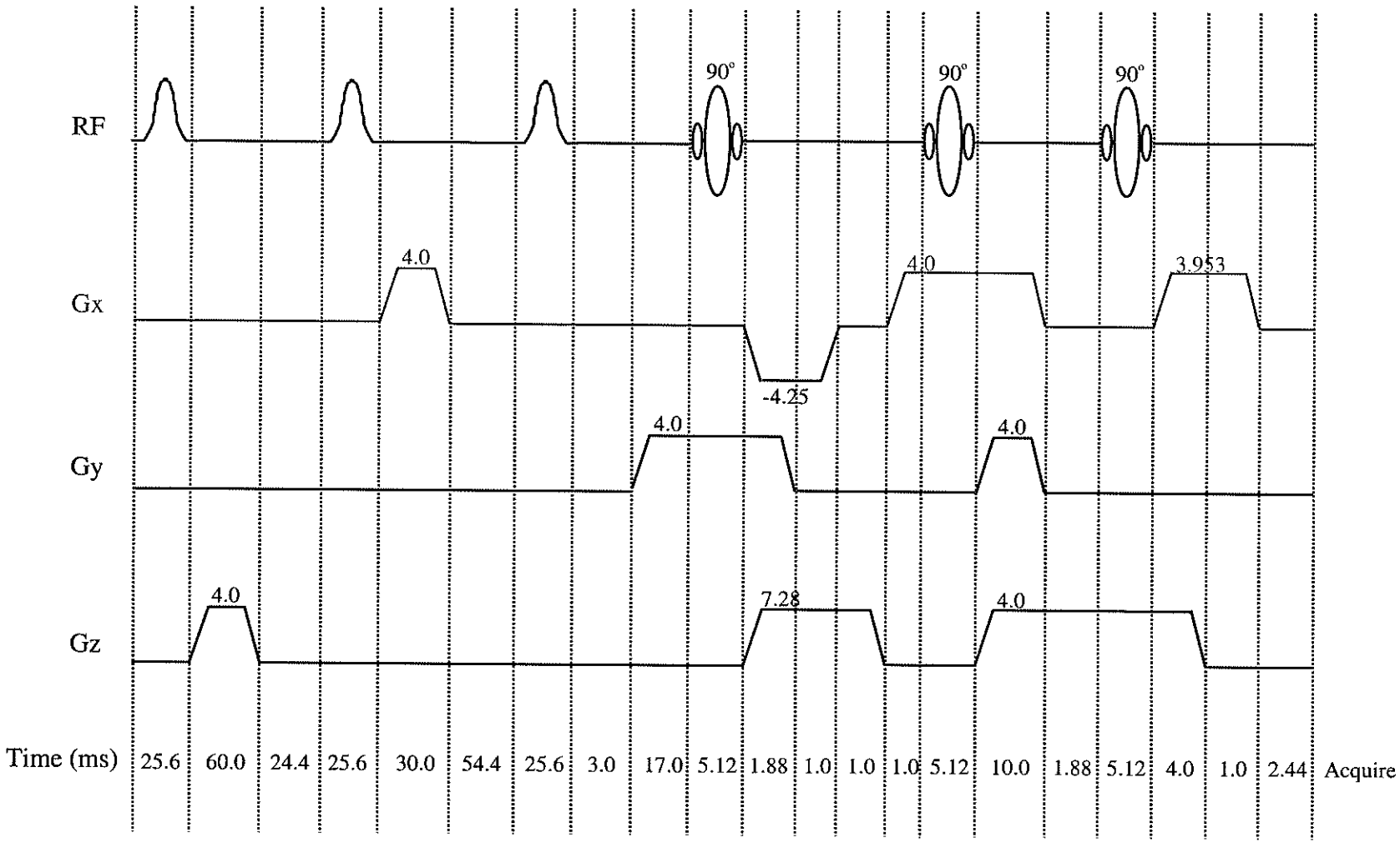

Figure 3.3: Timing diagram for the STEAM sequence (TE = 20ms, TM = 17ms, TR = 2000ms) preceded by water suppression using the CHESS sequence. Gradient amplitudes are given in mT/m, gradient rise and fall times are 1ms, and times are given in ms. CHESS pulses are Guassian, and 90^0 pulses are sinc pulses.

3.5.5 Spectral Processing

The FID's were transferred to a Unix based system for analysis. A program was written in IDL which allowed interactive manipulation of the individual FID's as well as the averaged FID's. The program was tested using spectra obtained from a spherical phantom (diameter = 18cm) containing 0.1M acetate and 0.1M lactate. Using the IDL program, each FID was fast Fourier transformed (FFT'd). The absolute magnitude water spectra were frequency shifted and the real and imaginary water spectra were phased to ensure that each acquisition was aligned and had the same phase. The individual water suppressed FID's were zero filled to 2048 points and multiplied by an exponential filter. They were then FFT'd and the individual spectra were frequency and phase corrected in the same manner as the water spectra. In cases where the signal to noise ratio was too low to identify accurately a peak or peaks in the spectra that could be used for frequency shifting and phasing, each set of 32 spectra were averaged, and the averaged spectra were corrected. The individual spectra were then examined, and where the signal to noise ratio was sufficient, further frequency shifting and phasing were performed. The frequency shifts and phases were saved and applied to the raw data with no zero filling or filtering.

The frequency and phase corrected water FID's were averaged. In cases where metabolite peaks were present in the water suppressed spectrum, the spectrum was multiplied by a filter, f(p), according to the following equation:

$$f(p) = \frac{1+\exp(-p_o / a_o)}{1+\exp\left[\frac{|p - p_c| - p_o}{a_o}\right]}$$

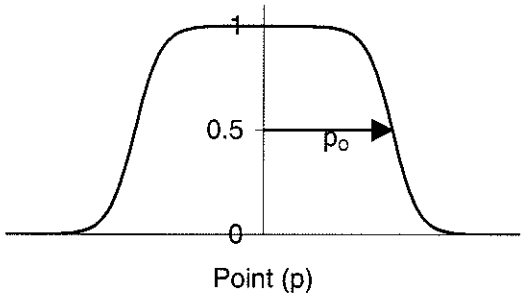

where p is the point on the x-axis, p_o is half the width at half height, p_c is the center point of the filter, and a_o is the width of the drop-off region of the curve.

The averaged water FID was used as the reference spectrum to correct the individual frequency and phase corrected water suppressed FID's for eddy currents. The eddy current correction was performed according to the method of Ordidge and Cresshull (1986). The water suppressed FID's were zero filled to 2048 points, multiplied by an exponential filter, and FFT'd to obtain the final spectrum.

3.6 Results

3.6.1 Coils

The signal to noise ratios for the Helmholtz-type volume coil, the circularly polarized spine coil, and the whole body coil as measured at the center of the magnet are listed in Table 3.3.

Table 3.3: Signal to noise ratios for three Siemens manufactured coils.

Coil	Signal to Noise Ratio
Helmholtz-type volume coil	17.8
Circularly polarized spine coil	8.8
Whole body coil	5.6

The maximum signal intensities of the water FID at time zero as a function of position along the x-axis (right to left across the bore of the magnet), y-axis (top to bottom of the bore of the magnet), and z-axis are plotted in Figure 3.4.

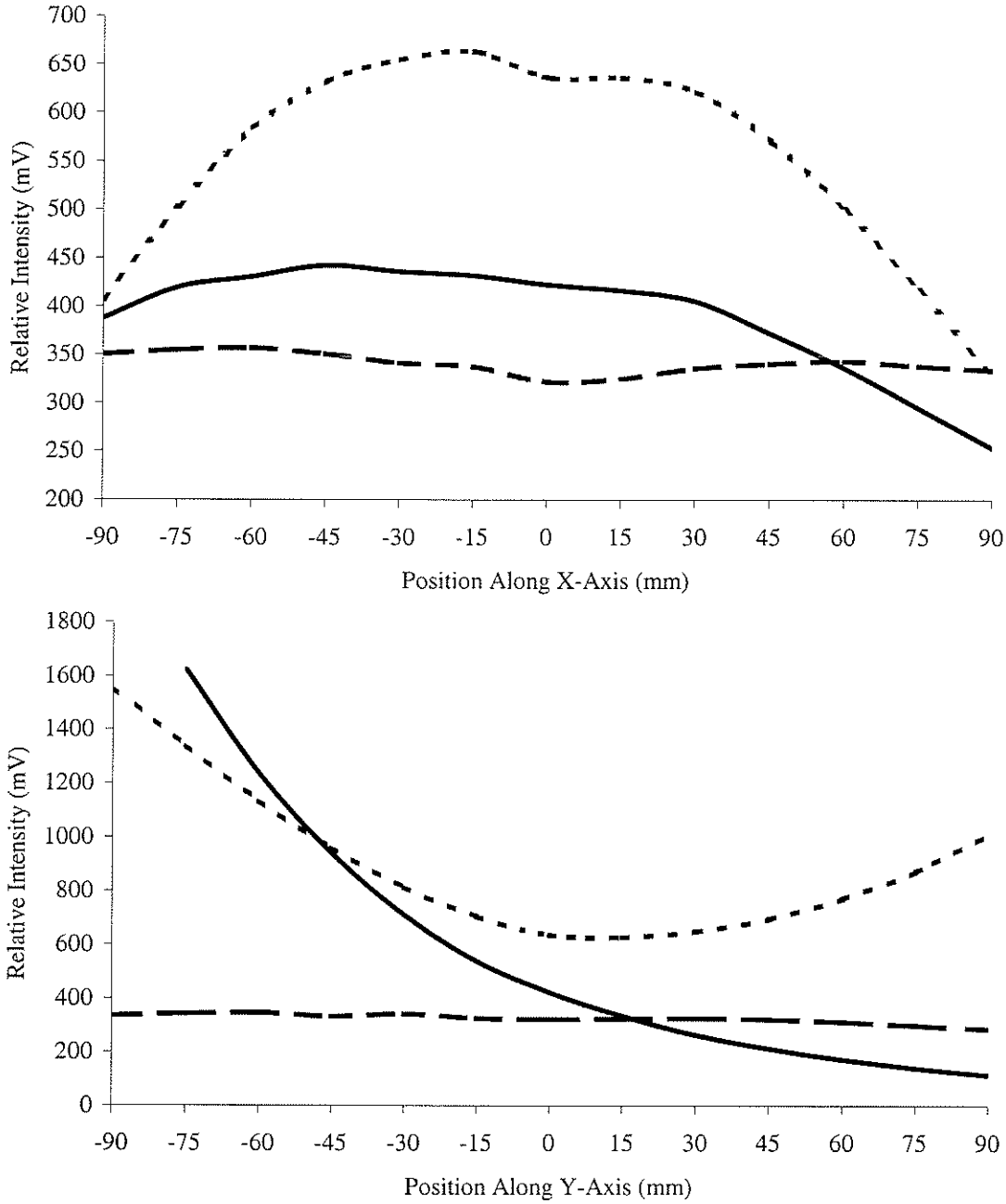

Figure 3.4: (Continued on next page) Signal intensities at time zero of the absolute magnitude water FID for 15x15x15mm^3 voxels positioned along the x-, y-, and z-axes. The intensities for the Helmholtz-type volume coil are illustrated by the dotted line, the solid line represents the cp spine coil, and the dashed line, the whole body coil.

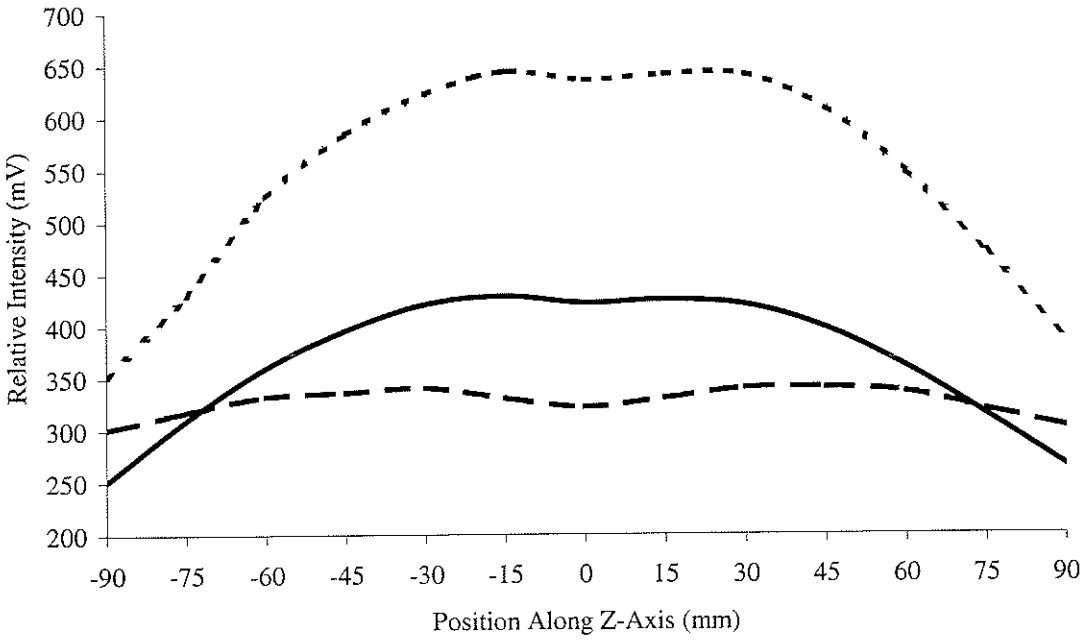

Figure 3.4: (Continued from previous page) Signal intensities at time zero of the absolute magnitude water FID for 15x15x15mm^3 voxels positioned along the x-, y-, and z-axes. The intensities for the Helmholtz-type volume coil are illustrated by the dotted line, the solid line represents the cp spine coil, and the dashed line, the whole body coil.

The plots along the x- and y-axes were asymmetric about the magnetic field center for the Helmholtz-type and cp spine coils. The plot for the Helmholtz-type coil was also assymetric around the magnetic field center along the y-axis. The Helmholtz-type volume coil gave the highest signal intensity along all three axes, except when the voxel was positioned at less than -45mm along the y-axis. The signal intensity decreased more rapidly for the Helmholtz-type coil than the cp spine and whole body coils as the voxel approached the coil extremities along the x- and z-axis. The cp spine coil gave a higher signal intensity than the whole body coil near the center of the magnetic field, but the

signal intensity dropped below that of the whole body coil at voxel positions greater than 70mm and less than -70mm along the z-axis, greater than 60mm along the x-axis, and greater than 15mm along the y-axis.

3.6.2 Imaging

Using the whole body coil for excitation and the cp spine coil for receiving the signal from the nuclei, FISP images were obtained (Figure 3.5). The resolution in these images was sufficient to locate the margins of the uterus. The cp spine coil was adjusted to lie directly beneath the uterus.

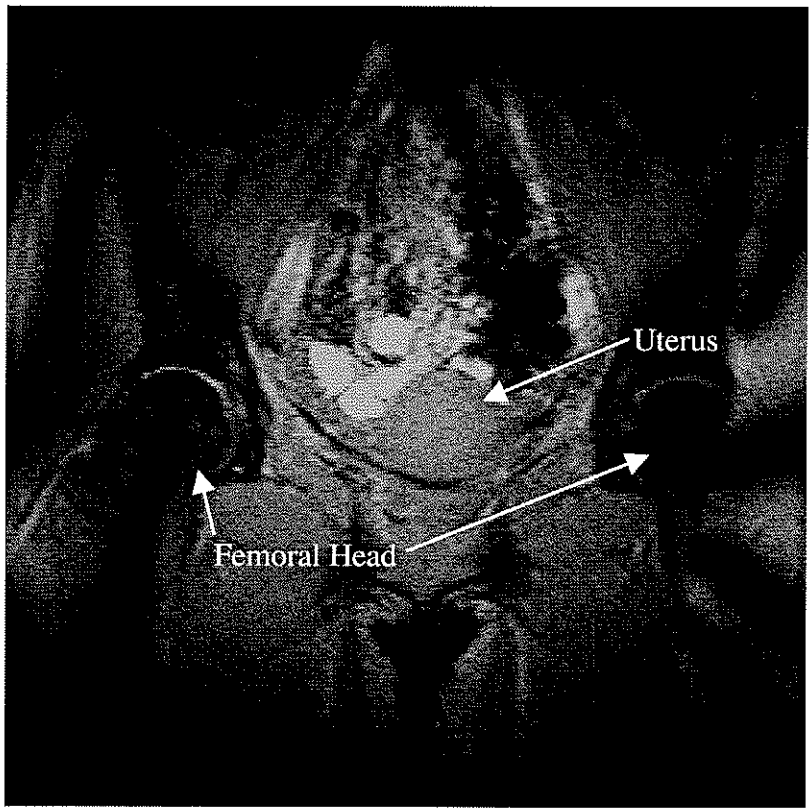

Figure 3.5: FISP image used to locate the uterus. The cp spine coil was positioned directly beneath the uterus.

The T_2-weighted Turbo Spin Echo sequence was used to obtain contiguous coronal and transverse images in premenopausal women. Sagittal images were obtained only when the ovaries were difficult to locate. The position of the ovaries varied (Figure 3.6). Typically, they lay between –5cm and +5cm along the x-axis, and –3cm and +3cm along the y- and z-axes with respect to the center of the static magnetic field.

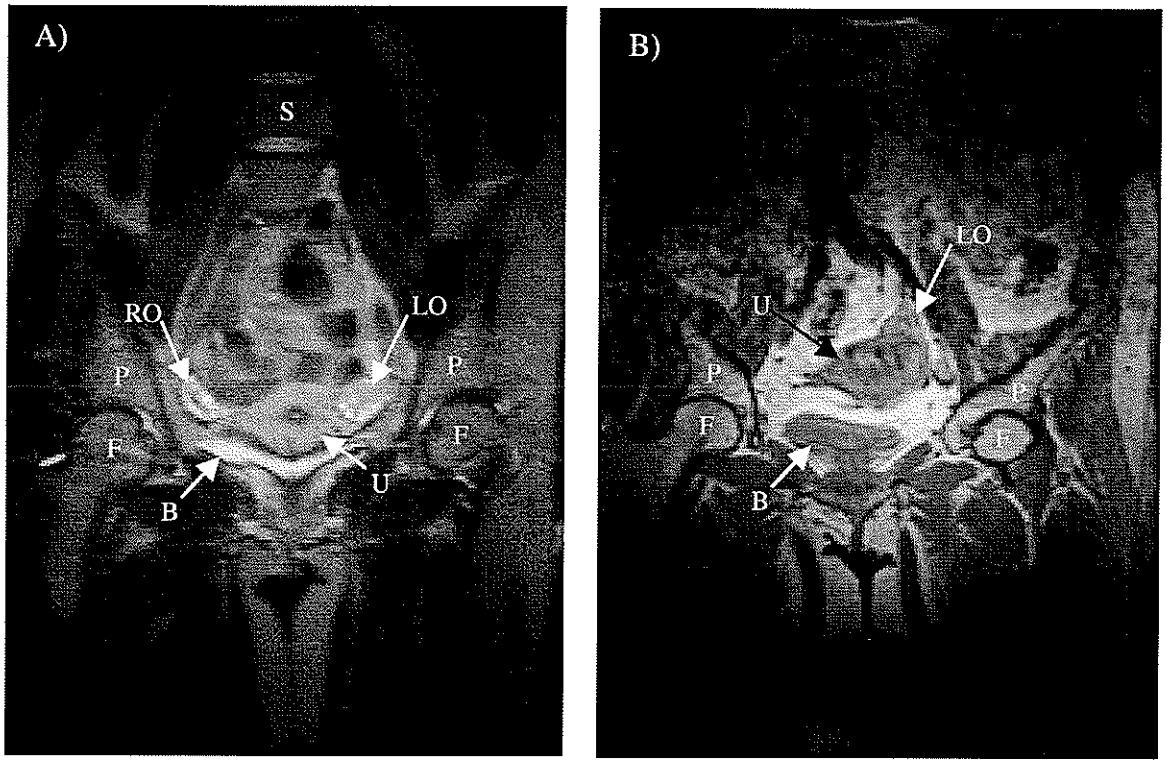

Figure 3.6: (Continued on Next Page) T_2-weighted Turbo Spin Echo coronal (A, B, and D), sagittal (C), and transverse (E and F) images. The follicular cysts appear hyperintense. The ovary(ies) are located: A) on either side of the uterus, B) superior to the anteverted uterus, C) superior to the uterine fundus, D) superior and not adjacent to the uterus, E) on either side of the uterus, and F) lateral to the uterus which is rotated and shifted to the left. The images are labelled as follows:

RO = Right ovary B = Bladder F = Femur

LO = Left ovary S = Spine P = Pelvic Bone

U = Uterus

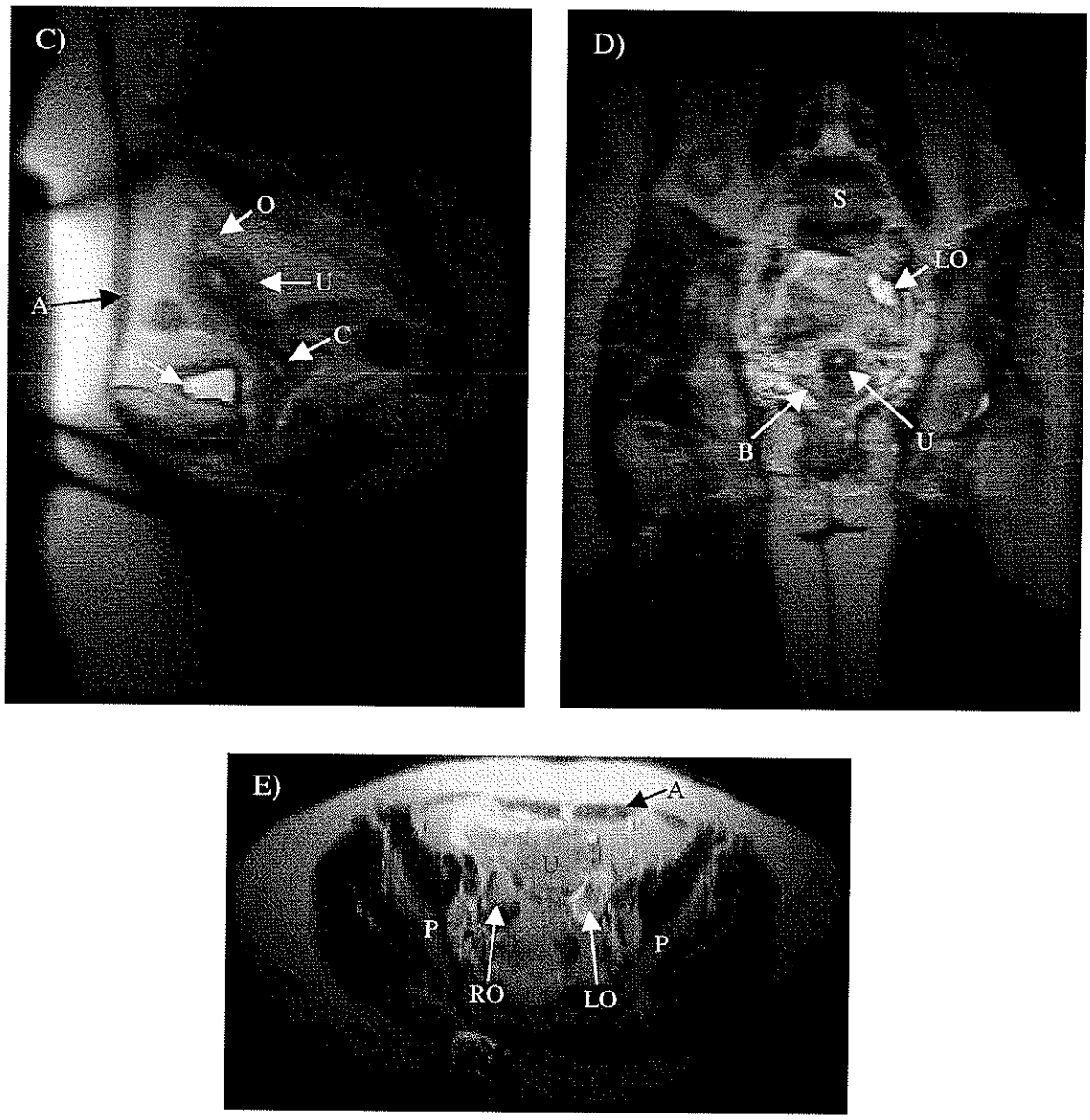

Figure 3.6: (Continued on Next Page) The ovary(ies) are located: C) superior to the uterine fundus, D) superior and not adjacent to the uterus E) on either side of the uterus. The images are labelled as follows:

RO = Right ovary	O = Ovary	B = Bladder
LO = Left ovary	S = Spine	P = Pelvic Bone
U = Uterus	C = Cervix	A = Abdominal Muscle

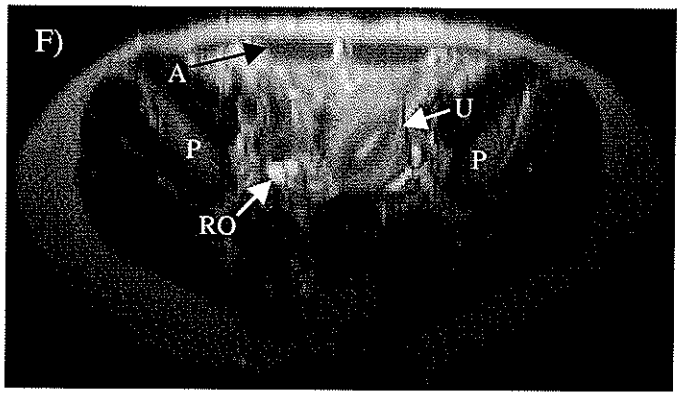

Figure 3.6: (Continued from previous page.) The ovary is located: F) lateral to the uterus which is rotated and shifted to the left. The image is labelled as follows:

RO = Right ovary P = Pelvic Bone

U = Uterus A = Abdominal Muscle

A cross sectional view of a portion of the bowel appeared as a round or oval structure in the images and had the same intensity as the ovaries in both T_2- and T_1-weighted images. Examples are shown in Figure 3.7. Bowel was easily distinguished from the ovaries in T_2-weighted images when follicular cysts were present on the ovaries because the follicular cysts were of high intensity, due to their high water content, while the ovaries and bowel were of low to intermediate intensity (Figure 3.7A). In T_1-weighted images, the bowel, follicular cysts, and ovary were of low to intermediate intensity (Figure 3.7B). When no follicular cysts were present, differentiation was more difficult. Contiguous slices aided in differentiation. The loops of bowel extended through multiple slices, while the ovaries did not.

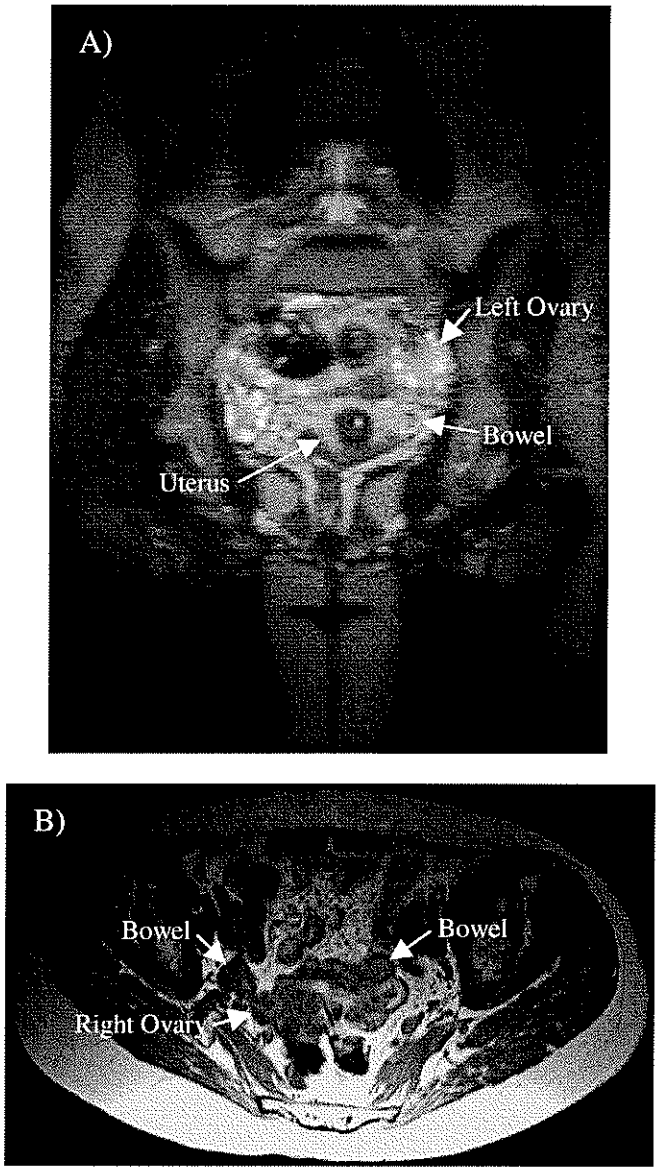

Figure 3.7: T_2-weighted (A) and T_1-weighted images (B) showing a cross sectional view of a portion of bowel. The bowel and ovaries are isointense.

The ovaries were successfully identified in 20 of the 21 premenopausal women with no known ovarian abnormalities and both of the 2 perimenopausal women. The woman whose ovaries could not be located was breast feeding her child and had stopped taking oral contraceptives approximately one month prior to her participation in the study. Breast feeding and oral contraceptives inhibit the formation of follicular cysts. No follicular cysts were observed on this woman's ovaries making location difficult. The ovaries could not be distinguished from bowel in the images. Of the 20 women whose ovaries were identified, 6 were found to have a cyst on one ovary that was large enough (>2cm) to measure using MRS. None of these cysts exceeded 5cm in diameter, and therefore were considered normal. One women was found to have polycystic ovaries.

The T_1-weighted Spin Echo sequence was used to obtain sequential transverse and coronal images in postmenopausal women. Representative images are shown in Figure 3.8:

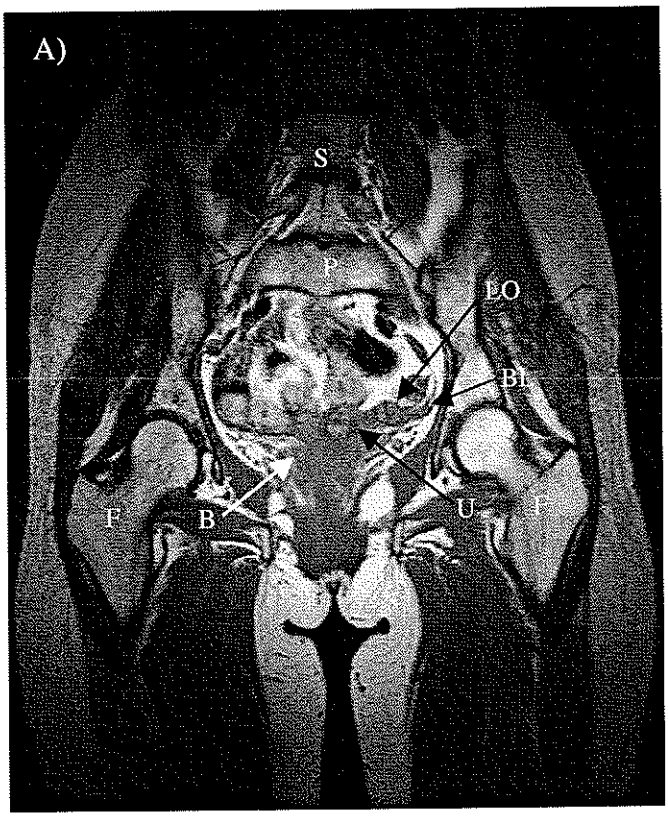

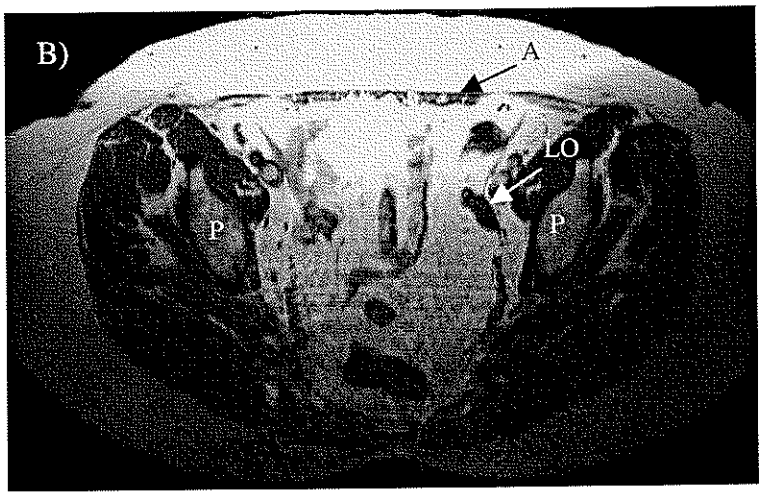

Figure 3.8: (Continued on next page) T_1-weighted Spin Echo coronal (A) and transverse (B and C) images. The images are labelled as follows:

LO = Left ovary	B = Bladder	F = Femur
U = Uterus	S = Spine	P = Pelvic Bone
BL = Broad Ligament	A = Abdominal Muscle	

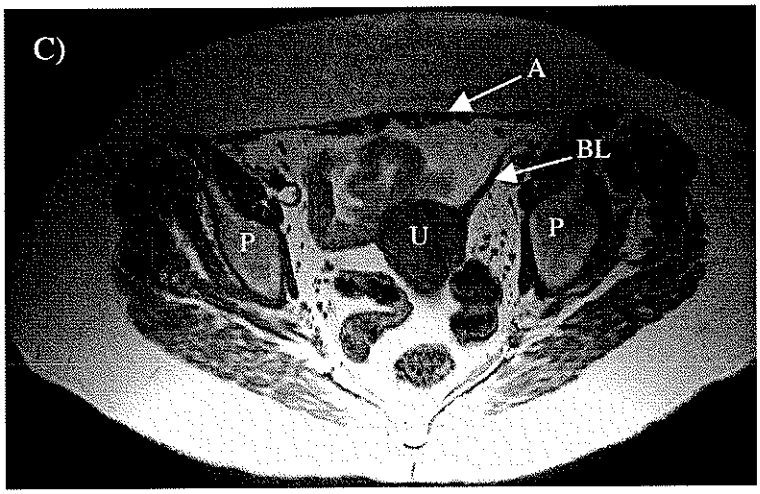

Figure 3.8: (Continued from previous page) T_1-weighted Spin Echo coronal (A) and transverse (B and C) images. The images are labelled as follows:

LO = Left ovary	B = Bladder	F = Femur
U = Uterus	S = Spine	P = Pelvic Bone
BL = Broad Ligament	A = Abdominal Muscle	

At least one ovary was successfully identified in 10 of the 17 postmenopausal women with no known ovarian abnormalities. One of these women had a large uterine fibroid that was 10cm in diameter and one woman had undergone an hysterectomy, but both ovaries and the broad ligament were intact. Another had early onset menopause (last period occurred at the age of 42). One woman, whose ovaries could not be identified, had a prolapsed uterus. In some cases where the ovary was adjacent to the uterus, T_2-weighted images confirmed the position (Figure 3.9).

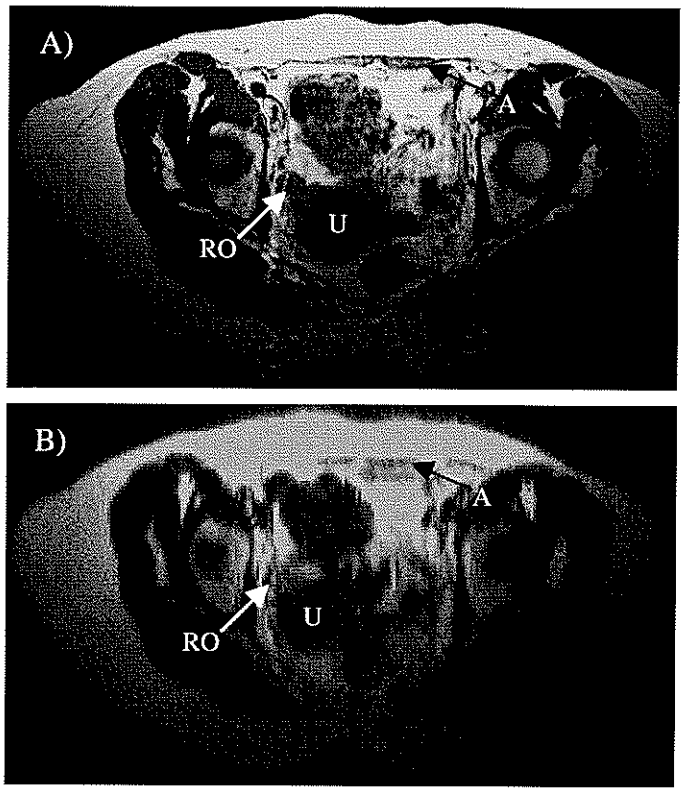

Figure 3.9: (A) T_1-weighted Spin Echo transverse image and (B) T2-weighted Turbo Spin Echo transverse image showing the right ovary adjacent to the uterus. (RO = right ovary, U = uterus, A = abdominal muscle)

3.6.3 Spectroscopy

MR spectroscopy of the ovaries was complicated by motion in the pelvis. Respiration and pulsation of the femoral arteries caused artifacts in the images (Figure 3.10), but these motions, along with peristalsis of the bowel, had minimal, if any, effects on the spectroscopic examination of the ovaries because they did not cause the ovary to move.

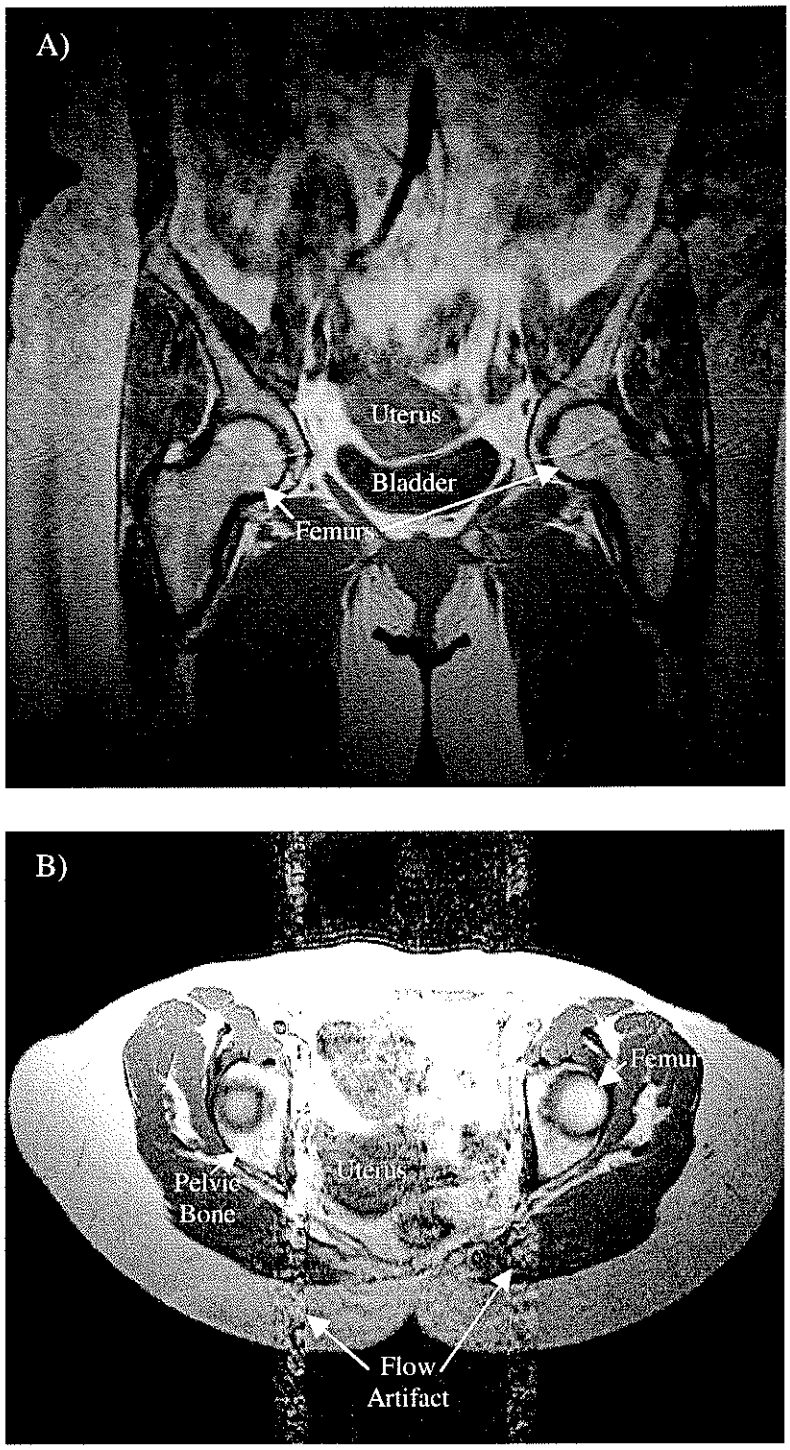

Figure 3.10: T_1-weighted images showing A) respiratory artifact as blurring of the upper portion of the image, and B) flow artifact due to pulsation of the femoral arteries

Motion of the urinary bladder as it filled as well as gas in the bowel had significant effects on the ovaries. The ovaries may be displaced by 2cm over a 90 minute period due to filling of the urinary bladder (Figure 3.11). The image displayed in Figure 3.11A was obtained using the high resolution, T_2-weighted Turbo Spin Echo (TSE) sequence. The image in Figure 3.11B was obtained using the shortened version of the same sequence. While the signal to noise ratio in Figure 3.11B is much lower, the resolution is adequate to determine the new position of the ovary. Note the position of the ovary in Figure 3.11A where the urinary bladder is almost empty. The bottom of the right ovary (RO) is in the same transverse plane as the top of the femur (F). In Figure 3.11B, the right ovary is displaced by the full bladder. The ovary is now superior to the top of the femur. The ovary may also rotate as a result of filling of the urinary bladder. Note in Figure 3.11B that the long axis of the ovary has rotated by approximately 20^{O} near the end of the study as compared to Figure 3.11A at the beginning of the study.

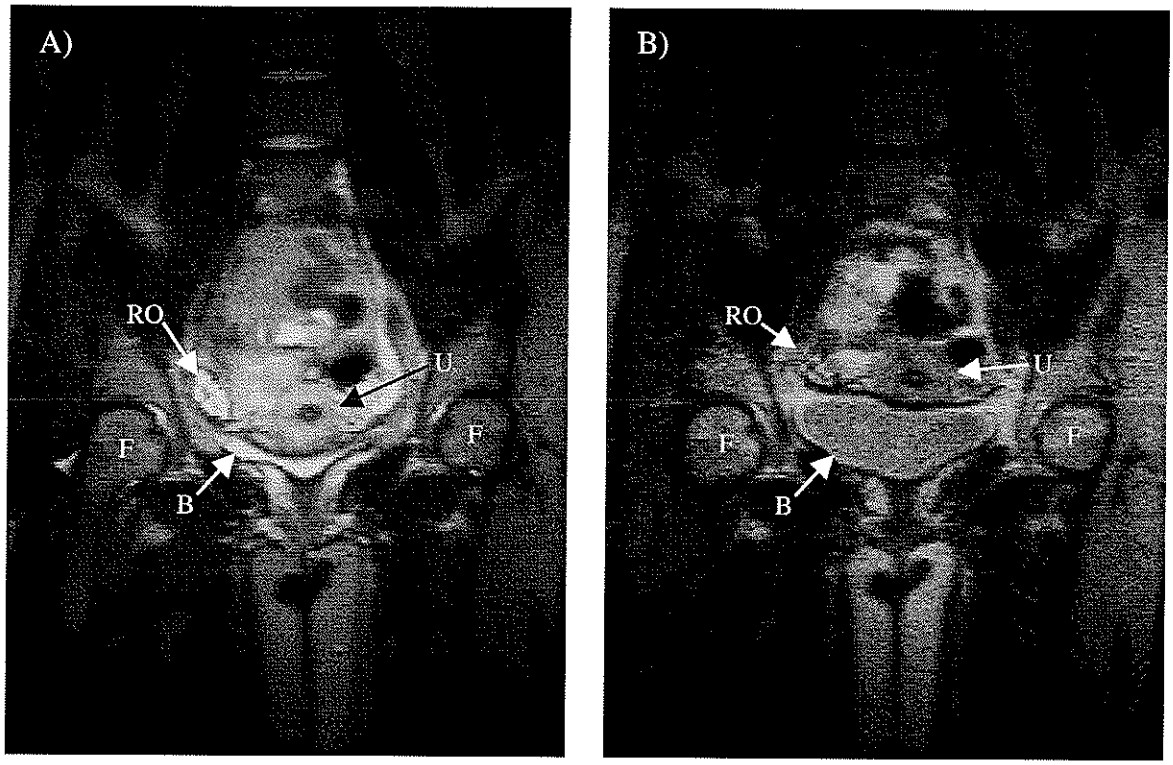

Figure 3.11: T_2-weighted coronal images of a premenopausal pelvis A) at the beginning of the study using the high resolution TSE sequence, and B) near the end of the study, approximately one hour later, using the lower resolution, shortened version of the TSE sequence. Note the filling of the urinary bladder and its effects on the position of the ovary. (RO = right ovary, B = bladder, U = uterus, F = femur)

Gas in the bowel proximal to the ovary (Figure 3.12) had no noticeable effect on motion of the ovary, but the tissue to air interface between the ovary and the gas caused magnetic field inhomogeneities that affected the line width and signal to noise ratio of peaks in the spectra (Figure 3.13). When no gas was present near the ovary, a narrow water peak was obtained (Figure 3.13A). Frequency and phase corrections to the individual acquisitions had virtually no effect on the line width and signal to noise ratio (compare Figure 3.13A to 3.13B). When bowel gas was proximal to the ovary, a much broader water peak was

observed (Figure 3.13C). Frequency and phase corrections to the individual acquisitions resulted in a narrower line width and an increase in the signal to noise ratio (compare Figure 3.13C to 3.13D). The full width, half maximum linewidth (FWHM) of the water peak varied from 5 Hz in some subjects to 30 Hz in others.

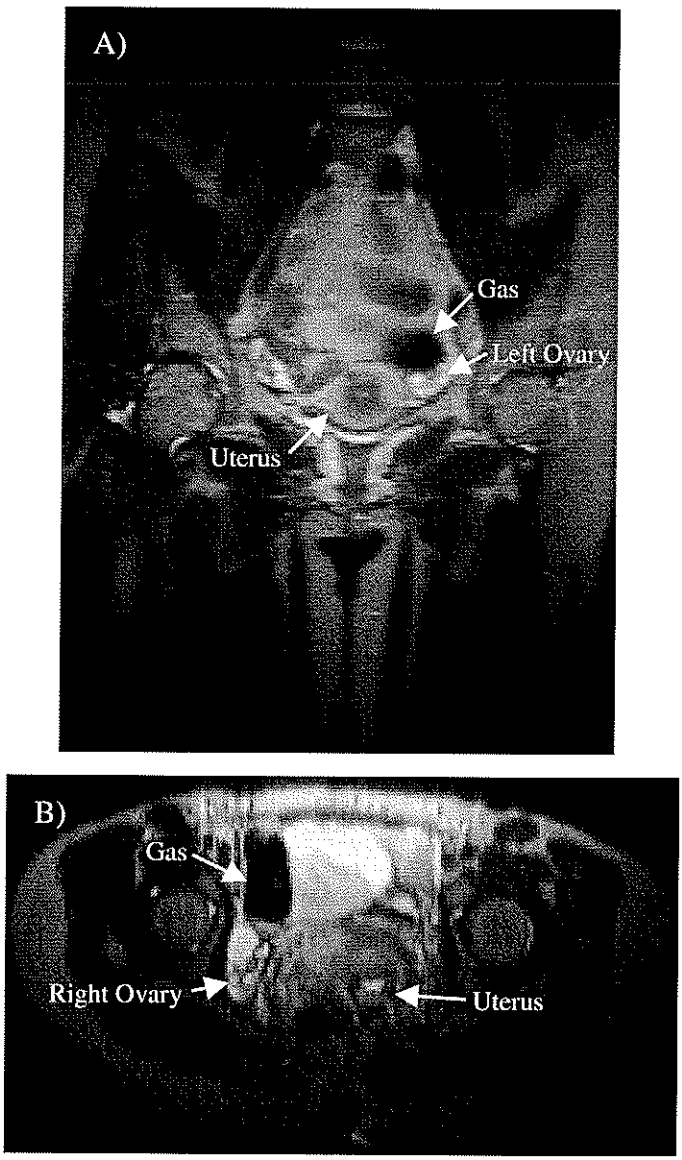

Figure 3.12: T_2-weighted coronal (A) and transverse (B) images illustrating gas in the bowel proximal to the ovary.

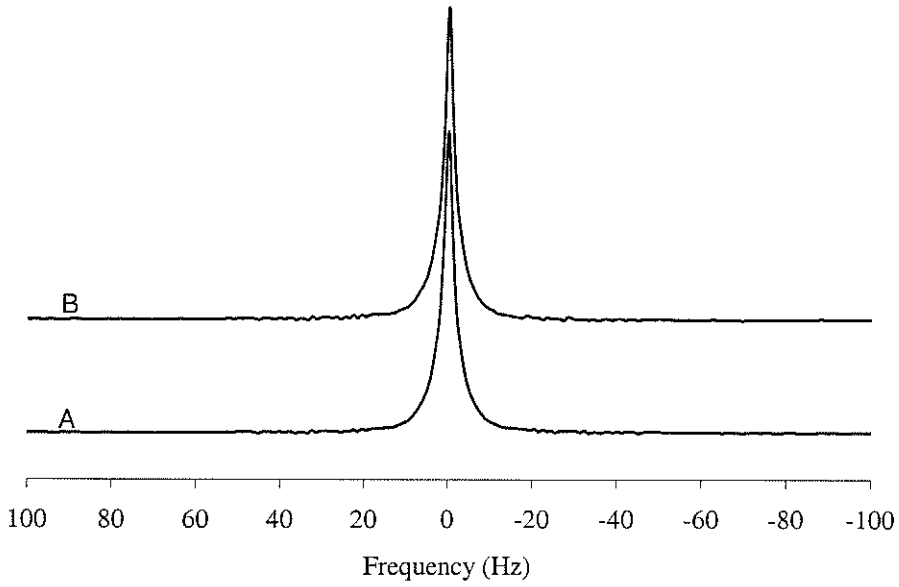

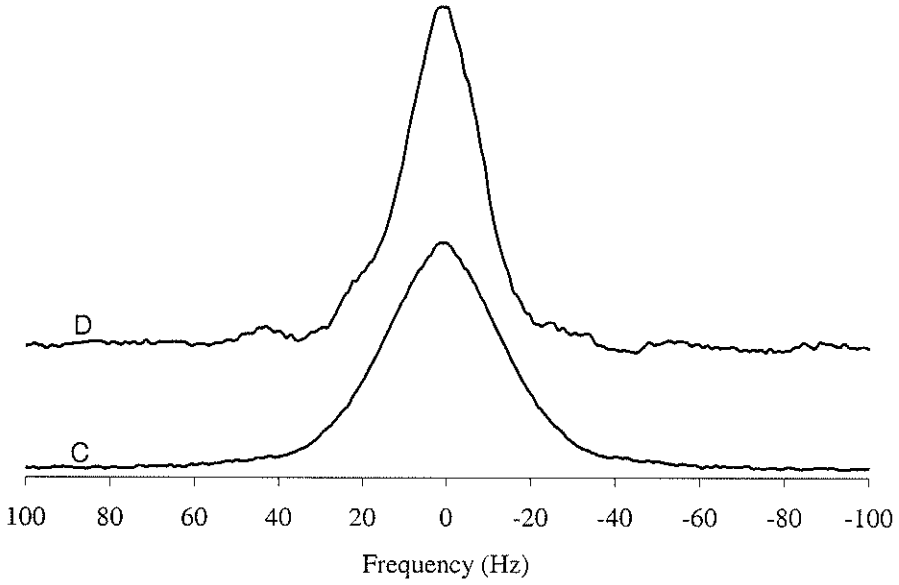

Figure 3.13: Eddy current corrected, raw water spectra acquired from ovaries of two women with A) no bowel gas (FWHM = 3.10Hz) and C) bowel gas (FWHM = 32.29Hz) near to the ovary. Each acquisition in A and C was frequency shifted and phased to obtain B (FWHM = 2.86Hz) and D (FWHM = 20.24Hz).

The frequency and phase corrections made to the individual acquisitions, as illustrated by the water spectra in Figure 3.13, were performed using an IDL program. The program was customised for this study. The source code is given in Appendix 2. The IDL program was designed to be interactive. Frequency shifting and phasing are accomplished using sliders which allow the user to view the effects on the spectra in real time. The windows of the program are shown in Figure 3.14. The data displayed in the windows were obtained from the spherical phantom that contained 0.1M acetate and 0.1M lactate.

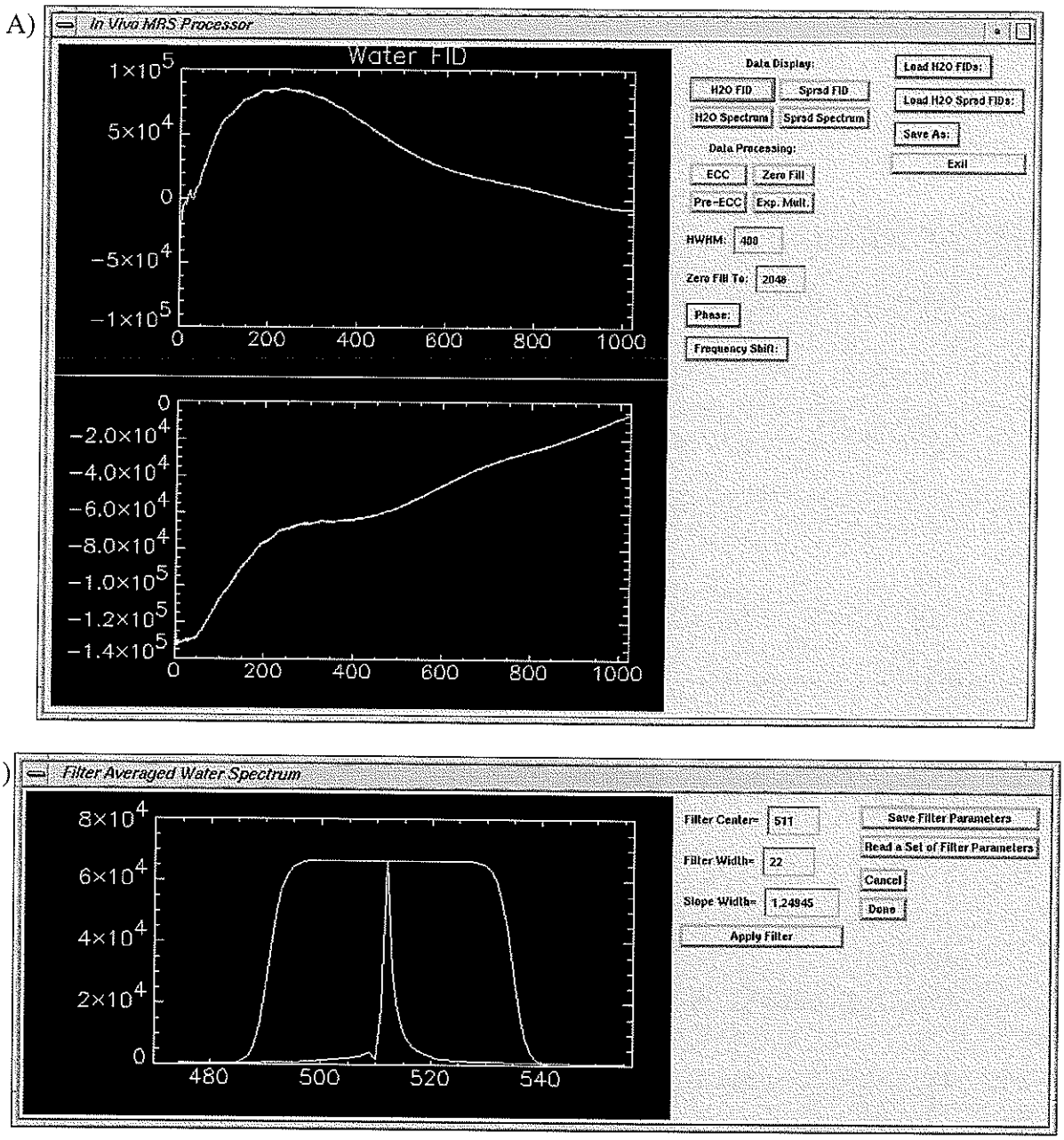

Figure 3.14: (Continued on next page) Windows from the IDL program used to frequency shift and phase the individual acquisitions. A) Main window showing averaged real and imaginary data. B) Filter window showing averaged, absolute magnitude water spectrum and filter. C) Phasing window showing non-averaged real and imaginary spectra. D) Frequency shifting window showing non-averaged absolute magnitude spectra.

C)

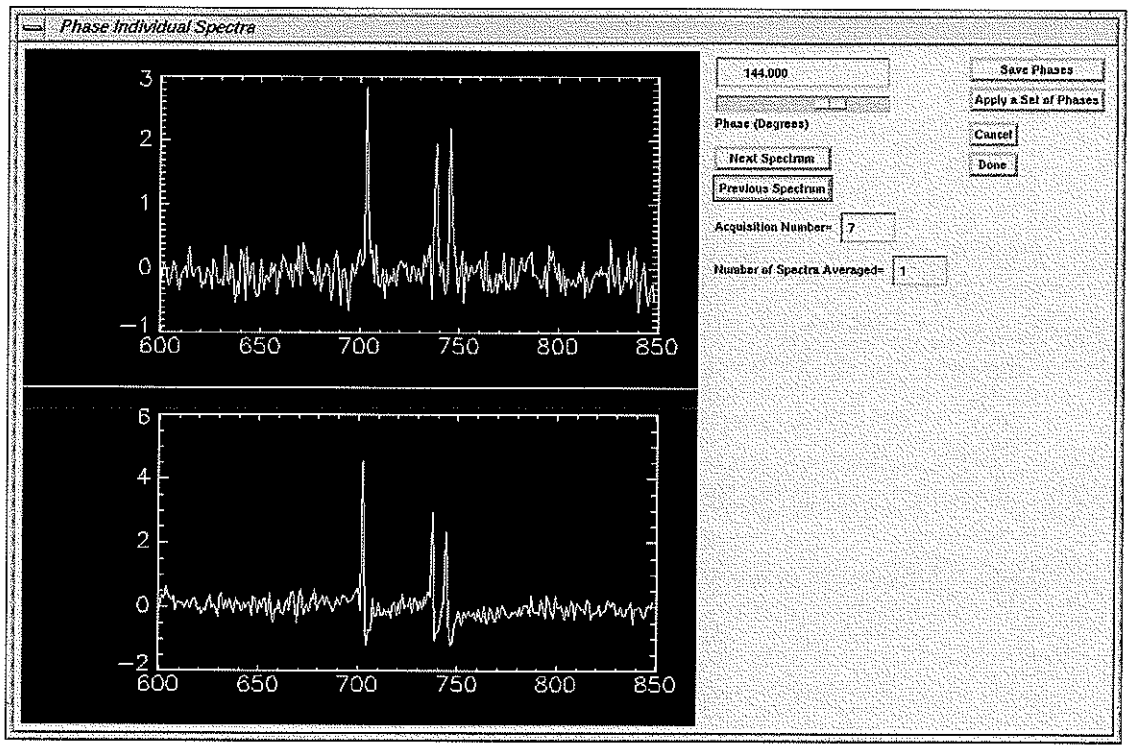

D)

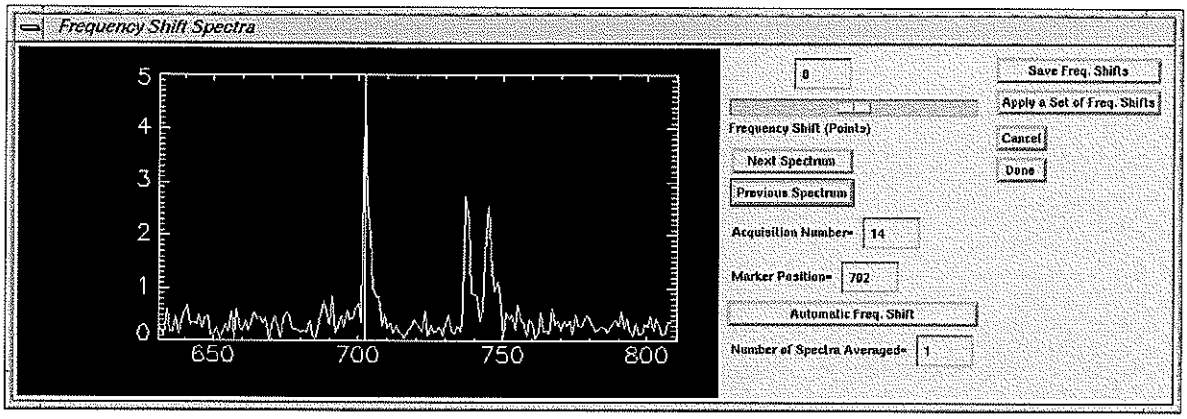

Figure 3.14: (Continued from previous page) Windows from the IDL program used to frequency shift and phase the individual acquisitions.

C) Phasing window showing non-averaged real and imaginary spectra. D) Frequency shifting window showing non-averaged absolute magnitude spectra.

Frequency shifting and phasing of the individual water suppressed spectra resulted in significant changes in the spectra including an improvement in the signal to noise ratio (Figure 3.15). The effects of these corrections on the spectra depended on which peak or peaks were used as the reference. The spectrum shown in Figure 3.15A was obtained from a healthy ovary. No manipulation of the individual acquisitions was performed prior to averaging. Figure 3.15B illustrates the same data as in Figure 3.15A after frequency shifting and phasing the residual water peak in each of the 128 acquisitions. After correction, the averaged spectrum was phased according to the metabolite peaks. The results of frequency and phase correcting the metabolite peaks in each acquisition is shown in Figure 3.15C. All three spectra were eddy current corrected, zero filled to 2048 points, and multiplied by an exponential filter (full width, half maximum = 64 points). The signal to noise ratio is greatest in Figure 3.15C and poorest in Figure 3.15A. The metabolite peaks appear at slightly different frequency shifts and are of different intensities in Figure 3.15C than in Figures 3.15A and B.

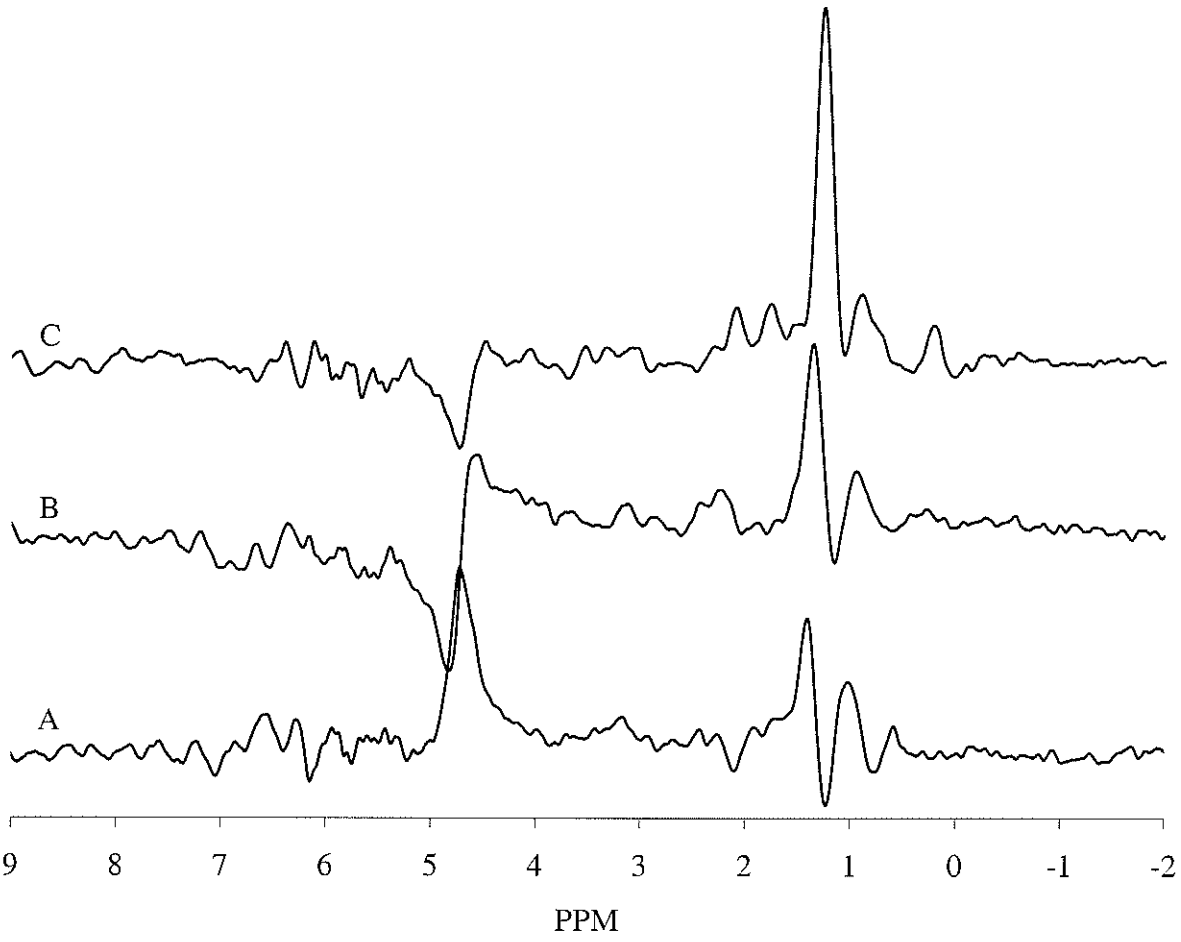

Figure 3.15: Water suppressed spectra from a healthy premenopausal ovary with A) no frequency and phase correction, B) frequency and phase correction on the residual water peak, and C) frequency and phase correction on the metabolite peaks. Voxel size = $12x12x12mm^3$.

Frequency shifting and phasing the residual water peak in each acquisition did not correspond to the same corrections applied to the metabolite peaks, and *vice versa*. This is illustrated in Figure 3.16. Each set of 32 acquisitions was frequency and phase corrected on A) the water peak, and B) the metabolite peaks before averaging, eddy

current correction, zero filling (2048 points) and exponential multiplication (full width, half maximum = 64 points). In Figure 3.16A, the water peaks in each set of 32 acquisitions have the same relative phase, but the metabolite peaks have different phases. Similarly, the metabolite peaks in each set of 32 acquisitions in Figure 3.16B have the same relative phase, but the water peaks do not. The sets of 32 acquisitions are representative of the individual acquisitions, since the relative frequency shifts and phases of the spectra within a set of 32 acquisitions were normally similar. The relative phases of each set of 32 acquisitions, however, differed by as much as 180^{O}. The frequency shifts and phases for each acquisition of the spectrum that was corrected using the metabolite peaks as the reference (Figure 3.15C) are plotted in Figure 3.17. Each averaged set of 32 was frequency shifted and phase corrected. Only individual acquisitions with sufficient signal to noise were further corrected. The frequency shifts and phases that are constant within each set of 32 acquisitions were obtained for acquisitions that either required no further corrections or had insufficient signal to noise ratios to allow further corrections.

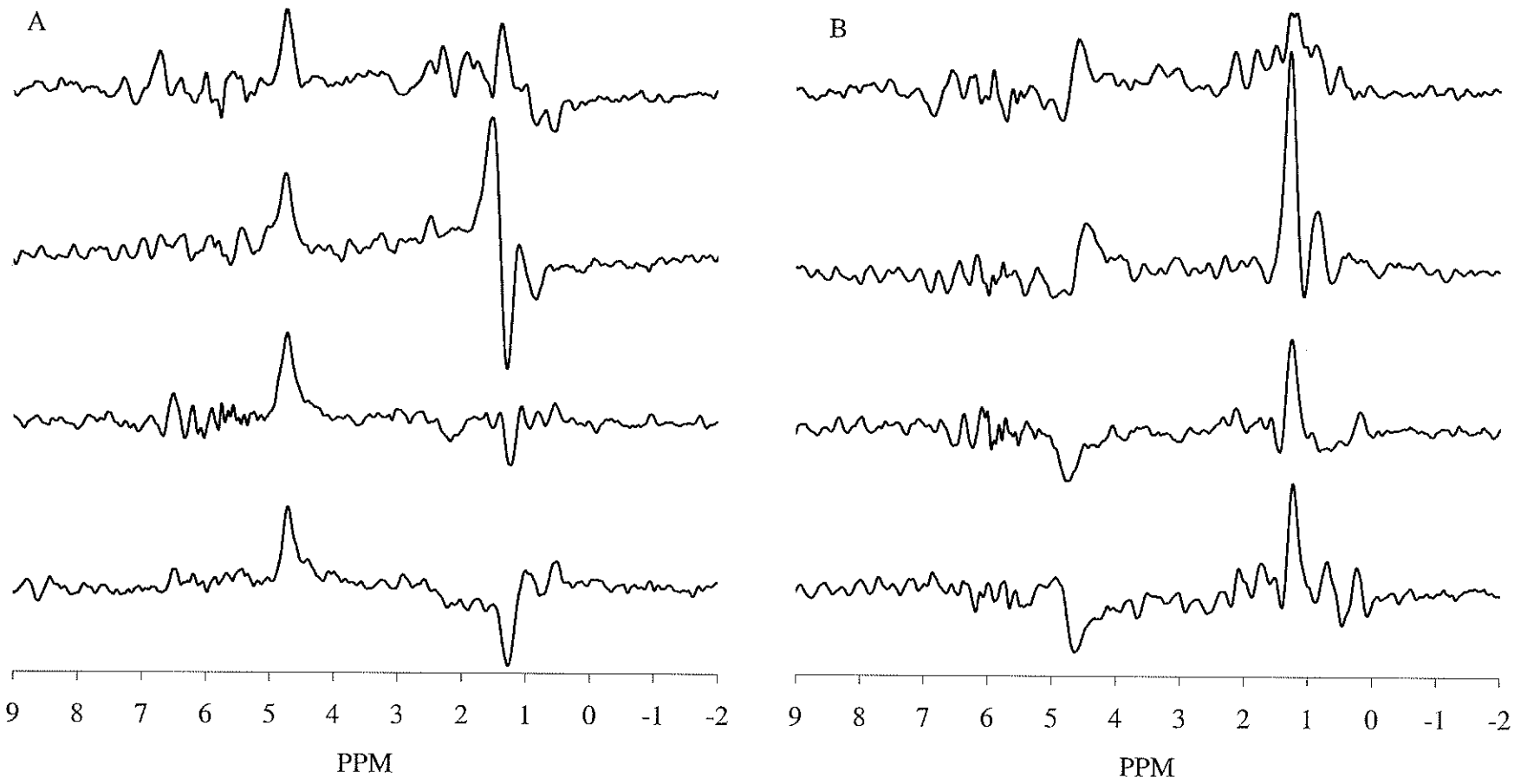

Figure 3.16: Water suppressed spectra averaged over 32 acquisitions after A) frequency shifting and phasing the residual water peak in each acquisition, and B) frequency shifting and phasing the metabolite peaks in each acquisition. (Refer to text for details.)

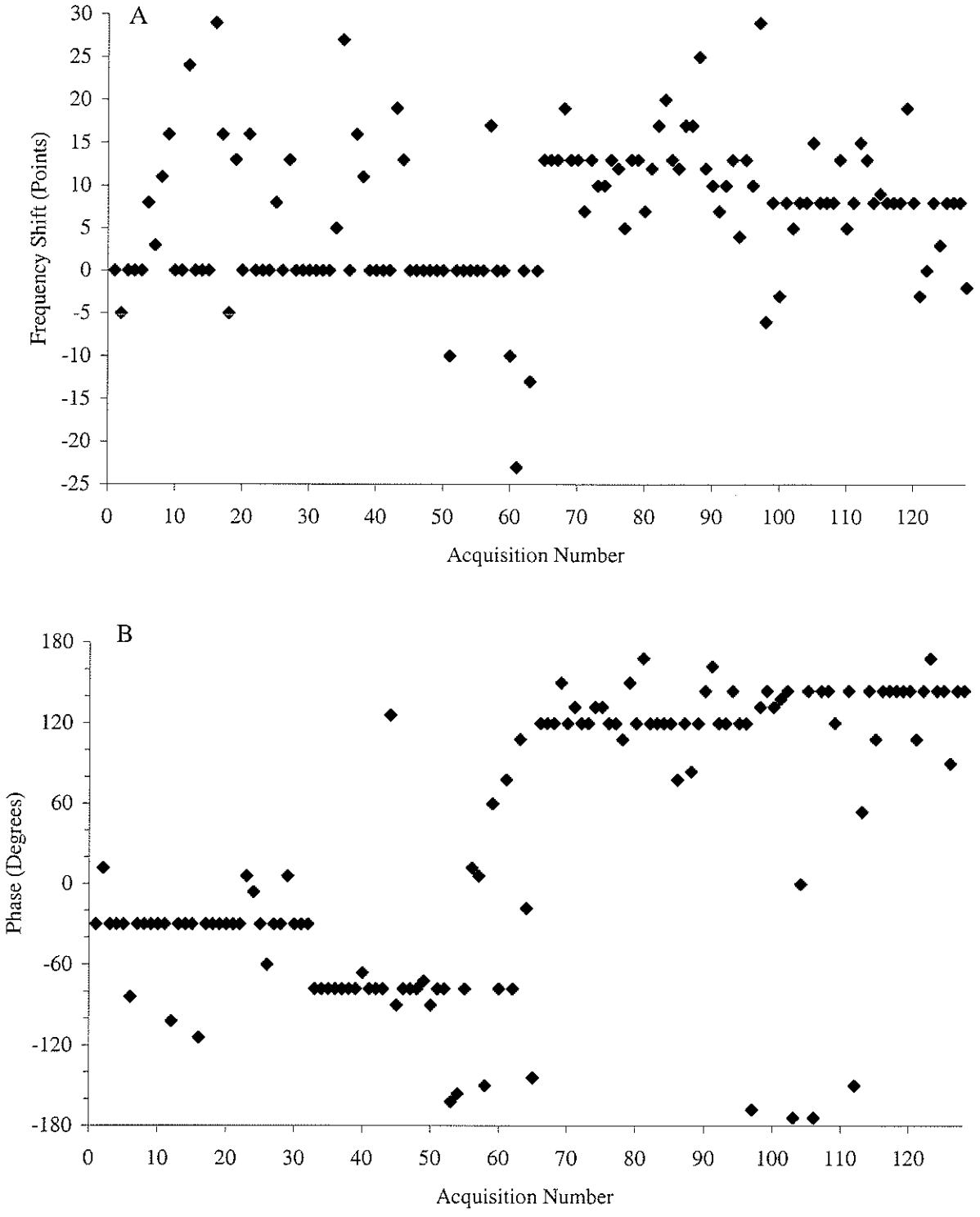

Figure 3.17: A) Frequency shifts and B) phases applied to each acquisition of the spectrum in Figure 15C. The total number of spectral points per spectrum was 2048 points.

MR spectra were obtained from the ovaries of pre- and postmenopausal women. The spectrum displayed in Figure 3.18 is representative of those obtained from postmenopausal ovaries. It is similar to the spectrum displayed in Figure 3.15C from a healthy, premenopausal ovary. Typically, postmenopausal ovaries were small necessitating small voxel sizes. In some cases, a voxel that was entirely within the ovary was so small that insufficient signal to noise was obtained in the spectrum. In these cases, the voxel size was increased and signal was obtained from the ovary as well as a small portion of the surrounding tissue.

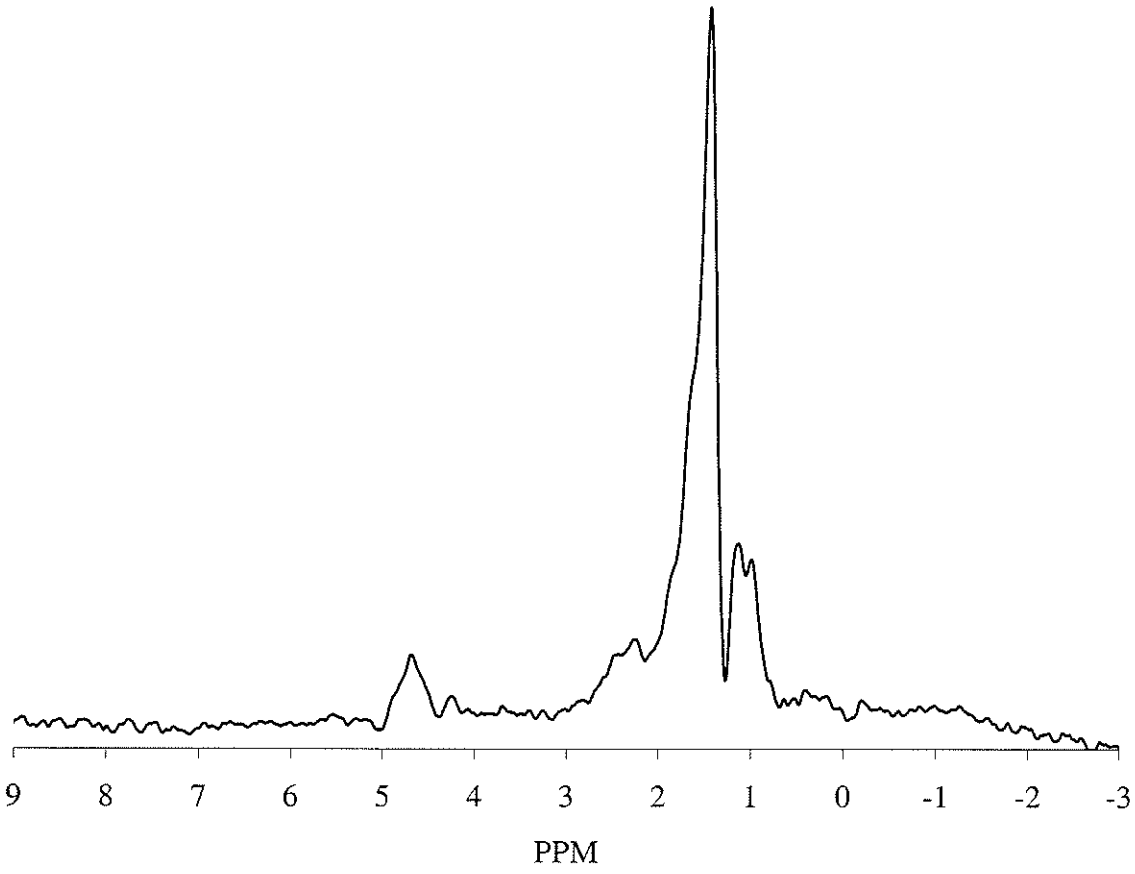

Figure 3.18: MR spectrum from a postmenopausal ovary (15 years since last menses). Voxel size = 8.0x8.0x12.0mm^3.

Five of the eight women who participated in the study of the ovaries through the menstrual cycle participated in all six visits. Illustrated in Figures 3.19 and 3.20 are six MR images and spectra representative of a healthy ovary belonging to a premenopausal woman. The images and spectra correspond to six days in one menstrual cycle of the woman. The first image (Figure 3.19A) was obtained on the second day of the menses (day 2 of the cycle). A few follicular cysts had formed on each ovary. The woman's second visit occured 8 days after the first visit (day 10 of the cycle), which was estimated to be midway between the onset of menses and the day of ovulation. The image in Figure 3.19B was obtained on the second visit, and shows a slight increase in the size of the follicular cysts on both ovaries. Figure 3.19C shows the image obtained on the third visit corresponding to the day before ovulation (day 21 of the cycle). In this image, the follicular cyst that will ovulate is clearly depicted as a region of high intensity on the left ovary. The day before ovulation was identified as the day when the ovulation test was positive for an increase in luteinizing hormone Further confirmation of the day before ovulation was obtained on the fourth visit, which was the day of ovulation (day 22 of the cycle). The image obtained on the day of ovulation (Figure 3.19D) confirms the rupture of the ovulating follicle by the absence of the cyst that previously exhibited high signal intensity. It appears that a small amount of fluid may be left in the ruptured cyst as evidenced by a small region of high intensity in the former position of the follicular cyst. Further confirmation of ovulation was obtained from the woman's record of her basal body temperature. A representative temperature chart is shown in Figure 3.22 showing the rise in body temperature on the day of ovulation. The images obtained on the day after ovulation (day 23 of the cycle, Figure 3.19E) and 7 days after the day of ovulation

(day 30 of the cycle, Figure 3.19F) illustrate a few cysts on each ovary. The cysts are mainly follicular cysts, but one is the corpus luteal cyst that formed from the follicular cyst that ruptured at the time of ovulation. The corpus luteal cyst can not be distinguished from the follicular cysts in the T_2-weighted images.

Representative spectra obtained from an ovulating ovary on each visit through the menstrual cycle are displayed in Figure 3.20. The voxel sizes varied slightly for each of the six visits due to the changing size of the ovary and its orientation. The voxel sizes ranged from $5x10x15mm^3$ to $10x14x14mm^3$. Due to equipment breakdown, only 96 acquisitions were obtained on the fourth visit (Figure 3.20D), and a water spectrum was not acquired. Hence, no eddy current correction was performed on this spectrum, leading to the excessive ringing in Figure 3.20D. A spectrum acquired from the ovulating ovary of another woman is displayed in Figure 3.21 along with the spectrum from Figure 3.20D. The spectrum in Figure 3.21 has a significantly better signal to noise ratio than the spectra in Figure 3.20 due to a greater number of acquisitions acquisition (192 acquisitions in Figure 3.21 and 128 acqusitions in Figure 3.20). Note that the spectra in Figures 3.20 and 3.21 are all similar with an intense peak at 1.3ppm. No significant differences were observed in the spectra acquired on each visit for each of the women who participated in the study.

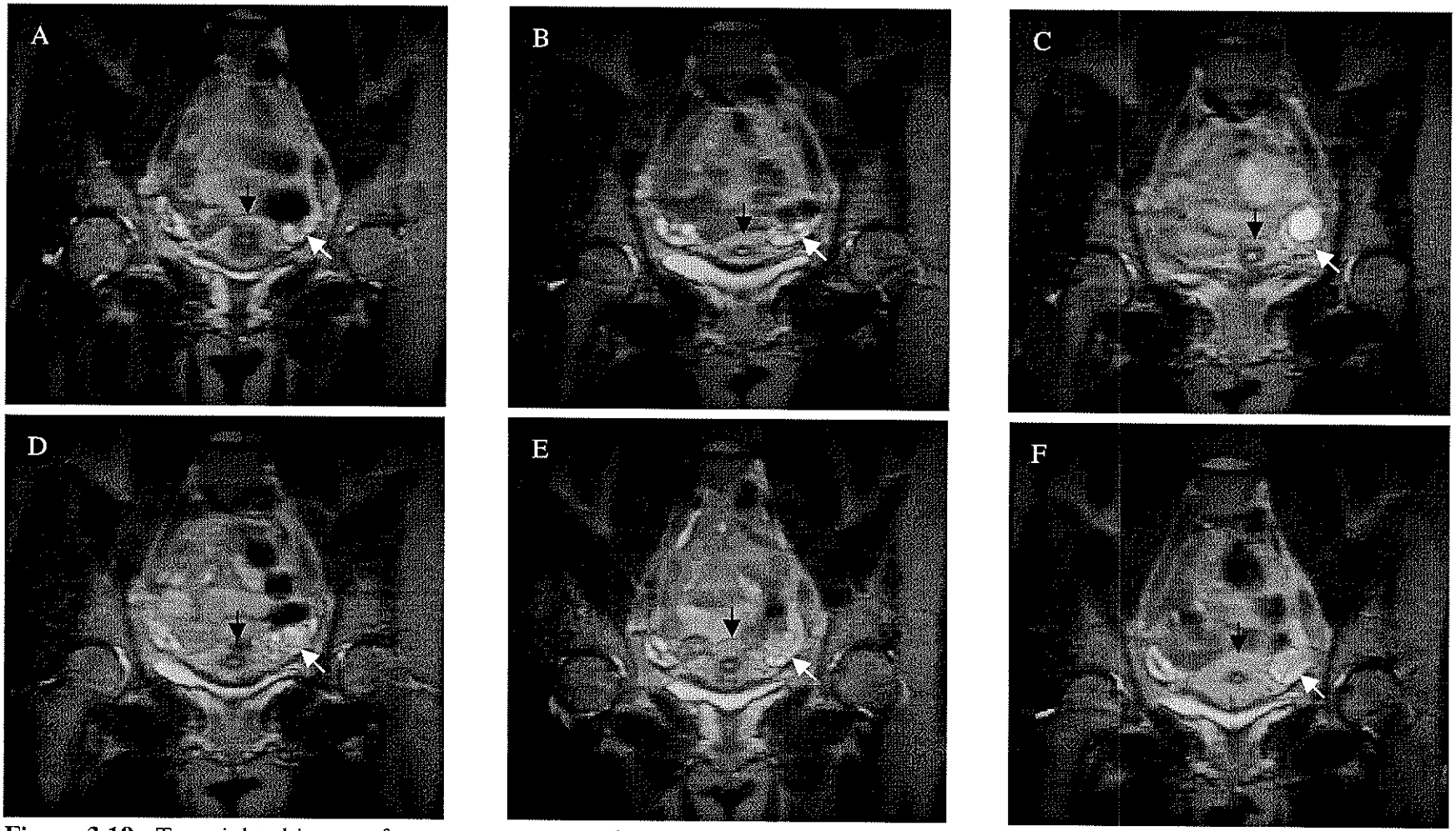

Figure 3.19: T_2-weighted images from a premenopausal woman on A) the second day of menses (cycle day 2), B) midway between menses and ovulation (cycle day 10), C) the day before ovulation (cycle day 21), D) the day of ovulation (cycle day 22), E) the day after ovulation (cycle day 23), F) midway between ovulation and the onset of menses (cycle day 30). The left ovary ovulated and is indicated by the white arrow. The uterus is indicated by the black arrow.

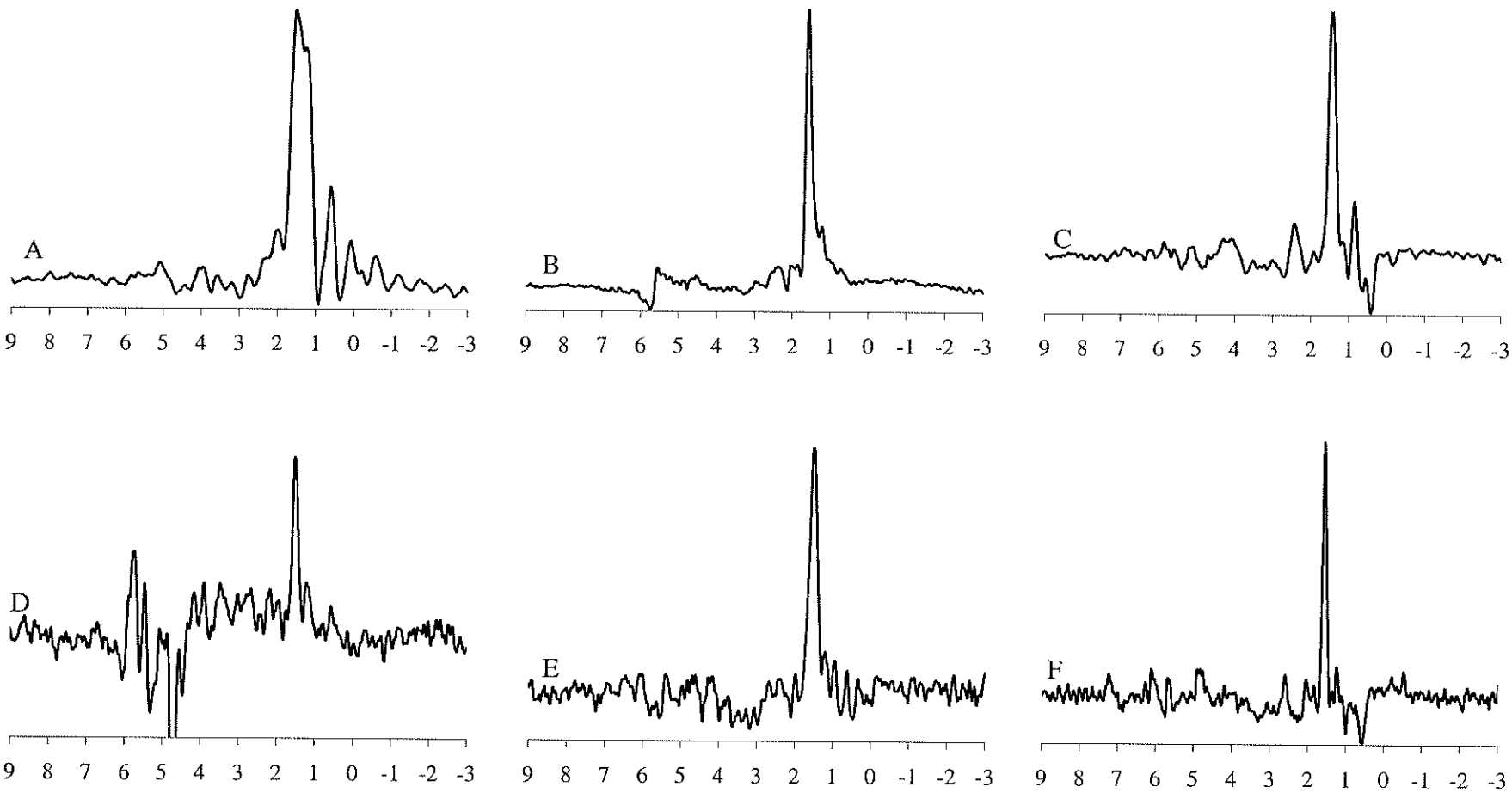

Figure 3.20: MR spectra from a premenopausal woman on A) the second day of menses, B) midway between menses and ovulation, C) the day before ovulation, D) the day of ovulation, E) the day after ovulation, F) midway between ovulation and the onset of menses.

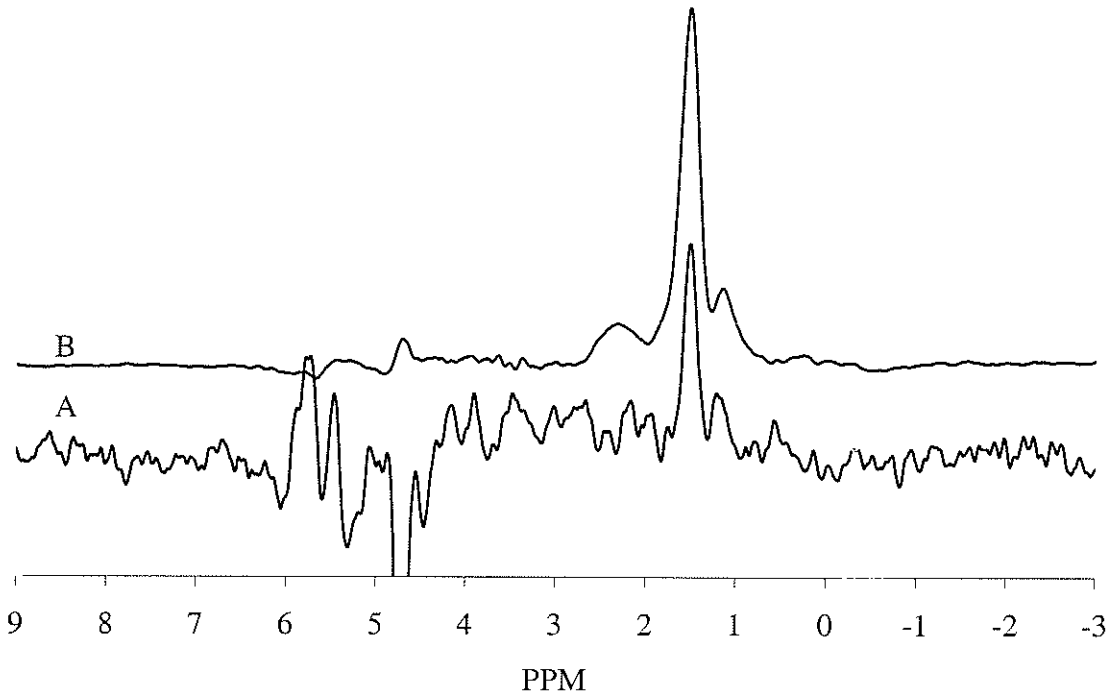

Figure 3.21: MR spectra obtained on the day of ovulation from the ovary that ovulated. Due to equipment failure, only 96 acquisitions were obtained for the spectrum in A and no eddy current correction was applied. Spectrum B consists of 192 averaged acquisitions and eddy current correction was performed. While the signal to noise ratio in B is significantly higher than in A, the peaks present in the spectra are similar.

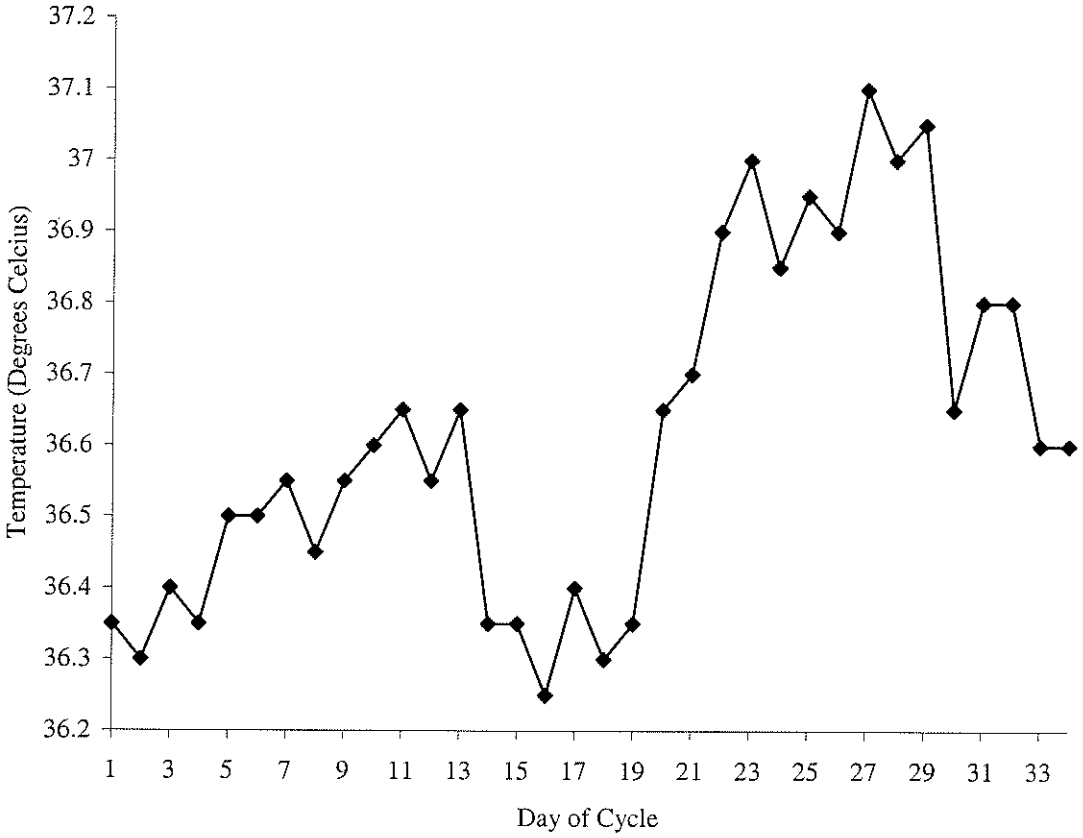

Figure 3.22: Basal body temperature measured each morning through one menstrual cycle (34 days long). Day one corresponds to the first day of menses. Ovulation occurred on day 22, as confirmed by the MR images and the rise in luteinizing hormone.

MR spectra were also obtained from five follicular cysts on healthy ovaries. These cysts were all less than 5cm in diameter and were therefore not considered abnormal. A representative image and the corresponding spectrum obtained from one of these follicular cysts is shown in Figure 3.23. The spectra from the cysts were similar, showing an intense peak at 1.3ppm.

Figure 3.23: T_2-weighted coronal image of a 4.5x3x3cm^3 follicular cyst on the right ovary and the corresponding MR spectrum with voxel size 20x20x20mm^3.

One woman who participated in the study was found to have polycystic ovaries (Figure 3.24A). Her ovaries were approximately twice the average size of a healthy premenopausal ovary and had numerous small (<0.5cm diameter) follicular cysts. The diagnosis was confirmed by a radiologist. The water suppressed spectrum obtained from the right ovary is displayed in Figure 3.24B. A spectrum with no water suppression obtained from the same voxel as in Figure 3.24B is displayed in Figure 3.24C. The intensity of the peak at 1.3ppm is equivalent to the intensity of the water peak at 4.7ppm. In healthy ovaries, the peak at 1.3ppm was either much less intense (approximately one tenth the intensity) than the water peak or could not be seen when no water suppression was applied.

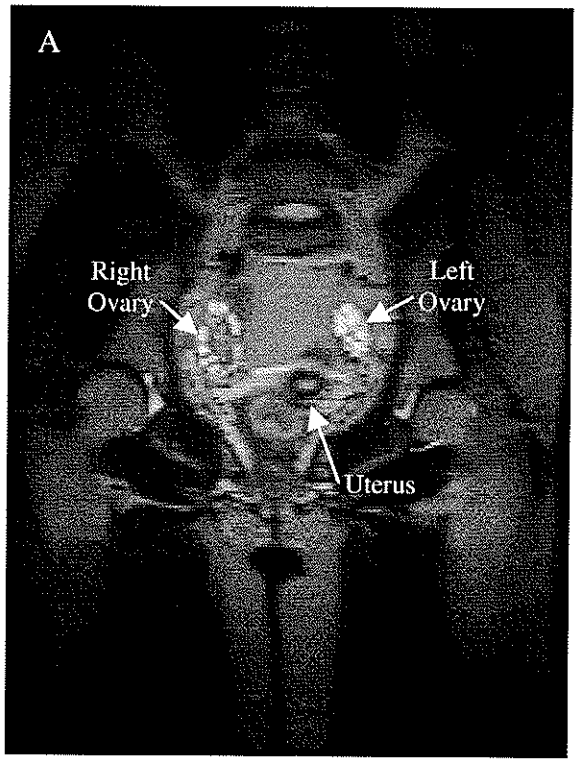

Figure 3.24: (Continued on next page) A) T_2-weighted coronal image of a polycystic ovary showing multiple small follicular cysts.

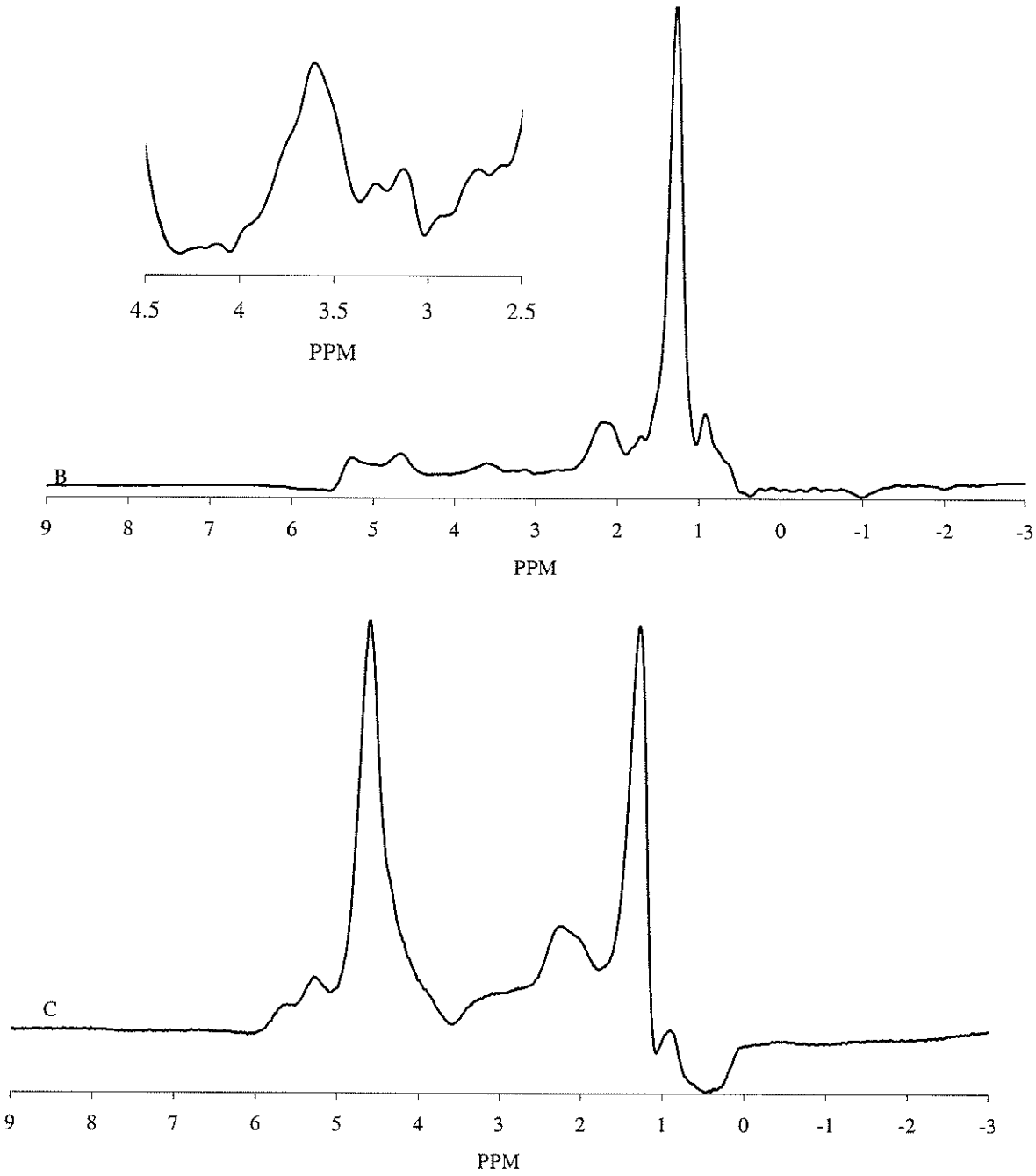

Figure 3.24: (Continued from previous page) B) water suppressed spectrum from the right ovary with expansion of the region between 2.5ppm and 4.5ppm, and C) water spectrum showing a peak at 1.3ppm with intensity equivalent to the water peak (4.7ppm). Voxel = 14x14x23mm^3.

One woman entered the study with no *a priori* knowledge of ovarian abnormalities. The images revealed that the left ovary was approximately one and a half times larger than the right ovary (Figure 3.25A). The presence of follicular cysts on the left ovary suggested that the ovary was functional. The MR spectrum of the left ovary was dominated by a peak at 1.3ppm (Figure 3.25B). Subsequent T_1-weighted images and fat saturated images confirmed the presence of a dermoid cyst (Figures 3.25C and D). Compare the spectrum in Figure 3.25B to the spectra in Figures 3.26A and B. These spectra were obtained from the ovaries of another woman referred to the study by a gynecologist. This woman was diagnosed with a 5cm diameter growth on her left ovary suggestive of a dermoid cyst. The T_2-weighted MR image showed this growth as a medium intensity growth with internal hypo-intense structures (Figure 3.27A). It was of medium intensity on the T_1-weighted and fat saturated images (Figures 3.27B and C respectively). The right ovary was of intermediate intensity in the T_2-weighted image (Figure 3.28A). The T_1-weighted image revealed a region of high intensity on the right ovary (Figure 3.28B) and the fat saturated image (Figure 3.28C) showed the same region with low intensity. Upon surgical removal, the presence of a dermoid cyst on the left ovary was confirmed. The right ovary was not removed, so post-surgical diagnosis was obtained. The MR spectra from the right ovary and the dermoid cyst on the left ovary are given in Figures 3.26A and B, respectively. The spectrum from the right ovary (Figure 3.26A) is similar to the spectrum in Figure 3.25B. The spectrum from the left growth (Figure 3.26B) is significantly different than those of Figures 3.25B and 3.26A.

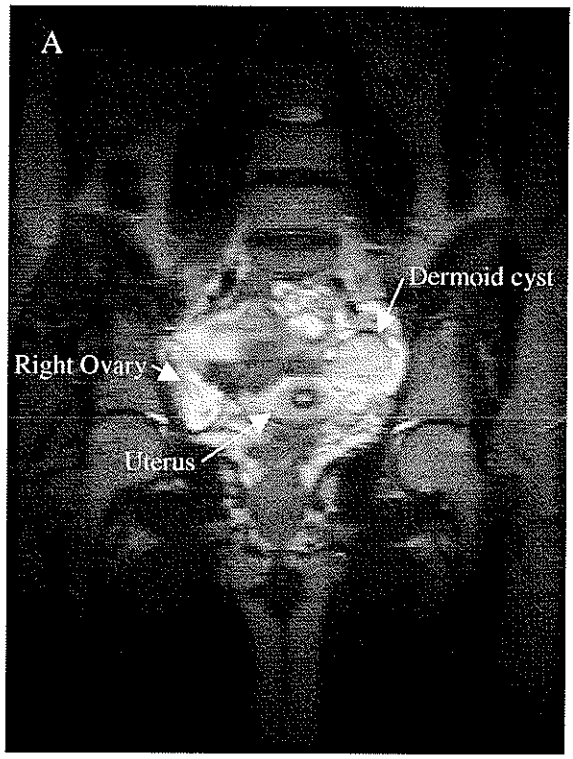

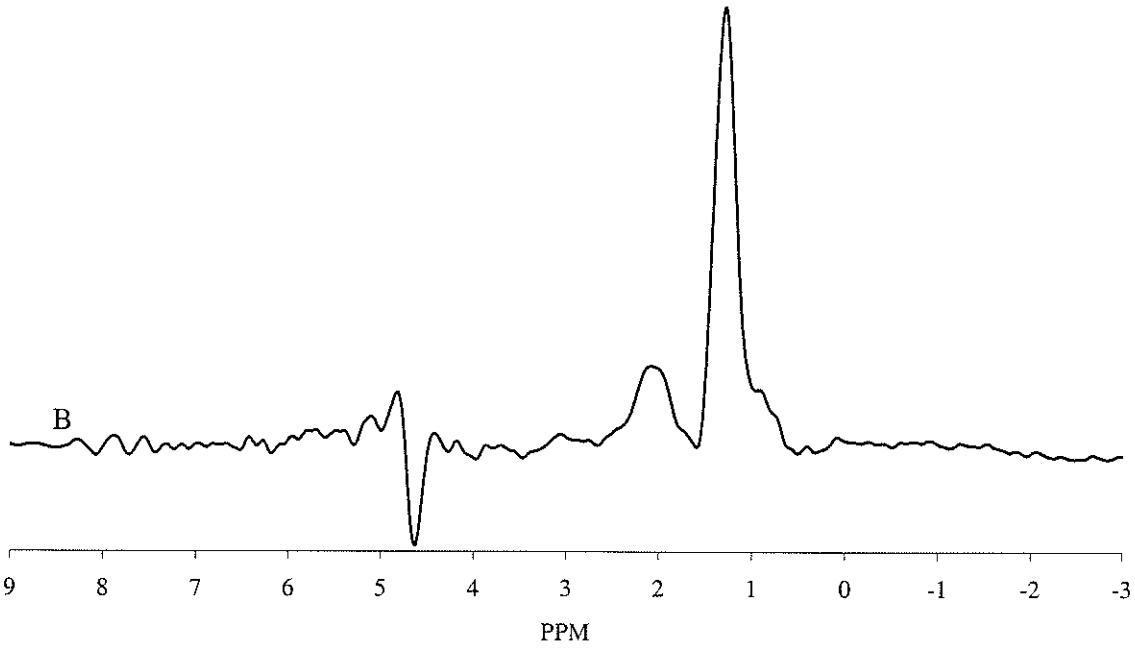

Figure 3.25: (Continued on next page) A) T_2-weighted image of a premenopausal women with a 3x3x3cm^3 left ovary. B) MR spectrum of the left ovary. Voxel size = 18x15x18mm^3. C) T_1-weighted image, and D) fat saturated image of the left ovary.

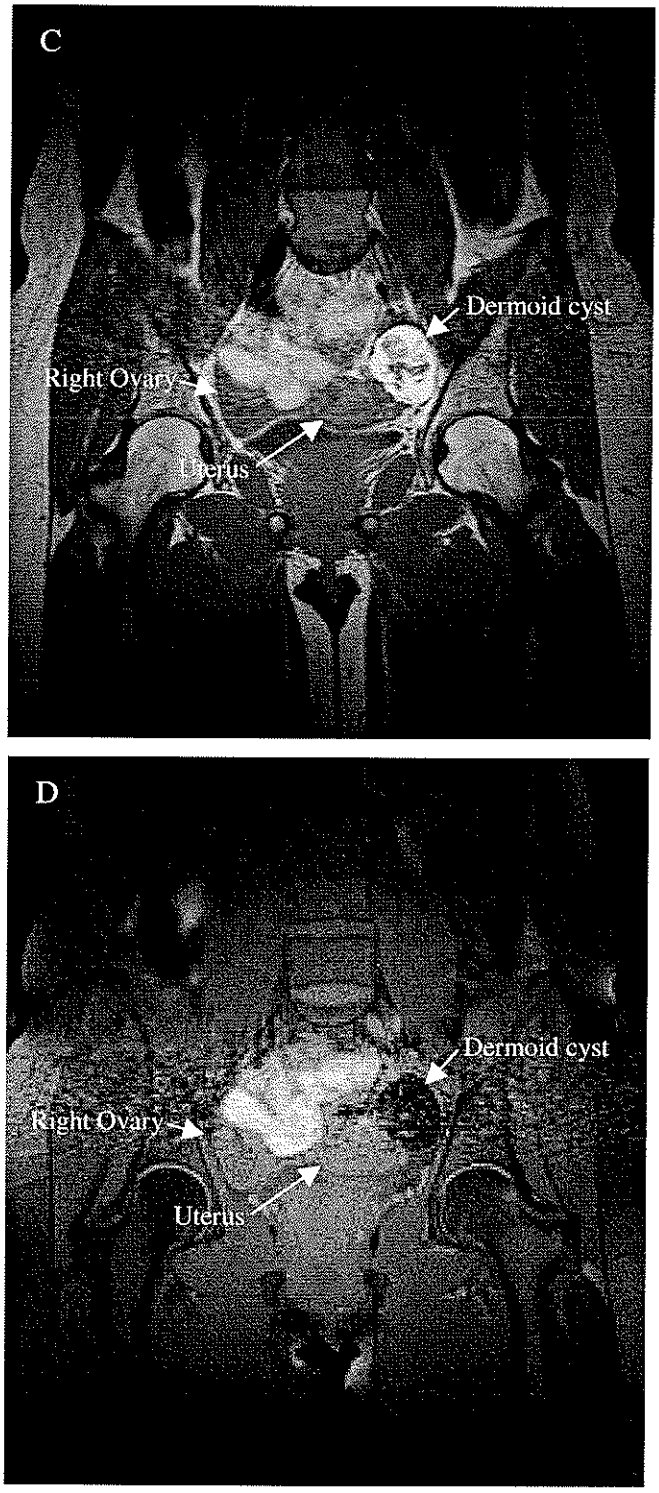

Figure 3.25: (Continued from previous page) C) T_1-weighted image, and D) fat saturated image of the left ovary.

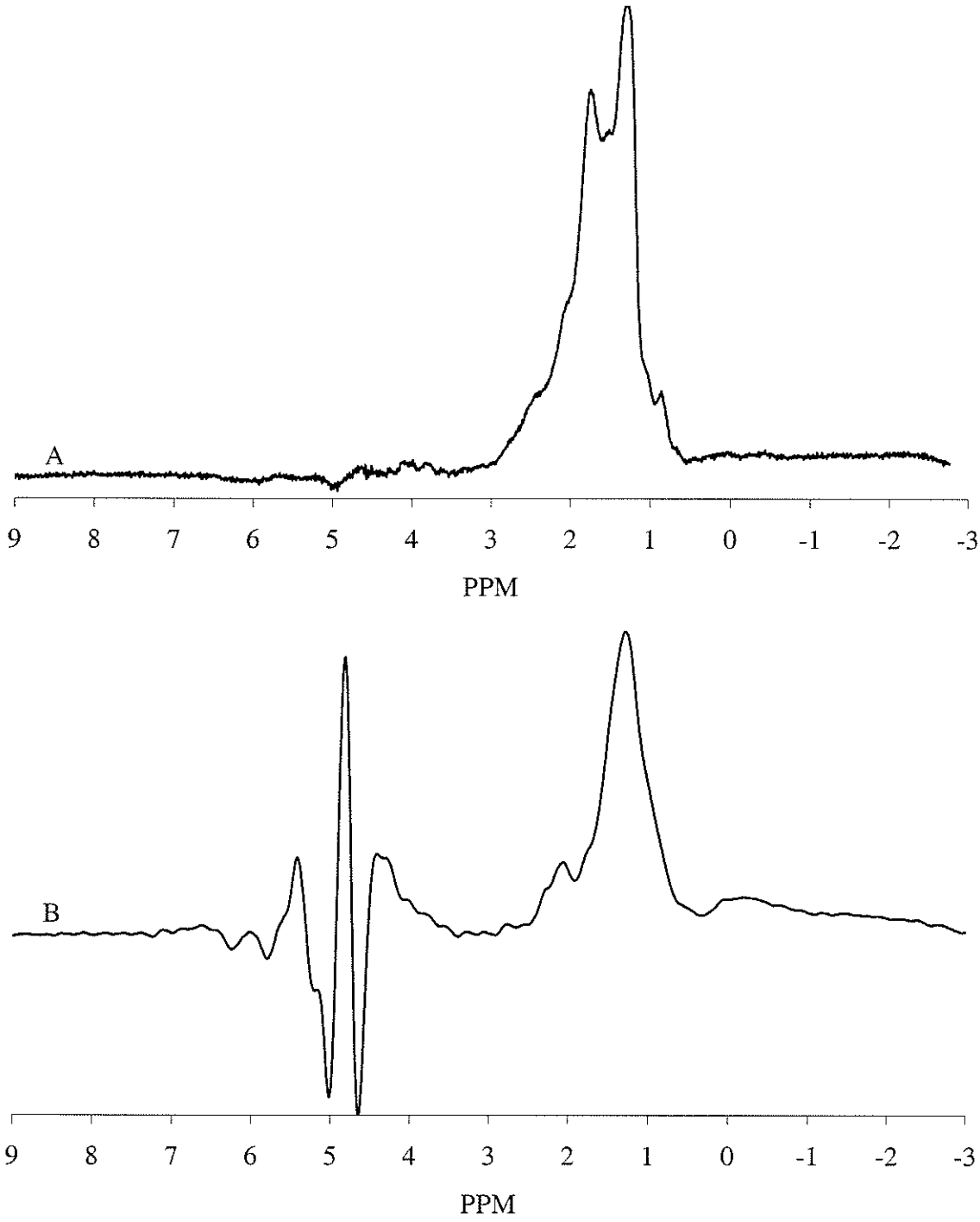

Figure 3.26: MR spectra from a woman with dermoid cysts on both ovaries. Spectrum A is from the cyst on the right ovary, and B is from the cyst on the left. (Images are displayed in Figures 3.27 and 3.28.)

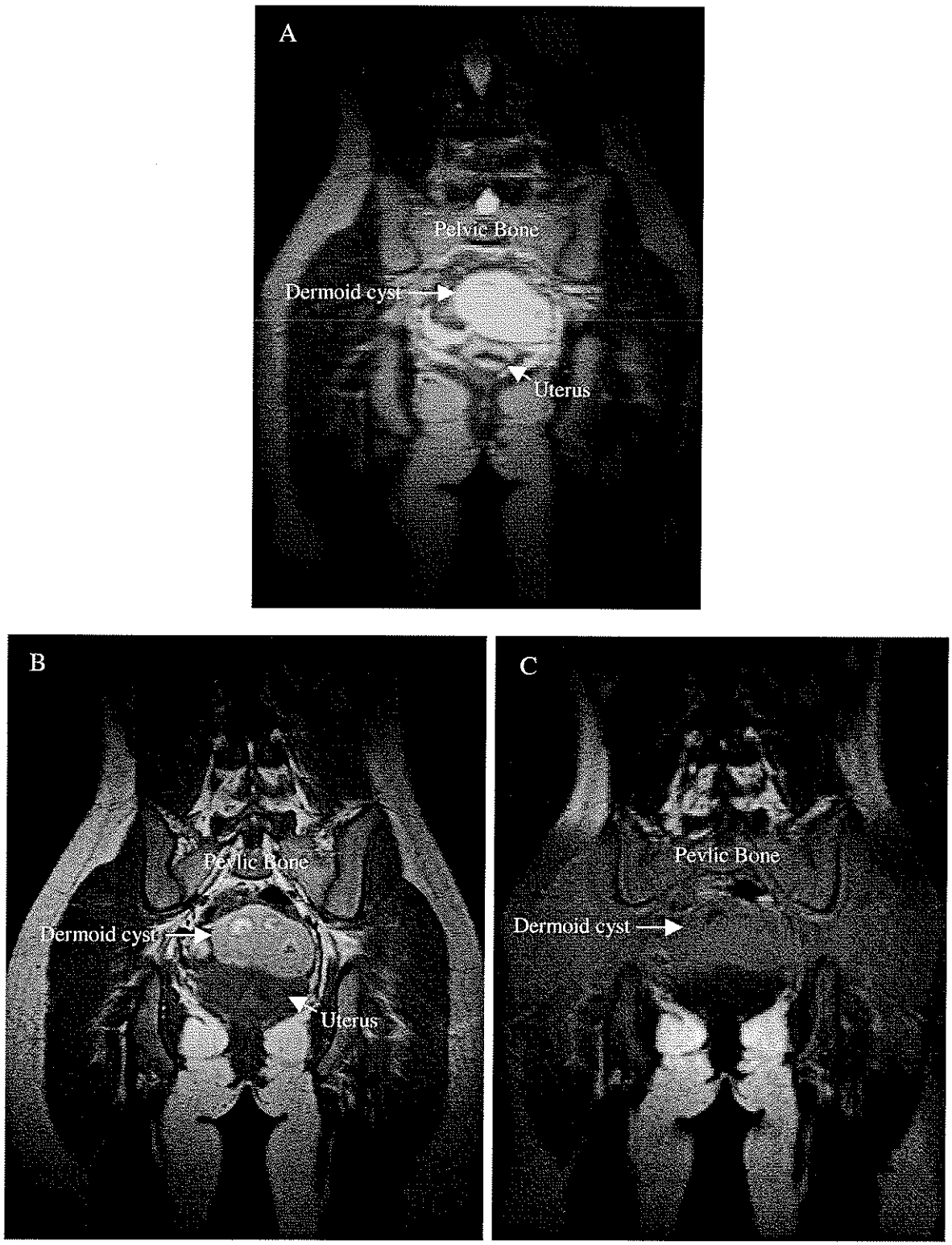

Figure 3.27: A) T_2-weighted, B) T_1-weighted, and C) fat saturated MR images of a dermoid cyst on the left ovary. (The spectrum from the dermoid cyst is displayed in Figure 3.26B.)

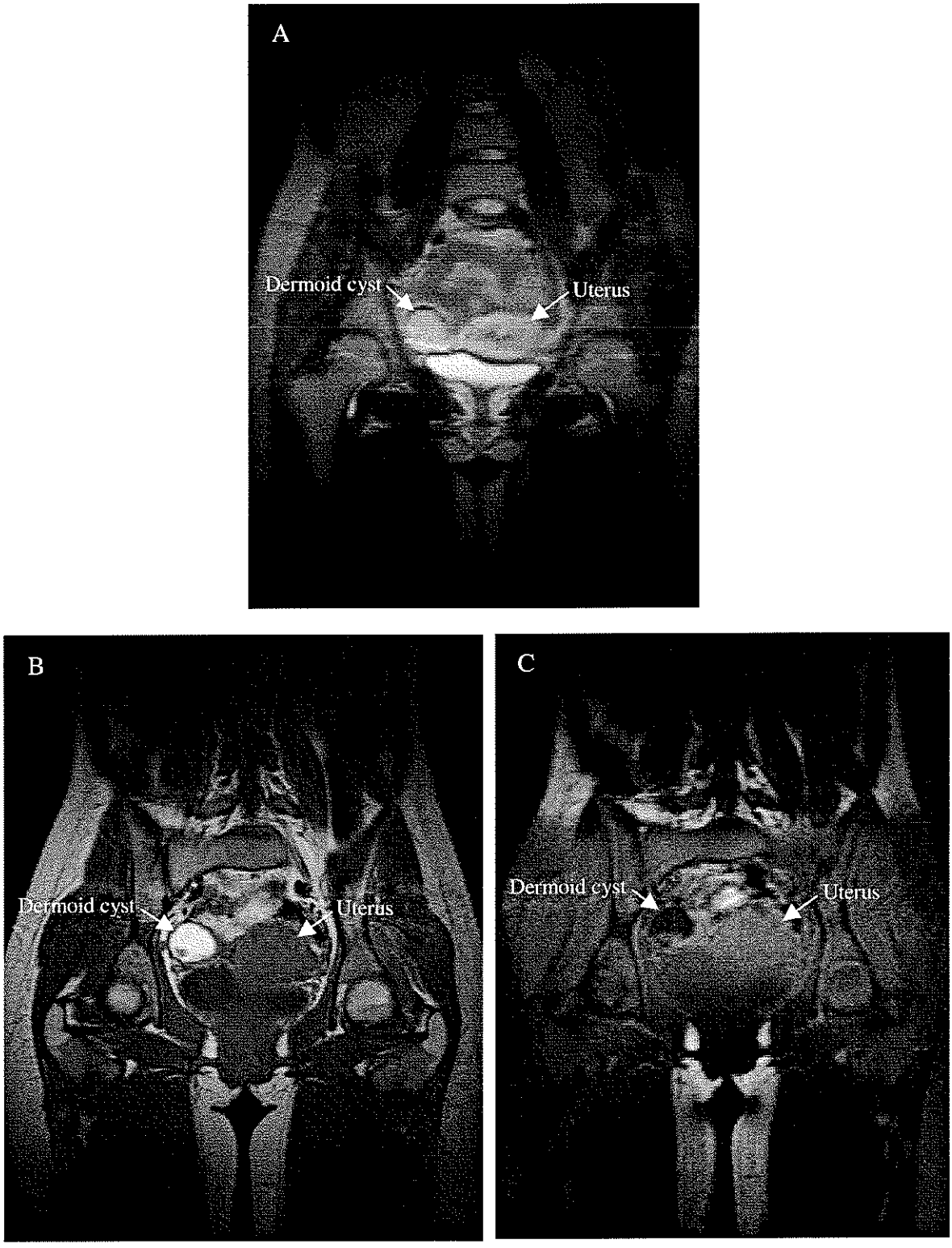

Figure 3.28: A) T_2-weighted, B) T_1-weighted, and C) fat saturated MR images of a dermoid cyst on the right ovary. (The spectrum from the dermoid cyst is displayed in Figure 3.26A.)

Finally, a woman with a 10cm malignant ovarian tumour was referred to the study by a gynecologist. The tumor had multiple cystic and solid components. The cystic components were hyperintense and the solid components were medium to low intensity in the T2-weighted images (Figure 3.29A). A spectrum obtained from the solid portion of the tumour labelled in Figure 3.29A with an asterisk is displayed in Figure 3.29B. No motion of the tumour occurred during spectral acquisition, so repositioning of the voxel was not required. The baseline of the spectrum drops below zero in several places and it is difficult to determine which are true peaks in the spectrum. After acquisition, it was learned that the power supplies to two of the gradients were unstable. Further, the rf shield surrounding the magnet was compromised. Many pieces of hospital equipment emit rf signal that resonate around 60MHz, which is close to the resonance frequency of the magnet (64MHz). This signal may have leaked through the faulty rf shield and was received by the cp spine coil within the magnet during spectral acquisition.

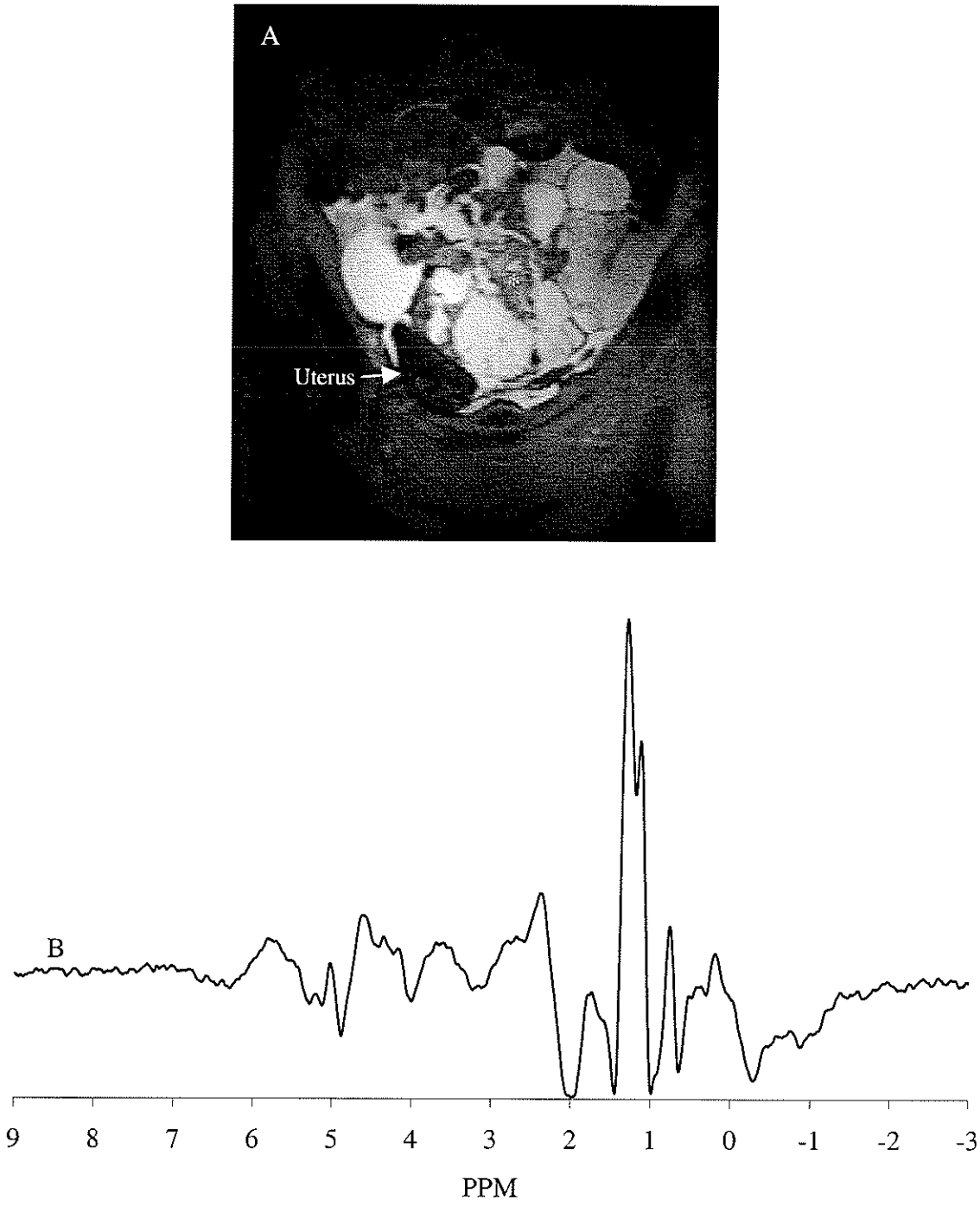

Figure 3.29: A) T_2-weighted image of a 10cm malignant ovarian tumour with cystic and solid portions. B) MR spectrum obtained from the solid portion of the tumour labeled in A with *. Voxel size = 15x15x20mm^3.

3.7 Discussion

3.7.1 Coils

Three coils manufactured by Siemens were tested to determine their suitability for MRI and MRS of the human ovary. The signal to noise ratios measured at the center of the static magnetic field for the Helmholtz-type volume coil, the circularly polarized spine coil, and the whole body coil are listed in Table 3.3. The Helmholtz-type coil is clearly superior to the other two coils in terms of the signal to noise ratio. The signal to noise ratio obtained for the Helmholtz-type volume coil was approximately double that for the cp surface coil. This may be attributed to the position of the voxel and the loading of the coils. For each of the three coils, the voxel was positioned at the center of the magnetic field. This corresponded to approximately the center of the whole body and Helmholtz-type coils. The signal to noise ratio obtained with a surface coil falls off with distance from the coil. In the case of the cp surface coil, the voxel was approximately 8cm away from the coil, so the signal to noise ratio measured was lower than might be expected nearer to the coil. Each of the three coils was loaded with the spherical phantom containing 0.1M acetate and 0.1M lactate. The cp surface coil and the whole body coil were also loaded with the body loader phantom. The Helmholtz-type volume coil was not loaded with the body loader phantom because it was too large and did not fit between the coils. While all three coils received noise from the volume of the spherical phantom that was outside the measured voxel, the cp surface and whole body coils also received noise from the whole body loader. This caused a decrease in the signal to noise ratio for the cp surface coil and the whole body coil. This accounted, in part, for the large difference in signal to noise ratio measured for the cp surface coil and the whole body

coil as compared to the Helmholtz-type volume coil. The whole body coil is much larger than the other two coils and its filling factor much lower, so a low signal to noise ratio was expected. Note that in a true Helmholtz coil, the upper and lower coils are separated by a distance equal to the radius of the coils. In this study, the separation was much greater. This resulted in a less homogeneous B_1 across the diameter of the coil.

Plotted in Figure 3.4 are the signal intensities at time zero of the absolute magnitude water FID's measured along the x-, y-, and z-axes. Because the noise acquired would remain constant, the signal to noise ratios along the axes would follow the same trends as seen in these plots of signal intensities. The relative intensity of the signal received by the whole body coil is relatively uniform across all three axes. Generally, the signal was also lower than the other two coils. As the voxel approached the edges of the Helmholtz-type volume and cp spine coils along the x- and z-axes, the intensities measured for each of these coils and the whole body coil became similar. Since the ovaries were rarely positioned further than 60mm off center along the x-axis and 30mm along the z-axis, voxels were not positioned in the region where the acquired signal intensity would be equivalent for each of the three coils. The signal falloff along the x- and z-axes for the Helmholtz-type volume coil was more severe than that measured for the cp spine coil. The optimal signal would be obtained if the Helmholtz-type volume coil was positioned such that the ovary was precisely in the center of the upper and lower coils, but the coils were not large enough to position in such a way that both ovaries were relatively close to the center of the coil. It is essential to examine both ovaries, particularly in premenopausal women, since the ovaries take turns ovulating and may not

give equivalent MR spectra on a single day of the menstrual cycle. As a result, the falloff of the signal at the edges of the coils was an important parameter. Despite the more rapid drop in the signal intensity with distance from the center for the Helmholtz-type volume coil, this coil was clearly superior to the cp spine and whole body coils along the x- and z-axes.

The signal intensity along the y-axis was significantly different than that measured along the x- and z-axes. Along the y-axis, the signal intensity obtained from the Helmholtz-type volume coil was consistently greater than that obtained from the whole body coil. In the case of the Helmholtz-type volume coil, as the voxel was positioned at increasing distances from the center of the static magnetic field, it approached the top or bottom coil. At these positions, the reception of the coil became similar to that of a surface coil. As expected, the signal intensity measured with the cp spine coil along the y-axes decreased as the distance of the voxel from the coil increased. At distances greater than 15mm, the whole body coil was superior to the cp spine coil, but at distances less than -45mm, the cp spine coil was superior to the Helmholtz-type volume coil. Typically, the ovaries did not lie at the center of the static magnetic field and did not lie in the center of the woman's pelvis. Whether the optimal signal with respect to the y-axis was obtained using the cp spine or Helmholtz-type volume coil was dependent on the position of the ovaries within the pelvis. For example, for women with small pelvises whose ovaries were not positioned in the center of the pelvis, the cp surface coil would be superior to the Helmholtz-type volume coil.

The minimum signal intensity along the y-axis for the Helmholtz-type volume coil did not occur at the center of the static magnetic field. This was due to the position of the coil on the patient bed. The center of the volume coil did not coincide with the static magnetic field's center. Note also that the plot of signal intensity along the x-axis for the cp spine coil is not symmetric about the magnetic field's center. The signal received by a surface coil, or the coil's B_1 field distribution, is assymetric with respect to the plane defined by the axis of the surface coil and the static magnetic field (Keltner *et al.* 1991). In the case of the cp spine coil, this plane lay along the x-axis, and this may account for the observed assymetry.

Typically, surface coils are used for studying anatomical features that are close to the surface of the body since a large penetration depth is not required in these cases. Because the penetration depth of a surface coil is proportional to the diameter of the coil (Keltner *et al.* 1991), as the required penetration depth increases, the diameter of the coil must also increase. The signal to noise ratio, however, decreases as the diameter of the coil increases because the coil acquires noise from a larger area. For this reason, studies of anatomical features deep within the body are best performed using a volume coil. Since the ovaries are situated deep within the pelvis, the optimal signal to noise ratio would be obtained in an MRS study of the ovaries by using the Helmholtz-type volume coil. Further, the two coils of the Helmholtz-type volume coil manufactured by Siemens are mounted in such a way that the separation between them can be adjusted to fit the patient. Unfortunately, the maximum possible separation between the coils is 28.5cm. Many healthy women with no known pelvic abnormalities do not fit within this

separation. Abnormalities within the pelvis commonly cause distension of the pelvis and abdomen, and many women who have ovarian cancer also suffer from collection of fluid, or ascites, in the pelvis that causes further distension of the pelvis. The separation of the Helmholtz-type coils is not sufficient to encompass the pelvis of a woman with a pelvic abnormality. While the inner diameter of the whole body coil (57cm) is large enough for almost all patients, the signal to noise ratio is poor. The cp spine coil was found to have a signal to noise ratio twice that of the whole body coil. Since the cp spine coil is a receive only coil and the whole body coil is the transmit coil, excitation of the nuclei deep within the pelvis is relatively uniform. This eliminates the non-uniformity of excitation and penetration problems associated with transmit surface coils. Further, the cp spine coil does not exclude larger women from the study. The cp spine coil was chosen for this MRS study of the ovaries.

3.7.2 Imaging

In order to obtain the maximum signal to noise ratio from the ovaries using the cp spine coil, it was essential that the coil be positioned to lie directly beneath the ovaries. Since the exact position of the ovaries could not be determined prior to imaging, the coil was initially placed approximately in the location of the ovaries. The initial scout images obtained using the FISP sequence (Figure 3.5) were not of sufficient resolution to determine the exact location of the ovaries. The resolution was, however, sufficient to locate the uterus. It was assumed that the ovaries were located on either side of the uterus. Based on this assumption, the cp spine coil was adjusted to lie directly beneath the uterus. The coil is mounted on a track beneath the patient table, and its position can

be adjusted precisely without the need to first remove the coil from the center of the magnet. This allowed rapid repositioning of the coil without moving the patient.

In nulliparous women, the assumption that the ovaries are lateral to the uterus is normally accurate, but in women who have been pregnant at least once, the assumption is more commonly inaccurate. During pregnancy, the ligaments in the pelvis, and particularly the ligaments which secure the position of the uterus such as the broad ligaments, stretch. After pregnancy, these ligaments do not necessarily tighten and return to their original position. This not only causes a relocation of the ovaries, but the stretched ligaments are no longer taut, which allows an increased ability of the ovary to move within the pelvis. Displayed in Figure 3.6 are six images that illustrate the variability of the location of the ovaries. Figures 3.6A and E show the ovaries lateral to the uterus as would be expected in a nulliparous woman. In parous women, the ovaries may be located superior and adjacent to the uterus as in Figures 3.6B and C. In some women, the ovaries are not adjacent to the uterus but are displaced cranially as in Figure 3.6D. In these cases, positioning of the coil directly beneath the uterus was not equivalent to positioning of the ovaries directly above the center of the coil. In these cases, the coil was repositioned a second time in order to ensure that the ovaries were directly above the coil and optimal signal to noise would be obtained in the spectroscopy portion of the study.

The position of the ovaries was also dependent on the position of the uterus. Displayed in Figure 3.6F is a transverse image showing the uterus rotated and shifted to

the left. Lateral displacement of the uterus may cause the ovary to be pushed to a position superior to the uterus. Rotation of the uterus as in Figure 3.6F causes the ovaries to be displaced posteriorly and anteriorly. The angle at which the uterus is tilted has a significant effect on the position of the ovaries and this was important to the MRS portion of the study. If the uterus is anteverted and minimal stretching of the pelvic liagments has occured, the ovaries typically lie anterior to the center of the pelvis, but if the uterus is retroverted, the ovaries lie posterior to the center of the pelvis. Because the signal acquired using a surface coil falls off with distance from the coil along the y-axis (Figure 3.4), the best signal to noise ratio was obtained when the ovaries were situated as close to the cp spine coil as possible. This required that women with anteverted uteri be placed in a prone position, and women with retroverted uteri be placed in a supine position.

Since the position (anteverted or retroverted) of the uterus and the location of the ovaries was unknown prior to imaging of the pelvis, and because scout images did not have adequate resolution for identification of the ovaries, optimal positioning of the patient with respect to the surface coil required high resolution imaging. From these images, the location of the ovaries could be determined allowing precise repositioning of the cp spine coil. Further imaging would then be required to determine the new location of the ovaries with respect to the coil. This protocol was not followed for several reasons. First, repositioning and re-imaging would add between five and fifteen minutes to the total experimental time depending on how many sets of images were required to locate the ovaries. Clinical imaging systems are typically overtaxed with waiting periods of up

to half a year for non-critical scans. If MR spectroscopy of the ovaries is to be used clinically as a diagnostic method, it is necessary to minimize the total experimental time. Further, the healthy patients who participated in this study complained of stiffness after lying motionless in the magnet for extended periods, and often could not refrain from moving near the end of the study. Patients with pelvic abnormalities or other health problems such as arthritis or back problems, which were common in the postmenopausal patients, were less likely to be able to lie still for the entire study. In order to maintain the relevance of spectroscopy of the ovaries as a clinically diagnostic technique, as well as to ensure patient compliance, the total experimental time was minimized by not repositioning the cp spine coil after location of the ovaries unless the ovaries were displaced from the center of the coil along the z direction (i.e. superior to the uterus) by more than 5cm. Since the ovaries were normally located approximately at the center of the pelvis, changing the patient's position from prone to supine or *vice versa* would have produced only a minimal improvement in the signal to noise ratio.

Due to the small size of the ovaries, MR image slices must be contiguous and thin in order to locate the ovaries. Large gaps between the imaged slices may result in positioning of the slices such that the ovaries fall within the gaps, and therefore obviously can not be located in the images. The ovaries can also be isointense with the bowel depending on the contents of the latter. Displayed in Figure 3.7 are T_1- and T_2-weighted images that show cross sectional views of the bowel. In the T_2-weighted image (Figure 3.7A), the bowel appeared round and isointense with the central portion of the ovary. Normally, the ovaries of premenopausal women were easily distinguished from

bowel due to the high intensity follicular cysts on the margins of the ovaries. In some premenopausal women, however, follicular cysts were not present on the ovaries after ovulation and prior to menses, and postmenopausal women typically did not have any follicular cysts on their ovaries. In these cases, it was difficult to differentiate the ovaries from bowel in the T_2-weighted images. The T_1-weighted image in Figure 3.7B illustrates the ovary and bowel as low intensity structures. The bowel loops around the ovary making it difficult to distinguish the margins of the ovary. The acquisition of contiguous slices made it possible to follow the loops of the bowel through the slices. The ovary was distinguishable from bowel because it did not extend through multiple slices. Thin slices were required in order to obtain high resolution of small structures, such as the ovaries, in the images. Due to motion in the pelvic region and the complexity of structures within the pelvis, imaging using thin (4mm), contiguous slices yielded images with unacceptable signal to noise ratios. To overcome this problem, two sets of nine images each were acquired with gaps between the slices that were equal to the slice thickness. The second set of slices were positioned between the gaps of the first set of slices. This, along with interleaved excitation of the slices within each set of nine images eliminated the cross excitation that occurs with acquisition of contiguous slices. Unfortunately, the acquisition of two sets of slices was done at the expense of a two-fold increase in the total acquisition time. The use of thin slices also resulted in less signal than would be obtained with thicker slices. While this allowed finer resolution of small structures, such as the ovaries, it also resulted in a reduction in the signal to noise ratio. Improved signal to noise was obtained by increasing the number of acquisitions for each slice from one to

four in the T_2-weighted images, and two in the T_1-weighted images. This was done at the expense of four-fold and two-fold increases in the total acquisition times.

Despite these improvements in the images, the ovaries of postmenopausal women were particularly difficult to locate. This was due to the lack of follicular cysts on the ovaries as well as the fact that ovaries shrink during and after menopause. The T_1-weighted Spin Echo sequence was used to obtain transverse images of the pelvis in postmenopausal women. These images were superior to the T_2-weighted images for locating the broad ligaments. The broad ligaments were of low to intermediate intensity in the T_2-weighted images, making them difficult to differentiate from the isointense pelvic fat and bowel. In the T_1-weighted images, the broad ligaments were of low intensity which was in sharp contrast to the high intensity pelvic fat. Since the ovaries are attached to the posterior side of the broad ligament, a thickening of the broad ligament corresponded to the location of the ovary. Unfortunately, this method of locating the ovaries in postmenopausal women was not always successful. Figure 3.8 illustrates three T_1-weighted images obtained from the pelvises of postmenopausal women. In some women, the ovary was identified by an obvious thickened portion of the broad ligament as in Figure 3.8A. In other women, the ovary was located in an image that did not contain the broad ligament (Figure 3.8B), or did not show a thickened portion of the broad ligament (Figure 3.8C). In some cases, the position of the ovary was confirmed by acquiring both T_1- and T_2-weighted images. For example, when the ovary was adjacent to the uterus, its location was difficult to determine because the ovary and uterus are both of low intensity in the T_1-weighted images (Figure 3.9A). When the ovary was identified

adjacent to the uterus, its margins were not clearly visualized in the T_1-weighted images. In these cases, both T_1- and T_2-weighted images were acquired. Figure 3.9A shows a transverse T_1-weighted image with a region of low intensity adjacent to the uterus. The T_2-weighted image displayed in Figure 3.9B confirms that this structure is the right ovary because it appears with higher signal intensity than the myometrium of the uterus, and lower intensity than the same region in the T_1-weighted image. The ovaries were successfully identified in only 10 of the 17 postmenopausal women who participated in the study. This low success rate was expected because the literature states that identification of the ovaries of postmenopausal women is normally difficult (Reviewed in Occhipinti 1994, Occhipinti *et al.* 1993, Pierson *et al.* 1994).

3.7.3 Spectroscopy

Traditionally, *in vivo* MRS has been performed in the brain and in large organs such as the liver and kidney. The relative homogeneity of these regions of the body allows good shimming that gives rise to narrow line widths and well resolved metabolite peaks in the spectra. More importantly, these regions of the body are relatively stationary. In regions of the body where there is a great deal of movement, such as in the pelvis, measurement using MRS is more complicated.

Respiratory motion was observed in the MR images obtained in this study as blurring of the image in the region of the abdomen (Figure 3.10A). The effects of respiratory motion on MRS would be to cause the ovary to move in and out of the defined voxel. The effects on the spectrum acquired are dependent on the time during which the

motion occurred. First, if motion occurred prior to the initial excitation of the spins, the spectrum would be acquired from tissue outside of the ovary, potentially resulting in peaks in the spectrum from biochemicals that are not present in the ovaries. Second, if motion occurred during excitation of the spins, refocussing would be incomplete if the ovary moved partially outside of the defined voxel, or refocussing would not occur if the ovary moved completely outside of the defined voxel. In the first case, the signal to noise ratio would be decreased in the spectrum. In the second case, no signal would be acquired, so there would be no peaks in the spectrum. Finally, if motion occurred during acquisition of the FID, the peaks in the spectrum would be broadened. Since respiratory motion is a slow process as compared to the time required for excitation of the spins and acquisition of the FID, it is probable that motion would occur prior to excitation, during excitation, and during acquisition. The effects on the MR spectrum would be a combination of the effects observed as a result of motion at all three times. The amount of respiratory motion observed was dependent on whether the patient tended to breath by expanding her chest or her abdomen. Placing the patient in a prone position caused slight pressure on the anterior pelvic wall. This encouraged expansion of the chest rather than the abdomen and thus reduced the up and down motion of the pelvis caused by respiration. While prone positioning of the patients was preferred, many women were not comfortable lying prone. These women were positioned supine. Respiratory motion could be reduced by placing gentle restriction across the pelvis in the form of restraining belts. Because respiratory motion is cyclic, its effects could be further reduced by respiratory gating of the STEAM sequence. It was found that this was unnecessary because normally, the ovaries were positioned deep within the pelvis. Respiratory motion

occurred superior to the pelvis, being confined to the chest and abdomen. Thus, respiratory motion should have little or no effect on MRS of the ovaries, since the images showed no effect.

Flow artifact was also seen in the MR images (Figure 3.10B) from the femoral arteries which pass through the pelvis and into the legs. This artifact was most apparent in the transverse slices and was seen as bands of high intensity that crossed the pelvis and extended beyond the outer wall of the pelvis. The flow of blood past the voxel defined for spectroscopy could cause the local magnetic field experienced by the spins in the ovary to change with time as the amount of ferromagnetic blood in the artery increased and decreased slightly with pulsation. This would cause broadening of the spectral peaks. It is unlikely that pulsation of the artery would cause the ovary to move unless the ovary were positioned immediately adjacent to the artery, but even in this case, motion of the ovary would be minimal. In any event, the femoral arteries typically lie in the anterior portion of the pelvis while the ovaries are located more posterior. Cardiac gating may have minimized the effects of the flow, but because there was a significant separation between the ovaries and the femoral arteries, the effects of pulsation of the femoral arteries had minimal, if any effect on the spectroscopic measurement of the ovaries.

While the effects of respiratory motion and pulsation of the femoral arteries had virtually no effect, motion of the urinary bladder had a significant effect on MRS of the ovaries. Because the ovaries are situated superior to the urinary bladder, as the bladder fills, the ovaries are displaced in a cranial direction (Figure 3.11). Several factors

influence the amount of displacement of the ovaries and the speed at which displacement occurs. First, ovaries that were situated immediately adjacent to and above the bladder often experienced approximately 2cm of displacement over a 90 minute study. The ovaries of women with retroverted uteri tended to be positioned posterior to the bladder, and thus, filling of the bladder caused either a very small displacment (<5mm), or no displacement of the ovaries. Second, the speed at which the bladder filled, and thus the amount of displacement which occurred during the study period, was dependent on the amount of liquid the patient had ingested prior to the study. A high liquid intake resulted in rapid and extensive filling of the bladder. Women were encouraged to minimize their liquid intake on the day of the study. While this did not eliminate filling of the urinary bladder, it did decrease the speed at which the bladder filled resulting in slower and less displacement of the ovaries. It was also noted that the speed at which the bladder filled was dependent on the time of day during which the study was performed. The urinary bladder tends to fill less quickly at night than during the day, so the ovaries of women who participated in the study after 10:00pm were normally displaced less throughout the course of the study than the ovaries of women who participated earlier in the day.

The effect on the MRS study of displacement of the ovaries due to filling of the urinary bladder was to move the ovary partially or completely out of the voxel defined by the slice selective gradients and rf pulses. This resulted in acquisition of the spectrum from a region not on the ovary. Commonly, the bladder extended such that the position of the voxel defined at the outset of the study was within the urine in the bladder near the end of the study (Figure 3.11). In order to acquire the spectrum solely from the ovary, it

was necessary to move the voxel as the ovary moved, ensuring that the voxel was always within the ovary. If the speed at which the bladder filled was constant and measurable, and if the direction of displacement of the ovary was known, it would have been possible to coordinate gradual movement of the voxel with the motion of the ovary. Unfortunately, the speed at which the bladder filled was not constant, and thus could not be predetermined. The ovaries, therefore, were not displaced at a constant speed. Also, the direction of displacement of the ovary did not occur in a single direction and was not uniform. The direction of motion of the ovary was dependent, in part, on its location with respect to the uterus. The direction of displacement of ovaries that were located posterior to the uterus and/or did not have direct contact with the uterus was unpredictable. In these cases, movement of the ovaries was dependent on the motion of the other structures within the pelvis, such as the bowel. In some cases, there was no movement of the ovaries. Ovaries that lay immediately superior to and in direct contact with the uterus tended to move in a cranial direction, and in many cases moved simultaneously in a posterior direction. Because the bladder often did not fill uniformly, one side of the bladder could have more urine than the other. This resulted in different rates of displacement for the left and right ovaries. Also, the liquid within the bladder was not stationary. Hence, the ovary could be displaced cranially for a period of time as one side of the bladder filled more quickly than the other, followed by caudal displacement as the urine flowed to the other side of the bladder. Clearly, the direction and speed of displacement of the ovaries due to filling of the urinary bladder can not be predicted. It was necessary to develop a method of tracking the motion of the ovaries.

Coordination of movement of the voxel with the motion of the ovary was accomplished by scout imaging between spectroscopic acquisitions. The high resolution turbo spin echo sequence and the spin echo sequence, initially used to obtain images for the purpose of locating the ovaries, were shortened by decreasing the number of slices imaged from nine to three, reducing the repetition time (TR), and reducing the number of acquisitions per slice by half. The spin echo sequence used for postmenopausal women was further modified by decreasing the matrix size such that the number of phase encoding gradients was reduced. These modifications allowed acquisition of two sets of images with three slices each in just over one minute for premenopausal women, and just over two minutes in postmenopausal women. Two sets of images, one set in the coronal orientation and one in the transverse orientation, were required in order to precisely determine the location of the ovary along all three axes. Compare the image in Figure 3.11A that was obtained using the high resolution, long version of the turbo spin echo sequence to the image in Figure 3.11B that was obtained using the faster, shortened version of the same turbo spin echo sequence. Note that the shortened sequence yielded a much poorer signal to noise ratio in the image and the contrast has changed as a result of the change in TR. Despite these changes, the ovary was easily identified because its approximate position was known from the previous images. Resolution and contrast were sacrificed in favour of speed. Based on these scout images, the voxel was repositioned to the new location of the ovary. This method of tracking the ovary allowed compensation for involuntary motion of the ovary caused by filling of the urinary bladder, and it had the added benefit of allowing compensation for small voluntary motions of the patient. Ideally, imaging should be performed before each acquisition, but the time

required for such a protocol would be formidable. Consider the premenopausal case. Assuming that two sets of TSE images, repositioning of the voxel, and a single acquisition of the FID using STEAM could be obtained in two minutes, it would take 4 hours, 16 minutes to obtain a FID with 128 averaged acquisitions. The study of postmenopausal ovaries would require a longer time because the SE sequence used for the scout images had twice the acquisition time as the TSE sequence. Obviously, this would not be practical in a clinical setting, and the patient could not be expected to lie motionless for this length of time. Typically, the ovary moved less than 3mm over a five minute period. Thus, it was found that scout imaging after every 32 acquisitions of the FID was sufficient to ensure that the voxel remained within the ovary at all times. In cases where the ovary was positioned away from the bladder and minimal or no displacement occurred, scout imaging was performed after every 64 acquisitions. The total time required to obtain a FID with 128 acquisitions was between 15 minutes and half an hour, depending on the amount of motion of the ovaries.

It should be noted that shimming was performed on the voxel only after the initial imaging and locating of the ovaries, but before the beginning of spectral acquisition. Shimming was not repeated during the spectral acquisition after movement of the voxel to compensate for motion of the ovaries. Additional shimming was not performed in part because the added time required was unacceptable, but mainly because the ovary continued to move during the shimming procedure. Thus, by the end of shimming, the ovary could have once again moved out of the defined voxel. Maximum homogeneity of the magnetic field was sacrificed in order to ensure that the voxel remained within the

ovary during spectral acquisition. In theory, only small changes in the spectra should be observed as a result of small displacements of the voxel since optimal shimming of the magnetic field within the voxel should lead to an improvement in the homogeneity of the field in the vicinity of the voxel. Experimentally, it was found that minimal, if any, improvement was obtained by shimming after moving the voxel by amounts that were typically less than 1cm.

Filling of the urinary bladder not only caused displacement of the ovaries, but in some cases, it also caused rotation of the ovaries. In Figure 3.11B, the long axis of the right ovary has rotated by approximately 20^{O} from its original orientation at the beginning of the study (Figure 3.11A). While the voxel may have been entirely within the ovary at the beginning of the study, rotation of the ovary during the study could cause the voxel to lie partially outside the ovary near the end of the study. This is illustrated in Figure 3.30. Consider the oval shape of a slice through an ovary as illustrated in Figure 3.30A with a rectangular box contained within the oval. The box is maximized such that it is as large as possible without extending outside of the oval. If the oval is rotated (Figure 3.30B) similar to the rotation of the ovary caused by filling of the urinary bladder, the rectangular box is no longer contained within the oval. Compensation for rotation of the ovary could be achieved either by setting the length, width, and height of the voxel to the smallest dimension of the ovary, or by adjusting the size of the voxel as the ovary moved to ensure that the voxel was always contained within the ovary. In this study, the former method was used.

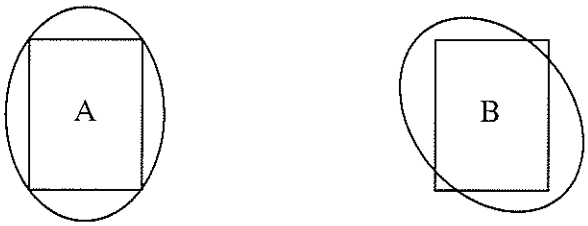

Figure 3.30: An oval representing an ovary with A) a rectangular box representing the voxel maximized to be as large as possible while remaining within the oval, and B) the rectangle extending outside of the oval after rotation of the oval, similar to rotation of the ovary caused by filling of the urinary bladder.

The final type of motion within the female pelvis that required consideration for the MRS study of the ovaries was the motion of the bowel. Peristalsis of the bowel occurs as the muscular walls of the bowel contract and relax to propel the contents along the bowel (Miller and Keane 1987). The contractions associated with peristalsis are normally irregular in intensity and frequency, but contractions typically cause only a few millimeters of motion in the walls of the bowel. The intensity and frequency of peristaltic contractions can be reduced, but not eliminated, by fasting (Private communications with Dr. Tedros Bezabeh and Dr. Charles Bernstein). Antispasmodic agents such as hyoscine butylbromide (trade name Buscopan) can be administered to temporarily stop peristalsis, but the potential side effects include discomfort, visual disturbances, and an increased pulse rate (Gillis 1998). The bowel is often adjacent to and in contact with the ovary. While precise determination of the effects of peristalsis on the MRS study of the ovaries could only be determined by performing the study with and without paralysis of the

bowel, it is unlikely that the small peristaltic motion would cause the ovary to move, and therefore would not affect spectroscopic measurements of the ovaries (Private communications with Dr. Tedros Bezabeh and Dr. Charles Bernstein). Conversely, the contents of the bowel had a significant effect.

As solid contents of the bowel were propelled through portions of the bowel adjacent to the ovary, they may have caused slight variations in the local magnetic field experienced by the ovary. This would result in broadening of the metabolite peaks in the MR spectra. As with the effects of peristalisis, the effects of the solid contents of the bowel on the MRS study could be minimized by fasting of the patient prior to the study or by paralysis of the persitaltic motion of the bowel. While the effects could be determined by performing the MRS study with and without paralysis of the bowel, the narrow line widths obtained in many of the spectra suggest that the passage of the solid contents of the bowel had minimal, if any, effects on the homogeneity of the local magnetic field at the ovary.

Gas was normally seen in the bowel, and when the gas was situated in a portion of the bowel adjacent to the ovary (Figure 3.12), large changes were observed in the MR spectra. The gas produced a tissue to air interface at the surface of the ovary that resulted in local magnetic field inhomogeneities due to the extremely different magnetic susceptibilities of gas and tissue. Shimming was difficult, and in some cases, yielded no improvement in the shape and intensity of the FID. The magnetic field inhomogeneities resulted in an increase in the line widths of the peaks in the spectra. Displayed in

Figures 3.13A and 3.13C are the water peaks of spectra obtained from ovaries of two women with and without gas in the adjacent bowel. Note the much broader peak in Figure 3.13C. Gas in the bowel also caused frequency shifting of the peaks between acquisitions and differences in the phases of the individual acquisitions. Each acquisition in Figures 3.13A and 3.13C was frequency shifted to align the water peaks, phased, and then averaged to obtain Figures 3.13B and 3.13D, respectively. These corrections had little effect in the absence of gas (compare Figures 3.13A and 3.13B). The full width at half maximum (FWHM) line width of the water peak decreased by 8% of the original line width (original line width = 3.10Hz, and corrected line width = 2.86Hz). Conversely, the corrections yielded a significant reduction of 37% in the FWHM line width of the water peak when gas was proximal to the ovary (original line width = 32.29Hz, and corrected line width = 20.24Hz).

The variations in the frequency shifts and phases of the individual acquisitions were caused by motion. As the ovary moved due to filling of the urinary bladder, it experienced slight changes in the local magnetic field, ΔB_{local}, due to inhomogeneities in the magnetic field. Slight variations in the local magnetic field also occurred as the contents of the bowel passed the ovary. The frequency (ω) and phase (ϕ) of the spins is dependent on the local magnetic field according to:

$$\omega = \gamma(B_o + \Delta B_{local})$$

$$\phi = \gamma B_o t + \int \gamma \Delta B_{local} dt + \int \gamma G_x x dt$$

where γ is the gyromagnetic ratio of the spins, B_o is the static magnetic field, ΔB_{local} is the change in the local magnetic field experienced by the spins, G_x is the magnetic field gradient along an axis x, x is the position of the spins, and t is the time of precession. While frequency shifts and phase differences were observed in spectra obtained from ovaries with no gas in the adjacent bowel, the differences between acquisitions were more extreme in cases where gas was proximal to the ovary. Because gas in the bowel was not stationary, the local magnetic field inhomogeneities caused by the different magnetic susceptibilities at the tissue to air interface changed more dramatically than when gas was not present. This accounted for the larger frequency shifts and phase changes between acquisitions that were observed when gas was proximal to the ovary.

Similar frequency and phase variations were observed by Star-Lack *et al.* (1998) in kidney and liver. The authors also reported improvements in the signal to noise ratio after frequency and phase corrections. In this study, however, the motion of the organ under study was not monitored, and thus, the voxel was not moved to compensate for motion. With large organs such as the kidneys and liver, large displacements do not normally occur, so motion may not pose a problem provided the organ is relatively homogenous and the voxel size is chosen to be small enough. Star-Lack *et al.* (1998) used the partially suppressed water peak in the spectrum as the reference for their frequency and phase corrections. Frequency and phase corrections applied to the individual acquisitions obtained in this MRS study of the ovaries suggested that the residual water peak can not be used as the reference. This may be attributed to the partial suppression of the water peak which results in a line shape that is not truly Lorentzian.

Displayed in Figure 3.15 are three spectra obtained from a healthy, premenopausal ovary. The three spectra originate from the same data, but different corrections have been applied. No frequency and phase corrections were applied to the spectrum in Figure 3.15A. In Figure 3.15B, the residual water peak was used as the reference peak for the frequency and phase corrections, and in Figure 3.15C, the metabolite peak at 1.3ppm was used as the reference. Significant differences between the corrected spectra were observed in the shift of the metabolite peaks as well as their relative intensities (Figures 3.15B and 3.15C). The effects of the frequency and phase corrections were dependent on which peak (water or metabolites) was used as the reference. Further evidence of this was observed in the individual acquisitions. For clarity, the data are displayed in Figure 3.16 as four spectra averaged over 32 acquisitions each, rather than a plot of each of the 128 acquisitions. The effects of partial water suppression on the residual water peak are dependent on the frequency at which suppression is applied with respect to the frequency of the water peak, and the line width of the water peak. In order to use the residual water peak as the reference for corrections, it must be assumed that the peak is approximately Lorentzian and that changes in its phase and frequency correspond to equivalent changes in the metabolite peaks. The results of this study negate this assumption. When the frequency shifts and phases of the residual water peak in each acquisition were optimized, the relative frequency shifts and phases of the metabolite peaks in each acquisition varied (Figure 3.16A). Similarly, when the frequency shifts and phases of the metabolite peaks were optimized, the relative frequency shifts and phases of the residual water peaks varied. For the purpose of this study, frequency and phase corrections could not be

applied using the residual water peak as the reference. Rather, the metabolite peaks were used as the reference.

The frequency shifts and phases applied to the individual acquisitions of the averaged spectrum displayed in Figure 3.15C are plotted in Figure 3.17. Typically, the frequency shifts and phases of the individual acquisitions were similar within each set of 32 acquisitions. The data were acquired in sets of 32 acquisitions. After acquisition of each set, the voxel was repositioned to account for the movement of the ovary. With each new position, the voxel experienced a slightly different local magnetic field due to magnetic field inhomogeneities, which resulted in different relative frequency shifts and phases for each set of 32 acquistions. In cases where the signal to noise ratio of the metabolite peaks in a single acquisition was too low to accurately frequency shift and phase correct, the acquisitions were averaged over each set of 32. Each averaged set of 32 was frequency shifted and phase corrected, and then the individual acquisitions were examined. Only individual acquisitions with sufficient signal to noise were further corrected. The frequency shifts and phases plotted in Figure 3.17 that are constant within each set of 32 acquisitions were obtained for acquisitions that either required no further corrections or had insufficient signal to noise ratios to allow further corrections. Since the frequency shifts and phases of each acquisition within a set of 32 were similar, further corrections to the individual acquisitions normally yielded small improvements in the signal to noise of the final, averaged spectrum.

MRS of the postmenopausal ovary is difficult due to its small size. Very small voxel sizes were required in order to ensure that the voxel was entirely inside the ovary. This resulted in a low signal to noise ratio. In some cases, the required voxel size was so small that insufficient signal was obtained. In these cases, the voxel size was increased such that the corners of the voxel were outside the ovary and thus, a small portion of the acquired signal was obtained from the tissue surrounding the ovary. The usefulness of this data is questionable since the signal from the surrounding tissue could give rise to peaks in the spectra that would not be observed if the signal was purely from the ovary. If used for diagnostic purposes, these peaks could be mistaken for abnormalities in the ovaries. Conversely, since the majority of the signal was obtained from the ovary, the contributions from the surrounding tissue may be small enough to have minimal effect on the spectrum. The effects of the signal acquired from the surrounding tissue could be determined by comparing spectra obtained from postmenopausal ovaries that were large enough to contain the voxel to spectra obtained from voxels in the same ovaries that were slightly larger than the ovary. Higher magnetic field strengths and improved rf coils may allow smaller voxel sizes that would be entirely within small ovaries while still providing sufficient signal to noise. No differences were observed in the spectra obtained from postmenopausal women in this study, but only 10 spectra were obtained. A larger number of spectra are required to determine if there are any differences between the spectra. A representative spectrum with good signal to noise obtained from a postmenopausal ovary that was large enough to contain the voxel is displayed in Figure 3.18.

Both ultrasound and MRI are able to image the development of follicular cysts through the menstrual cycle (Brown *et al.* 1994, Occhipinti *et al.* 1993, Pierson *et al.* 1994b). Displayed in Figure 3.19 are six T_2-weighted images of a female pelvis corresponding to six days in one menstrual cycle. The follicular cysts appear with characteristic high signal intensity, as expected (Table 3.2), and grow through the follicular phase of the cycle with the dominant follicle easily visualized on the day before ovulation (Figures 3.19A-C). After ovulation, it is not normally possible to distinguish between the follicular cysts and a non-hemorrhagic corpus luteal cyst because their MR appearances are identical in both T_1- and T_2-weighted images. If hemorrhaging occurs in the corpus luteal cyst, its T_1-weighted appearance changes from low/intermediate intensity, to intermediate/high intensity, thus allowing differentiation from follicular cysts (Semelka *et al.* 1997). Because the focus of this study was on the MRS and not the MRI, visualization of the corpus luteum was not attempted. Determination of the day of ovulation was accurately determined in 6 of the 8 women who participated in the study through use of the urine test for the surge in LH. The day of ovulation was missed in two women due to irregular menstrual cycles. In these women testing for ovulation was started after ovulation occurred. While measurement of the woman's basal body temperature was not essential for determination of the day of ovulation (Figure 3.22), it was useful in confirming the results of the urine test.

Because it is much less expensive, ultrasound is normally used rather than MRI for visualization of the changes in the ovaries through the menstrual cycle. Neither ultrasound nor MRI, however, has the ability to monitor biochemical changes in the

ovaries through the menstrual cycle. The technique developed in this study to acquire MR spectra of the ovaries measures the biochemical content of the ovaries. Representative spectra obtained from one woman on six days during one menstrual cycle are displayed in Figure 3.20. The six days chosen from the cycle were those on which the most significant changes in hormonal concentrations and morphology occurred (Figure 3.1). The spectra are dominated by a peak at 1.3ppm. No significant differences were noted between the spectra obtained on the six different days of one menstrual cycle for each of the women who participated. While hormonal changes differ significantly during the menstrual cycle (Figure 3.1) and remain relatively constant after menopause, these changes would not be seen in the MR spectra because the concentrations of the hormones are normally on a nanomolar level which is too low to be detected with MRS at 1.5T. While it is possible that no MR observable differences exist in the biochemical content of the ovaries through the menstrual cycle and after menopause, it is also possible that the signal to noise ratio of the spectra was not sufficient to resolve differences in the spectra. No peaks were observed in the region from 3.0ppm to 4.0ppm of the spectra displayed for the postmenopausal ovary (Figure 3.18) or the premenopausal ovary (Figure 3.20). Note, however, that in the spectrum acquired on the day of ovulation in Figure 3.21B, obtained from a different woman than that of Figure 3.20, the improved signal to noise in the spectrum shows a few small peaks present between 3.0ppm and 4.0ppm. The signal to noise ratio of these peaks was not sufficient for any analysis. This study should be performed at higher magnetic fields with improved coils in order to improve the signal to noise ratio.

In two *ex vivo* studies (Mackinnon *et al.* 1995, and Wallace *et al.* 1997), high resolution spectra acquired from biopsies of malignant ovarian tumours were found to be dominated by peaks at 1.3ppm and 0.9ppm. These peaks were assigned to the lipid methylene and methyl groups, respectively. Spectra from healthy ovaries and benign ovarian tumours also contained these peaks, but they were less intense. Similar peaks were observed in this *in vivo* study, but the *ex vivo* studies showed additional peaks in the spectra that were not observed in the *in vivo* study. Mackinnon *et al.* (1995) found that a simple analysis of the ratios of peak intensities at 3.0ppm to 1.7ppm and 1.7ppm to 1.3ppm could be used to differentiate malignant tumours from benign tumours and healthy ovarian tissue. Using linear discriminant analysis, Wallace *et al.* (1997) determined that the peak at 1.3ppm was not diagnostic of malignancy, but could be used to differentiate spectra obtained from untreated and recurrent ovarian tumours. Both of these analyses relied on less intense metabolite peaks between 2.0ppm and 4.0ppm. Resonances in this region of the spectra obtained from healthy ovaries were either poorly resolved or not visible in the *in vivo* study performed here. This may be due to the lower signal to noise ratio, or it may be due to the type of tissue examined. Different types of tissue give rise to different MR observable biochemical fingerprints (Brière *et al.* 1995, Moreno *et al.* 1993). The *ex vivo* studies examined epithelial tissue, while the voxel placed on the ovary in the *in vivo* study contained virtually no epithelial tissue.

The tissue surrounding the ovaries is typically rich in lipids as evidenced by the regions of high signal intensity surrounding the ovaries in the T_2-weighted images. Excitation and subsequent acquisition of signal outside the defined voxel could result in

leakage of signal into the spectrum from non-ovarian tissue. Because gradient magnetic fields, G_x, were applied during excitation, resonances from metabolites that are located a distance Δx from the voxel experience a shift in their resonance frequencies, $\Delta \nu$, according to:

$$\Delta \nu = \frac{\gamma}{2\pi} G_x \Delta x$$

The three rf excitation pulses of the STEAM sequence were applied at the frequency of the water resonance, but metabolites outside the voxel whose resonant frequencies were shifted by an amount such that their resonances were equal to that of the water were also excited. At the time of acquisition, no gradients were applied, so the acquired resonances of excited metabolites external to the voxel were equivalent to those of the same metabolites within the voxel. This would result in a false increase in the intensity of peaks. Metabolites external to the voxel that did not exist within the voxel could also give rise to unexpected peaks in the spectrum. This phenomenon is commonly referred to as chemical shift artifact. The separation between the water resonance and the lipid methylene resonance at 1.3ppm is 217Hz at a static magnetic field of 64MHz. In this study, the strength of the slice selection gradients was 4.0mT/m. Substitution of these values into the above equation gives Δx equal to 1.3mm. Hence, for a voxel placed on the ovary, the methylene group of the lipid molecules at a maximum distance of 1.3mm outside the voxel were excited and therefore contributed to the spectral peak at 1.3ppm.

Consider a two dimensional case with a square voxel, $1 \times 1 cm^2$, inside a circular ovary with a diameter of 1.5cm (Figure 3.31). At the middle of a side of the voxel, the

distance from the side to the edge of the ovary would be 2.5mm. Since the lipid methylene spins external to the voxel were excited at a maximum distance of 1.3mm, most of the excited spins external to the voxel were still within the ovary. The only lipid molecules outside of the ovaries that contributed to the spectrum were at the external corners of the voxel. Hence, lipid external to the ovaries contributed only minimally to the spectra, and the intense peak at 1.3ppm can be attributed mainly to molecules within the ovary.

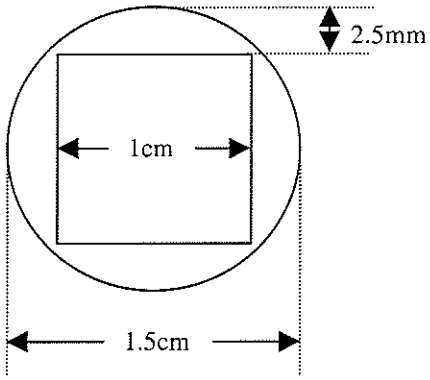

Figure 3.31: Two dimensional view of a 1x1x1cm^3 voxel inside a spherical ovary with diameter 1.5cm. Distance from the middle of one side of the voxel to the side of the ovary is 2.5mm.

Spectra were obtained from several follicular cysts that were large (≥ 2cm in diameter), but clinically normal (≤ 5cm in diameter). One of these spectra and the corresponding image are displayed in Figure 3.23. Similar to the spectra obtained from the healthy ovaries, these spectra were dominated by a peak at 1.3ppm. Less intense peaks at 0.9ppm and 2.0ppm, visible as shoulders to the 1.3ppm peak in Figure 3.23, and

at 5.2ppm are suggestive of a lipid spectrum. A broad peak appeared between 3.0ppm and 4.0ppm. It is not surprising that the spectra from these follicular cysts were similar to the spectra obtained from healthy ovaries because these cysts are not abnormal and thus, may have biochemical content similar to that of the ovaries.

MR spectra were also obtained from four women with ovarian abnormalities. The first of these was a woman who entered the study with no *a priori* knowledge of an ovarian abnormality. The MR images (Figure 3.24A) revealed numerous small (<0.5cm diameter) follicular cysts on both ovaries, and the ovaries were approximately twice the average size of healthy ovaries. These characteristics are consistent with polycystic ovarian disease. The MR spectrum obtained from the right ovary is displayed in Figure 3.24B. As with the spectra obtained from healthy ovaries, this spectrum is dominated by an intense peak at 1.3ppm. Less intense peaks at 0.9ppm, 2.0ppm, and 5.2ppm are consistent with the presence of lipid. Unlike the spectra obtained from healthy ovaries, the spectrum acquired from the polycystic ovary contains peaks in the region between 3.0ppm and 4.0ppm. Two distinct peaks occurred at 3.1ppm and 3.5ppm, while a third less intense peak was seen at 3.2ppm. The spectra displayed in Figures 3.24B and C were obtained from the same voxel, but no water suppression was applied to the spectrum in Figure 3.24C. Typically, the peak at 1.3ppm was either not seen, or was barely resolved in the water spectra obtained from healthy ovaries, but in Figure 3.24C, its intensity is almost equivalent to that of the water peak at 4.7ppm. The less intense peaks at 0.9ppm, 2.0ppm, and 5.2ppm, attributed to lipid, were also seen in the spectrum without suppression of the water resonance. This suggests that the

polycystic ovary contains more lipid than healthy ovaries. In order to determine the diagnostic significance of the intense lipid peaks as well as the less intense peaks between 3.0ppm and 4.0ppm, more spectra of polycystic ovaries must be obtained.

Dermoid cysts are composed mainly of lipids (Lewis and Chamberlain 1989, Sloane 1985). Hair growths and calcium deposits which are common to dermoid cysts would most likely not be seen in *in vivo* MR spectra, or would appear as very broad underlying peaks. Hence, an MR spectrum of a dermoid cyst should contain only lipid peaks. MRS was performed on two women with dermoid cysts. The first woman entered the study with a regular menstrual cycle and no knowledge of ovarian abnormalities. In the T_2-weighted images (Figure 3.25A), the left ovary was found to be larger than the right ovary, but it was not considered abnormal. The presence of follicular cysts was further suggestive of a normal, functioning ovary. The MR spectrum obtained from the left ovary was dominated by a peak at 1.3ppm (Figure 3.25B). The less intense peaks at 0.9ppm and 2.0ppm were suggestive of a lipid spectrum. While the signal to noise ratio is relatively high in this spectrum, no peaks were seen in the region between 3.0ppm and 4.0ppm. Because lipid has a short T_2 relaxation time, it appears with high intensity in T_1-weighted images. The left ovary was of high intensity in the T_1-weighted images (Figure 3.25C). Fat saturation images showed the left ovary with low signal intensity, which was also suggestive of high lipid content and thus, the diagnosis of a dermoid cyst.

The second woman was referred by a gynecologist. She had a 5cm diameter growth on her left ovary that was a suspected dermoid cyst. Images of the growth were

not consistent with a dermoid cyst. The growth appeared as a region of high intensity in the T_2-weighted images (Figure 3.27A). It was of intermediate intensity in T_1-weighted images, rather than the expected high intensity (Figure 3.27B). Fat saturation did not result in the expected low signal intensity in the growth (Figure 3.27C). While the images were not suggestive of a dermoid cyst, surgical removal of the growth confirmed that it was a dermoid cyst. The spectrum contained only peaks consistent with a lipid spectrum, as would be expected from a dermoid cyst (Figure 3.26B). Complete water suppression could not be obtained in the spectrum which suggested a high water content within the dermoid cyst. This is consistent with the fat suppression images where the signal from the cyst was not well suppressed by suppression of the fat resonance. The spectrum obtained from this dermoid cyst is similar to that obtained from the first woman (Figure 3.25B). The peaks obtained from the suspected dermoid cyst in Figure 3.26B are significantly broader than those in Figure 3.25B. This may be due to the inhomogeneities in the dermoid cyst of the spectrum in Figure 3.26B. These inhomogeneities, possibly attributable to calcium deposits and/or hair growths, were well visualized in the T_1-weighted image in Figure 3.27B.

A second dermoid cyst was detected on the right ovary of the woman who was referred to the study by a gynecologist. Images showed the intermediate signal intensity in T_2-weighted images (Figure 3.28A), high signal intensity in T_1-weighted images (Figure 3.28B), and low signal intensity in fat saturated images (Figure 3.28C) typical of a dermoid cyst. The spectrum obtained from the cyst, however, was not a typical lipid spectrum (Figure 3.26A). It consisted of two intense peaks at 1.3ppm and 1.7ppm. The

peak at 1.3ppm and the less intense shoulder peaks at 0.8ppm and 2.0ppm show that the spectrum contains lipid, but the intense peak at 1.7ppm is not typically from lipid. Note that shoulder peaks are seen at 0.8ppm, 1.1ppm, 2.0ppm, and 2.3ppm. The spectrum could be the combination of two lipid spectra with one spectrum shifted by 0.3 to 0.4ppm. It is possible that the lipid within the cyst is compartmentalized or that the lipid exists in two forms, one of which is less mobile. This could lead to the lipid spins resonating at two different frequencies and would result in two sets of lipid peaks, with the peaks from the more mobile lipids shifted to a slightly higher frequency. This dermoid cyst was not removed during surgery, so its exact composition is unknown.

Two of the three dermoid cysts examined in this study were correctly diagnosed using only MR imaging. Two of the MR spectra obtained from these three cysts contained intense lipid peaks. The third spectrum appeared to contain two lipid spectra with slightly different chemical shifts. While more spectra are required to determine the ability of MRS to diagnose dermoid cysts, the combination of MR imaging and spectroscopy may provide a more accurate diagnosis than MR imaging alone.

Finally, a woman with a 10cm diameter, malignant ovarian tumour was referred to the study by a gynecologist. The woman had begun chemotherapy treatments prior to her participation in the MR study. The T_2-weighted images showed a large tumour with many compartments (Figure 3.29). The tumour was highly cystic, as evidenced by the many high intensity compartments of the tumour. Fewer intermediate intensity regions associated with solid components of the tumour were also visualized. The uterus was

displaced to the right side of the pelvis by the tumour. An MR spectrum obtained from the solid component of the tumour labeled with an asterisk in the image of Figure 3.29A is displayed in Figure 3.29B. The baseline of the spectrum drops below zero, particularly in the region of the metabolite peaks. The main cause of this was probably the unstable power supplies for two of the gradients, but spurious signals due to the compromised rf shield may have also contributed. At any rate, the validity of this spectrum is questionable. While it is difficult to determine which peaks are real, there is definitely an intense peak at 1.3ppm. This is consistent with *ex vivo* studies (Mackinnon *et al.* 1995, Wallace *et al.* 1997) which showed that malignant ovarian tumours are dominated by lipids. Also, this woman was undergoing chemotherapy, which causes necrosis, or death, of the cells. Kuesel *et al.* (1994) found elevated lipid levels in necrotic brain tumour biopsies. The intense peak at 1.3ppm in the spectrum shown in Figure 3.29B may be due to areas of chemotherapy induced necrosis in the tumour.

3.8 Summary and Conclusions

The ovaries are located deep within the pelvis. Hence, use of a volume coil as the transmit coil is preferable to a surface coil because the volume coil ensures homogenous rf penetration to the required depth. It is important, however, to ensure that the volume coil is constructed with sufficient space within the coil to allow positioning of women with ovarian abnormalities that have distended pelvises. The receive coil must also penetrate to the required depth, and must achieve a high signal to noise ratio. It is important to determine the location of the ovaries and ensure that they are located within the center of the receive coil in order to obtain the best possible signal to noise. A surface coil may be used for reception, but it must have a large enough diameter to allow examination of both ovaries. Examination of one ovary, repositioning of the coil, and examination of the other ovary is too time consuming. For this study, the whole body coil was used as the transmit coil and the cp spine coil was used to receive.

T_2-weighted images were most suitable for identification of premenopausal ovaries due to the high signal intensity of follicular cysts. Postmenopausal ovaries were identified by a broadening of the broad ligaments. The broad ligaments and postmenopausal ovaries were best visualized in T_1-weighted images. Ovarian abnormalities were typically large, and thus were easily identified in both T_1- and T_2-weighted images. Dermoid cysts, however, may be mistaken for enlarged ovaries in T_2-weighted images, and T_1-weighted images and fat saturated images did not always allow accurate diagnosis of dermoid cysts.

Motion of the ovaries was caused predominantly by filling of the urinary bladder. Fast scout images were obtained periodically to track the motion of the ovaries. While the resolution of these images was low, the ovaries were easily visualized because their approximate location was previously determined by the high resolution images. Movement of the voxel defined by the STEAM sequence compensated for motion of the ovary and ensured that signal was obtained only from within the ovary. Motion within the pelvis causes frequency shifts and phase changes in the individual acquisitions of the FID. Correction of these shifts and phases prior to averaging improved the resolution of the peaks and the signal to noise ratio obtained in the spectra. *In vivo* MR spectra of the ovaries and ovarian abnormalities were dominated by an intense peak at 1.3ppm which probably originated from lipid. Those spectra that had high signal to noise also contained peaks between 3.0ppm and 4.0ppm which may be diagnostic of disease.

It is concluded that the techniques developed in this study allow *in vivo* acquisition of spectra from the healthy, human ovary as well as ovarian abnormalities.

3.9 Future Perspectives

Design of faster imaging sequences with high resolution would allow more rapid location of the ovaries at the beginning of the experiment, thus reducing the examination time. This would be beneficial in the clinical setting since clinical scanners are highly overtaxed and have long waiting lists. Also, shorter examination times mean that patients do not have to remain motionless for a long time, and this typically improves patient

compliance. Fast, high resolution imaging sequences could be used for the scout images that were required for tracking of the movement of the ovaries. This would allow more accurate coordination of the movement of the voxel with the displacement of the ovaries as the urinary bladder fills. Scout images could be acquired more frequently without a significant increase in the total examination time. Improvements in the resolution of the images may also allow automation of the movement of the voxel. Algorithms that detect the edges of structures in the images are available. These could be used to calculate the position of the ovary, and the new position of the voxel could be automatically adjusted.

The signal to noise ratio of the MR spectra obtained from healthy ovaries in this study was low due to the small size of the ovaries and their location deep within the pelvis. Improvements in the homogeneous penetration of B_1, the signal to noise, and filling factors of the rf coils would yield improvements in the signal to noise of the spectra, providing better resolution of low intensity peaks. Recent developments in phased array volume coils may make these coils suitable for this study (Stark and Haacke 1996, Takahashi *et al.* 1998). Further improvements in the signal to noise could be obtained at higher static magnetic fields. This would require design and construction of specialized coils, since the coils currently available for magnetic fields above 1.5T have been designed for studies of the head or anatomical structures near the surface of the body. Construction of a large diameter volume coil, such as a whole body coil, for high magnetic fields is complicated, because standard, large diameter, volume coil designs suffer from standing waves and rf penetration problems at these fields. This results in inhomogeneous rf magnetic fields. These coils require large rf power supplies which are

expensive, and due to the rf penetration problem, the increase in rf power may lead to unacceptable increases in the specific absorption rate (SAR), or the amount of power deposited in the patient.

This study involved the development of the techniques required to obtain accurate *in vivo* MR spectra of the ovaries. Multiple spectra must now be acquired from healthy ovaries and benign and malignant ovarian tumours to determine if the biochemical differences seen in *ex vivo* MR spectra (Mackinnon *et al.* 1995, Wallace *et al.* 1997) can also be seen in the *in vivo* spectra. Wallace *et al.* (1997) also found that the MR spectra obtained from untreated and recurrent ovarian tumour biopsy specimens contained different biochemical information. This suggests that *in vivo* MRS may be able to distinguish malignant ovarian tumours that respond to chemotherapy from those that do not. If this is true, *in vivo* MRS may be useful in the determination of treatment regimens for ovarian cancer patients.

Currently, the chemical changes associated with abnormalities such as polycystic ovarian disease and recurrent enlargement of follicular and corpus luteal cysts can only be determined by surgical removal of part or all of the ovary. MRS may provide a non-invasive method of analysis in these cases. The MR spectra may also provide insight into the causes of infertility and might allow determination of the effects of drugs, such as fertility drugs, on the ovaries. The technique developed here could also be used to obtain spectra from other structures within the pelvis. For example, abnormalities of the uterus, including uterine cancer and fibroids, could be studied using the MRS technique. The

uterus is also displaced as the urinary bladder fills, so scout imaging and movement of the voxel would be required as in the ovary study. Healthy fallopian tubes are too small to be examined using the current technology, but abnormalities on these anatomical structures may be large enough to study using MRS.

3.10 References

Abramowicz JS, Jaffe R, Pierson RA. Transvaginal color doppler ultrasonography in the assessment of uterine and ovarian blood flow. In *Imaging in Infertility and Reproductive Endocrinology*. R Jaffe, RA Pierson, JS Abramowicz, eds. Lippincott Company, Philadelphia, 1994, 167-169.

Adashi EY, Rock JA, Rosenwaks Z, eds. Reproductive Endocrinology, Surgery, and Technology. Lippincott-Raven Publishers, Philadelphia, 1996, 18-28.

Al-Took S and Tulandi T. Surgical management of polycystic ovarian syndrome: Laparoscopic ovarian drilling. *J. Soc. Obstet. Gynecol. Can.* **19**: 721-732, 1997.

Bäckström T, Nakata M, Pierson RA. Ultrasonography of normal and aberrant luteogenesis. In *Imaging in Infertility and Reproductive Endocrinology*. R Jaffe, RA Pierson, JS Abramowicz, eds. Lippincott Company, Philadelphia, 1994, 143-144.

Bomsel-Helmreich O and Al-Mufti W. Ultrasonography of normal and abnormal follicular development. In *Imaging in Infertility and Reproductive Endocrinology*. R Jaffe, RA Pierson, JS Abramowicz, eds. Lippincott Company, Philadelphia, 1994, 117-120.

Briére KM, Kuesel AC, Bird RP, Smith ICP. ^{1}H MR visible lipids in colon tissue from normal and carcinogen-treated rats. *NMR Biomed.* **8**: 33-40, 1995.

Brown HK, Hazelton TR, Parsons AK. Magnetic resonance imaging of the normal female pelvis. In *Imaging in Infertility and Reproductive Endocrinology.* R Jaffe, RA Pierson, JS Abramowicz, eds. Lippincott Company, Philadelphia, 1994, 238-241.

Canada Communication Group: Canadian Cancer Incidence Atlas. Ottawa, Canada, Vol.1, 1995.

Clement PB. Anatomy and histology of the ovary. In *Blaustein's Pathology of the Female Genital Tract.* RJ Kurman, ed. Springer-Verlag, New York, 3rd ed. 1987a, 438.

Clement PB. Nonneoplastic lesions of the ovary. In *Blaustein's Pathology of the Female Genital Tract.* RJ Kurman, ed. Springer-Verlag, New York, 3rd ed. 1987b, 486.

Evers JLH and Heineman MJ. Gynecology: A clinical atlas. C.V. Mosby Company, St. Louis, 1990, 108.

Friedman WN, Perlman ES, Rosenfield AT. Computed tomography of normal and abnormal female pelvic anatomy. In *Imaging in Infertility and Reproductive Endocrinology.* R Jaffe, RA Pierson, JS Abramowicz, eds. J.B. Lippincott Company, Piladelphia, 1994, 292-294.

Gillis MC, ed. Compendium of pharmaceuticals and specialties. Webcom Limited, Toronto, Ontario, 33rd ed. 1998, 230-231.

Gray H. Gray's Anatomy. TP Pick and R Howden, eds. Bounty Books, New York, 1977, 1028-38.

Haase A, Frahm J, Hanicke W, Matthaei D. 1H NMR chemical shift selective (CHESS) imaging. *Phys. Med. Biol.* **30**: 341-344, 1985.

Hart WR. Pathology of malignant and borderline (low malignant potential) epithelial tumors of ovary. In *Gynecologic Oncology.* M Coppleson, ed. Churchill Livingstone, Edinburgh, 2nd ed. Vol. 2, 1992, 863-865, 870, 875.

Hearn-Stebbins B, Jaffe R, Brown HK. Ultrasonographic evaluation of normal pelvic anatomy. In *Imaging in Infertility and Reproductive Endocrinology.* R Jaffe, RA Pierson, JS Abramowicz, eds. Lippincott Company, Philadelphia, 1994, 9-13.

Hillier SG, ed. Ovarian Endocrinology. Blackwell Scientific Publications, Oxford, 1991, 1-19, 134-7.

Hoskins WJ. Primary surgical management of advanced epithelial ovarian cancer. In *Ovarian Cancer.* SC Rubin and GP Sutton eds. McGraw-Hill Inc., New York, 1993, 241-242.

Hricak H and Carrington BM. MRI of the pelvis; A text atlas. Martin Dunitz Ltd., London, 1991, 188-189.

Jaffe R, Mesonero CE, Eggers PC. Ultrasonography of abnormal pelvic anatomy. In *Imaging in Infertility and Reproductive Endocrinology.* R Jaffe, RA Pierson, JS Abramowicz, eds. Lippincott Company, Philadelphia, 1994, 32-40.

Jansen RPS. Oncological endocrinology. In *Gynecologic Oncology.* M Coppleson, ed. Churchill Livingstone, New York, 1992, 140-143.

Keltner JR, Carlson JW, Roos MS, Wong STS, Wong TL, Budinger TF. Electromagnetic fields of surface coil *in vivo* NMR at high frequencies. *Magn. Reson. Med.* **22**: 467-480, 1991.

Kuesel AC, Kroft T, Prefontaine M, Smith ICP. Lipoprotein(a) and CA125 levels in the plasma of patients with benign and malignant ovarian disease. *Int. J. Cancer* **52**: 341-346, 1992.

Kuesel AC, Sutherland GR, Halliday W, Smith ICP. ^{1}H MR spectroscopy of high grade astrocytomas: Mobile lipid accumulation in necrotic tissue. *NMR Biomed.* **7**: 149-155, 1994.

Lewis TLT and Chamberlain GVP, eds. Gynaecology by ten teachers. Edward Arnold, London, 15th ed. 1989, 43-44, 142-156, 160-161, 222, 226.

Lipson SA and Hricak H. MR imaging of the female pelvis. *Radiol. Clin. North Am.* **34**: 1157-1182, 1996.

Look KY. Epidemiology, etiology, and screening of ovarian cancer. In *Ovarian Cancer.* SC Rubin and GP Sutton, eds. McGraw-Hill Inc., New York, 1993, 181-184.

Lynch HT, Schuelke GS, Wells IC, Cheng S-C, Kimberling WJ, Biscone KA, Lynch JF, Danes BS. Hereditary ovarian carcinoma; Biomarker studies. *Cancer* **55**: 410-415, 1985.

Mack TM, Cozen W, Quinn MA. Epidemiology of cancer of the endometrium, ovary, vulva and vagina. In *Gynecologic Oncology.* M Coppleson, ed. Churchill Livingstone, Edinburgh, 2nd ed. Vol. 1, 1992, 38-39.

Mackinnon WB, Russell P, May GL, Mountford CE. Characterisation of human ovarian epithelial tumours (*ex vivo*) by proton magnetic resonance spectroscopy. *Int. J. Gynecol. Cancer* **5**: 211-221, 1995.

McGuire WP. Primary chemotherapy of epithelial ovarian cancer. In *Ovarian Cancer.* SC Rubin and GP Sutton, eds. McGraw-Hill Inc., New York, 1993, 255.

Medl M, Kulenkampff KJ, Stiskal M, Peters-Engl C, Leodolter S, Czembirek H. Magnetic resonance imaging in the preoperative evaluation of suspected ovarian masses. *Anticancer Res.* **15**: 1123-1126, 1995.

Miller BF and Brackman Keane C. Encyclopedia and dictionary of medicine, nursing, and allied health. W.B. Saunders Company, Philadelphia, 4th ed. 1987.

Miralles RM. Pelvic masses and endoscopic surgery: diagnosis. *Eur. J. Obstet. Gynecol. Reprod. Biol.* **65**: 75-79, 1996.

Mishell DR, Nakamura RM, Grosignani PG, Stone S, Kharma K, Nagata Y, Thorneycroft IH. Serum gonadotropin and steroid patterns during the normal menstrual cycle. *Am. J. Obstet. Gynecol.* **111**: 60-65, 1971.

Moore DH. Primary surgical management of early epithelial ovarian carcinoma. In *Ovarian Cancer.* SC Rubin and GP Sutton, eds. McGraw-Hill Inc., New York, 1993, 219, 222-225.

Moreno A, Mercé R, Montane JM, Alonso J, Arús C. ^{1}H NMR spectroscopy of colon tumors and normal mucosal biopsies; Elevated taurine levels and reduced polyethyleneglycol absorption in tumors may have diagnostic significance. *NMR Biomed.* **6**: 111-118, 1993.

Morrow CP. Malignant and borderline epithelial tumors of ovary: Clinical features, staging, diagnosis, intraoperative assessment and review of management. In *Gynecologic Oncology.* M Coppleson, ed. Churchill Livingstone, Edinburgh, 2nd ed. Vol. 2, 1992, 910-911.

National Cancer Institute of Canada: Canadian Cancer Statistics 1998, Toronto, Canada, 1998.

NIH Consensus Statement. Ovarian cancer: Screening, treatment, and followup. April 5-7, 1994, **12**: 1-30.

Occhipinti KA. Magnetic resonance imaging of abnormal pelvic anatomy. In *Imaging in Infertility and Reproductive Endocrinology.* R Jaffe, RA Pierson, JS Abramowicz, eds. Lippincott Company, Philadelphia, 1994, 262-263.

Occhipinti KA, Frankel SD, Hricak H. The ovary: Computed tomography and magnetic resonance imaging. *Radiol. Clin. North Am.* **31**: 1115-1132, 1993.

O'Keane JA. Aging and reproduction: The biological clock – an alarming experience? *J. Soc. Obstet. Gynecol. Can.* **18**: 755-763, 1996.

Ordidge RJ and Cresshull ID. The correction of transient B_o field shifts following the application of pulsed gradients by phase correction in the time domain. *J. Magn. Reson.* **69**: 151-155, 1986.

Outwater EK and Dunton CJ. Imaging of the ovary and adnexa: Clinical issues and applications of MR imaging. *Radiology* **194**: 1-18, 1995.

Outwater EK, Talerman A, Dunton CJ. Normal adnexa uteri specimens: Anatomic basis of MR imaging features. *Radiology* **201**: 751-755, 1996.

Perez RP, Hamilton TC, Ozols RF. Chemotherapy resistance in ovarian cancer. In *Ovarian Cancer.* SC Rubin and GP Sutton, eds. McGraw-Hill Inc., New York, 1993, 39.

Pierson RA and Chizen DR. Transvaginal ultrasonographic assessment of normal and aberrant ovulation. In *Imaging in Infertility and Reproductive Endocrinology.* R Jaffe, RA Pierson, JS Abramowicz, eds. Lippincott Company, Philadelphia, 1994, 129-133.

Pierson RA, Chizen DR, Olatunbosun OA. The role of ultrasonography in ovulation induction. In *Imaging in Infertility and Reproductive Endocrinology.* R Jaffe, RA Pierson, JS Abramowicz, eds. Lippincott Company, Philadelphia, 1994, 155, 176.

Prayer L, Kainz C, Kramer J, Stiglbauer R, Schurawitzki H, Baldt M, Schima W, Poelzleitner D, Reinthaller A, Koelbl H, Imhof H. CT and MR accuracy in the detection of tumor recurrence in patients treated for ovarian cancer. *J. Comput. Assist. Tomogr.* **17**: 626-632, 1993.

Romero JA, Kim EE, Tresukosol D, Kudelka AP, Creighton LE, Kavanagh JJ. Recurrent ovarian endodermal sinus tumor: demonstration by computed tomography, magnetic resonance imaging, and positron emission tomography. *Eur. J. Nucl. Med.* **22**: 1214-1217, 1995.

Scott RT and Hofmann GE. Prognostic assessment of ovarian reserve. *Fertil. Steril.* **63**: 1-14, 1995.

Scoutt LM and McCarthy SM. Female pelvis. In *Magnetic Resonance Imaging.* DD Stark and WG Bradley, eds. Mosby-Year Book Inc., St. Louis, Missouri, 2nd ed. Vol. 2, 1992, 1978-1982.

Semelka RC, Ascher SM, Reinhold C. MRI of the abdomen and pelvis; A text-atlas. John Wiley and Sons Inc., New York, 1997, 654, 663.

Sloane E. Biology of Women. John Wiley and Sons Inc., New York, 2nd ed. 1985, 289-291, 388, 390-391, 490-493.

Speroff L, Vande Wiele RL. Regulation of the human menstural cycle. *Amer. J. Obstet. Gynec.* **109**: 234-247, 1971.

Star-Lack JM, Adalsteinsson E, Gold GE, Spielman DM. Motion correction and lipid suppression for in vivo 1H MRS – Applications to the study of the human kidney and liver. In *Proc. Int. Soc. Magn. Reson. Med.* Vol. 1, 1998, 356.

Stark HA and Haacke EM. Helmet and cylindrical shaped CP array coils for brain imaging: A comparison of signal-to-noise characteristics. In *Proc. Int. Soc. Magn. Reson. Med.* Vol. 3, 1996, 1412.

Sutton GP. Ovarian tumors of low malignant potential. In *Ovarian Cancer.* SC Rubin and GP Sutton, eds. McGraw-Hill Inc., New York, 1993, 425-426, 429, 440-441.

Symonds EM, Powell MC, Worthington BS. Magnetic resonance imaging (MRI), computerized axial tomography (CAT) and immunoscintigraphy. In *Gynecologic Oncology.* M Coppleson, ed. Churchill Livingstone, Edinburgh, 2nd ed. Vol. 1, 1992, 372-373.

Takahashi T, Iizuke C, Shimizu H, Yasugi K, Matsunaga Y. 8-element QD domed head array coil using inductive decouplers. In *Proc. Int. Soc. Magn. Reson. Med.* Vol. 3, 1998, 2028.

Talerman A. Germ cell tumors of the ovary. In *Blaustein's Pathology of the Female Genital Tract.* RJ Kurman, ed. Springer-Verlag, New York, 3rd ed. 1987, 659, 686.

Wallace JC, Raaphorst GP, Somorjai RL, Ng CE, Fung Kee Fung M, Senterman M, Smith ICP. Classification of ^{1}H MR spectra of biopsies from untreated and recurrent ovarian cancer using linear discriminant analysis. *Magn. Reson. Med.* **38**: 569-576, 1997.

Willson JR. Ultrasonography in the diagnosis of gynecologic disorders. *Am. J. Obstet. Gynecol.* **164**: 1064-1071, 1991.

SUMMARY OF THESIS

In this thesis, application of magnetic resonance imaging and spectroscopy to structures in the female pelvis was examined. In particular, the suitability of MRS for the grading of pre-cancerous lesions of the uterine cervix was determined, and a technique for acquisition of *in vivo* MR spectra of the human ovary was developed.

It was shown that the differences in the MR spectra obtained from non-dysplastic and dysplastic cervical tissue could not be determined by visual examination or a simple analysis of peak ratios. Classification of the spectra according to the clinical diagnoses was performed using multivariate methods. A set of the spectra was consistently misclassified by each of the different multivariate methods. From this, it was concluded that either the clinical diagnosis, the gold standard to which the spectral classifications were compared, was flawed, or the MRS technique detected biochemical changes that preceded the morphological changes. It was also shown that the accuracy of classification of spectra into two adjacent classes was comparable to that of non-adjacent classes. The results obtained here do not support, but can not refute, the theory that cervical lesions follow a continuous progression from CIN 1 to CIN 3.

In vivo MRS of the human ovary was performed using the whole body coil for excitation because it gave uniform excitation within the pelvis. A circularly polarized surface coil was used to receive the signal rather than the whole body coil because it gave better signal to noise ratios. Location of premenopausal ovaries was accomplished using

T_2-weighted images, and postmenopausal ovaries, though difficult to locate, were identified in T_1-weighted images. MRS of the ovary was complicated by motion in the pelvis. Displacement of the ovaries was caused predominantly by filling of the urinary bladder. It was shown that periodic acquisition of fast scout images could be used to track the motion of the ovaries. Repositioning of the voxel after every set of scout images ensured that the MR signal was obtained from the ovaries and not the surrounding tissue. Motion in the pelvis was also shown to cause frequency shifts and phase changes in the individual acquisitions of the FID. Correction of these shifts and phase changes prior to averaging yielded a significant improvement in the signal to noise ratio in the spectra. It was concluded that the techniques developed in this thesis can be used to obtain *in vivo* MR spectra of the human ovary and ovarian abnormalities.

In conclusion, magnetic resonance imaging and spectroscopy was used to examine structures in the female pelvis. This thesis has shown that ^{1}H MRS, in conjunction with multivariate methods, provides information regarding the progression of dysplastic lesions of the uterine cervix. It was also concluded that the techniques developed in this thesis may be used to obtain *in vivo* MR spectra from the human ovary.

APPENDIX I:

MULTIVARIATE METHODS

I.1 Enhanced Forward Selection (EFS)

The biochemical content of healthy tissue differs from that of unhealthy tissue. These differences are observable in magnetic resonance spectra via the presence of different peaks and/or the variation in intensity of the peaks in spectra obtained from different tissue types. Often these differences are too subtle to detect with the human eye. Enhanced forward selection (EFS) is a computer algorithm that determines which points in the spectra are diagnostic (Nikulin *et al.* 1998). From these points, the spectra may be separated into diagnostic classes which correspond to the different tissue types.

Consider a spectrum containing M points. The enhanced forward selection (EFS) algorithm developed by Nikulin *et al.* (1998) can be used to find a subset, K, of these points that will allow differentiation of the spectra into diagnostic classes. Initially, each point is individually placed in a set ($\Omega_1=\{1\}$, ..., $\Omega_M=\{M\}$) and tested to determine its ability to classify the spectra correctly. An objective (fitness) function, F, is used to rank the classification accuracy of a subset of the original complete set of points. This function is a test of the between group differences and is given by:

$$F = \frac{1}{N \bullet C} \sum_{q=1}^{C} \sum_{j=1}^{N} (p_{jq} - l_{jq})^2$$

N is the total number of spectra, C is the number of diagnostic classes, p_{jq} is the probability that spectrum j is in class q, and l_{jq} is the class indicator, such that l_{jq} is equal to one if spectrum j is in class q, and is equal to zero for spectrum j in all other classes. The value of p_{jq} is determined by linear discriminant analysis (LDA) using the leave-one-out (LOO) method as described below. Objective functions are then determined with two points in each set: $\Omega_1=\{1, \alpha_1^{(2)}\}$, ..., $\Omega_M=\{M, \alpha_M^{(2)}\}$, where $\alpha_i^{(2)}$ is not equal to the first point in the set. Each set is updated with the point that gives the lowest value of the objective function in combination with the point already present in the set. The process is repeated for a specified number of K points in each set ($\Omega_J=\{J, \alpha_J^{(2)} \ldots \alpha_J^{(K)}\}$). Normally, K is limited to 10 or less. At larger values of K, classification results tend to be excellent on the training set and poor on the test set. After the selection process is complete, the best set of points is chosen for diagnostic classification of the spectra.

While EFS is robust, it has some limitations. First, EFS does not test every combination of points and does not allow backtracking. As a result, it does not guarantee that the best set of points will be found. Nevertheless, it always produces a good suboptimal subset. Second, EFS chooses points in the spectra. It does not have the flexibility to merge or overlap these points, and can not choose regions of varying widths. A genetic algorithm, which allows determination of regions of varying widths, has been developed (Nikulin *et al.* 1998), but was not used for this work. Finally, EFS is relatively slow. It requires approximately 30 minutes on a SGI workstation to choose 10 diagnostic points out of 100.

I.2 Linear Discriminant Analysis (LDA)

A spectrum with p points, or attributes, can be considered a data vector $\mathbf{x} = (x_1, x_2, \ldots, x_p)$ with p attributes. A set of LDA coefficients are obtained. These coefficients are based on the pooled covariance matrix and the class centroids computed from the training set (James 1985), such that one coefficient vector, α, exists per class. In order to determine the probability of a single spectrum belonging to a class c, a discriminant function, d_c, is calculated for each class such that:

$$d_c = \alpha_{oc} + \sum_{n=1}^{p} \alpha_{nc} x_n$$

The largest d_c computed for the c classes is called d_{max}. The discriminant functions of the classes make p-dimensional sample spaces. The surface that separates the p-dimensional sample spaces is a (p-1)-dimensional hyperplane. It is assumed that the distribution of the sample spaces is Gaussian. Hence, the following is computed for each class:

$$g_c = \exp(d_c - d_{max})$$

d_{max} is not essential, however it helps to prevent computational overflow. The probability of a single spectrum belonging to class c is determined by the partition function:

$$p_c = \frac{g_c}{\sum_c g_c}$$

Linear discriminant analysis was performed using the leave-one-out method of cross validation (Lachenbruch 1975). This method involves leaving out one spectrum at a time from the original training set. The coefficients, α, and the discriminant function,

d_c, are computed, and the omitted spectrum is classified using these values to determine the probability of belonging to each of the c classes, p_c. The spectrum is assigned to the class with the highest p_c. Each spectrum in the test set is then submitted to the classifier and assigned to one class in the same manner. A counter for the assigned class is incremented for the current test spectrum. This method is repeated leaving out each spectrum from the original training set. The class probabilities for the spectra in the test set are the final values of the counters for each class divided by the number of training spectra (method unpublished; developed by R. Somorjai).

I.3 Artificial Neural Networks Using Backpropagation

Artificial neural networks (ANN) attempt to model networks of neurons in the brain. For classification problems, the neurons are commonly grouped into layers. Typically, two layers are used, as shown in Figure I.1. Data vectors are submitted in parallel via N input connections. In the first stage of computation, the inputs are weighted using a random set of weights, w_{jp}, and the weighted inputs are combined to produce M outputs, or scores. These scores are passed to the first layer of neurons, y_j, called the hidden layer. Each neuron in the hidden layer is activated in accordance with the input to the neuron, the activation function, and the threshold of the neuron. Once activated, the neurons are again weighted with another random set of weights, W_{ij}, and combined to produce the neurons of the output layer, O_i. The output layer has one output, or classification probability, for each of the classes. Each neuron in the output layer is compared to the expected output for the class, and the error is determined. Training of the neural net involves minimization of this error. Based on the error,

changes to the weights of the output layer, ΔW_{ij}, are determined. The weights of the hidden layer, Δw_{jp}, are also determined, and their value is calculated in terms of ΔW_{ij}. Thus, the errors are propagated backwards. With the new and updated weights, the outputs are again calculated in a feed-forward manner. The training of the neural net via the process of updating the weights and recalculation of the outputs is repeated for a user-specified number of iterations.

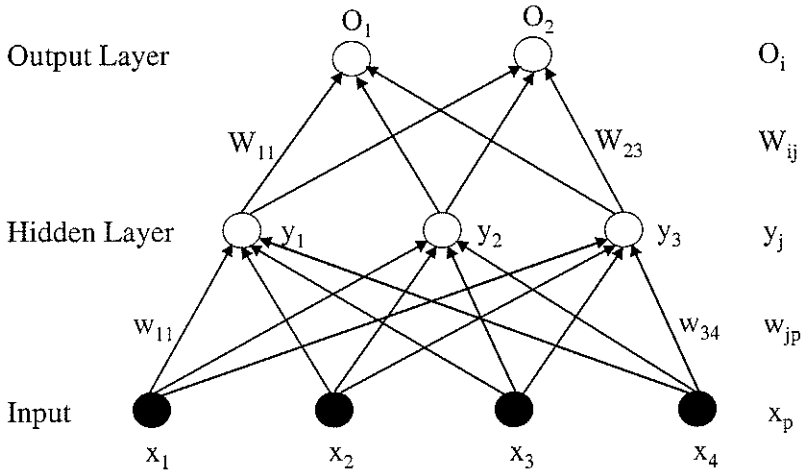

Figure I.1: Two-layered ANN with one hidden layer showing the notation for units and weight, where x_p is the input data vector, w_{jp} is the weighting coefficient between the input and hidden layers, y_j is the output from the hidden layer, W_{ij} is the weighting coefficient between the hidden and final layers, and O_i is the output in the final layer. (Adapted from Hertz *et al.* 1991)

Consider a two-layer network as illustrated in Figure I.1. Each spectrum can be considered an input data vector, **x,** and the spectral points are attributes of the vector.

The attributes of **x** are weighted and summed to form the input for each component, j, of the hidden layer H according to:

$$h_j = \sum_p w_{jp} x_p + \theta_j$$

where w_{jp} is the weighting coefficient, and θ_j is a threshold value.

The inputs, h, to the hidden layer are passed through a non-linear equation to produce the outputs of the hidden layer, **y**. In this case, the non-linear equation is the hyperbolic tangent:

$$y_j = \tanh(h_j)$$

The output values of the hidden layer are weighted according to a new weighting coefficient, **W**, and summed to form the input for each component, i, of the final layer.

$$H_i = \sum_j W_{ij} y_j + \theta_i$$

The number, i, of neurons in the final layer is equal to the number of classes. The values H_i are once again passed through the hyperbolic tangent to yield the output in the final layer:

$$O_i = \tanh(H_i)$$

Training the network requires optimization of the weighting coefficients. The back-propagation algorithm accomplishes this via the gradient descent rule which increments the coefficients by the gradient of an error function. The error function, E, is determined via:

$$E = \frac{1}{2} \sum_i [\Phi_i - O_i]^2$$

$$E = \frac{1}{2}\sum_i \left[\Phi_i - \tanh\left(\sum_j W_{ij} \tanh\left(\sum_p w_{jp} x_p \right) \right) \right]^2$$

where Φ_i is the expected output for class i.

The gradient descent rule increments the weighting coefficients, **W**, by a value ΔW proportional to the gradient of the error function, E, according to:

$$\Delta W_{ij}(t) = -\varepsilon \frac{\partial E}{\partial W_{ij}} + \mu \Delta W_{ij}(t-1)$$

where W(t-1) is the previous weight change, and ε and μ are constants called the learning rate and momentum parameter, respectively. The learning rate controls the amount by which increments to the coefficient are made, and the momentum parameter has the effect of using the history of past weight changes to influence the current change.

The weighting coefficients, **w**, applied between the input layer and the hidden layer are also optimized. The increments for these weighting coefficients, Δw, may be written in terms of ΔW. Hence the errors, are propagated backwards through the weighting coefficients. The newly determined weighting coefficients are applied, and the outputs are again calculated in a feed-forward manner. This process of forward computation of the outputs **O** and backwards computation of the errors in the weighting coefficients is carried out multiple times. Figure I.2 illustrates this process, with the solid arrows showing the forward propagation of the outputs and the dashed arrows showing the back-propagation of the errors.

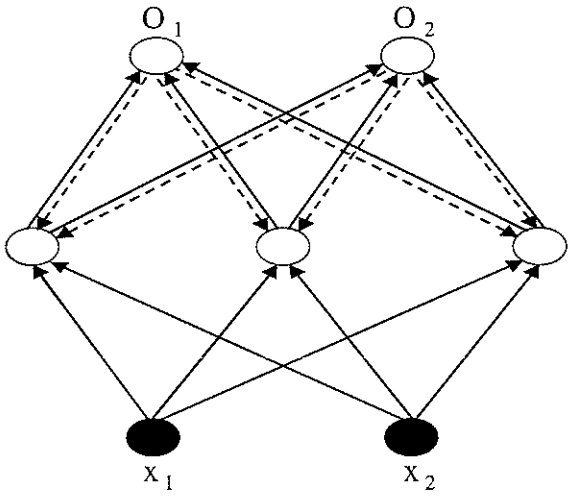

Figure I.2: Back-propagation with one hidden layer. The solid lines show forward propagation of the inputs, and the dashed lines show backward propagation of the modified weighting coefficients. (Adapted from Hertz *et al.* 1991)

I.4 Computerized Consensus Diagnosis

Computerized consensus diagnosis attempts to minimize classification errors by considering simultaneously the outputs of more than one classifier. In this study, two methods were used to combine the results from the LDA and the ANN classification – Wolpert's stacked generalization method and the median method. Both of these methods use LDA for classification of the spectra, however, the inputs for the methods are different. In Wolpert's method, the inputs are the classification probabilities determined by LDA and ANN. The number of elements in each input data vector is the number of classification methods times the number of diagnostic classes. In the median method, the inputs are the medians of the classification probabilities determined by LDA and ANN,

and hence the number of elements in each input data vector is the number of diagnostic classes (Somorjai *et al.* 1995, Private communications with B. Dolenko).

I.5 References

Hertz J, Anders K, Palmer RG. Introduction to the theory of neural computation. Addison-Wesley Publishing Company, Redwood City, California, 1991, 115-120.

Lachenbruch PA. Disciminant Analysis. Hafner Press, 1975, 36-37.

Lippman RP. An introduction to computing with neural nets. *IEEE ASSP Magazine* April, 1987, 4-22.

James M. Classification algorithms. Collins, London, 1985, 1-29.

Nikulin AE, Dolenko B, Bezabeh T, Somorjai RL. Near-optimal region selection for feature space reduction: Novel preprocessing methods for classifying MR spectra. *NMR Biomed.* (in press), 1998.

Pao Y-H. "Adaptive Pattern Recognition and Neural Networks. Addison-Wesley Publishing Company, Inc., Reading, Massachusetts, 1989, 120-129.

Somorjai RL, Nikulin AE, Pizzi N, Jackson D, Scarth G, Dolenko B, Gordon H, Russell P, Lean CL, Delbridge L, Mountford CE, Smith ICP. Computerized consensus diagnosis: A classification strategy for the robust analysis of MR spectra. I. Application to ^{1}H spectra of thyroid neoplasms. *Magn. Res. Med.* **33**: 257-263, 1995.

APPENDIX II:

IDL PROGRAM FOR SPECTRAL ANALYSIS

The program is located on the attached compact disc.

The program can be initiated by typing '@spec' from within IDL.

APPENDIX III:

GLOSSARY

anteverted Tipped forward.

ascites Abnormal collection of fluid in the pelvic cavity.

atretic Degeneration and absorption of cells.

basal lamina The membrane that surrounds the granulosa cells and an oocyte in the ovary. This membrane contains the follicular cyst.

broad ligaments Two of the eight ligaments that hold the uterus in place. These ligaments extend from the walls of the uterus to the lateral pelvic walls.

CA-125 An antigen that was initially found to have elevated concentrations in malignant, epithelial, ovarian tumours but was subsequently found to have elevated levels in many healthy women as well.

carcinoma in situ (CIS) A lesion composed of abnormal cells of irregular order that extends through the entire epithelial layer but does not invade the basement membrane and underlying mucosa.

caudal Toward the inferior part of the body.

cervical intraepithelial neoplasia (CIN) Change in the size, shape, and/or organization of cells in the epithelial layer of the cervix. Also called squamous intraepithelial lesion (SIL).

cervicitis Inflammation of the uterine cervix.

coitus Sexual intercourse involving penetration of the vagina.

colposcopy Examination of the uterus and cervix by means of a magnifying lens.

columnar epithelium Epithelial cells that are much greater in height than in width.

condyloma A wart-like lesion that is elevated from the surface layer of the tissue.

coronal The plane that extends through the body from the left to right side and from superior to inferior.

corpus luteum Cyst that forms on the ovary after maturation and ovulation of the follicular cyst. This cyst is rich in lutein, a yellow, fat-soluble hydrocarbon pigment.

cranial Toward the head, or superior portion of the body.

crisp classification The percentage of the total number of spectra classified correctly by a multivariate method with high probability (≥75%)).

cytology The study of the size and shape of cells.

dermoid cyst Abnormal cysts on the ovaries that are normally rich in lipids and heterogeneous, commonly containing skin, sebaceous and sweat glands, hair, cartilage, muscle, and/or calcium deposits.

dominant follicle The follicular cyst on the ovary that will reach maturity and rupture at the time of ovulation.

dysplasia Changes in the size, shape, and/or organization of cells to a form that is abnormal.

endocervix The canal of the uterine cervix which extends from the cervical connection of the vagina to the opening of the uterus.

exocervix The lower portion of the uterine cervix which extends downward into the vagina.

external os The opening to the exocervix.

endometriosis A disease in which cells from the endometrium, or inner lining of the uterus, are found in the form of growths, or lesions, outside of the uterus. These lesions are commonly found on the ovaries.

epithelium The cellular covering of the body and organs of the body.

follicular cyst A fluid filled cavity in the ovary containing an oocyte and the surrounding granulosa cells.

follicular phase The time during the menstrual cycle between the end of the luteal phase and the beginning of the ovulatory phase when the follicular stimulating hormone induces growth of follicular cysts in the ovaries.

follicular stimulating hormone (FSH) A hormone produced by the pituitary gland that is responsible for simulating growth of follicular cysts in the ovaries.

granulosa cells The cells that surround the oocyte in the ovary.

histopathology The study of the minute structure, composition, and function of tissue.

human papillomavirus (HPV) A DNA virus that infects the skin, mucous membranes, oral cavity, larynx, trachea, esophagus, bladder, anus, and genital tract of both women and men. It may manifest as koilocytosis and/or condyloma on the cervix. There are over 90 types of HPV, of which approximately 20 types infect the cervix.

inferior Situated below or towards the feet of the body.

infundibulpelvic ligament A ligament that extends from the pelvic brim to the superior aspect of the lateral side of the ovary and contains the vessels that supply blood to the ovary. Also called the suspensory ligament.

keratin A protein found in the epithelium of the exocervix.

koilocytosis Wart-like lesions with hollowed or concave cellular structure.

lateral Toward the right or left side of the body.

luteal phase The time during the menstrual cycle between the end of the ovulatory phase and the beginning of the follicular phase when growth of the corpus luteal cyst occurs.

luteinizing hormone A hormone produced by the pituitary gland that is responsible for stimulating ovulation as well as growth of the corpus luteum in the ovaries.

menses The cyclic shedding of the lining of the uterus and bleeding that occurs at the end of the menstrual cycle. Also known as menstruation, or the period.

metaplasia A change of adult cells into an abnormal form that is not malignant.

morphology The study of the form and structure of an organ.

mucosa The tissue layer that lies underneath the epithelium.

neoplasia The formation of an abnormal growth in which cell multiplication is uncontrolled and progressive. The growth may be benign or malignant.

nulliparous Describing a woman who has not been pregnant.

oocyte An immature egg in the ovary.

ovarian ligament The ligament that extends from the medial side of the ovary to the wall of the uterus slightly inferior to the insertion of the fallopian tube.

ovarian reserve The number and quality of oocytes present in the ovaries.

over sampling An MR imaging technique in which a larger field of view is sampled than is required in order to reduce aliasing artifacts in the region of interest.

ovulatory phase The time during the menstrual cycle between the end of the follicular phase and the beginning of the luteal phase when ovulation occurs.

parous Describing a woman who has been pregnant at least once.

pathology The study of the nature of disease.

peristalsis The wormlike movement of the bowel by which the contents are propelled along the bowel. It consists of a wave of contraction passing along the tube.

polycystic ovarian disease Enlargement of the ovaries to two to five times their normal size as well as the presence of an abnormally large number of small follicular cysts that vary in size but seldom exceed 5mm in diameter.

prone Lying face downward.

reactive changes A term used to describe abnormal changes in the shape, size, and organization of the cells in the cervix. These changes are not dysplastic.

reproductive potential The ability of a woman to conceive.

retroverted Tipped backwards.

sagittal The plane that extends through the body from superior to inferior and from posterior to anterior.

sensitivity The conditional probability that the presence of an abnormality will be correctly diagnosed. The number of true positive results divided by the sum of the number of true positive results and the number of false negative results.

specificity The conditional probability that the absence of an abnormality will be correctly diagnosed. The number of true negative results divided by the sum of the number of true negative results and the number of false positive results.

squamocolumnar junction The location on the uterine cervix where the endocervical canal and the vaginal surface of the exocervix meet. Also called the transformation zone. It contains both squamous and columnar cell types.

squamous cancer Cancer that originates in the epithelial tissue layer.

squamous intraepithelial lesion (SIL) Change in the size, shape, and/or organization of cells in the epithelial layer of the cervix. Also called cervical intraepithelial neoplasia (CIN).

stratified squamous epithelium The cellular covering of the body and organs of the body. The cells are arranged in layers with the top layer being squamous, or flattened.

stroma The tissue forming the ground substance, or framework of an organ.

stromal hyperthecosis An increase in the size of the ovaries due to growth of normal cells and excessive accumulations of lutein in the cells of the stromal layer.

superior Situated above or towards the head of the body.

supine Lying face upwards.

suspensory ligament A ligament that extends from the pelvic brim to the superior aspect of the lateral side of the ovary and contains the vessels that supply blood to the ovary. Also called the infundibulopelvic ligament.

transformation zone The location on the uterine cervix where the endocervical canal and the vaginal surface of the exocervix meet. Also called the squamocolumnar junction.

transverse The plane that extends across the body from the left to right side and from posterior to anterior.

uterine fundus The part of the uterus that is farthest away from the vagina.

Reference:

Miller BF and Brackman Keane C. Encyclopedia and Dictionary of Medicine, Nursing, and Allied Health. W.B. Saunders Company, Philadelphia, 4th ed. 1987.